



Dissertation

Energy Harvesters and Low Power MEMS Strain Sensors for Wind Turbine Applications

Zur Erlangung des akademischen Grades
Doktor der technischen Wissenschaften (Dr. techn.)

Institut für Sensor- und Aktuatorssysteme
Technische Universität Wien

Dipl. Ing. Matthias Schlögl
Matrikelnummer 0626613

Wien, 2023

Rigorosum: Wien, März 2023

Betreuer:

Univ.-Prof. Dr.rer.nat. Ulrich Schmid
Technische Universität Wien, Österreich

Gutachter:

Prof. Dr.-Ing. Marc Christopher Wurz
Leibniz Universität Hannover, Deutschland

Univ.-Prof. Dr.sc. Silvan Schmid
Technische Universität Wien, Österreich

Abstract

This thesis is about the fabrication of a hybrid piezoelectric/electromagnetic energy harvester and a piezoelectric MEMS resonant strain sensor for wireless sensor nodes to monitor wind turbine rotor blades. In addition, piezoelectric materials, namely aluminum nitride and its alloyed variants AlScN and AlYN, are investigated for the piezoelectric energy harvesting component as well as for the low-power strain sensor.

The optimal sputter deposition conditions of aluminum nitride alloyed with scandium and yttrium were studied by varying power, pressure and gas composition. The microstructure of the resulting thin films was analyzed by X-ray diffractometry, scanning electron microscopy, transmission electron microscopy and energy dispersive X-ray spectroscopy whereas the best thin films showed a highly c-axis oriented, columnar crystal structure for both alloying elements. Additionally, the piezoelectric coefficient d_{33} and the intrinsic thin film stress σ were characterized. For the first time, piezoelectric $Al_{0.91}Y_{0.09}N$ thin films were sputter deposited, showing an increased d_{33} of 7.79 pC N^{-1} compared to pure AlN and matching the theoretical predictions of density functional theory predictions. The $Al_{0.71}Sc_{0.29}N$ thin films showed also increased piezoelectric values, similar to those published in research. Both alloying materials showed a very high compressive stress of more than 1 GPa which led to the development of a new stress tailoring sputter process. Through this process it was possible to reduce the compressive intrinsic stress by 76% for pure AlN and by 50% for $Al_{0.71}Sc_{0.29}N$. Simultaneously, the piezoelectric coefficients were slightly increased by 14% and 9% for AlN and $Al_{0.71}Sc_{0.29}N$, respectively. These material-related results were the basis for their integration into piezoelectric harvesters and the MEMS strain sensors.

The hybrid energy harvester is specifically designed for the use in a rotor blade of a wind turbine with a targeted output power of 10 mW . It contains a piezoelectric harvesting element based on a cantilever structure including a magnetic proof mass, which gets excited through magnetic plucking initiated through the electromagnetic harvesting element containing a bigger movable permanent magnet. The piezoelectric harvester is fabricated at the institute's cleanroom facilities. Next, the hybrid energy harvester is characterized in the lab by measuring the output voltage and output power of the two harvesting elements separately. Additionally, it was successfully tested in a real-world wind turbine over a period of four days.

The MEMS strain sensor is based on a piezoelectric microbridge resonator, whereas the piezoelectric material is used for excitation and sensing. Different MEMS microbridge designs were fabricated with varying length, width and thickness. The mechanical frequency spectra as a function of strain and the mode shapes of the sensor devices were characterized by laser Doppler vibrometry. Additionally, the devices were electrically characterized by impedance spectroscopy, with special focus on the conductance spectra as a function of strain. Both measurement techniques were compared to each other and the influence of the device dimensions on both measurement techniques were analyzed in detail. A frequency dependent gauge factor of the strain sensor was developed, showing very high values up to 6 500, representing a fourfold increase to current state-of-the-art strain sensors. The Q-factor as a function of strain was measured and showed an interesting behavior, especially for devices with increased width. Additionally, several effects like buckling due to the presence of a high, compressive thin film stress, curve veering due to the varying influence of strain on different modes and non-linear resonance phenomena were studied. Finally, the previously mentioned stress-tailoring sputter deposition process was integrated to fabricate low stressed sensor devices. Those devices showed an improved sensor behavior with an increased gauge factor of up to 17 000, which represents, to the best of the author's knowledge, one of the highest measured gauge factors of strain sensors reported in literature.

Kurzfassung

Diese Arbeit beschreibt die Herstellung eines hybriden piezoelektrischen/elektromagnetischen *Energy Harvesters* und eines piezoelektrischen, resonanten MEMS-Dehnungssensors für den Einsatz in drahtlosen Sensorknoten zur Überwachung von Rotorblättern von Windturbinen. Zusätzlich wurde die Eignung von gesputtertem Aluminiumnitrid und entsprechende Legierungsvarianten auf Basis von Scandium und Yttrium auf ihren möglichen Einsatz in piezoelektrischen *Energy Harvestern* und *low-power* MEMS-Dehnungssensoren hin untersucht.

Die optimalen Abscheidebedingungen für gesputtertes Aluminiumnitrid, dem Scandium und Yttrium zulegiert wurde, wurde durch Variation von Plasmaleistung, Kammerdruck und Gaszusammensetzung ermittelt. Die Mikrostruktur der abgeschiedenen Dünnschichten wurde mittels Röntgendiffraktometrie, Raster-Elektronenmikroskopie, Transmissions-Elektronenmikroskopie und Energiedispersive Röntgenspektroskopie untersucht, wobei die besten Dünnschichten ein kolumnares Schichtwachstum und eine hohe c-Achsenorientierung aufweisen. Zusätzlich wurden der piezoelektrische Koeffizient d_{33} und der intrinsische Dünnschichtstress σ charakterisiert. Zum ersten Mal wurden $Al_{0,91}Y_{0,09}N$ -Dünnschichten mit piezoelektrischen Eigenschaften abgeschieden, wobei der d_{33} 7.79 pC N^{-1} betrug, wie von der Dichtefunktionaltheorie Berechnung vorhergesagt. Die $Al_{0,71}Sc_{0,29}N$ -Dünnschichten zeigten erhöhte piezoelektrische Koeffizienten mit Werten für den d_{33} , wie sie in der Literatur zu finden sind. Beide Legierungen zeigten sehr hohe, kompressive Stresswerte von über 1 GPa . Dies führte zur Entwicklung eines modifizierten Sputterprozesses, mit dem es möglich ist den intrinsischen Stress zu verringern. Dadurch konnten Schichten abgeschieden werden, bei denen die Druckverspannung in AlN um 76% und bei $Al_{0,71}Sc_{0,29}N$ um 50% reduziert wurde. Anschließend wurde versucht die Erfahrung aus diesem Teil der Arbeit in die Realisierung von piezoelektrischen *Energy Harvestern* und resonanten MEMS-Dehnungssensoren zu integrieren.

Der hybride *Energy Harvester* wurde speziell für den Einsatz in Rotorblättern von Windturbinen mit einer spezifizierten Ausgangsleistung von 10 mW entwickelt. Er beinhaltet einen piezoelektrischen *Harvester* basierend auf einem *Cantilever* mit einer zusätzlichen magnetischen Masse an der Spitze des *Cantilevers*. Er wird durch eine magnetische Impulsanregung in Schwingung versetzt, die durch den elektromagnetischen *Harvester*, der einen größeren beweglichen Permanentmagneten beinhaltet, erzeugt wird. Die Herstellung des piezoelektrischen *Energy Harvesters* wurde im institutseigenen Reinraum durchgeführt. Die Charakterisierung der beiden *Harvester* erfolgte separat im Labor durch Messung der Ausgangsspannung und der generierten Ausgangsleistung. Zusätzlich wurde ein erfolgreicher Feldtest in einer Windturbine über einen Zeitraum von vier Tagen durchgeführt.

Der MEMS-Dehnungssensor basiert auf einer piezoelektrischen, resonanten Mikrobrücke, welche in verschiedenen Dimensionen hergestellt wurde. Dabei wurde Länge, Breite und Dicke des Mikrobalkens variiert. Das mechanische Frequenzspektrum als Funktion der Dehnung und die Modenformen der Sensorelemente wurden mittels Laser-Doppler-Vibrometrie ermittelt. Zusätzlich wurde die elektrische Antwort des piezoelektrischen Materials durch Impedanzspektroskopie aufgenommen, wobei der Fokus auf dem Leitfähigkeitsspektrum als Funktion der von außen angelegten Dehnungswerte gelegt wurde. Beide Messtechniken wurden verglichen und der Einfluss der verschiedenen Geometrie Größen auf die Messergebnisse analysiert. Ein frequenzabhängiger Gauge Faktor wurde ermittelt, welcher sehr hohe Werte bis 6 500 zeigt, was einer vierfachen Erhöhung zu modernen Standard-Dehnungssensoren entspricht. Der gemessene Gütefaktor zeigte ein sehr interessantes und nicht vollständig erklärbares Verhalten, speziell bei Sensorelementen, welche sich in der Breite unterscheiden. Zusätzlich wurden Effekte wie das Beulen der Strukturen aufgrund des kompressiven Schichtstresses, *Mode Veering* aufgrund der unterschiedlichen Frequenzabhängigkeit der unterschiedlichen Moden von der Dehnung und nicht lineare Resonanzeffekte untersucht. Zum Abschluss wurde der vorher erwähnte Sputterprozess zur Herstellung von stressmodifizierten Dünnschichten verwendet. Die modifizierten Sensorelemente zeigten einen erhöhten Gauge Faktor von 17 000, was einem Vielfachen der in der Literatur gemessenen Gauge Faktoren entspricht.

Contents

- 1. Introduction..... 1
 - 1.1. Motivation 2
 - 1.2. Outline of the Thesis 4
- 2. State of the Art 5
 - 2.1 Piezoelectric Materials 5
 - 2.2 Energy Harvesting..... 7
 - 2.2.1. Gas Flow 7
 - 2.2.2. Thermal..... 8
 - 2.2.3. Light 8
 - 2.2.4. Radiofrequency 8
 - 2.2.5. Mechanical Energy Harvesting 9
 - 2.3 Strain Sensing 12
- 3. MEMS Fabrication Technologies and Experimental Methods 15
 - 3.1 Sputtering 15
 - 3.2 Characterization of piezoelectric constants 15
 - 3.3 X-Ray Diffractometry 16
 - 3.4 Electron Microscopy 18
 - 3.4.1. Scanning Electron Microscopy 18
 - 3.4.2. Transmission Electron Microscopy 18
 - 3.4.3. Electron Dispersive X-Ray 19
 - 3.5 Vibrational Excitation 19
 - 3.6 Laser Doppler Vibrometry 20
 - 3.7 Strain Measurement Setup 22
 - 3.8 Impedance Spectroscopy 23
 - 3.9 Quality Factor 24
- 4. Piezoelectric Thin Film Materials..... 25
 - 4.1 Aluminum Nitride 25
 - 4.2 Aluminum Scandium Nitride 27
 - 4.2.1. Deposition of AlScN thin films 27
 - 4.2.2. Structural Characterisation 28
 - 4.2.3. Electro-mechanical Characterization 31
 - 4.3 Aluminum Yttrium Nitride 34
 - 4.3.1. Deposition of AlYN thin films..... 34
 - 4.3.2. Structural Characterisation 35
 - 4.3.3. Oxygen Contamination of AlY and AlYN thin films 40

4.3.4. Electro-mechanical Characterisation	42
4.4 Stress Tailored Aluminum Nitride	45
4.4.1. Deposition of Aluminum Nitride Thin films.....	45
4.4.2. Microstructural and electro-mechanical characterization of AlN thin films.....	46
4.4.3. Stress Tailored Scandium Aluminum Nitride.....	50
4.5 Conclusions.....	52
5. Energy Harvester	53
5.1 Basic Considerations.....	53
5.2 Design Aspects.....	55
5.3 Piezoelectric Harvester.....	59
5.3.1. Cantilever Model	59
5.3.2. Fabrication.....	61
5.3.3. Harmonic Excitation	62
5.3.4. Magnetic Plugging	67
5.4 Electromagnetic Harvester	75
5.4.1. Design and Fabrication	75
5.4.2. Characterization	81
5.5 Measurements in a Wind Turbine.....	84
5.5.1. Hybrid Energy Harvester	84
5.5.2. Optimized Electromagnetic Harvester	87
5.6 Conclusions.....	90
6. Resonant MEMS Strain Sensors	91
6.1 Basic Sensor Design Considerations.....	91
6.2 Analytical Model.....	92
6.3 Design and Fabrication Aspects.....	94
6.3.1. Buckling	94
6.3.2. Electrode Design.....	95
6.4 LDV Measurements for MEMS Sensor Evaluation	97
6.4.1. Resonance Spectrum.....	97
6.4.2. Displacement.....	98
6.4.3. Non-Linear Effects	99
6.4.4. Influence of the Adhesive.....	99
6.5 Electrical Characterization.....	101
6.6 Design-dependent MEMS Sensor Performance	102
6.6.1. Length.....	102
6.6.2. Thickness	102
6.6.3. Width.....	103

6.7 Curve Veering	107
6.8 Q-Factor	109
6.9 Responsivity and Sensitivity	112
6.10 Influence of Intrinsic Thin Film Stress	115
6.10.1. Buckling	115
6.10.2. Frequency Response	116
6.10.3. Responsivity.....	117
6.11 Conclusions.....	119
7. Conclusions and Outlook.....	121
Bibliography.....	123
Abbreviations	143
Publications	145

1. Introduction

In 1990 the Intergovernmental Panel on Climate Change (IPCC) released their first assessment report where they stated that since the second industrial revolution in the late 19th century the global mean surface temperature (GMST) has increased by 0.3 – 0.6 °C [1], an unprecedented fast rise in the last 10 000 years. The reason for this can be found in the natural greenhouse effect due to emissions of greenhouse gases like CO_2 , methane, $CFCs$ and other gases coming from human activities. For the years to come they predicted, under a “Business as usual” approach an increase of 0.3 °C per decade. Furthermore, they gave predictions of implications for an increase in GMST in the range of 1.5 °C to 4.5 °C. Such an increase will lead to significant consequences in terrestrial ecosystems, water resources, human health, oceans and costal zones only to name the major areas. Over the following years the IPCC released several more assessment reports in 1995 [2], 2001 [3], 2007 [4], 2014 [5] and 2022 [6] to reassess the situations and to include more areas of interest where research became available.

During this time the assumption that manmade greenhouse gas emissions, especially CO_2 are mainly responsible for the current warming was more and more confirmed, compare Figure 1 with data taken from [7]. As a consequence, guidelines on how to counteract this threat were developed and as a reasonable goal a maximum increase of the GMST of 1.5 °C was set, which would keep the consequences on a manageable level.

As of now the governments of this world recognized the importance of acting against climate change but failed yet to agree on how to turn the recommendations into action. In December 2019 the European Commission announced the European Green Deal (EGD), which provides a roadmap for the European Union to translate their economy to achieve carbon neutrality by 2050 and fulfill their part to keep the GMST to 1.5 °C [8]. Beside the transformation of the transportation and agricultural sector, one of the key policies is the transition from carbon-based energy production like oil, coal or gas to sustainable energy sources like solar, wind, hydro or geothermal power only to name a few. Some forms of renewable energy sources have certain drawbacks, one of them being their non-continuous availability *e.g.*, solar energy can only be generated during daytime if the sun is shining or wind energy is only available when there is wind. Therefore, a mix of several technologies including a significant increase in energy storage capacity is necessary.

While the global primary energy consumption of renewable energy sources is estimated to be 27 870 *TWh* in 2020, it only represents 12.5% of the total energy consumption, shown in Figure 2 (a). One of the fastest growing energy sectors in the last decade was wind power with an annual share of 0.63% in 2010 and already 2.5% in 2020, compare Figure 2 (a) and (b) with data taken from [9]. For the close future the European Union released the “Fit For 55” package which targets an increased emission reduction of 55% by 2030 [10]. To realize this goal, it is estimated that EU total wind power capacity has to be increased to 451 *GW* from 180 *GW* in 2020 [11]. For the later

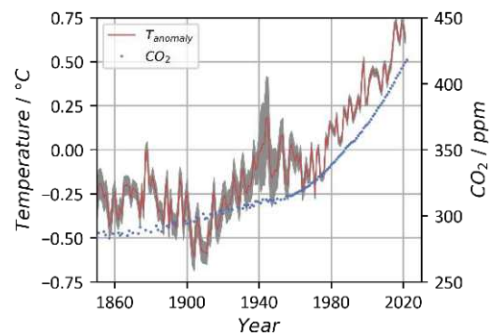


Figure 1: Yearly temperature anomalies, given as the deviation from 1951-1980 mean and atmospheric carbon dioxide concentration for the time period 1850-2020. Data taken from [7].

future the European Commission anticipates an increase in offshore wind power from 23 *GW* in 2019 to 250 *GW* by 2050.

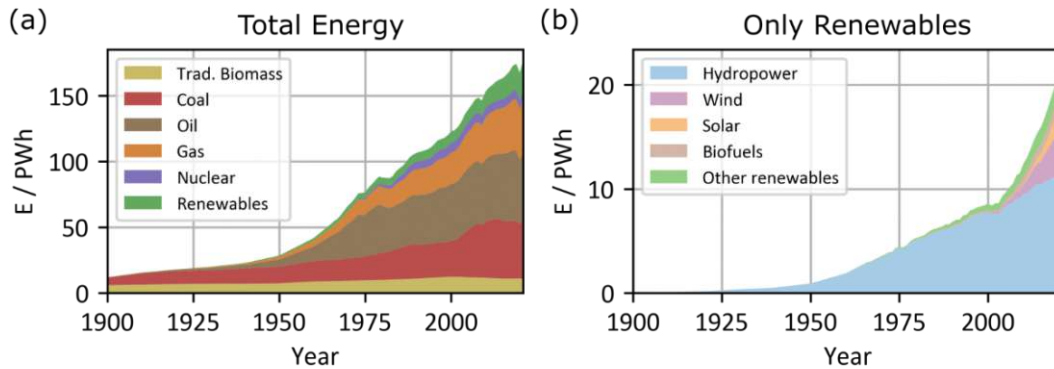


Figure 2: (a) Total global primary energy consumption and (b) global primary energy consumption of renewable energy sources between 1900 and 2021 generated from data taken from [9].

To realize these goals, it is not only necessary to expand renewable energy generation, but also to increase its efficiency and operational lifetime. If thinking about time frames of 30 years and more, it also has to be considered that every wind turbine built today, most probably will not be in operation by 2050 due to its estimated average lifetime of 20-25 years [12], which is also true to some extent for photovoltaic based power generation systems [13]. Therefore, a compact system which continuously monitors certain key parameters of the energy generators would be most beneficial to circumvent premature end-of-life, to find inefficiencies due to wear as well as tear and to reduce costs for maintenance and service.

1.1. Motivation

Wind turbines can be exposed to harsh weather conditions and therefore, must have a high tolerance to wear and tear. Additionally, regular maintenance is very important, due to various factors listed below, to keep the machines operational. However, not all wear and inefficiencies can be discovered by human inspection *e.g.*, delamination or cracks inside the rotor blade material made of carbon-reinforced fiber. Additionally, the power and size of a single wind turbine increases every few years [15], [16]. In 2020, 1.5 *MW* was state-of-the-art, whereas nowadays wind turbines with 10 – 12 *MW* offshore and 5 – 7 *MW* onshore are built, compare Figure 3 taken from [14]. This also means that a reduction of lifetime or a reduction of power output through wear and misalignment of the turbine will also increase ten-fold.



Figure 3: Historical and estimated wind turbine power and project size of offshore wind parks over a timeframe of 2000-2050 generated by the EU parliament [14]

An extensive but not complete list of multiple sources of wind turbine wear effects is given in the following:

- Delamination of rotor blade material [17]–[19]
- Fabrication errors (bubbles) in rotor blade material [20]–[22]
- Leading edge corrosion through precipitation [23], [24]
- Damage through icing [23]
- Lightning strikes [23]
- Wear and tear on the foundation structure [23]
- Corrosion (e.g. bolts of foundation or rotor blades) [25]
- Wear on bearings [26]
- Lubrication aging [27]

Through maintenance, wear caused by all of these sources is regularly controlled but depending on the maintenance intervals or time between occurrence and discovery of a beginning deterioration, the consequential damage can significantly increase service and repair costs if not detected as early as possible [28].

Another factor reducing the efficiencies of wind turbines are misalignments of blade pitch and turbine yaw. The blade pitch refers to a method where the rotor blade angle of attack is varied depending on wind speed to maintain constant torque on wind turbines [29], [30], schematically depicted in Figure 2 (a). The pitch misalignment is mainly a calibration error, occurring during installation and commissioning at the wind site and leads to an increased torque on the wind turbine during high wind speeds – reducing its life time – and reducing the power output during low wind speeds [31]. Yaw misalignment refers to a deviation of the wind turbine’s nacelle orientation and the wind direction, shown in Figure 2 (b). This deviation can have multiple sources, one of them being a physical misalignment between the nacelle’s orientational axis and the weathervane or anemometer axes, typically installed behind the rotor blades. Another reason comes from the suboptimal placement of the anemometer, which measures wind directions behind the rotor blades, where the air is turbulent, which influences and often falsifies the measured wind direction. Wind turbine manufacturers account for that with a nacelle transfer function. As the turbine ages this transfer function must be adapted, otherwise the error leads to an increase in yaw misalignment with time. In an ideal case the wind direction and speed are measured several meters in front of the wind turbine, where it is not already altered by the wind turbine itself and the according parameters are calibrated against these measurements. This can be achieved by so called LiDAR measurement campaigns, where the LiDAR is installed on top of the nacelle and measures all possible wind conditions during a period of several weeks to months. Afterwards the LiDAR is moved to the next turbine and so on. This process is extremely time-consuming and therefore very expensive [32].

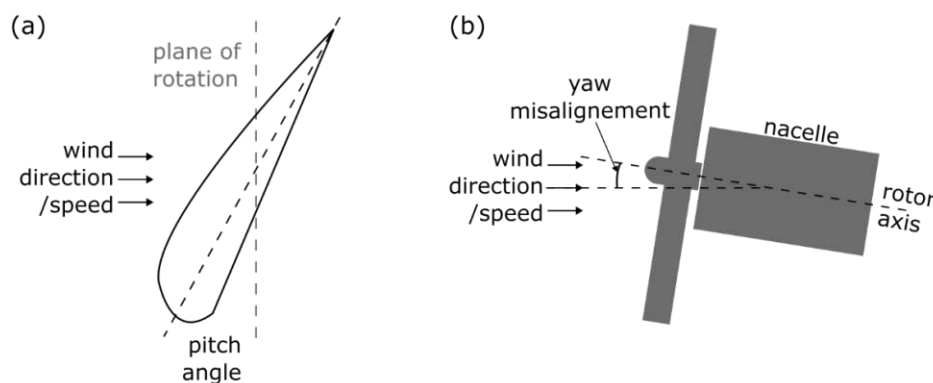


Figure 4: Schematic representation of (a) pitch misalignment and (b) yaw misalignment of a wind turbine and its rotor blades.

One approach to all these problems could be a monitoring system containing sensor nodes measuring various physical quantities in the wind turbine and its rotor blades, like temperature, humidity, acoustic emissions [33], vibrational frequency spectra [34], [35] or dynamic strain characteristics [36]. With such a system aging effects or even small damages can be detected instantly and wind turbines can be stopped or maintenance schedules can be adapted to prevent further damage. This has been researched intensively in the last decade and showed promising results [33], [34], [37]–[39]. However, there are two main challenges when such sensor nodes are deployed, data transfer and power supply. For sensor nodes installed inside the tower or the nacelle, conventional cabling can be used. However, for sensor nodes installed inside a rotor blade, cabling becomes very challenging. While a sliding contact could be used for providing a connection from the turning rotor blade to the stationary nacelle, it is also prone to outages due to contact problems and wear of the contacts itself. Additionally, standardization guidelines make such a solution difficult. Furthermore, lightning strikes can lead to a destruction of the sensor nodes due to induced over-voltages [40].

A solution to all this could be wireless sensor nodes, where the node placed in the rotor blade transmits data to a base station in the nacelle without the need for cables between base station and sensor node. However, depending on the amount of data to transmit and the distance of the sensor node from the base station, a substantial amount of energy at least in the mW range or above is needed. Even big lithium-ion batteries cannot power such a sensor node for the required lifetime [34]. A solution to this problem is an energy harvester converting environmental energy into electricity and thus powering the sensor node.

1.2. Outline of the Thesis

This thesis is about the fabrication of a hybrid piezoelectric/electromagnetic energy harvester and a piezoelectric micro electromechanical system (MEMS) resonant strain sensor for sensor nodes to monitor wind turbine rotor blades. In addition, piezoelectric materials, namely aluminum nitride with and without various dopants, are investigated for the piezoelectric energy harvesting component as well as for the low-power strain sensor.

Chapter 2 gives an overview of state-of-the-art research for all three topics and analyses typical pros and cons for various competing alternatives. Chapter 3 describes in detail the MEMS fabrication and measurement methods used in this thesis. Chapter 4 describes the deposition and characterization of aluminum nitride as piezoelectric material, followed by an analysis of doping with scandium and yttrium to enhance the piezoelectric coefficient and other electrical parameters, such as the permittivity. In chapter 5 the hybrid piezoelectric/electromagnetic energy harvester is presented. First, a detailed explanation of the design and its fabrication is given, followed by a characterization in the lab where initial results were taken to further optimize the design. With this knowledge, a final prototype was built and tested in field measurements under real-world conditions in a wind turbine. Chapter 6 introduces a newly designed piezoelectric MEMS resonant strain sensor device. After an analysis of the design and its fabrication, detailed characterizations of the behavior are given and hypothesis of the root cause for certain unexpected results are made. At the end of the chapter a newly developed fabrication process for low-stress AlN deposition is introduced which improves the performance of the strain sensor substantially. Chapter 7 concludes the thesis and gives an outlook over further improvements of the two devices, also for other application areas.

2. State of the Art

This chapter gives a basic introduction on piezoelectricity and summarizes state-of-the-art research to piezoelectric materials used for the integration into MEMS devices. Specific applications areas as investigated in this thesis are in the field of wireless sensors nodes in wind turbines and for piezoelectric MEMS resonators enabling energy harvesting and low-power strain sensing.

2.1 Piezoelectric Materials

Piezoelectricity is a property of certain solid materials to generate electrical charges when they experience mechanical strain, which is also called direct piezoelectric effect. In cases when materials are deforming as a result of applying an electric field, it is called indirect piezoelectric effect.

The cause of this effect can be found in the point- or Centro symmetry of negative and positive partial charges, depicted in Figure 5. In an unstrained state (a), both negative and positive charge centers cancel each other out and the measured voltage between the opposing surfaces equals zero. In a strained state (b) the charge centers separate, which is measurable between the surface-electrodes as a polarization. In general, the piezoelectric effect can be described by four mutual related coefficients d_{ij} , e_{ij} , g_{ij} and h_{ij} which relate the electrical to the mechanical material properties [41]. For materials like aluminum nitride the charge or strain coefficient d_{ij} is usually used. Depending on the directions of the applied force and the directions of the emerging polarization three piezoelectric coefficients can be defined, the longitudinal piezoelectric coefficient d_{33} , the transversal piezoelectric coefficient d_{31} and the shear piezoelectric coefficient d_{15} .

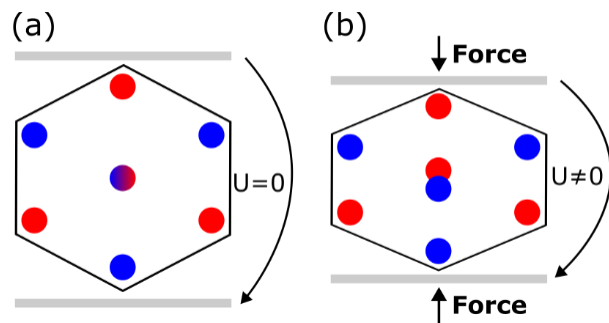


Figure 5: Schematic of the (a) direct and (b) converse piezoelectric effect.

In case the measured or applied electric field is in the same geometrical direction *e.g.*, z-direction, as the mechanical strain, they are related through the longitudinal piezoelectric coefficient d_{33} . The transversal piezoelectric coefficient d_{31} relates mechanical strains in the x- and y-direction to electric fields in the z-direction and the piezoelectric shear coefficient d_{15} relates shear strains in x- or y-direction with electric fields in z-direction, shown in Figure 6 (a-c).

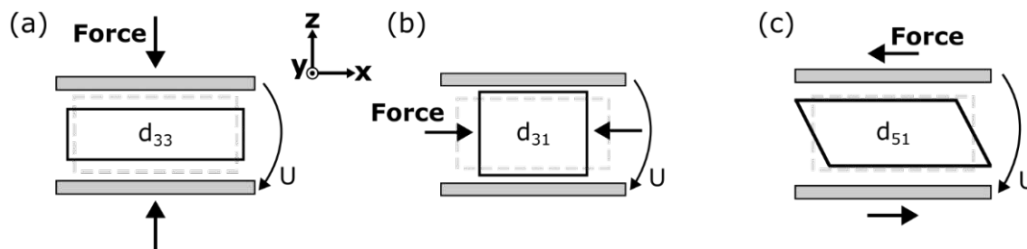


Figure 6: Schematic of (a) longitudinal, (b) transversal and (c) shear piezoelectric coefficient.

The transversal piezoelectric coefficient, the most important out of these three for the mentioned device applications, can be described by the piezoelectric constitutive equations (2.1) and (2.2) [42]:

$$S_1 = s_{11}^E T_1 + d_{31} E_3 \quad (2.1)$$

$$D_1 = d_{31} T_1 + \epsilon_{33}^T E_3 \quad (2.2)$$

With the elastic compliance coefficient s_{11}^E and the relative permittivity ϵ_{33}^T relating the mechanical strain S , the mechanical stress T , the electrical displacement field D and the electrical field E . The subscripts represent the geometrical directions and the superscripts E and T indicate constant electrical field conditions and constant mechanical strain conditions. For a more general mathematical description the reader is referred to [41], [43].

Lead zirconate titanate (PZT) is one of the most used piezoelectric material for MEMS actuators and energy harvesters, showing very high piezoelectric coefficients [44]–[47]. However, the piezoelectric coefficients alone are not sufficient to determine if a material is an optimal choice for an application. For sensing or energy harvesting, additionally the mechanical properties and the dielectric constant of the material are also important. Roundy et al. developed an analytical expression to estimate an upper boundary for the generated power of a cantilever type resonator, which is shown in equation (2.3) [48].

$$P_{max} = \frac{e_{31,f}^2}{\epsilon_r \epsilon_0} \cdot \frac{(1 - \nu_s)^2}{Y_S} \cdot \frac{m}{4\omega} Q_{tot}^2 a^2 \quad (2.3)$$

The colored circles around parts of the equation show the impact of resonator parameters related to geometrical dimensions, mechanical parameters coming mainly from substrate material and the parameters specific to piezoelectric materials. The latter can also be summarized by the Figure of Merit (FOM) for piezoelectric materials, often used to estimate the performance of materials for piezoelectric energy harvesting and is described by equation (2.4)

$$FOM = \frac{e_{31,f}^2}{\epsilon_r \epsilon_0} \quad (2.4)$$

While PZT and its variants show the highest piezoelectric coefficients, for sensing and energy harvesting applications, where a combination of piezoelectric and dielectric coefficients is crucial, AlN and its doped variants are competitive or even exceed PZT in their FOM, shown in Table 1.

Material	d_{33} $pC N^{-1}$	d_{31} $pC N^{-1}$	$e_{31,f}$ $C m^{-2}$	ϵ_{33}	FOM GPa	Ref.
PZT	60..130	-	-8 ... - 12	300 – 1300	6 ... 18	[44]
PZT-5A	593	-274	n.a.	3400	n.a.	[45]
PMmN-PZT		-184	-14.9	834	30.0	[46]
KNNS-BNZH	380	-140	-11.20	2000	12.5	[49]
ZnO	5.9		-1.0	10.9	10.3	[44]
AlN	5.53	-2.65	1.37	9.5	22.3	[47]
$Al_{67}Sc_{33}N$	18	-11	-3.0	17.5	31.1	[50]–[52]

Table 1: Material parameters and references of various piezoelectric materials.

2.2 Energy Harvesting

In general energy harvesting, also sometimes called energy scavenging, is the conversion of environmental energy into another, better useable form of energy – mostly electrical energy. Macroscopic forms of energy harvesters, like thermoelectric, hydroelectric or wind powerplants have been around for decades and are used to convert large amounts of energy into electricity to power industry and households. While the term energy harvester (EH) also comprises large power generating facilities like wind turbines or photovoltaic power stations in the $MW - GW$ range, it is more commonly used for smaller forms of energy generators, capable of powering remote self-dependent electronic devices with a restricted energy demand, like wireless sensors [53], biomedical implants [54], aeronautic applications [55], structural health monitoring [56], watches [57], Bluetooth headsets [58] or other internet of things (IoT) devices [59].

Energy harvesters can be categorized by the different energy forms they convert [60]:

- Gas or fluid flow
- Thermal energy
- Light
- Radio frequency
- Mechanical energy

Obviously, not every energy source is always available or provides enough energy under all circumstances and therefore, the energy harvester must be specifically designed for a given energy source and application. Considering the use-case of a wireless sensor node inside a wind turbines rotor blade with a typical power consumption between $10 - 100 mW$ [61], [62], we can determine the best type of energy harvesters.

2.2.1. Gas Flow

As the rotor blade is a closed object, an energy harvester based on gas flow would not experience any flow if it were placed inside the rotor blade. Therefore, this form of energy harvesting is excluded from further investigations.

2.2.2. Thermal

Converting thermal energy into electricity can be done via the thermoelectric effect, which separates electric charges resulting in an electric field at the junctions between different metals, when exposing the two materials to different temperature levels [63], [64]. In a wind turbine there are two forms of temperature differences. One is the difference between operational equipment in the nacelle e.g., generators, transformers, voltage converters and other objects like the frame of the nacelle. The other is the change in ambient temperature through the day and night cycle.

For sensor nodes in the nacelle this could be a viable option, although those could also be supplied conventionally from the voltage generator in the nacelle. In the rotor blade the only temperature gradient comes from the change in ambient temperature, which changes slowly during the day. The temperatures are in the range of $\pm 15^{\circ}\text{C}$ under normal conditions as can be seen in [65]. Furthermore, the energy harvester has to be optimized for a bigger temperature range than the normal day cycle, due to the change of temperature during the year, which can span from -30°C to $+50^{\circ}\text{C}$ [66] depending on where the wind turbine is located. Therefore, other forms of energy harvesting are preferred.

2.2.3. Light

Converting energy in the form of light into electricity has been a big field of research since several decades, not only in the form of huge solar farms, generating mega- or gigawatts, but also for remote applications which only need small amounts of energy. Obviously, inside a rotor blade there is no possibility to harvest sun light directly, but a few studies have shown that it is possible to power sensor nodes with energy from laser-light, transferred via a fiber optical cable from the blade hub reaching powers of up to 177 mW [67]. This circumvents the problems of metallic wiring which is prone to lightning strikes – a huge threat for wind power plants – but it still needs the additional expenses of cabling and additional educational costs for field engineers handling the fiber optics. However, this technique falls more into the category of power transfer than energy harvesting.

2.2.4. Radiofrequency

Generating energy from radio frequency (RF) can either be achieved through harvesting ambient radiation or by transmitting power through intentionally directed radiation through air [68]. While ambient radiation is always present and has been shown to provide sufficient power to operate wireless sensor networks (WSN) [69], it cannot be guaranteed that there is always enough power. Especially in remote areas e.g., offshore locations or in mountainous areas the coverage is not always guaranteed. Intentional directed power transmission has shown great potential in recent years [38], [70]. However, for power transmissions in the field of WSN for wind turbine rotor blades there are several challenges to overcome. The transmitted power density decreases with the inverse of the square of the propagation distance and additionally depends on the targeted transmission frequency. Both factors limit the possible distance between transmitter and receiver. Other restrictions come from the national regulations about the maximum allowed radiated power, which differs substantially depending on the country but also differ on the used frequency range [71]. As a result, RF energy harvesting might be a viable option but cannot be the only energy source to power a WSN which should be always operational.

2.2.5. Mechanical Energy Harvesting

Mechanical energy harvesting, as the name suggests is the transfer of mechanical into electrical energy, whereas the mechanical energy can be categorized in periodically occurring events *e.g.*, vibrations of a structure or machinery, and randomly occurring incidents like cars driving by a street or waves at sea and can be categorized in:

- Vibrational EHs
- Impact based EHs

Another way of categorizing those devices is by the transduction mechanism:

- Electrostatic
- Electromagnetic
- Piezoelectric

First, the transduction mechanisms are explained, followed by the design categories and an extensive collection of examples from current research is given.

Electrostatic Transduction

The main principle in electrostatic transduction energy harvesters is based on a capacitor structure with two opposing electrodes and varying the gap distance between them. By biasing the electrodes with a constant voltage V , charges are moving from one electrode to the other when the capacity changes, according to the relation $\Delta Q = \Delta C \cdot V$. Due to MEMS-technology the area covered by those electrodes can be made very large, while the overall volume of the device remains small. However, the voltage has to be generated permanently. Through leakage currents a loss of energy is occurring over time, which is a problem for periods without energy generation or start-up scenarios after longer idle periods. As this work targets an energy harvester used in a rotor blade of wind turbines, which naturally have longer idle periods, an electrostatic energy harvester is deemed not optimally suited.

Piezoelectric Transduction

Piezoelectric transduction transforms strain into electrical charges which is explained in detail in section 2.1. Important to note is that the strain must change over time to continuously generate charges. This can be achieved by using mechanical resonators like cantilevers. Explanations of various designs of vibrational energy harvesters are given later in this section.

Electromagnetic Transduction

Electromagnetic transduction is based on a changing magnetic field inducing current in a coil. The magnetic field is generated through permanent magnets and the change in field strength is generated by either moving the coil or the permanent magnet. Designs of vibrational EHs or impact based EHs can be realized, similar to those mentioned in the piezoelectric transduction section.

Vibrational Energy Harvesters

In most cases the energy harvester has to be designed to the applications requirements, which means that no single energy harvester will fit every use case. In the case of structural health monitoring one possible method is to use resonators and tune their resonances to the same frequencies occurring in the underlying structures.

One of the most used geometrical designs for vibrational energy harvesting is a cantilever, which is a single side clamped beam structure, using a piezoelectric layer for energy conversion, as shown in Figure 7. Through bending of the cantilever in z -direction, the piezoelectric material is strained in x -direction, which is also referred to as a d_{31} configuration. The advantage of cantilever type resonators compared to bridge-type or plate-type resonators of similar size is the much bigger displacement and strain and hence higher generated voltage for equal excitation force/acceleration. Several studies have shown that a further increase of the displacement and thus the generated power of a cantilever-type EH can be achieved with a proof mass fixed to the tip of the cantilever. A proof mass can either be glued to the cantilever or it can be realized by not removing substrate material below the cantilever during etching as reported in [72].

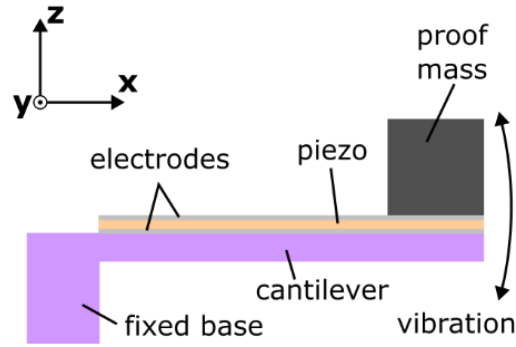


Figure 7: Schematic of a cantilever type vibrational energy harvester with proof mass and electrode/piezo stack.

As already mentioned, the resonance frequencies of the resonator must be tuned to frequencies occurring in the environment. This can be achieved by varying the geometrical dimensions of length, thickness and shape of the cantilever or the weight of the proof mass [73]. To further enhance the generated power, Du *et al.* investigated varying the electrode coverage of the cantilever and showed that the optimum can be found at about 50% of the cantilever's length. Another increase in power generation can be achieved by changing the shape of the cantilever. Instead of the conventional rectangular form, trapezoidal or concavely shaped single clamped beams have a higher amount of charge generation per volume, when the maximum tip displacement is kept constant [74], [74], [75]. Table 2 gives an overview of several mentioned vibrational energy harvesters including the device featured in this work in chapter 5 with the parameters power p , acceleration a and their power density p_{NPD} . The power density is the power divided by the overall volume and the square of the applied acceleration and is used for better comparability between different types and shapes of energy harvesters. A more detailed explanation of the power density is given in chapter 5.

Nr.	Author	Year	Transduction Mechanism	p_{NPD} $mW\ cm^{-3}g_0^2$	p μW	f_R Hz	Dimensions cm^3	a g_0	Ref.
1	This work	2023	piezo	0.082	6.54	210	1.27	0.25	-
2	S. Du	2017	piezo	0.001	0.222	1208	0.631	0.5	[76]
3	L. Deng	2014	piezo	0.009	21.360	228	9.410	0.5	[77]
4	D. Pan	2018	piezo	0.047	29300	22	153 403	2	[78]
5	S. S. Chauhan	2019	piezo	0.009	1.03	205	0.648	0.4	[79]
6	Y. Liu	2021	piezo	2.123	38.09	331	17.942	1	[80]
7	X. He	2021	piezo	0.784	54.1	161	82.219	1	[74]
8	I. Gablech	2020	piezo	0.861	10.33	2520	23.995	2	[72]

Table 2: Comparison of vibrational piezoelectric energy harvesters and their properties.

Impact based Energy Harvesters

MEMS resonators typically feature resonance frequencies of the fundamental mode in the range of several hundred Hz due to their small size. In larger structures like wind turbines or buildings, occurring frequencies are typically in the range of 0.1 – 50 Hz, compare Figure 76 in chapter 5. Therefore, different approaches are needed for MEMS EHs in these applications. One approach is frequency-up-conversion, also called impact driven excitation. With this method it is possible to use the resonator’s own resonance frequencies independently of the available frequencies coming from the base structure. This is achieved through a plucking mechanism, whereas the plucking frequency is equal to the resonances of the underlying structure. Every plucking event acts as a rectangular impulse excitation of the cantilever and it starts to resonate in its own resonance frequency. One typical design comprises an object moving close to the cantilever in regular time intervals and plucking it either mechanically or through magnetic interaction. The objects trajectory can either be linear or circular [81]–[84]. Another design for frequency up-conversion consists of two cantilever beams, whereas one has a much lower resonance frequency, representing an ambient vibration source and the other cantilever having a much higher resonance frequency and being plucked by the former one, once or twice during each period [85]–[87]. Beside exciting the cantilever by displacing its tip, it can also be excited by displacing or hitting the base [88]–[91], which has been used for wearable energy harvesting devices [92]. A comparative summary of results of power p , power density p_{NPD} and resonance frequency f_R for impact based EHs is given in Table 3.

Nr.	Author	Year	Type	p_{NPD} $\mu W cm^{-3}$	p μW	f_R Hz	Dimensions cm^3	Ref.
1	This work	2023	EM	374		5		-
2	Q. C. Tang	2011	Piezo	7	22.5	15	3.2	[81]
3	H. Jung	2013	Piezo	450	-	33	-	[83]
4	W.-H. Wu	2017	Piezo	878	1230	25	1.4	[84]
5	E. Fakeih	2021	Piezo	22	38	12	1.7	[84]
6	Z. Xu	2017	Piezo	44	769	13	17.2	[86]
7	L. Gu & C Livermore	2011	Piezo	26	429	8.2	16.8	[87]
8	K. Fan	2018	Piezo	41	1500	6	36	[92]
9	Q. Luo	2017	EM	256		8.5		[93]
10	Y. Shen	2020	EM	748		4.5		[94]
11	Z. Li	2019	EM	484		24		[88]
12	A. Nammari	2018	EM	133		15.5		[90]
13	K. Fan	2019	EM	98		7.5		[95]
14	L. Zhang	2019	EM	41		3.1		[91]
15	A. Luo	2020	EM	129		0.1		[89]

Table 3: Overview of energy harvesters with an electromagnetic transduction mechanism operated with impact-based designs.

2.3 Strain Sensing

As mentioned in section 1.1, monitoring the local strain distribution of wind turbine rotor blades at certain positions along the rotor blade [96], [97], the tower [98] or its foundation [99] would be highly beneficial. A typical sensor type used for this application is the conventional resistive strain gauge sensor, invented in the late 1930s [100], [101], which was a state-of-the-art strain measuring technique for many decades. Improvements have been achieved by introducing tailored materials and designs to overcome typical restrictions like a limited operational temperature range [102], a high cross-sensitivity to temperature [103], [104] or the impact of parasitic effects like a high transverse strain sensitivity [105], [106]. It is based on the change in electrical resistance when a conductive structure like a wire is deformed which can be electrically measured by e.g., an Wheatstone bridge [107]. They feature gauge factors of 2-12 for pure metal foil strain gauges [108]–[111]. The low gauge factors can be overcome by using semiconductor strain sensors which are based on the piezoresistive effect providing gauge factors of up to 200 [108], [112], [113]. More recent research, also based on the piezoresistive effect resulted in enhancements of the gauge factor up to 3000 by exploiting effects arising in nanostructures like nanobelts [114] or nanotubes [115]. However, those sensors have certain disadvantages like high dependence on temperature and high non-linearity, making them unsuitable for most applications.

Optical strain sensors are often based on fiber Bragg gratings which reflect certain frequencies of the transmitted light spectrum. This modified light spectrum is depended on the strain ε applied to the fiber changing the spacing of the Bragg gratings and hence, this technique enables mechanical strain sensing [116]. Due to the low internal losses and the possibility to fabricate long optical fibers with high precision, this technique is most beneficially applied to large structures having dimensions up to several kilometers. Furthermore, they are insensitive to interfering electrical fields and immune to chemical corrosion making them most suitable for harsh environmental applications [117].

Other forms of strain sensors are based on digital image correlation [118], electronic speckle pattern interferometry [119], integrated optical ring resonators [120] or the spintronic effect [121], just to mention a few of the recently emerging technologies.

The recent rise of wireless sensor networks demands, however, reliable sensors with very low power consumption in the range of micro- or nano watts. Especially, when larger amounts of sensor data have to be collected and distributed wireless as e.g., the application of monitoring the rotor blades of wind turbines, compare chapter 5. Furthermore, lifetimes up to 20 years [122], [123] are necessary especially for e.g. automotive and structural health monitoring applications. MEMS sensors offer a most excellent and reliable technology platform to fulfill both key requirements. Due to their small size, they can be designed for exceptionally low power consumption.

The last decade showed a strong trend towards piezoelectric MEMS sensors, due to their compact design and their low power consumption. Most often they are operated in resonance, with key mechanical building blocks for the resonating element such as beams, cantilevers or plates. Furthermore, the piezoelectric transducer enables to simultaneously stimulate the mechanical resonance electrically and read out the mechanical response by recording the electrical impedance spectrum. Specific resonances can be excited with different efficiency depending on resonator design parameters such as length, thickness and mass [124], but also electrode design [125]. By tracking the change of resonance frequency or quality factor the devices can be used to measure physical quantities such as viscosity of a liquid [126], mass of a particle [127] and much more. Double-clamped beam-like MEMS resonators also called microbridges, can be used to sense axially applied strain by measuring the frequency response, which depends on the stress/strain state of

the microbridge [128]–[130]. This principle and experimental prototypes are discussed in chapter 6.

The most common methods for electric actuation are by electrostatic forces, via capacitive structures [129], [131]–[133] and by piezoelectric forces [128], [130] which in turn reduces the necessary high voltages associated with the prior mentioned transducer principle [103]. Table 4 gives a comparative overview of the mentioned strain sensing devices.

Author	Year	Type	Material	Gauge Factor	Sensitivity $\text{Hz } \mu\text{m}^{-1}$	ε Range %	Ref.
This work	2023	Res. Piezo. MEMS	Si/AlN	17000	n.a.	± 0.1	-
Gosh & Lee	2017	Res. Piezo. MEMS	Si/AlN	2510	150	n.a.	[128]
Goericke	1996	Res. Piezo. MEMS	Si/AlN	244	243	0.037	[130]
Belsito	2016	Res. Cap. MEMS	Si	539	164	0.063	[134]
Do	2016	Res. Cap. MEMS	Si	15	2.8	0.1	[129]
Azevedo	2007	Res. Cap. MEMS	SiC	318	66	0.0035	[131]
Belsito	2019	Res. Cap. MEMS	SiC	128	41.7	0.005	[132]
Chan	2011	Res. Cap. MEMS	Si	97	20.8	0.063-	[133]
Suster	2006	Cap. MEMS	Si	400	n.a.	0.1	[135]
Zhang	2021	Cap. MEMS	Si	430	n.a.	0.1	[136]
Song	2021	Piezoresistive	SR/graphene	326	n.a.	10%	[137]
Smith	1953	Piezoresistive	Si	155	n.a.	n.a.	[112]
Edwards	1969	Piezoresistive	Ge	100	n.a.	0.04	[113]
Li	2020	Piezoresistive	B-Doped SiC Nanobelts	-1800	n.a.	n.a.	[114]
Stampfer	2006	Piezoresistive	Carbon Nanotubes	2900	n.a.	0.4	[115]
Fuji	2017	Spintronic	RL/Mg-O BL/FE-B	5072	n.a.	± 0.1	[121]
Li	2020	Opt. Ring Res.	CdS Nanowire	68	n.a.	5	[120]
Schmid	2020	Metallic	Pt/AlN	5	n.a.	n.a.	[109]
Lu	2020	Metallic	Zr	3.4	n.a.	1	[110]
Lu	2020	Metallic	Cu	1.4	n.a.	1	[110]
Meyer	1967	Metallic	Ni	-12.2	n.a.	n.a.	[111]

Table 4: Key parameters of various strain sensing MEMS devices.

3. MEMS Fabrication Technologies and Experimental Methods

This chapter gives an overview of the most important fabrication technologies and the experimental methods to characterize both the materials in chapter 4 and the sensor devices in chapters 5 and 6. Evaluation methods, if diverging from standard methods, are explained in more detail as well as standard parameters for different measurement equipment.

3.1 Sputtering

Sputter deposition is a physical vapor deposition (PVD) process where a target material is bombarded with ionized particles and the sputter-ejected atoms are then deposited onto a substrate material e.g., a Si wafer. The ionized particles are generated by igniting a plasma in a vacuum chamber when applying a high voltage between target and substrate. The positively charged ions are accelerated towards the negative electrode (target) where the target atoms are ejected through collision cascades. To increase the yield a magnetron can be used, which consists of several high flux magnets placed above the vacuum chamber. The magnetic field leads to a lateral acceleration of the electrons and traps them close to the target surface, which increases the amount of ion generation for the same amount of electrons during the discharge and as result the sputter rate is increased. [138]

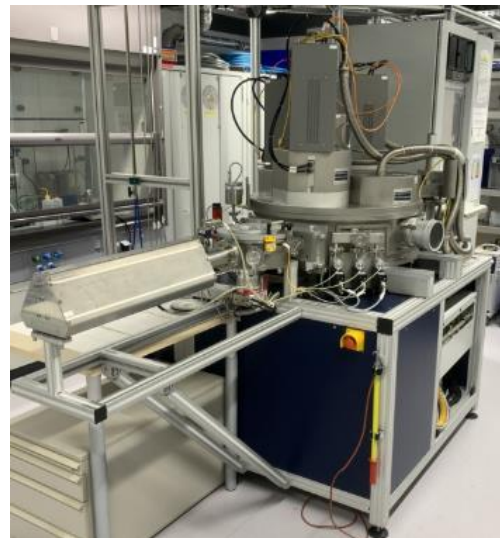


Figure 8: Optical photograph of a sputter system "Von Ardenne" LS730S.

The sputter gas can be an inert gas like Argon, which is used to deposit pure target materials. Another possibility is to reactively sputter deposited e.g. nitrides or oxides by using nitrogen or oxygen as sputter gas. In this process the sputter-ejected atoms react with the reactive gas radicals on the substrate surface. As nitrogen is smaller and lighter than argon, the sputter rate typically decreases which can be circumvented by a mixture of both gases.

In this work a "Von Ardenne" LS730S magnetron sputter system is used to reactively sputter deposit AlN, AlScN and AlYN thin films. Additionally, metal thin films such as aluminum or gold, used as electrode material, were also sputter deposited if they are not vapor deposited. The purity of the gases was 99.9999%, the target to substrate distance during all sputter depositions was 65 mm and a constant pressure value was attained by using a flow controller. Other deposition parameters are varied and explained in detail in the according chapters.

3.2 Characterization of piezoelectric constants

The piezoelectric constant d_{33} was characterized by a piezometer PM300 from Piezotest Ltd., which is based on the Berlincourt method, shown in Figure 9 (a). For this measurement procedure a sample is clamped between two electrodes with a diameter of 1 mm with a preloading force, shown

in Figure 9 (b). Then an oscillating force is superposed and mechanically strains the device under test periodically. As a result, the piezoelectric material generates charges which are measured by a charge amplifier. The AC force is related to the corresponding charge signal and the piezoelectric coefficient d_{33} can be calculated [139]. To improve the electrical contact between the electrodes and the piezoelectric thin film, aluminum pads with a diameter of 1 mm and a thickness of 200 nm were sputter-deposited on top of the sample, compare Figure 9 (b). The bottom side was fully coated with 200 nm of aluminum for the same reason. For every sample, nine pads have been measured, whereas the deviation from the average for all measurements was in the range of $\pm 0.5 \text{ pC N}^{-1}$ and is marked in the according plots with error bars.



Figure 9: (a) Optical photograph of a piezometer PM300 from Piezotest Ltd. and (b) a sample with a piezoelectric thin film and several aluminum pads, clamped between the electrodes of the piezometer.

3.3 X-Ray Diffractometry

X-ray diffraction is a measurement technique making it possible to study the occurring crystallographic phases within a sample. This measurement method uses X-rays, coming from a radiation source and targeted at the sample surface under a certain angle ω , where they are diffracted on the crystallographic planes. These diffracted X-rays can then be measured by a detector placed with an angle α to the sample surface. The special case where $\omega = \alpha = \Theta$ is called Bragg-Brentano configuration, which is mainly used in this work and is shown in Figure 10 (a). When the angle Θ is varied between $0^\circ < \Theta < 90^\circ$ only diffracted X-rays which fulfill the Bragg equation (3.1) produce a measurable signal and are depicted with their intensity as peaks in a diffractogram.

$$n\lambda = 2d \sin (\Theta) \quad (3.1)$$

The parameter n is an integer, λ the wavelength of the X-rays and d is the distance between the crystal planes parallel to the surface [140]. An exemplary diffractogram of an AlN thin film deposited on a (100) Si wafer is shown in Figure 10 (b) showing various existing crystal directions of both materials.

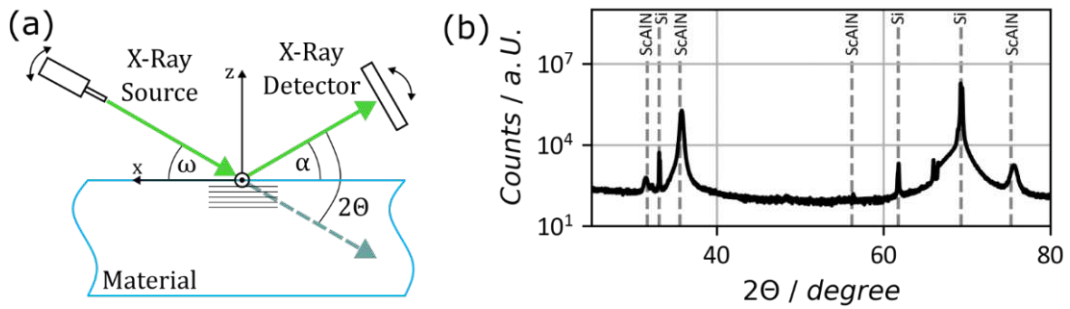


Figure 10: (a) Schematic of the working principle of an XRD in Bragg-Brentano configuration. (b) Sample plot of a Bragg-Brentano scan.

To study single peaks from the Bragg-Brentano scan in more detail a rocking curve measurement can be used. This technique measures the deviation or tilt angle, which is the inclination of crystal axis from the ideal Bragg condition [141]. The angle between the X-ray source and the detector is therefore fixed at the angle where the peak appears in the Bragg-Brentano scan. Then the angle ω between the X-ray source and the sample surface is varied to produce the rocking curve plot, shown in Figure 11 (a-b)

While ideally aligned crystallites would appear as a single line in the rocking curve, misaligned crystallites are shifted by their deviation angle and the resulting peak shape can be best fitted by a pseudo-Voigt equation [142]. The full width at half maximum (*FWHM*) can then be used as a quantitative measure for the alignment of the crystallites. Typical values of the *FWHM* for AlN thin films grown in (002) directions lie between $1^\circ - 8^\circ$ [143, p.] with lower values meaning higher alignment.

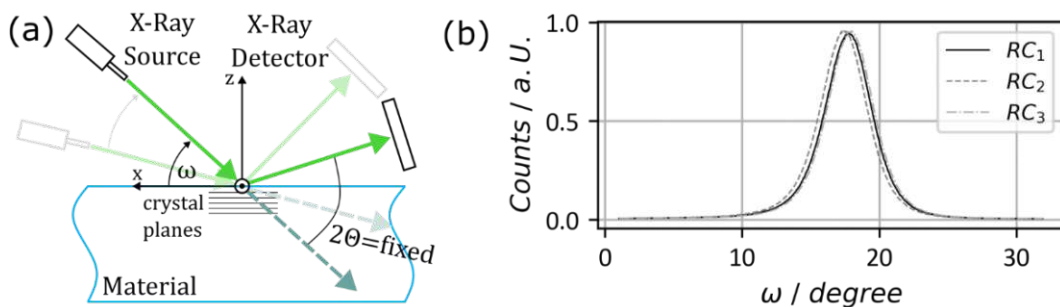


Figure 11: (a) Schematic of the working principle of an XRD for a rocking curve measurement. (b) Sample plot of a rocking curve of the second AlScN peak at 36° from Figure 10 (b).

All Bragg-Brentano scans in this work are performed with a Malvern PANalytical X'Pert PRO containing a copper tube, operated at 45 kV and 40 mA . The sample source distance is set to 140 mm and an X'Celerator detector with an active length of 2.546° is used. The incident beam is equipped with a 0.04 rad soller slit, a 2° anti scatter slit and a 0.5° divergence slit, whereas the diffracted beam is limited with a 0.04 rad soller slit. Bragg-Brentano scans are performed with angles between $2\theta = 20^\circ \dots 80^\circ$ to analyze which crystallographic phases are present. Subsequently, an additional rocking curve of the (002) peak is performed. When recording the rocking curve, the selected angle is set to the maximum peak between $34^\circ - 38^\circ$ of the Bragg-Brentano scan, which correspond to the typical location of the (002) peak of AlN, which is at 36° . Then three measurements are performed, whereas the sample is rotated around the z-axis by 90° for each measurement. This was done to notice a possible misplacement of the sample.

3.4 Electron Microscopy

This chapter gives a brief introduction and overview about the different electron microscopy techniques used in this work, which are scanning electron microscopy (SEM), transmission electron microscopy (TEM) and electron dispersive X-ray (EDX).

3.4.1. Scanning Electron Microscopy

Scanning electron microscopy refers to a method where an electron beam is focused towards a single point at the specimen and after interacting with it the generated electrons leaving the sample are detected [144]. The electron beam is raster scanned over the surface of the sample through which it is possible to produce an image of its surface. The acceleration voltage, which is used to accelerate the electrons towards the specimen ranges between 1 – 30 kV with

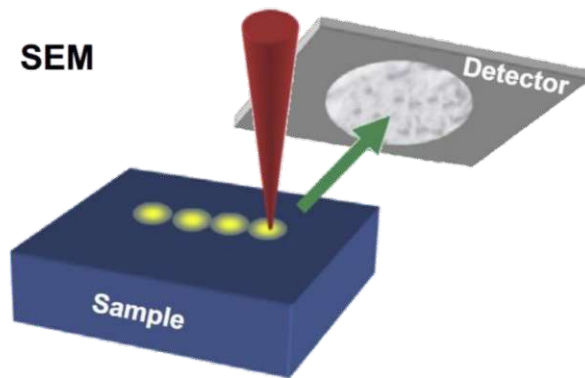


Figure 12: (a) Schematic of a SEM from [144].

emission currents lying in the range of 5 – 20 μA . When the primary electrons hit the surface, they interact with the material and can either be backscattered or secondary electrons are emitted, coming from the material surface. Backscattered electrons provide information about the chemical composition of the material, meaning heavier atoms appear brighter in the SEM image. Secondary electrons provide higher lateral resolution than the backscattered electrons. The maximal magnification reaches approximately 10^6 in comparison to optical light microscopy providing a magnification of approximately 10^3 [144]. The SEM used in this work is a Hitachi SU8030 and the corresponding parameters are stated in the according chapters.

3.4.2. Transmission Electron Microscopy

In contrast to SEM, in a transmission electron microscope the electron source and the detector are placed on opposite sides of the specimen and electrons transmitted through the sample are detected, compare Figure 13 (a). It is used to analyze the nanostructure of the specimen e.g., thin films. With high-resolution TEM (HRTEM), where sample thicknesses are in the range of 5 – 20 nm it is possible to visualize interference patterns of the incoming electron waves, which correspond to periodicity of the crystal lattice [144].

To reach the requested low thickness, the analyzed thin films in this work have been prepared by the following steps. First a sample is split into half and glued together with the surfaces of interest opposing each other, shown in Figure 13 (b). The resulting stacked sample is cut into several 1 cm wide and 100 μm thick slices. The later pieces are then grinded down in multiple steps, to a thickness of ~ 20 nm. In the last step, a hole is cut into the middle of the slice with a focused ion beam reducing the thickness on the boards around this hole to a few nanometers, making it possible to make HRTEM images, compare Figure 13 (c-d).

The used HRTEM was a FEI Tecnai F20 offering a maximum lattice resolution of 0.14 nm and a maximum point resolution of 0.21 nm.

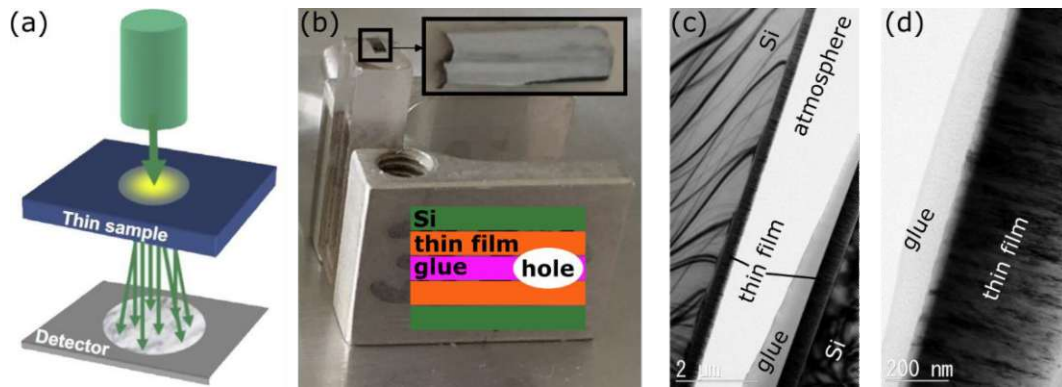


Figure 13: (a) Schematic of a TEM from [144]. (b) Sample holder with a zoomed specimen and a schematic of the specimen. (c) and (d) images of a real AlYN sample.

3.4.3. Electron Dispersive X-Ray

EDX is a technique where the emitted X-rays, when the primary electrons hit the specimen, are measured and analyzed. Since the electron shell configuration is element specific, the elemental composition of the specimen can be deduced from the energy spectrum of the detected X-ray spectrum. In this study, the EDX detector is either an Oxford X-Max integrated into the SEM Hitachi SU8030 or an Apollo XLT SDD from EDAX with a line resolution of 129 eV arranged in the TEM.

3.5 Vibrational Excitation

One possibility to characterize MEMS resonators is by exciting them through harmonic mechanical shaking and measuring an output parameter e.g., displacement or electrical output voltage in case of a piezoelectric device. Therefore, a vibrational exciter (VE, type 4809) from B&K (I) is used. It contains a permanent magnet and an electromagnetic coil which is displaced when an AC signal is applied, similar to a conventional loudspeaker. It has a force rating of 45 N over a frequency range of 10 Hz – 20 kHz and can provide accelerations of up to 75 g. The input signal is generated from a standard frequency generator amplified with a power amplifier of the type 2718 from B&K (II). To control the acceleration produced with the VE, an accelerometer of the type ADXL001 (III) from Analog Devices was mounted in between the mounting plate of the VE and the specimen (IV). It provides an acceleration range of $\pm 70 g_0$ and a sensitivity of $24.2 mV g_0^{-1}$. Additional spacers (V) between the shaker and the specimen are placed to avoid possible influences between the magnetic core of the shaker and a magnetic specimen. The output signal is measured by a data acquisition box DN2.441-02 *digitizerNETBOX* from SPECTRUM instrumentation. The whole setup is shown in Figure 14 (a) and a close-up image of the accelerometer and the specimen is shown in Figure 14 (b).

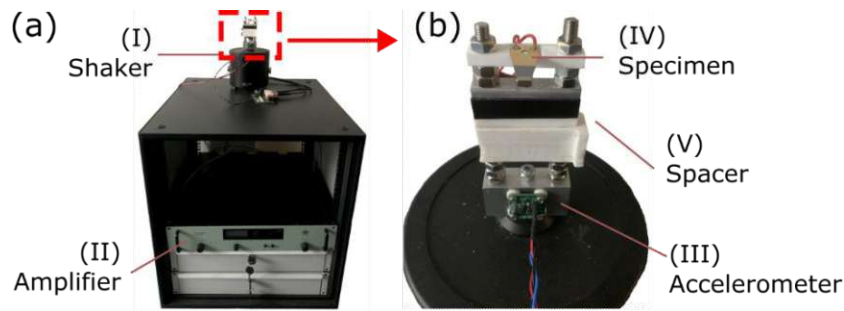


Figure 14: Optical photograph of the vibrational exciter setup including the exciter stage, the power amplifier and a frequency generator.

3.6 Laser Doppler Vibrometry

Laser Doppler Vibrometry (LDV) is a contactless, high precision measurement technique to measure displacements and velocities of a mechanically vibrating surface in the out-of-plane direction. It is an interferometer which measures the frequency difference of two laser beams, depicted in Figure 15. This is achieved by splitting a laser beam into a so-called reference and a measurement beam both initially having a frequency f_0 . The measurement beam is guided towards the specimen, where it is reflected and its frequency is shifted depending on the movement velocity of the specimen, on basis of the Doppler effect adding a frequency shift of f_d . The reference beam is guided through a Bragg cell which shifts the frequency to $f_0 + f_b$. The two beams with different wavelengths are then combined, through which interferences appear, detected by a photodetector.

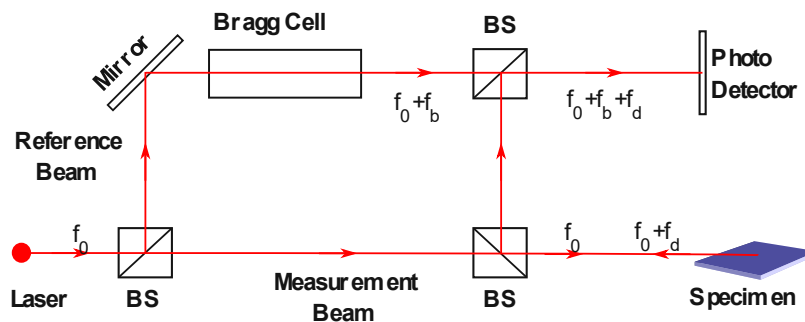


Figure 15: Schematic illustrating the working principle and the most important components of an LDV.

LDVs are used in a wide field of applications, like detection of unwanted resonances [145], structural damage detection [146], on-line quality control [147], [148], biomedical applications [149] and in the modal analysis of MEMS/MOEMS/NEMS [150], only to name a few. Typically, an LDV measures only a single point on the surface, but by raster scanning approach (compare Figure 16 (a)) modal-analyses of vibrational structures is also possible which makes it especially interesting in the field of MEMS/MOEMS/NEMS resonators [151].

The type of LDV used in this work to characterize the MEMS strain sensor in chapter 6, is a micro system analyzer (MSA) 400 from Polytec, shown in Figure 16 (b). It provides a bandwidth of 1.5 MHz, a displacement resolution in the pm-range and a velocity resolution of $< 1 \mu m s^{-1}$. It has a built-in frequency generator, which among other modes provides a chirp signal. In this work, the chirp signal with a bandwidth of 1 MHz and a voltage amplitude of 100 mV was used for all LDV measurements if not otherwise stated.

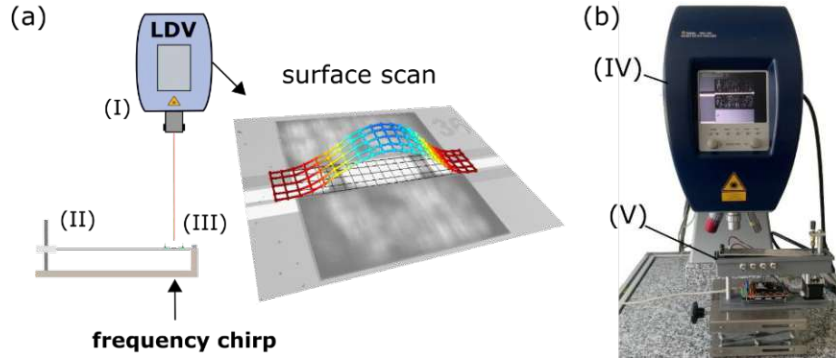


Figure 16: (a) Schematic of the measurement setup and an optical photograph of the LDV (IV), the strain measurement setup (V), which is explained in more detail in chapter 3.7.

Important to note is that the LDV initially measures the velocity, from which it then derives the displacement. Therefore, it only gives information about the dynamic component of the displacement, ignoring the static deflection of the specimen *e.g.*, buckling, compare chapter 6.

When the LDV is operated in scanning mode a frequency response for the displacement d_n or the velocity v_n is generated for each scanned point n . In this mode it is possible to generate a three-dimensional image of the measured mode shape, as illustrated in Figure 16 (a). In certain cases, it is advantageous to calculate the averaged frequency response $d_a = \frac{\sum d_n}{n}$ for each frequency when comparing the frequency responses of different states (*e.g.*, applied strain) of the specimen.

The frequency responses of the resonators measured in this work are characterized by one or more resonances. A sample plot of a frequency spectrum is given in Figure 17 (a). The typical parameters like resonance frequency f_0 are obtained by fitting the function given in equation (3.2) to the spectrum, shown in Figure 17 (b).

$$D_{fit}(f) = \frac{D_0}{4\pi^2 \sqrt{4\zeta^2 f_0^2 f^2 + (f_0^2 - f^2)^2}} \quad (3.2)$$

The parameter ζ represents the damping coefficient which can be used to calculate the quality factor using equation (3.3) and D_0 represents the maximum amplitude.

$$Q = \frac{\sqrt{1 - 2\zeta^2}}{2\zeta} \quad (3.3)$$

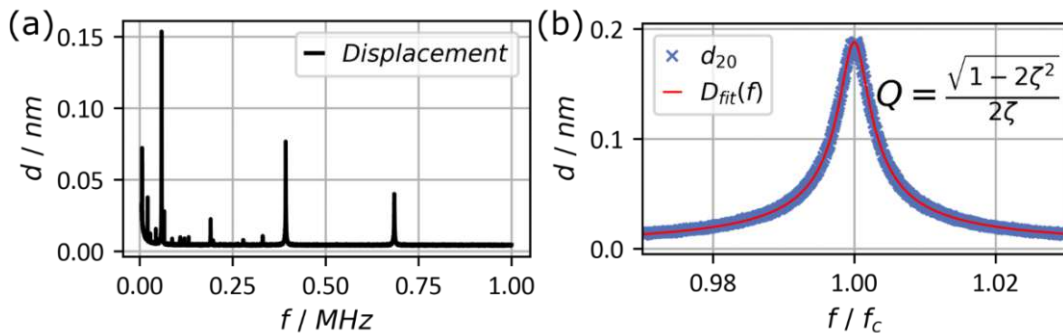


Figure 17: (a) Exemplary frequency response of a MEMS resonator, measured with the LDV. (b) Frequency response of the 20-mode of an exemplary device, with fitted function $D_{fit}(f)$.

3.7 Strain Measurement Setup

To apply mechanical strain over a broad range in a defined and reliable way to the resonant strain sensor discussed in chapter 6, a custom-built measurement setup is designed consisting of a deflectable cantilever made of aluminum (Al), shown in Figure 18 (a). Figure 18 (b) shows a schematic overview with the sensor device (I) and its connecting PCBs (II) glued onto the macroscopic Al cantilever (III). The tip of the Al cantilever was displaced by a stepper motor (IV) of the type Stepperonline Nema 17 with a spindle (V) which has a pitch of 1 mm rev^{-1} . The stepper motor was controlled by an Arduino Mega with a motor driver board (VI) and provided a resolution for the spindle of 0.05 revolutions translating to $50 \mu\text{m}$ for the tip displacement of the Al cantilever.

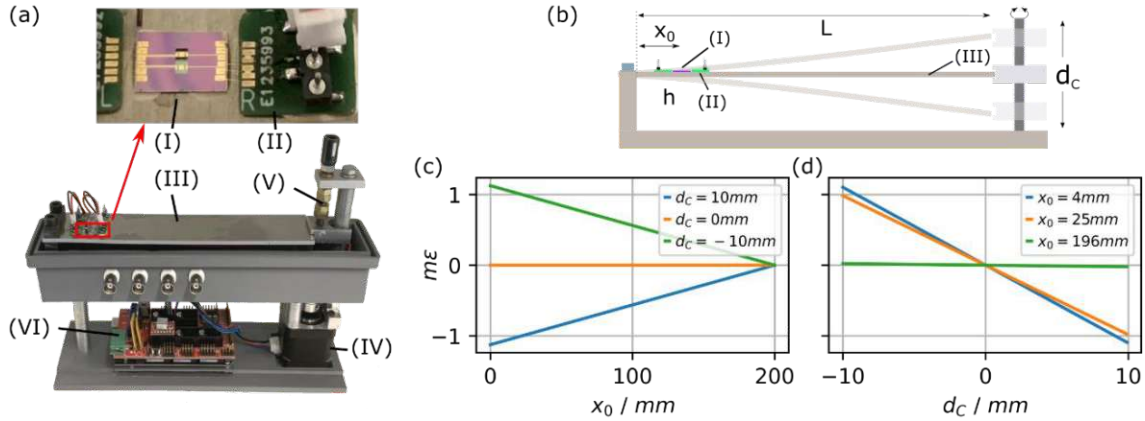


Figure 18: (a) Optical photograph of the custom-made strain characterization setup with (1) the sensor device, (2) the connecting PCBs and (3) the Al cantilever, (4) the stepper motor connected to (5) the spindle and (6) the controller consisting of an Arduino Mega with a motor driver board. (c) Correlation between mechanical strain at the sensor position x for different maximum tip displacements d_0 of the Al cantilever. (d) Correlation between mechanical strain and tip displacement for various sensor positions x_0 .

Based on the Al cantilever thickness h_c , the sensor thickness h_s (including device layer, electrodes and the piezoelectric layer), the length L of the Al cantilever and the tip displacement d_c of the Al cantilever the strain sensor can be exposed to a certain strain ϵ_x at the position x_0 depending on the local distribution of the latter parameter on the Al cantilever surface. It can be calculated by the Euler-Bernoulli beam equations [152] in general to

$$\epsilon_x = -3 \frac{d_c z}{L^3} (L - x) , \quad (3.4)$$

whereas z is the distance from the neutral axis to the point of interest and x is the distance from the clamping point of the Al cantilever. They can be expressed with

$$x = x_0, \quad z = h_c/2 + h_s , \quad (3.5)$$

which then leads to the strain at position x of the MEMS sensor, given in equation (3.6).

$$\epsilon_x = -\frac{3 d_c (h_c + 2h_s)}{2 L^3} (L - x_0) \quad (3.6)$$

Figure 18 (c) shows the strain dependence on the sensor position along the Al cantilever for three different maximum tip displacements d_c . If the Al cantilever is bent down the sensor is stretched, resulting in positive values for ϵ and *vice versa*. Figure 18 (d) shows the strain dependence on the tip displacement for three different sensor positions. The closer the sensor is mounted to the fixed Al cantilever base ($x = 0$), the more strain is applied to the sensor. As the whole strain sensor chip including contact pads is 7.5 mm long, the minimal sensor position measured from the base of the

Al cantilever is half the chip length, therefore 3.75 mm and the maximal position is about 196 mm. The distance chosen for further characterizations in this work was 25 mm (orange curve in Figure 18 (d)), which leaves enough space for connecting the PCBs for electrical read-out.

The strain sensor was glued at an elevated temperature of 120°C for 20 minutes with a two-component epoxy resin EC101 from Polytec onto the Al cantilever. The pads of the device were connected with wire bonds to PCBs, which provide connectors to the electrical measurement equipment.

3.8 Impedance Spectroscopy

The electrical conductance spectrum $G(f)$ was measured with a Zurich Instruments MFIA impedance analyzer (IA) while the sensor was excited with the built-in frequency generator providing a frequency sweep between 1 kHz and 1 MHz and a voltage amplitude of 100 mV.

Similar to the optical measurements from section 3.5 the conductance spectra were fitted with the function $G_{fit}(f)$ from equation (3.7), derived from a basic series LCR resonant circuit.

$$G_{fit}(f) = \frac{G_0}{1 + \frac{1}{4\xi^2} \frac{f_0^2}{f^2} \left(\frac{f^2}{f_0^2} - 1\right)^2} \quad (3.7)$$

The parameter ξ represents the damping coefficient and G_0 the conductance amplitude at $f = f_0$. The quality factor of the conductance resonance peak can then be calculated with:

$$Q = \frac{\sqrt{1 - 2\xi^2}}{2\xi} \quad (3.8)$$

Since equation (3.2) and (3.7) describe the same mechanical system, both damping parameters are identical in the absence of noise and measurement related drifts, thus $\zeta = \xi$.

Figure 15 shows a sample conductance spectrum in (a) and a sample fit of one resonance in (b), which is corrected by a linear offset to account for the baseline prior to the fit.

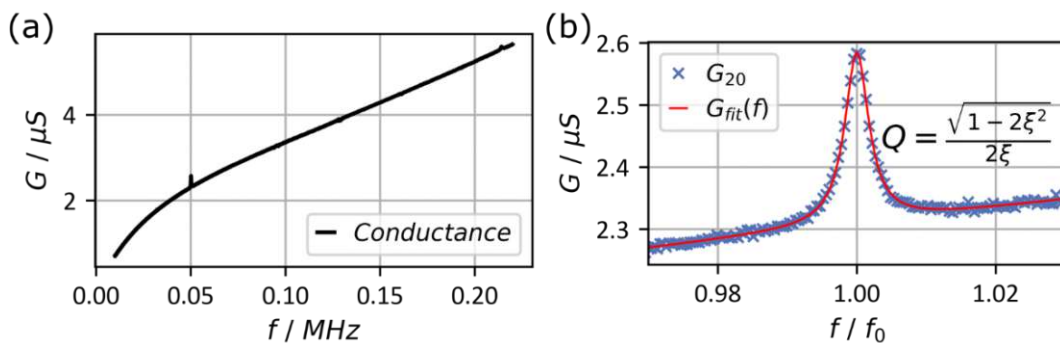


Figure 19: (a) Frequency response of a typical MEMS resonator, measured with the impedance analyzer. (b) Frequency response of the 20-mode of an exemplary resonator, with fitted function $G_{fit}(f)$.

3.9 Quality Factor

The Quality factor or Q-factor is a dimensionless parameter and can be obtained in three ways:

The **Bandwidth method** relates the center frequency of a resonance to the peak width at half the power (or at 3 dB) also called full width at half maximum (FWHM), depicted in Figure 20 (a). This method is rather simple but has a few drawbacks, as it does not give equivalent results with respect to the two other definitions for low Q-factors, as explained below. For very high Q-factors (> 10000) the precise measurement of the FWHM becomes more and more difficult as it highly depends on the frequency resolution of the measurement equipment and therefore results in a larger error. In this work this method has been replaced by the two methods explained below.

As a second approach, Q can be derived from the **damping coefficient** which generally describes how underdamped a system is. It is most suited when attaining the Q-factor from an available frequency response and was done in sections 3.6 and 3.8 when fitting a function to the resonance curve and then deriving the Q-factor.

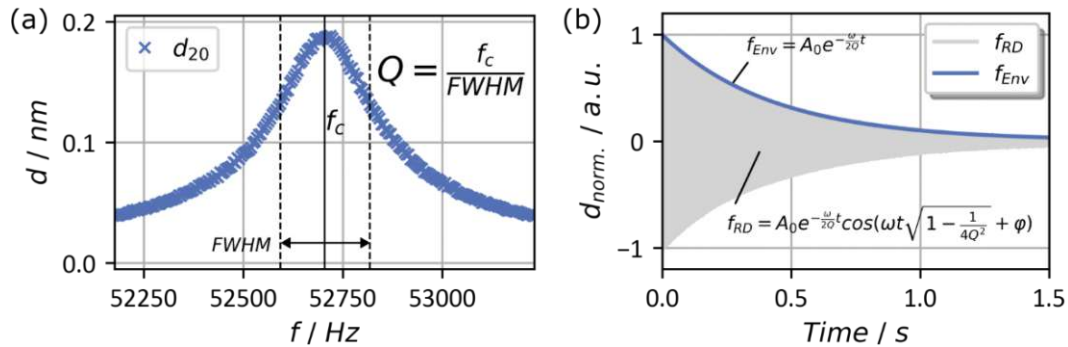


Figure 20: (a) Frequency response of the 20-mode of an exemplary MEMS resonator with marked full width at half maximum (FWHM) and center frequency f_c to attain Q-factor with the bandwidth method. (b) Ring down of an exemplary resonator and the fitted function f_{fit} fitted to the envelope.

Finally, the Q-factor can be defined as the ratio of the energy stored in a resonating system to the lost energy in one cycle of its oscillation. It can be obtained by exciting the resonator, turning off the driving force and analyzing the **ring down**, shown in Figure 20 (b). It can be described by a linear homogeneous differential second order equation. The general solution to this differential equation is shown in equation (3.9) and consists of a sinusoidal part representing the oscillation with constant amplitude and an exponentially decaying part which is also referred to as the envelope f_{Env} and is used to attain the Q-factor.

$$f_{RD} = A_0 e^{-\frac{\omega}{2Q}t} \cos\left(\omega t \sqrt{1 - \frac{1}{4Q^2}} + \varphi\right) \quad (3.9)$$

4. Piezoelectric Thin Film Materials

Parts of this chapter are published in [153], [154].

In this chapter piezoelectric aluminum nitride thin films and their variants, alloyed with scandium and yttrium are discussed. After analyzing the characteristic properties of AlN thin films and possible deposition techniques, the influences of the previously mentioned alloying elements on the microstructural composition, piezoelectric coefficients and the residual intrinsic stress are analyzed. Finally, a specific sputter process is presented, which makes it possible to tailor the intrinsic stress of AlN and alloyed AlN thin films, which facilitates their integration into a MEMS fabrication process.

4.1 Aluminum Nitride

Aluminum nitride (AlN) is a colorless solid material from the group III-V nitrides. Its exceptional properties like chemical resistance, thermal stability up to 1150 °C [155], a high thermal conductivity of $321 \text{ W m}^{-1} \text{ K}^{-1}$ [156], a high breakdown voltage of up to 2.6 MV cm^{-1} [157], [158] and a high electrical resistivity of approximately $10^{14} \Omega \text{ cm}$ [159] led to a broad range of applications like anticorrosive coatings [160], [161], passivation layers for semiconductor devices [162], [163] or as a substrate for high power electronics [164]–[166]. Its electromechanical properties, which are expressed through the piezoelectric coefficients d_{33} , d_{31} and d_{15} , its low dielectric constant ϵ_r and the compatibility to the CMOS process makes it a most interesting material for MEMS sensors [[126], [167]–[170]]. Values for the mentioned properties can be found in Table 5.

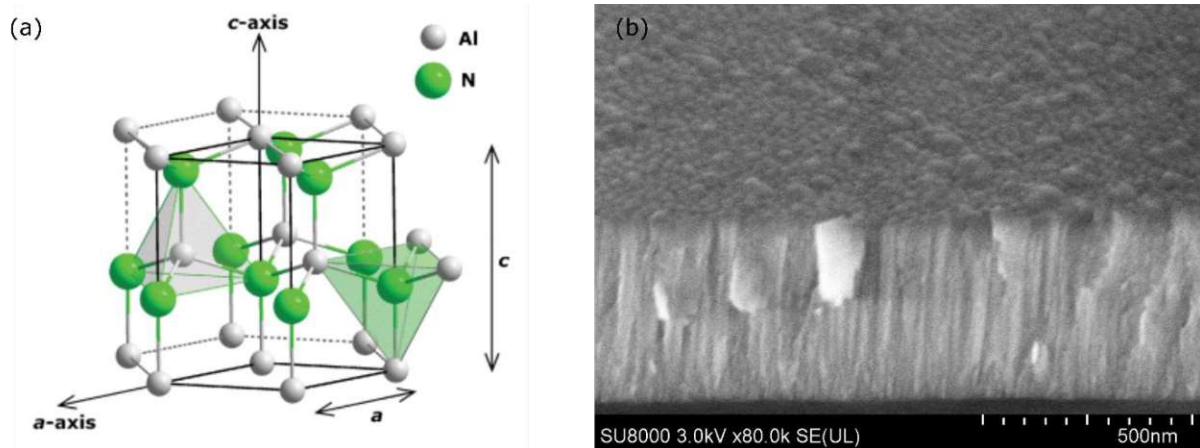


Figure 21: (a) Hexagonal wurtzite crystal lattice of aluminum nitride with tetrahedron binding structure, taken from [168]. (b) Cross-sectional SEM micrograph of a tilted aluminum nitride thin film.

Various deposition techniques *e.g.*, molecular beam epitaxy [171], metal organic chemical vapor deposition [172], pulsed laser deposition [173] or radio-frequency [174], pulsed-DC [175] or DC [176] sputter deposition can be used to synthesize AlN thin film. As this work solely focuses on DC sputter deposited thin films, only information regarding this technique is mentioned in the following.

In general, AlN crystallizes in a hexagonal wurtzite structure, whereas each Al atom is surrounded by 4 N atoms, forming a tetrahedron. In this pyramid-like structure the bond in c-direction differs from the other 3 bond directions [177], shown in Figure 21 (a) which is taken from [168]. Typical values of the c- and a-axis distance of the crystals can be found in Table 5. When sputter deposited

under the right conditions, AlN forms a columnar microstructure and the crystallographic c-axis is oriented perpendicular to the substrate surface (002), shown in the SEM micrograph in Figure 21 (b). In this crystal phase AlN exhibits significant piezoelectric properties [168].

Parameter	Value	Ref.
a / nm	~ 0.31	[168], [178]
c / nm	~ 0.50	[168], [179]–[181]
$d_{33} / \text{pC N}^{-1}$	5 – 6	[182]–[184]
$d_{31} / \text{pC N}^{-1}$	–2.5	[185]–[187]
$d_{15} / \text{pC N}^{-1}$	~ 3.6	[188]
ϵ_r	~ 10.5	[183], [189], [190]

Table 5: Characteristic properties of aluminum nitride thin films.

Beside the microstructural and piezoelectric properties, another important parameter, especially when targeting MEMS applications is the intrinsic thin film stress. The residual stress in polycrystalline AlN thin films can range from compressive to tensile levels [191]–[193], depending on the deposition technique and its conditions. Compressive stress can lead to delamination of the thin film during fabrication [194] or warped structures like microbridges [195] or cantilevers [196], [197] whereas excessive stress can even lead to complete failure of the whole device. Tensile stress can lead to cracking of the thin film [198] which in turn can lead to electrical short cuts. As thin film stress may change over time through relaxation, the devices performance is also prone to parasitic drift effects [199], [200].

This residual stress can originate from various sources, *e.g.* lattice mismatch [197], [201], [202], atomic peening [203] or from different thermal expansion coefficients of substrate and the deposited thin films [204], occurring either due to temperature loads during fabrication or when operating the device. Additionally, AlN often exhibit a stress gradient along the thickness of the thin film [196]. One way to influence the residual stress of pure or alloyed AlN is by varying the thickness [193], [197], [205], sputter gas composition [197], [206], [207] or sputter pressure [176], [208] of the thin film and is studied in section 4.2 and 4.3 for AlScN and AlYN thin films, respectively. However, changing sputter conditions not only influence the residual stress but also other properties like the piezoelectric coefficients, which makes it necessary to monitor those properties simultaneously.

4.2 Aluminum Scandium Nitride

As already mentioned, aluminum nitride can be alloyed by various other elements, whereas scandium is the most promising one up to date. While DFT simulations show the possibility of increasing the scandium content up to 50% and still preserve piezoelectric properties [209], [210], experimental work done by several authors showed different results, especially for higher scandium concentrations, shown in Figure 22. The maximum achieved increase in the piezoelectric longitudinal coefficient of approximately 500% to 27.6 pC N^{-1} for a scandium concentration of 43%, was reached by Akiyama *et al.* [211] and Umeda *et al.* [52]. Higher concentrations of scandium content led to a change from the hexagonal to the cubic microstructure of scandium aluminum nitride (AlScN) thin films [212]–[214].

As a consequence, scandium aluminum nitride thin films were studied in the following for their use in piezoelectric MEMS energy harvesters and sensors.

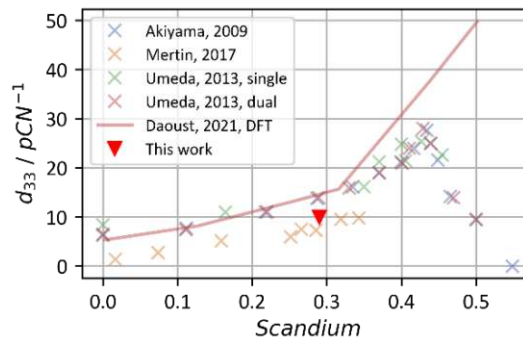


Figure 22: Piezoelectric constants d_{33} as a function of scandium content from Akiyama 2012 [211], Mertin 2017 [215] Umeda 2013 [52], Daoust, 2021 [209] and this work.

4.2.1. Deposition of AlScN thin films

Scandium aluminum nitride thin films with an elemental composition of 71% aluminum and 29% scandium were synthesized from a 6'' target, manufactured by a powder metallurgic sintering process, with 67% of aluminum and 33% scandium. The difference in the elemental composition of the sputtered thin film and the target material most probably originates from the different size and weight of the different elements. Scandium with a radius of $r_{Sc} = 162 \text{ pm}$ and a standard atomic weight of $A_r(Sc) = 44.95$, is much bigger and nearly twice as heavy as aluminum with $r_{Al} = 143 \text{ pm}$ and $A_r(Al) = 26.98$. This reduction in Sc concentration in the deposited film was also observed by Akiyama *et al.* who sputter deposited an $Al_{62}Sc_{38}N$ thin film from an $Al_{58}Sc_{42}$ target [51] and several others [216]–[218]. Furthermore, this effect could also be observed for $Al_{91}Y_9N$ thin films sputter deposited from an $Al_{85}Y_{15}$ target studied in section 4.3. It shows a larger difference in yttrium concentration compared to the $Al_{71}Sc_{29}N$ thin films, which could be due to the even bigger and heavier yttrium atoms, again confirming this hypothesis.

Several differently sputtered thin films were synthesized on wafer level and characterized for their differences in crystallographic structure (section 4.2.2), the piezoelectric coefficients and intrinsic stress (section 4.2.3). Details about various parameters including thin film thickness D and thin film stress σ can be found in Table 6.

No.	Mat.	Power <i>W</i>	Pressure <i>Pa</i>	Ar/N <i>sccm</i>	Sputter rate <i>nm s⁻¹</i>	D <i>nm</i>	<i>RC_{FWHM}</i> (002) °	<i>d₃₃</i> <i>pC N⁻¹</i>	<i>σ</i> <i>GPa</i>
S1	Al _{0.71} Sc _{0.29} N	1000	0.2	0/40	0.60	258	4.50	4.66	-1.75
S2	Al _{0.71} Sc _{0.29} N	1000	0.2	0/40	0.57	545	3.99	9.3	-1.45
S3	Al _{0.71} Sc _{0.29} N	1000	0.2	0/40	0.58	1050	3.82	8.38	-1.03
S4	Al _{0.71} Sc _{0.29} N	1000	0.2	0/40	0.56	2040	3.94	5.7	-0.71
S5	Al _{0.71} Sc _{0.29} N	600	0.2	0/40	0,31	501	4.63	7.26	-1.13
S6	Al _{0.71} Sc _{0.29} N	800	0.2	0/40	0,42	520	3.76	9.74	-1.30
S7	Al _{0.71} Sc _{0.29} N	600	0.2	4/36	0,34	502	4.04	9.72	-0.95
S8	Al _{0.71} Sc _{0.29} N	800	0.2	4/36	0,45	499	3.71	10.88	-1.17
S9	Al _{0.71} Sc _{0.29} N	1000	0.2	4/36	0,60	512	3.52	11.98	-1.23
S10	Al _{0.71} Sc _{0.29} N	600	0.2	6/36	0,35	518	4.04	9.90	-0.88
S11	Al _{0.71} Sc _{0.29} N	800	0.2	6/36	0,44	489	3.59	11.52	-1.28
S12	Al _{0.71} Sc _{0.29} N	1000	0.2	6/36	0,61	477	3.57	12.22	-1.35
S13	Al _{0.71} Sc _{0.29} N	1000	0.6	0/40	0,48	553	8.796	2.70	-0.26
S14	Al _{0.71} Sc _{0.29} N	1000	1.0	0/40	0,42	449	12.134	1.56	+0.02
S15	Al _{0.71} Sc _{0.29} N	1000	1.4	0/40	0,37	450	15.86	1.10	+0.05

Table 6: Deposition conditions for the sputtered AlScN thin films and results of their microstructural and electro-mechanical characterization.

4.2.2. Structural Characterisation

In a first step, thin films varying in thickness from 250 *nm* – 1000 *nm* were analyzed. The Bragg-Brentano scans from Figure 23 (a) show that all thin films exhibit a distinct (002) peak at ~35.8°, indicating the presence of the preferred crystallographic direction for piezoelectric thin films. However, while thicker films were expected to have a higher crystallinity, they also show a higher number of differently orientated crystals. This could also be observed in the SEM images in Figure 24 (a-d). Especially the insets, representing images of the surface of the thin films show a higher density of those grains. The occurrence of those crystallites was observed by several different groups and it was shown that the relation between those abnormal grains and the crystallites in (002) direction depends strongly on the selected sputter parameters. Sandu *et al.* reported that a higher RF-bias led to a reduction in non-(002) oriented grains and thicker films developed larger grains with different orientations, which in turn replaced the (002) grains [219]. The FWHM of the rocking curve in Figure 23 (b), measured at the (002) peaks show that thicker films exhibit a lower FWHM and hence, better oriented (002) grains. A similar trend could be observed by Knisely *et al.* who received FWHMs between 5.85° – 1.34° for thicknesses of 14 *nm* – 1100 *n* [220].

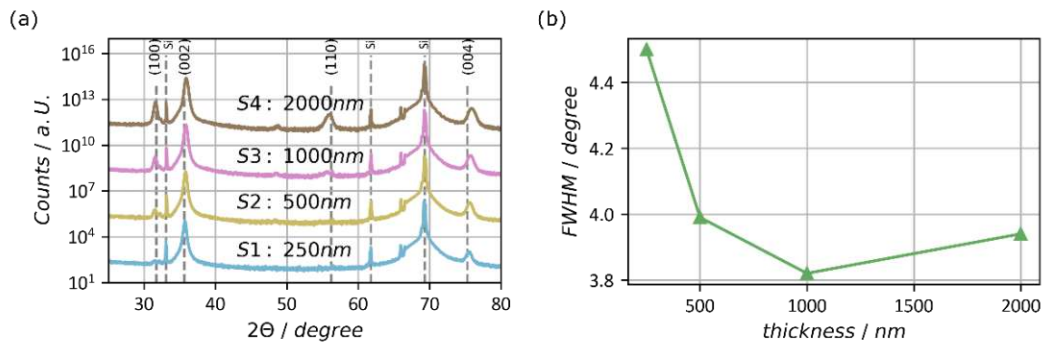


Figure 23: (a) Bragg-Brentano scans for samples with varying thickness S1-S4 and (b) FWHM of the rocking curve as a function of thickness for the same samples. Lines in (b) serve as guide to the eye.

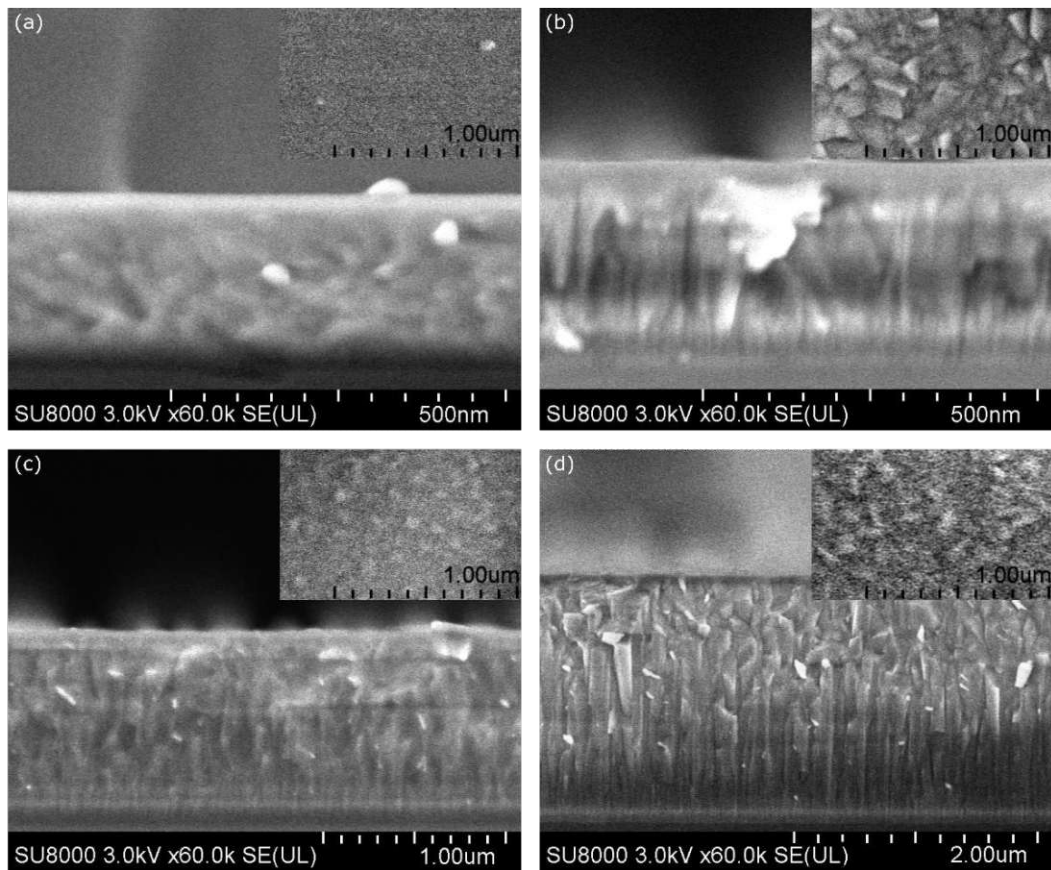


Figure 24: SEM micrographs of the cross-section and the related surface of samples (a) S1, (b) S2, (c) S3 and (d) S4.

Another influencing parameter when depositing AlScN thin films is the sputter power. The Bragg-Brentano scans of the studied samples are shown in Figure 25 (a-c), whereas equally colored curves represent equal gas compositions with a nitrogen content of 100% in blue, 90% in ochre and 85% in pink. For all three gas compositions the peak-intensity at 33° reduce with increasing power. Additionally, the rocking curve performed around the (002) peak show lower *FWHMs* for higher sputter powers independent of the gas composition. This confirms observations done by other groups [221], [222].

The addition of argon leads to a similar behavior, meaning that more argon content in the sputter gas composition reduces the intensity of the peak around 33° and additionally reduces the *FWHM* of the rocking curve of the (002) peak. This can be linked to the higher sputter rate due to the higher atomic weight of argon, in comparison to nitrogen. However, various groups showed that when

increasing the argon content over a certain threshold, thin film quality reduces again [223]. One of the reasons might be the insufficient availability of nitrogen atoms when scandium or aluminum atoms react on the wafer surface, possibly leading to metal clusters in the deposited thin film.

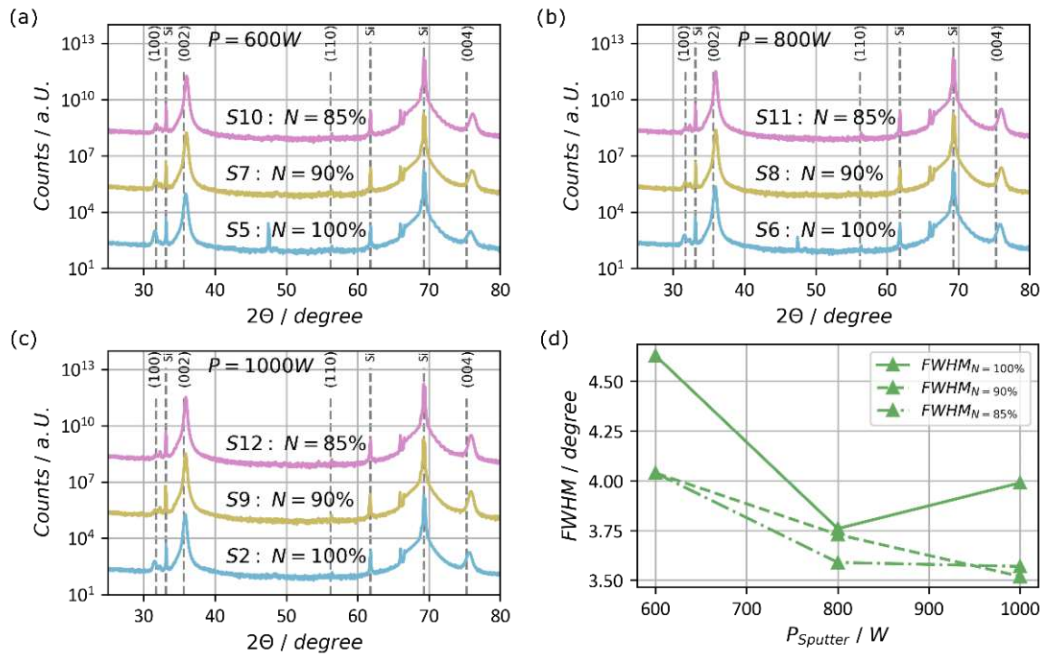


Figure 25: Bragg-Brentano scans for varying gas compositions and fixed sputter power of (a) 600 W (S5, S7, S10), (b) 800 W (S6, S8, S11) and (c) 1000 W (S2, S9, S12). (d) FWHM of the rocking curve as a function of sputter power for all previously mentioned samples. Lines in (d) serve as guide to the eye.

The third parameter studied is the working pressure which shows the highest influence on the microstructure and on the thin film quality. Four different pressure levels between 2 – 14 μbar were used. Beside the already discussed abnormal peak at 33° the Bragg-Brentano scans in Figure 26 (a) show that in addition to the (002) peak at 35.8°, another peak at 36.5° forms and gets more pronounced with higher pressure values. A possible reason for the formation of this second peak might be a change in residual thin film stress during deposition, due to changed growth conditions. The formation of pure ScN crystals can most probably be excluded as diffraction patterns of pure ScN only exhibit peaks below 35° and above 40° [224], [225]. The ultimate explanation for the presence remains unclear and shows the need for further future studies. As expected, the *FWHM* of the rocking curves illustrates increasing values with increasing sputter pressure, showing a high value of 8.8° already at 6 μbar . This again confirms similar measurement results reported in [221], [226].

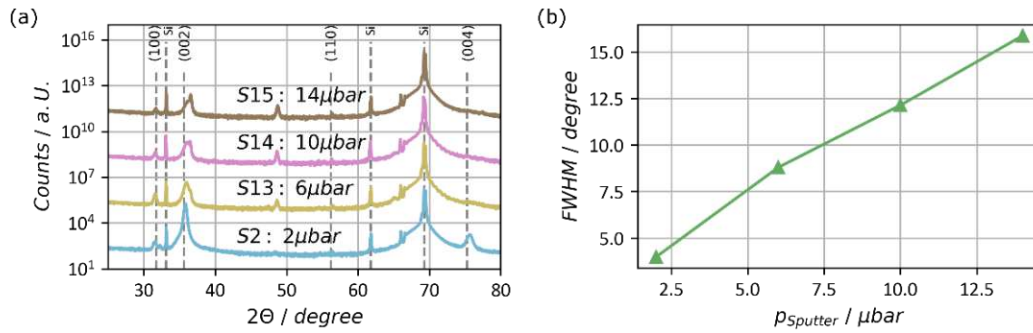


Figure 26: (a) Bragg-Brentano scans for samples with varying sputter pressure S2, S13, S14 and S15 and (b) FWHM of the rocking curve as a function of sputter pressure for the same samples. Lines in (b) serve as guide to the eye.

The SEM images of the cross-section of thin films in Figure 27 (a-d) and of the surface (insets) show an interesting observation. While the low-pressure sample exhibits big abnormal grains, as already discussed before, the higher-pressure sample shows similar structures but with a much finer grain size. Again, this indicates a change in the growth conditions under higher sputter pressure, when comparing to low pressure.

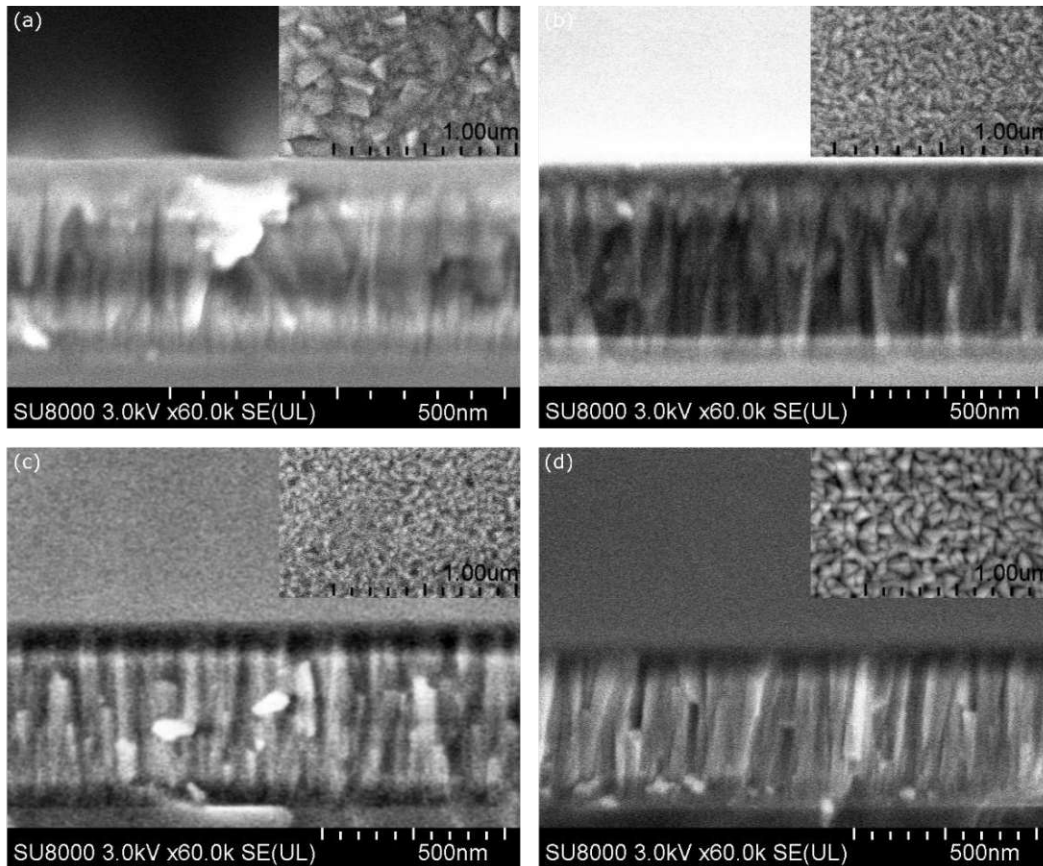


Figure 27: SEM micrographs of the cross-section and the related surface for samples (a) S2, (b) S13, (c) S14 and (d) S15 sputtered with different pressure.

4.2.3. Electro-mechanical Characterization

Figure 28 (a-c) show the intrinsic stress σ (blue curves) and the piezoelectric longitudinal coefficient d_{33} (orange curves) for all previously presented samples. With increasing thickness, the intrinsic

stress changes from highly compressive to less compressive, while the d_{33} varies only slightly around $8 \pm 2 \text{ pC N}^{-1}$. These results show a similar trend as previously reported studies about pure AlN thin films [196], [202], [227], [228]. They also correspond to the trend of the FWHM of their according rocking curve from the previous chapter.

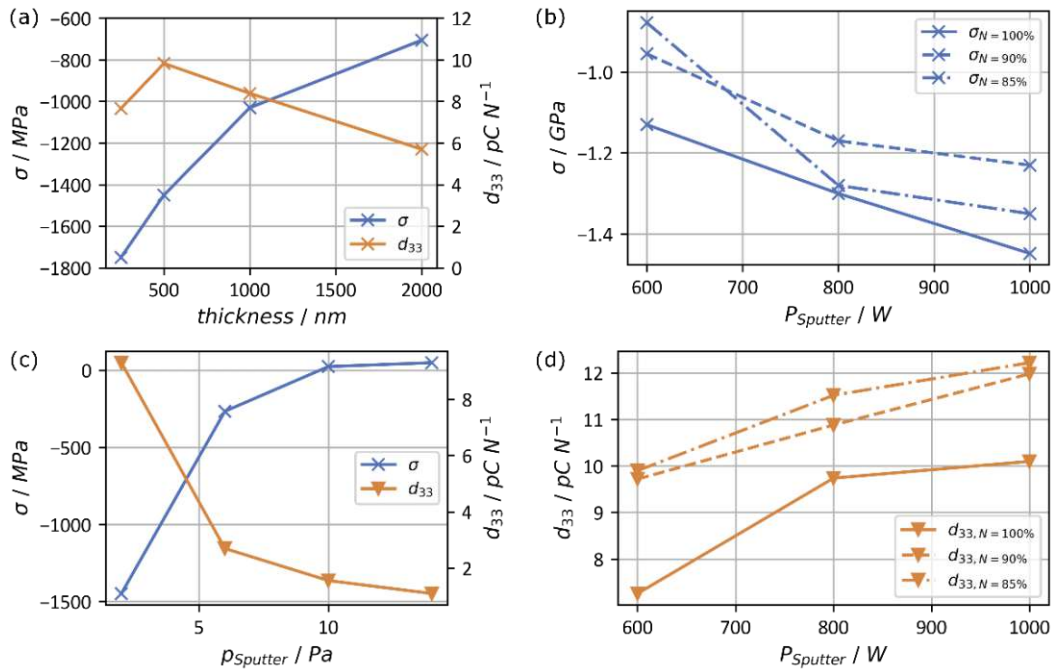


Figure 28: Thin film stress σ and piezoelectric coefficient d_{33} as a function of (a) thin film thickness for samples S1-S4, (b) and (d) sputter power for samples S5, S6, S2 (N=100%), S7, S8, S9 (N=90%), S10, S11, S12 (N=85%) and (c) sputter pressure for samples S2, S13-S15. Lines in (a-d) serve as guide to the eye.

The sputter power has an inverse effective on the intrinsic stress, meaning that higher power leads to higher compressively stressed thin films, although the absolute amount of change was the lowest within the given parameter range. This behavior is similar for all used gas compositions, except an outlier sputtered with 600 W and 90% nitrogen. The piezoelectric coefficient d_{33} increases by approximately 20% while increasing the power from 600 W – 1000 W and this effect is similar for all three gas compositions. These results are generally in good agreement with the rocking curve FWHMs which decrease with increasing power and increasing argon content.

The sputter pressure p_{sputter} showed the highest influence on the thin film stress and on the piezoelectric coefficient ranging from -1448 MPa to $+49 \text{ MPa}$ and 9.3 pC N^{-1} to 1.1 pC N^{-1} , respectively for a pressure ranging from 0.2 Pa to 1.4 Pa . This again confirms similar observations reported in literature [51], [221], [226].

When comparing the FWHM of the rocking curve to the piezoelectric coefficient shown in Figure 29, it is clearly visible that a high FWHM correspond to a low d_{33} , but measuring a low FWHM is not sufficient for having a high d_{33} . This was also shown by Olivares *et al.* [229] for pure AlN thin films and will be discussed again in section 4.3.4 for AlYN thin films, which shows a similar behavior.

In summary, it can be stated that thicker thin films sputtered with higher power and argon content increased by 15% in the sputter atmosphere, show increased thin film quality and a good piezoelectric coefficient, but also a high compressive intrinsic stress. The sputter pressure has the exact opposite effect – reducing the intrinsic stress to nearly unstressed thin films for a pressure above 1.0 Pa , but at the same time the piezoelectric coefficient degrades to very low values. A method to circumvent this drawback being essential for the later integration into MEMS devices

(i.e., low film stress in combination with high piezoelectric coefficients) will be introduced in section 4.4, where a stress tailoring method is developed for pure AlN and also tested on the same AlScN thin films presented in this chapter.

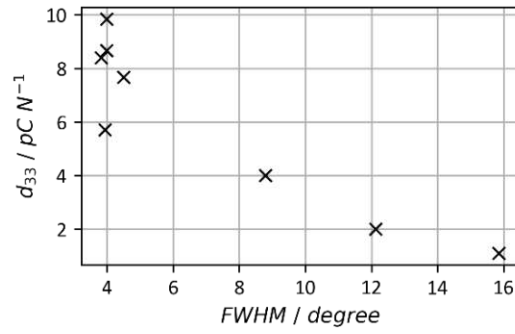


Figure 29: Piezoelectric coefficient d_{33} as a function of the FWHM of the rocking curve.

4.3 Aluminum Yttrium Nitride

Another alternative to scandium for alloying is yttrium, which belongs to the same group III transition metals as scandium and is located right below the latter element in the periodic table of elements. In its pure form yttrium is a silvery metallic rare earth metal and is chemically very similar to other elements in the lanthanides group. Its atomic radius $r_{Atom,Y} = 180 \text{ pm}$ is a lot larger than the radii of aluminum ($r_{Atom,Al} = 143 \text{ pm}$) and scandium ($r_{Atom,Sc} = 162 \text{ pm}$), which already makes it obvious, that mixing yttrium and aluminum in the same crystal lattice is a challenging task.

Mayrhofer *et al.* and Žukauskaitė *et al.* did *ab initio* density functional theory (DFT) simulations to estimate the mechanical and piezoelectric properties [230], [231]. They predicted, that AlN alloyed with yttrium can exceed the piezoelectric coefficients of AlScN with a maximum $d_{33} = 35 \text{ pC N}^{-1}$ at 50% yttrium content. Furthermore, Mayrhofer *et al.* showed that it is possible to grow crystalline AlYN thin films by reactive co-sputtering. Although the lattice parameters calculated from the DFT simulations were in excellent agreement with the results of the XRD measurements, the layers underperformed with respect to the piezoelectric properties, which was attributed to an oxygen rich amorphous region in the AlYN thin film at the interface to the silicon substrate. Another contradictory result was found by Tholander *et al.* by their DFT simulations [232]. They studied a mixture of $Al_{50}Y_{50}N$ and argued that the high-volume difference between YN and AlN leads to high structural distortions within the wurtzite crystal lattice. This prevents the giant enhancement of the piezoelectric coefficients, compared to *e.g.*, aluminum scandium nitride alloy, where the volume difference is less. These contradictory results indicate that there is a strong need for further experimental investigations on this promising alloying material, which will be addressed in the following.

Due to the high affinity of yttrium towards oxygen [233], manufacturing high-quality yttrium aluminum alloy targets with low oxygen contamination is a very challenging task, especially if a high yttrium concentration is targeted. Therefore, we decided to investigate the impact of sputter parameters on basic properties of $Al_{0.91}Y_{0.09}N$ thin films, synthesized from an $Al_{0.85}Y_{0.15}N$ alloy target. In detail, the microstructure of the sputter-deposited layers and their piezoelectric properties are characterized.

4.3.1. Deposition of AlYN thin films

$Al_{0.91}Y_{0.09}N$ with a thickness of $500 \pm 50 \text{ nm}$ were deposited on $1.5 \times 1.5 \text{ cm}^2$ sized snippets of (100) silicon. The 6" sputter target manufactured with a powder metallurgical sintering process at "RHP Technology", consisted of 15 at% yttrium and 85 at% aluminum. To evaluate the best conditions for sputter deposition pressure, plasma power, gas composition plus the corresponding flow rates these parameters were varied and are listed in Table 7. The purity of the gases was N6, the target to substrate distance during all sputter depositions was 65 mm and the base pressure in the sputter chamber was $1.2 \cdot 10^{-7} \text{ Pa}$. Prior to the deposition, the substrate pieces were cleaned by an ultrasonic bath with acetone and isopropyl alcohol and finally rinsed in deionized water to remove any organic contamination. In order to remove any surface oxides and other surface contaminants from the target surface, the target was sputter cleaned at closed shutter position for 60 s under pure argon atmosphere before each deposition. As a reference, a pure aluminum nitride thin film (S_1) was first synthesized and characterized.

No.	Mat.	Power <i>W</i>	Pressure <i>Pa</i>	Ar/N <i>sccm</i>	Sputter rate <i>nm s⁻¹</i>	D <i>nm</i>	RC_{FWHM} (002) °	d_{33} <i>pC N⁻¹</i>	σ <i>GPa</i>
S_1	AlN	800	0.2	0/40	0.533	500	3.90	5.02	-0.58
S_2	$Y_{0.09}Al_{0.91}N$	600	0.2	0/40	0.263	579	7.54	2.38	n.a.
S_3	$Y_{0.09}Al_{0.91}N$	800	0.2	0/40	0.356	570	5.72	2.82	-2.15
S_4	$Y_{0.09}Al_{0.91}N$	800	0.2	10/30	0.423	661	15.92	0.26	-2.07
S_5	$Y_{0.09}Al_{0.91}N$	800	0.2	6/34	0.397	579	7.74	2.73	-1.97
S_6	$Y_{0.09}Al_{0.91}N$	800	0.4	0/40	0.274	465	6.05	3.97	-1.66
S_7	$Y_{0.09}Al_{0.91}N$	800	0.6	0/40	0.250	500	6.41	2.09	-1.38
S_8	$Y_{0.09}Al_{0.91}N$	1000	0.2	0/40	0.452	543	6.16	5.24	-2.12
S_9	$Y_{0.09}Al_{0.91}N$	1000	0.4	0/40	0.385	460	5.73	7.79	-1.90
S_{10}	$Y_{0.09}Al_{0.91}N$	1000	0.6	0/40	0.304	480	10.14	0.64	-1.79
S_{11}	$Y_{0.09}Al_{0.91}N$	1000	0.2	6/34	0.477	512	n.a.	n.a.	-1.73
S_{12}	$Y_{0.09}Al_{0.91}N$	1000	0.2	10/30	0.494	532	n.a.	n.a.	-1.45

Table 7: Deposition conditions for the sputtered AlYN thin films and results of their microstructural and functional characterization. Samples S_{11} and S_{12} were used for oxygen characterization under heat treatment.

4.3.2. Structural Characterisation

To investigate the film morphology, SEM images were recorded of both the film cross-section and of the surface of the $Al_{0.91}Y_{0.09}N$ thin films, as shown in Figure 30. The microstructure of the surface exhibits the presence of circularly shaped grains, comparable to AlN and AlScN samples [234], [235]. The average grain diameter can be estimated from the surface image to about 40 nm. Schneider *et al.* showed a slightly smaller grain diameter of about 20 nm for similar layer thicknesses of pure AlN [157], whereas Akiyama *et al.* reached comparable grain diameters with $Al_{0.64}Sc_{0.36}N$ layers of about 45 nm [211]. They argued that a lower grain size leads to a film graining with a higher degree of ordering, which in turn results in enhanced piezoelectric coefficients.

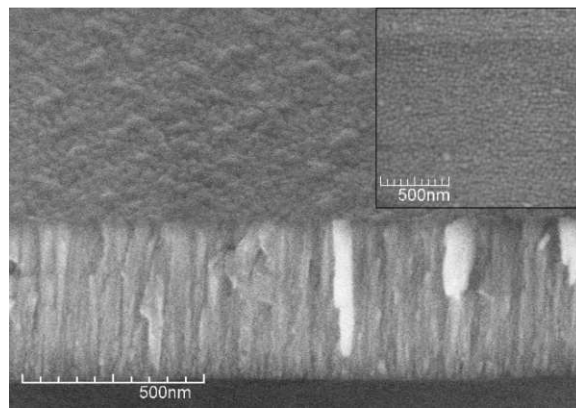


Figure 30: SEM images of the AlYN sample 10 with 30° tilted cross-section and the surface morphology given by the inset.

To study the microstructure of the $Al_{0.91}Y_{0.09}N$ layer in more detail, the sample with the highest piezoelectric coefficient S_9 was investigated by TEM. In addition, high spatially resolved EDX analysis provides information about the local chemical composition. Figure 31 (a) shows a dark field image of the cross-section of the entire $Al_{0.91}Y_{0.09}N$ layer. Figure 31 (b) is a high-resolution TEM image of the interface between the silicon substrate and the $Al_{0.91}Y_{0.09}N$ layer. It can be seen that there is a

continuous layer of native SiO_2 separating the silicon substrate and the $Al_{0.91}Y_{0.09}N$ layer, followed by a mixture of crystalline growth and amorphous regions, whereas the crystallite size increases with increasing layer thickness.

The selected area electron diffraction (SAED) image, Figure 31 (c) has been taken from the center of the layer and the lattice constants have been calculated to $c = 0.515nm$ and $a = 0.323nm$. Compared to the previous mentioned DFT simulations the a lattice constant is in good agreement, while the c -lattice constant is higher than the predicted ones from several different DFT simulations [230], [231], [236], shown in Figure 32. In contrast, the experimental values of Žukauskaitė *et al.* and Mayrhofer *et al.* were lower than the calculated values, which might also be an indicator why the piezoelectric constants were lower than expected.

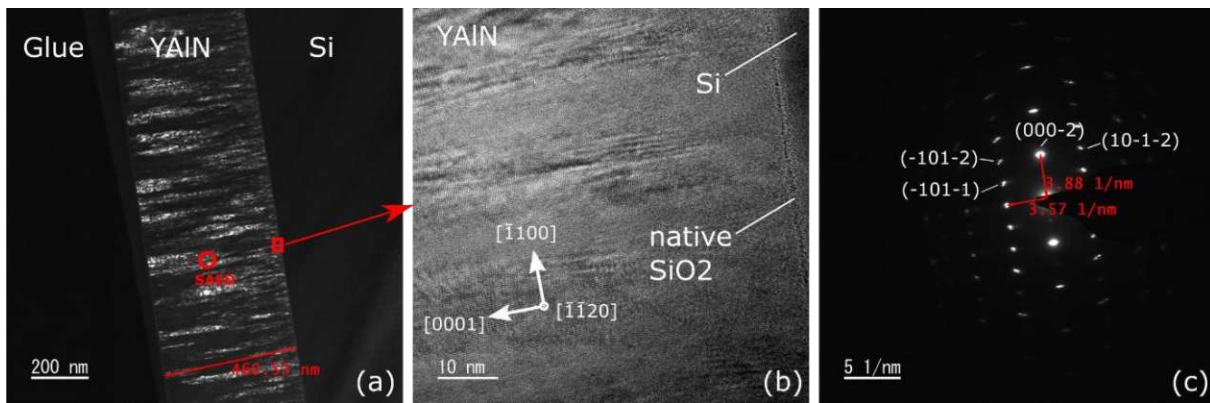


Figure 31: TEM and SAED images of sample 9. (a) Dark field TEM image of the film cross-section. (b) High resolution image of the interface region between the silicon substrate and the AlYN thin film. (c) SAED image of the AlYN thin film taken from the center of the thin film.

When calculating the Bragg-Brentano angle for the (002) peak from the measured c -lattice constant, we get $2\theta = 35.1^\circ$, which is a reduction by $\sim 1^\circ$ compared to pure unstressed AlN [237]. The reduced angle indicates a compressively stressed thin film, which is typical for sputter deposited aluminum nitride thin films. More discussion about the thin film stress of $Al_{0.91}Y_{0.09}N$ will be done together with wafer bow measurements in section 4.3.4.

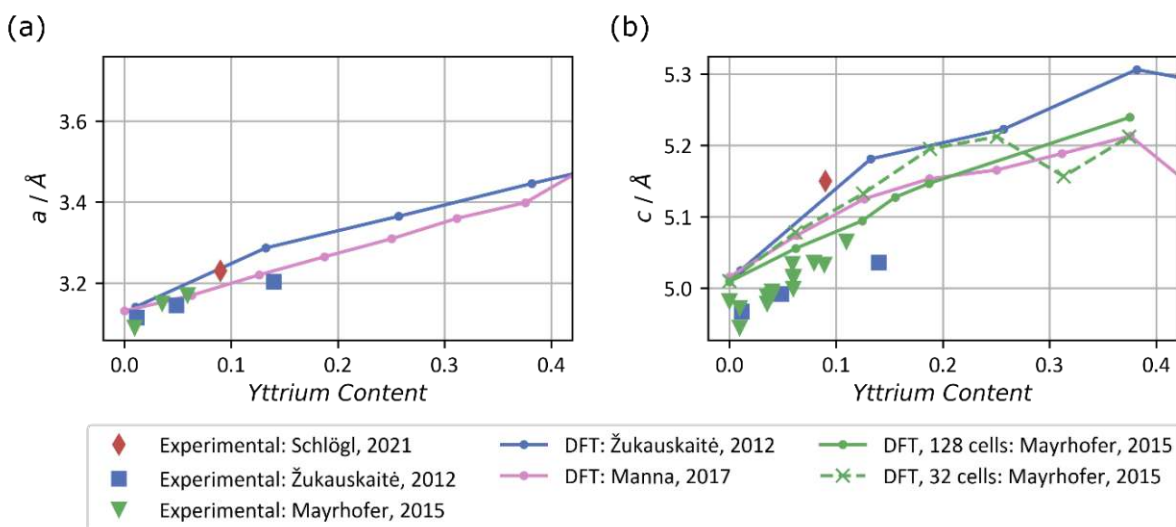


Figure 32: Comparison of the lattice constants from DFT simulations and experimental data for (a) the a-axis lattice constant and (b) c-axis lattice constant.

To determine the chemical composition of the thin film, an EDX area scan was conducted. Figure 33 (a-f) shows the complete area scan and the components of aluminum, nitrogen, oxygen and yttrium. The $Al_{0.91}Y_{0.09}N$ thin film in the middle is confined by the glue on the left side (pink) and by the silicon substrate on the right side (green). The line scan in Figure 34 is an integration along the y-axis of the area scans and gives a better qualitative overview of the local distribution of the different elements in the thin film. The oxygen content in the $Al_{0.91}Y_{0.09}N$ layer remains on 30–50 counts in the EDX spectra which translates to 2.91% of oxygen contamination in the $Al_{0.91}Y_{0.09}N$ thin film, compare Table 8. The interface between the $Al_{0.91}Y_{0.09}N$ thin film and the Si substrate has a sharp peak of about 120 counts, which indicates the native oxide of the silicon substrate, as stated before. The high amount of oxygen on the left side of Figure 33 (f) is due to the chemical composition of the glue. The experimentally determined chemical composition from the EDX spectrum of the $Al_{0.91}Y_{0.09}N$ thin film in Figure 34 is given in Table 8.

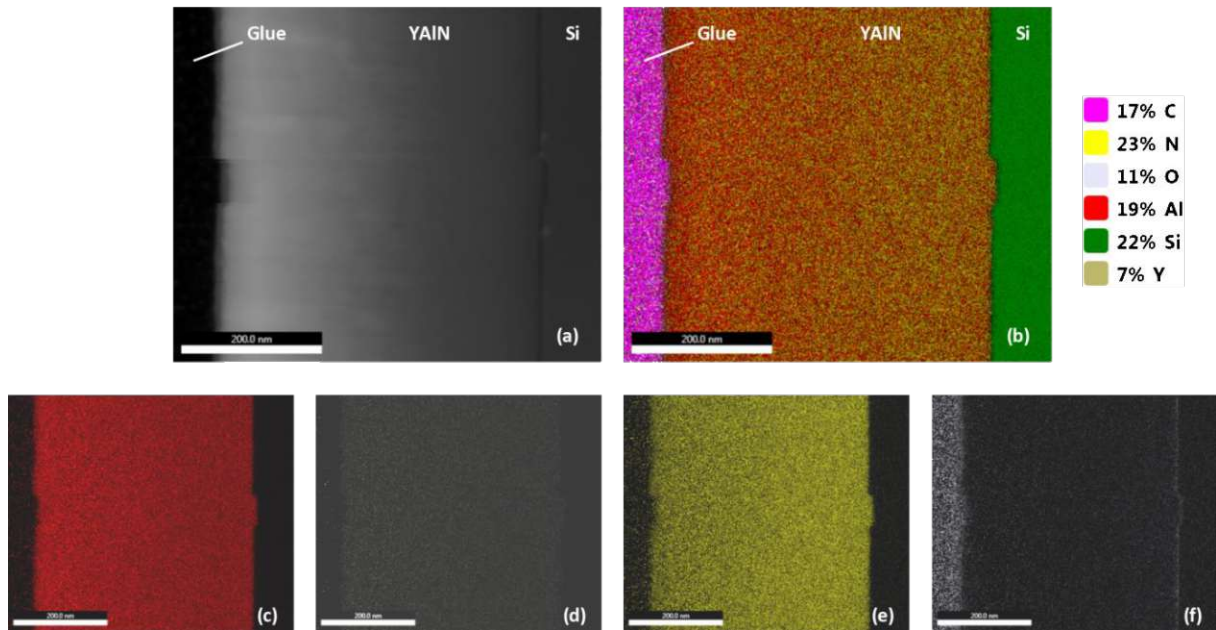


Figure 33: EDX area scan of sample 10. (a) shows the TEM image and (b) shows the complete EDX area scan with chosen elements carbon (pink), nitrogen (yellow), oxygen (grey), aluminum (red), silicon (green), yttrium (golden). Further area scans for single elements are (c) aluminum, (d) yttrium, (e) nitrogen and (f) oxygen. (For interpretation of the references to color in this figure legend, the reader is referred to the web version of this article.)

Mayrhofer *et al.* argued that the incorporation of oxygen, predominantly in the initial film growth results in an amorphous region near the interface and affects the effective values of the piezoelectric coefficients negatively [230]. In contrast, our EDX measurement indicates a lower oxygen content in the film compared to Mayrhofer *et al.* [230] and hence, higher piezoelectric coefficients are expected.

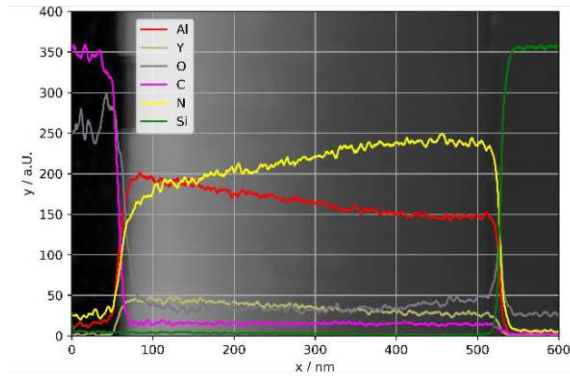


Figure 34: EDX line scan of sample 10.

Elements	Atomic %	Net Error %
	Measured	Measured
Yttrium	4.15	0.76
Aluminum	41.56	0.15
Nitrogen	49.26	0.29
Oxygen	2.91	1.98

Table 8: Elemental composition of the AlYN thin film, extracted from the EDX spectra.

The pure AlN shows a (002) peak around 36.15° with a $FWHM$ of 3.90° , which indicates the presence of a wurtzite microstructure with the c-axis normal to the surface (Figure 35 (a-b)). (100) peaks around 33° indicate crystals growing with a different orientation, which do not contribute to the piezoelectric effect and are therefore unwanted. Žukauskaitė *et al.* showed that for yttrium contents up to 75% the wurtzite phase is the energetically preferred crystallographic phase in the growing film [231]. When neglecting additional effects on the XRD characteristics such as film stress, similar peak positions as for pure AlN are expected as a first approximation.

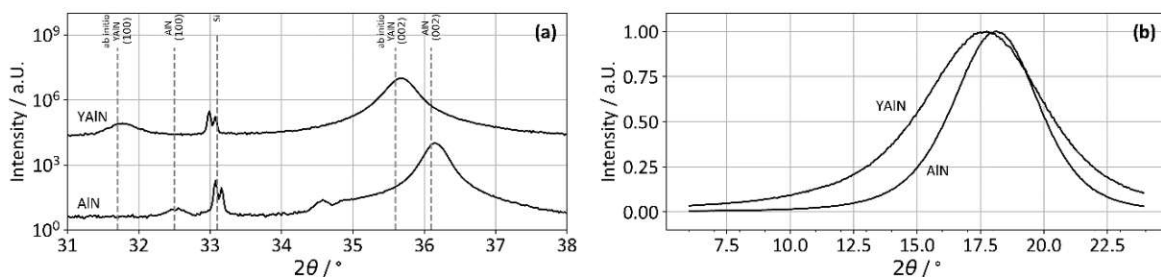


Figure 35: (a) Bragg-Brentano scans and (b) rocking curves of pure AlN S_1 and S_9 .

The variation of sputtering power in Figure 36 (a) was done at a fixed pressure of $0.2 Pa$ in a 100% nitrogen atmosphere. We expected a better crystal growth at higher plasma power values during sputtering, due to an increased sputter rate, resulting in a higher self-heating of the substrate which provides more energy to the surface atoms as reported in literature for pure aluminum nitride [238]–[240]. While a higher sputter power led to a continuously decreasing formation of (100) peaks, the growth of (002) reaches a maximum at $800 W$. This also compares to the $FWHM$ of the rocking curve in Figure 37 (a), which shows 5.72° and 6.16° for $800 W$ and $1000 W$, respectively. Only the thin film sputtered at $600 W$ shows an increased $FWHM$ of 7.54° , which indicates worse growth conditions at lower sputter powers.

Figure 36 (b) illustrates the influence of the gas composition on the crystallographic phase composition. In these experiments, the plasma power of 800 W and a pressure of 0.2 Pa in the deposition chamber were fixed. Higher nitrogen concentrations were preferred as these led to a more pronounced (002) and a less intense (100) peak characteristics, respectively. This is also confirmed by the rocking curve measurements in Figure 37 (b) with decreasing *FWHMs* at higher nitrogen concentrations. Different studies have found a strong impact on the crystallinity of pure AlN [176], [241], [242] as well as AlScN [50], [243] thin films when admixing argon to the nitrogen atmosphere during sputtering. While higher argon content leads to a higher sputter rate due to its higher atomic weight [244], it additionally increases the specific sputter rate of the heavier yttrium compared to aluminum [245]. This increase in yttrium content could influence the growth process towards the less preferred (100) crystallographic direction.

The variation of sputter pressure was done under 100% nitrogen atmosphere at 800 W and 1000 W of sputter power, as illustrated in Figure 36 (c) and (d). Both Bragg-Brentano scans show that with decreasing pressure, the (002) peak intensifies, while the (100) peak height decreases. This can be explained by the larger mean free path of the sputtered particles, which leads to a higher energy level for adatoms at lower sputter pressure. Other works have shown independently that lowering the sputter pressure leads to an enhanced growth of the (002) peak for sputtered AlN thin films [176], [207].

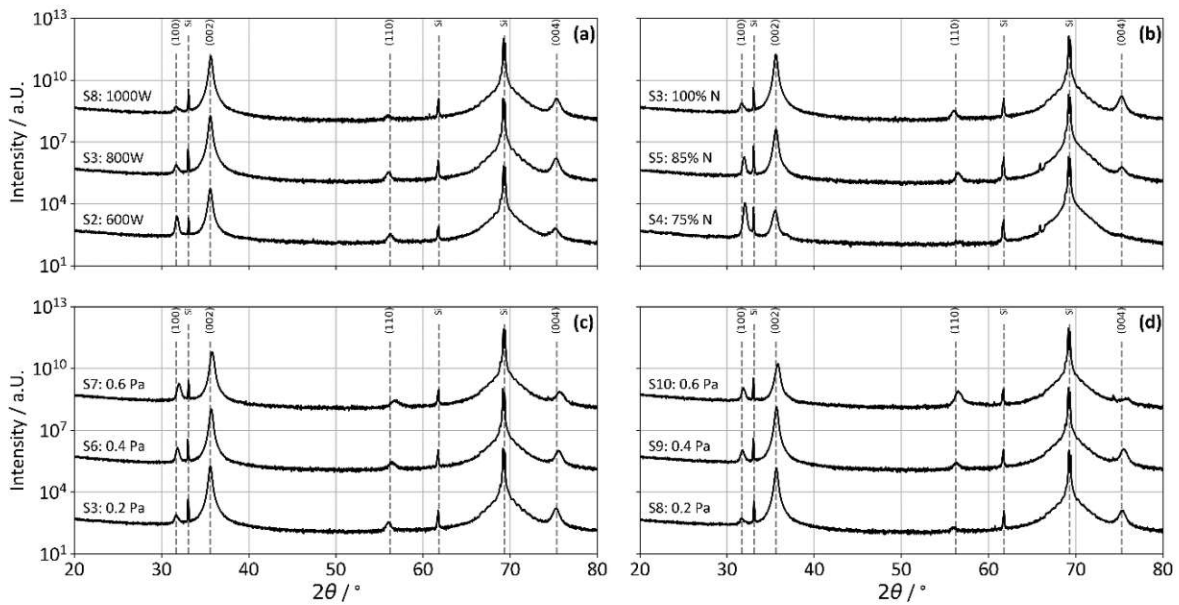


Figure 36: (a-d) show XRD measurements in Bragg-Brentano configuration of layers deposited with varying sputter deposition parameters. Independent of the parameters, all Al_YN layers show a distinct (002) peak around 35.6°. The sharp double peak at 33° originates from the silicon substrate. The corresponding rocking curve measurements of the (002) peaks are given in Figure 37 (a-c).

While the rocking curve measurements in Figure 37 (c) at a plasma power of 1000 W indicate only a minor influence on the *FWHM* with rising sputter pressure, the measurements of the 800 W Al_{0.91}Y_{0.09}N sample show the expected behavior, of rising *FWHM* values with increasing sputter pressure.

The comparison of the Bragg-Brentano scans of pure AlN with the best Al_{0.91}Y_{0.09}N sample in Figure 35 (a) shows, that the (002) peak shifts to lower 2θ values from 36.16° to 35.62°. By using Bragg's law $2d \cdot \sin\theta = n\lambda$ we can calculate the lattice constant of the c-axis to 0.507 nm, neglecting any impact on peak position e.g. by film stress. Comparing this to the DFT simulations of the lattice

constants from Mayrhofer *et al.* [230] we would estimate an yttrium content of 9% if we interpolate the values between his simulated values of 6.25 *at%* and 12.5 *at%* of yttrium content.

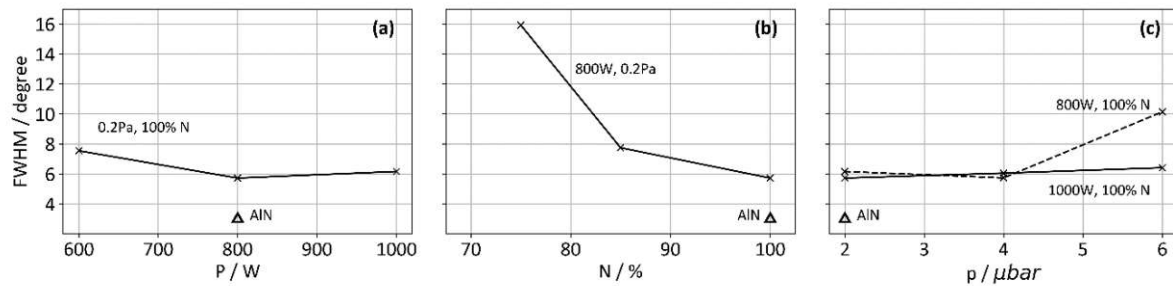


Figure 37: FWHM of rocking curves of $Al_{0.91}Y_{0.09}N$ layers at the (002) peak when varying (a) the plasma power, (b) the nitrogen admixture and (c) the pressure values, including a pure AlN sample as reference. Lines in (a-c) serve as guide to the eye.

4.3.3. Oxygen Contamination of AlY and AlYN thin films

Oxygen is a highly reactive element and can influence the properties of thin film materials if incorporated into the microstructure or it can disturb the crystal growth during sputter deposition [246]–[248]. Mayrhofer *et al.* found significant amounts of oxygen contamination in their thin films and argued that the low piezoelectric coefficients are caused by an amorphous, oxygen-rich layer at the interface to the substrate. As our samples also contained a considerable amount of oxygen, we analyzed our sputtered AlYN thin films and the target material with respect to the presence of oxygen. We defined three different sources of oxygen which have to be considered:

- (1) Oxygen contamination in the sputter gas
- (2) Surface oxide layer formed on top of the AlYN when exposed to air
- (3) Oxygen originating from the target material

Based on the low base pressure of $1.2 \cdot 10^{-7} Pa$ and the high purity of both sputter gases nitrogen and argon of N6, it is reasonable to assume, that oxygen impurities of the **sputter gas (1)** will not be a major influencing factor.

Surface oxidation (2) can occur as soon as thin films are exposed to air, but it is normally a self-limiting process only affecting only the top most few nano meters [249]. However, to further study the impact of surface oxide on the AlYN thin films, EDX measurements were conducted with acceleration voltages U_{acc} of 3, 5, 6 and 10 kV. Increasing U_{acc} results in a larger X-ray emission plume during EDX analysis reaching further into the specimen. As a consequence, a surface oxide of only a few nanometers will produce a less intense signal with increasing U_{acc} , which can be seen Figure 38 (a). The oxygen content in *at%* is decreasing when U_{acc} is increased from 3 to 6 kV. The increased amount of oxygen for the 10 kV measurement lies within the error range of $\pm 0.5\%$ (compare Figure 38 (b)), but it could also be related to an oxygen layer originating from the silicon substrates surface. Additionally, the inset in Figure 38 (a) shows that all other elements show relatively constant values when varying U_{acc} .

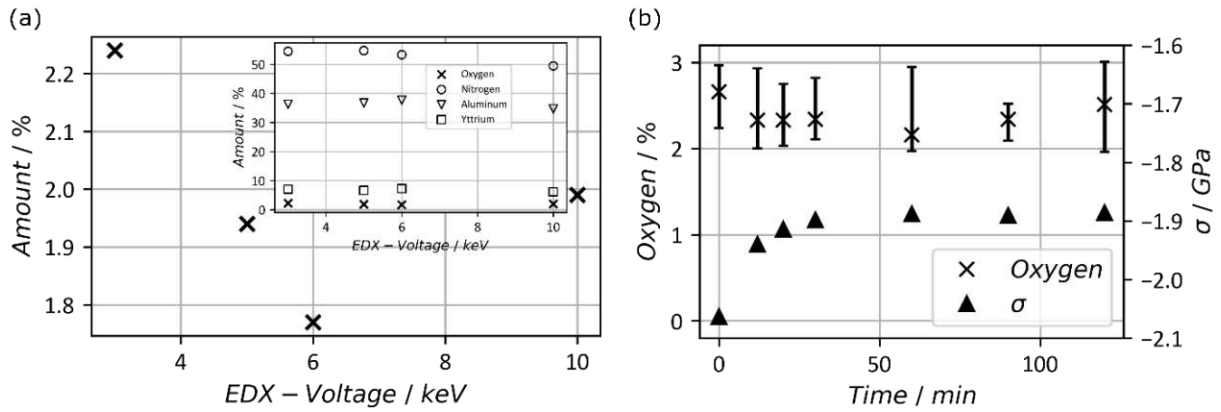


Figure 38: (a) Amount of oxygen in the AlYN thin film for different acceleration Voltages. The inlay shows the complete elemental composition of the AlYN thin film for different acceleration voltages. (b) Change of oxygen content and thin film stress over time during an elevated temperature of 220 °C for a different sample.

Another way to exclude an increased oxygen contamination through surface oxidation at ambient temperature is to measure the change in the elemental composition of an AlYN thin film under heat treatment. Therefore, two AlYN thin films were sputter deposited on a wafer with parameters seen in Table 7. The wafers were then placed on a hotplate at an elevated temperature of 220 °C for 120 min under an ambient atmosphere, to increase the rate of surface oxidation. EDX measurements were performed in regular intervals to determine the elemental composition, shown in Figure 38 (b). Intrinsic stress measurements were also conducted, which additionally indicate a change in the thin film structure, if oxygen is incorporated. The oxygen content during the whole duration stayed within the 2 – 3% range indicating no major influence of oxidation originating from the ambient atmosphere even at an elevated temperature of 220 °C. The thin film stress showed a relaxation within the first 30 min. of the experiment from -2.06 GPa to -1.89 GPa , where it then remained constant. This relaxation of thin film stress may occur through effusion of trapped gas molecules in the thin film, most probably nitrogen [250].

To estimate the influence of oxygen originating from the **target material (3)**, a $10 \mu\text{m}$ thin layer of pure $\text{Al}_{0.85}\text{Y}_{0.15}$ was sputter-deposited in pure argon atmosphere with a sputter pressure of 0.3 Pa , a flow rate of 50 sccm and a sputter power of 500 W . The base pressure of the sputter chamber was the same as stated before and the sputter rate was 3.64 nm s^{-1} . This layer was investigated by EDX within the SEM with an acceleration voltage of 3 – 20 kV to estimate the chemical composition of the target. The peaks in the EDX spectra shown in Figure 39 (a) show different intensities of the present elements. The change in the background signal can be led back to U_{acc} , as lower voltages also give lower signals for the same excitation voltage. Figure 39 (b) shows the oxygen content for all values of U_{acc} , which resulted in a composition of about 83 at% aluminum, 13 at% yttrium and 4 at% oxygen. The higher oxygen content for lower U_{acc} values most probably originates from a surface oxide layer.

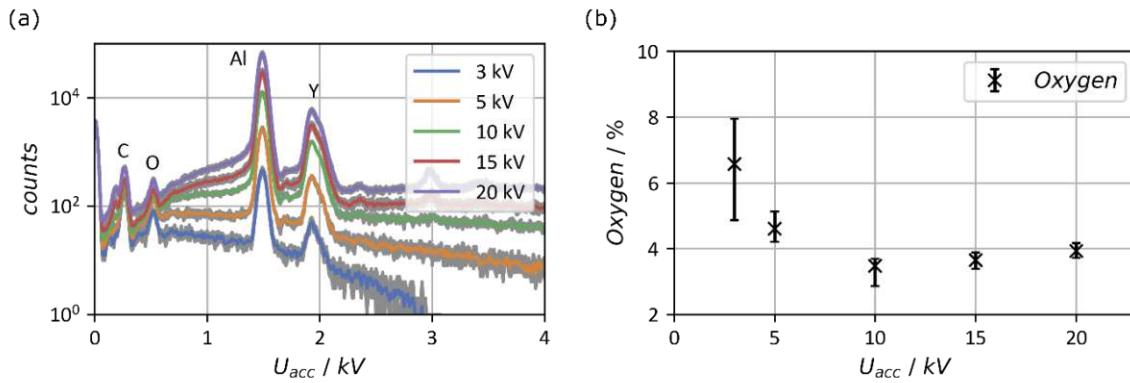


Figure 39: (a) EDX spectra of a metallic $Al_{0.85}Y_{0.15}$ thin film with a thickness of $10 \mu m$ for acceleration voltages of 3, 5, 10, 15 and 20 kV . (b) Oxygen Content measured with the same acceleration voltages.

As a rough estimate, 4 out of 100 sputtered target atoms are oxygen atoms. Given that $Al_xY_{1-x}N$ consists of 50 *at%* nitrogen and assuming, that every sputtered oxygen atom which reaches the substrate replaces one nitrogen atom, we can expect to find approximately half the oxygen concentration of the target in the deposited thin film, which is in excellent agreement with our measurements of the $AlYN$ thin film (shown in section 4.3.2). This leads to the conclusion that most of the oxygen incorporated in the $AlYN$ thin film originates from the target material itself, again emphasizing the importance of a chemically clean, uncontaminated source material and the difficulties arising with the high affinity of yttrium towards oxygen during target fabrication.

4.3.4. Electro-mechanical Characterisation

The *ab initio* calculations from Mayrhofer *et al.* [230] predict an increase in the longitudinal piezoelectric coefficient d_{33} from 5 pm V^{-1} for pure aluminum nitride to 7.8 pm V^{-1} for an yttrium concentration of 9%. Figure 40 (a-c) shows the piezoelectric coefficient d_{33} for various sputter power values, gas compositions and sputter pressures. The dots represent the average value of 9 measured pads, whereas the error bars represent the minimum and maximum measured value. It can be concluded that with increasing power and increasing nitrogen content during deposition, the d_{33} increases. The highest piezoelectric coefficient of 7.79 pm V^{-1} resulted with a pressure value of 0.4 Pa at a plasma power of 1000 W in a pure nitrogen atmosphere during sputter deposition.

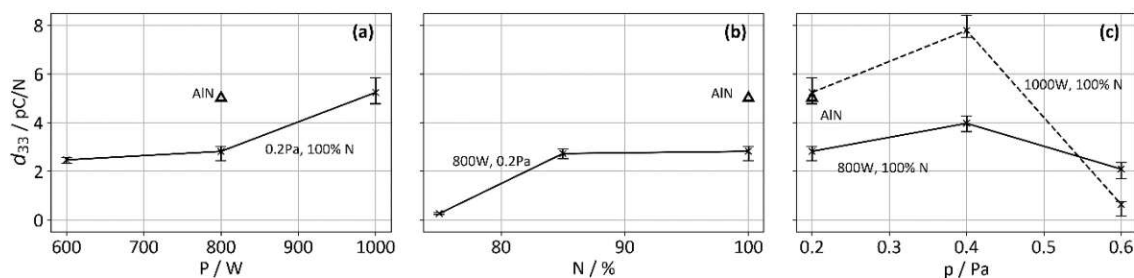


Figure 40: FWHM of rocking curves of $Y_{0.09}Al_{0.91}N$ layers when varying (a) the plasma power, (b) the nitrogen admixture and (c) the pressure values, including a pure AlN sample as reference.

Compared to the experimental results from Mayrhofer *et al.* [27] we reached higher piezoelectric coefficients. Furthermore, our measured d_{33} of 7.79 pC N^{-1} is in excellent agreement with the predicted values from their DFT simulations. It is reasonable to assume that this improvement results from the lower amount of oxygen, especially on the interface region in the thin film

compared to the measurements from Mayrhofer *et al.* [27]. Furthermore, the quality, especially the oxygen content of the target material is of utmost importance, to receive thin films of highest quality.

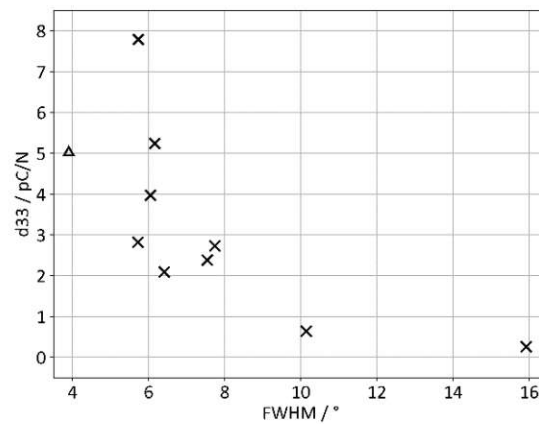


Figure 41: FWHM of rocking curves of Y_{0.09}Al_{0.91}N layers when varying (a) the plasma power, (b) the nitrogen admixture and (c) the pressure values, including a pure AlN sample as reference.

Figure 41 shows the piezoelectric coefficient d_{33} as a function of the FWHM of the rocking curve. It indicates a correlation for high to medium FWHM values ($FWHM \geq 7$), which results in low to medium values in the piezoelectric coefficient up to 2 pC N^{-1} . Below a value of 7° , however, this direct correlation vanishes and the thin films show a d_{33} between 2 and 7.79 pC N^{-1} . We can conclude that a narrow rocking curve width is necessary but not sufficient to reach high piezoelectric coefficients. Olivares *et al.* showed that this behavior can result from the presence of crystals with a (101) orientation in the XRD scans. These crystals can also be clearly observed by the triangular shape, in the surface microstructure of their thin films [229]. In contrary, our samples do not show any (101) peaks, but a minor presence of (100) and (110) oriented grains. However, crystals exhibiting a triangular shape were not observed in any SEM images and might play a negligible role in AlYN thin films when low values of the d_{33} are measured.

Figure 42 shows thin film stress as a function of pressure in (a) and of nitrogen content in the sputter gas in (b). In both plots samples sputtered at 800 W and 1000 W are shown. Independent of the selected parameters the film stress is highly compressive. Additionally, it is also highly dependent on the sputter pressure ranging from -2.15 GPa at $2 \mu\text{bar}$ to -1.38 GPa at $6 \mu\text{bar}$. While the sputter power does not have as much influence compared to the chamber pressure, the 800 W samples show up to 27 % higher compressive stresses when varying the gas composition than the 1000 W sample especially for lower nitrogen contents. As a result, it can be concluded that lower nitrogen concentrations and higher pressures lead to lower compressive stress values.

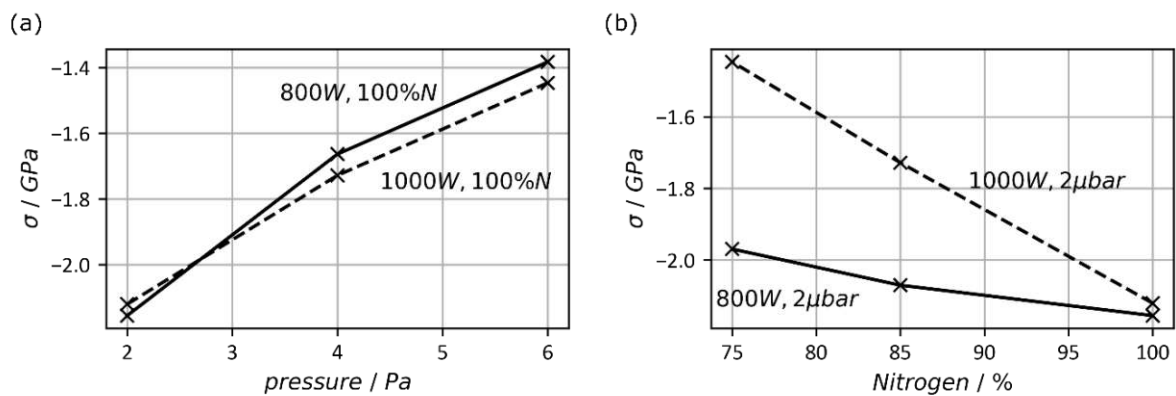


Figure 42: (a) Film stress as a function of pressure and (b) as a function of nitrogen admixture for samples sputtered at 800 W and 1000 W.

4.4 Stress Tailored Aluminum Nitride

In this chapter a modified sputter process is introduced, which allows to tailor the intrinsic thin film stress of AlN and its alloyed variants and simultaneously guarantee high piezoelectric coefficients. The work of Tabaru *et al.* served as a reference [251], who sputter deposited AlScN thin films in a two step process with low and high sputter pressure conditions. They showed thin films sputtered under low pressure conditions have high piezoelectric coefficients but suffer from high compressive residual stress, which is also common in pure AlN thin films as stated before. In contrast thin films sputtered under high pressure conditions showed low stress values but at the same time the piezoelectric performance diminished. To combine the advantages of both conditions, they introduced their two step process which had equally high piezoelectric values as the thin films sputter under low pressure conditions and at the same time showed stress values comparable with the thin films sputtered with high-pressure conditions. They attributed this effect to atomic peening during the first phase and a selective layer-by-layer adsorption of incoming atoms with lower energy levels during the second phase of the process.

In this work a sputter process for pure AlN thin films with a continuously shifted pressure value during deposition is realized and the resulting material is compared with other thin films deposited with low pressure, high pressure and the two step process from Tabaru *et al.* [251]. Beside the measurements of thin film stress and the piezoelectric coefficient d_{33} , the microstructural composition of all four differently sputtered thin films is studied with SEM, XRD and AFM.

4.4.1. Deposition of Aluminum Nitride Thin films

AlN thin films were synthesized with a magnetron sputter system from “Von Ardenne LS730S” at a temperature below 100 °C on p-type (100) silicon wafers with different parameter sets listed in Table 9.

	Low Pressure	High Pressure	2 Steps	Pressure Sweep
Sample Nr.	S41	S42	S43	S44
Sputter Pressure / Pa	0.2	0.6	0.2 + 0.6	0.2 + 0.2 to 0.6
N₂ Flow / sccm	50	50	50	50
Target Substrate Distance / mm	65	65	65	65
Power / W	800	800	800	800
Sputter Time / s	1465	1928	1756 (406 + 1350)	1544 (406 + 1138)
Thickness / nm	523	511	524 (148 + 376)	500 (150 + 350)

Table 9: Sputter parameters for AlN thin films deposited with standard conditions and to achieve stress reduced thin films.

Deposition parameters differ only in the back pressure of the pure nitrogen atmosphere in the sputter chamber while keeping all other parameters fixed such as plasma power, target-substrate distance, or gas flow rate. Within the first and second set constant pressure values of 0.2 Pa and 0.6 Pa were selected for a deposition time of 1465 s and 1928 s. The third and fourth set target to fabricate stress-reduced AlN thin films, whereas the third contained an abrupt change from 0.2 Pa (for 406 s) directly to 0.6 Pa (for 1350 s). In contrast, the fourth set consisted of two phases. First, the pressure was kept constant at 0.2 Pa for 406 s to create a seed layer. Then the pressure was

gradually increased from 0.2 Pa to 0.6 Pa over a time period of 1138 s without interrupting the sputter process. The timings and pressure values for all four sets are depicted in Figure 43.

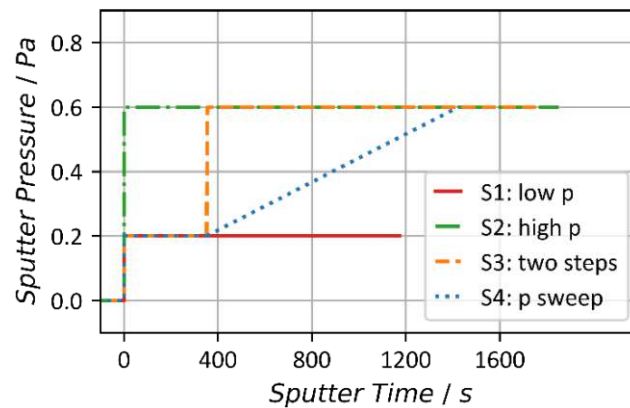


Figure 43: Pressure variation as a function of time for the AlN thin films sputtered under standard conditions and with modified pressure conditions for stress-reduced thin film synthetization.

Additionally, a tailored substrate holder was used to enhance the thermal connection during sputtering between the substrate and the holder as reported in [252], [253]. This leads to more reproducible deposition conditions and allows to fine tune stress more reliably. Prior to the thin film deposition, the 6'' aluminum target was sputter cleaned at a chamber pressure of 0.6 Pa in a pure argon atmosphere and at a power of 800 W with a closed shutter for one minute. For reasons of comparison, all AlN thin films were fabricated with a nominal thickness of 512 ± 12 nm.

4.4.2. Microstructural and electro-mechanical characterization of AlN thin films

To determine the crystallographic quality, Figure 44 shows the Bragg-Brentano scans of the X-ray diffraction measurements for $2\theta = 30^\circ - 45^\circ$ for all four parameter sets of the sputtered AlN thin films. High quality piezoelectric AlN thin films show a (002) peak indicating a wurtzite crystalline microstructure without the presence of any other peaks e.g., (100) or (101) [254], [255].

The thin film sputtered at a chamber pressure of 2 μ bar shows a pronounced (002) peak, indicating c-axis oriented crystallites extending perpendicular to the device surface. This is also confirmed by the piezometer measurements showing a d_{33} of 4.14 pC N⁻¹. The crystal growth along the (002) direction in AlN thin films is often accompanied with high intrinsic stress as already described above, in this case shown by a high compressive stress of $\sigma = -722$ MPa, which makes the integration in MEMS devices challenging.

In contrast, the sample sputtered with 6 μ bar shows a substantially reduced compressive stress of $\sigma = -102$ MPa, but also a reduced d_{33} of 0.61 pC N⁻¹. The Bragg Brentano scan shows a (002) peak with reduced intensity and an additional peak at 38.1° indicating the presence of crystallites with a (110) direction, so that poor piezoelectric values result.

When comparing the two processes selected for stress reduction, it is obvious that both show a distinct (002) peak but the two step process additionally shows a peak at 38.1° again indicating a mixed crystallographic phase configuration, similar to the sample sputtered with 6 μ bar. This shows, that while the process with the gentle pressure sweep takes up the crystal structure from

the underlying seed layer, in the two step process the crystal growth changes if the sputter pressure is modified abruptly. This impact can also be seen in other film parameters, such as biaxial stress and piezoelectric coefficients. While both processes reduce the compressive stress of the resulting thin film, the two-step process results in a d_{33} of only -1.47 pC N^{-1} , while an enhanced d_{33} of 5.76 pC N^{-1} is achieved when applying the pressure sweep.

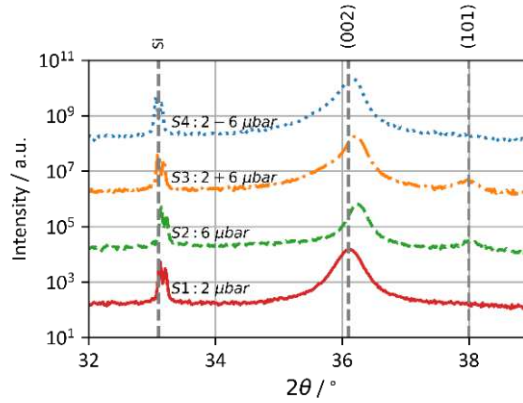


Figure 44: Bragg-Brentano scans of sputtered AlN thin films with varying sputter pressure.

Figure 46 shows SEM images in cross-sectional view as well as in top view of all four differently sputtered AlN thin films. While all four layers show a clear crystal structure in the upper part of the thin film only the low-pressure and the samples synthesized with a pressure sweep show crystal growth starting from the bottom. The high-pressure sample appears to have an amorphous starting layer leading to an irregular growth of grains of about $100 - 150 \text{ nm}$, before developing to the well-known regular, columnar growth in the top part. In contrast, the two-step sample shows a fine-grained bottom layer of 148 nm as intended and a larger grained top layer of 352 nm with a clearly visible cut between those two layers. The thin film with the pressure sweep shows a very similar structure to the low-pressure sample with grains starting from the bottom and extending over the film cross-section to the top surface.

Wafer	Low Pressure	High Pressure	2 Steps	Pressure Sweep
σ / MPa	-722	-102	-389	-170
$d_{33} / \text{pC N}^{-1}$	4.14 ± 0.3	0.61 ± 0.1	1.47 ± 0.3	5.76 ± 0.5
$d_{\text{AlN}} / \text{nm}$	523	511	514	500
XRD Intensity	18973	6224	17677	23170
XRD $2\theta / ^\circ$	36.079	36.225	36.214	36.161
$R_{\text{RMS}} / \text{nm}$	0.53	5.12	1.98	0.81
$d_{\text{grain}} / \text{nm}$	19.2 ± 3.1	36.6 ± 12.5	32.9 ± 4.2	19.2 ± 3.7

Table 10: Various measured parameters of all four AlN thin films.

From the surface images one can see that the high pressure and the two-step sample appear similar and have larger grains with more extended dark areas between the grains, shown in Figure 46 (b) and (c). This originates from the higher surface roughness, which AlN thin films typically exhibit when sputtered at higher pressures [256]. The higher surface roughness is also confirmed by the AFM images in Figure 45 (b) and (d) with $R_{\text{RMS}} = 5.12 \text{ nm}$ for the high-pressure sample and $R_{\text{RMS}} = 1.98 \text{ nm}$ for the two-step sample. The samples sputtered with low pressure shown in

Figure 46 (a) and the pressure-sweep sample shown in Figure 46 (d) also show a similar microstructure with finer grains and less pronounced grain boundaries, which again might result from a lower surface roughness of $R_{RMS} = 0.53 \text{ nm}$ and $R_{RMS} = 0.81 \text{ nm}$ determined by the AFM measurements in Figure 45 (a) and (c), respectively. The measured grain diameters show a similar trend towards larger lateral mean grain diameters with higher scattering probability for the high-pressure sample and the two-step sample than for the low-pressure and the pressure-sweep sample, which are in the expected range according to various published results [254], [257], [258]. More results of the measurements can be found in Table 10. They confirm the trend of various publications which showed that higher sputter pressure leads to both larger grains and higher surface roughness [254], [258], [259]. Furthermore, Kar *et al.* who studied AlN thin films sputtered under varied sputter pressure showed similar surface structures to our low- and high-pressure samples in their SEM analysis [258].

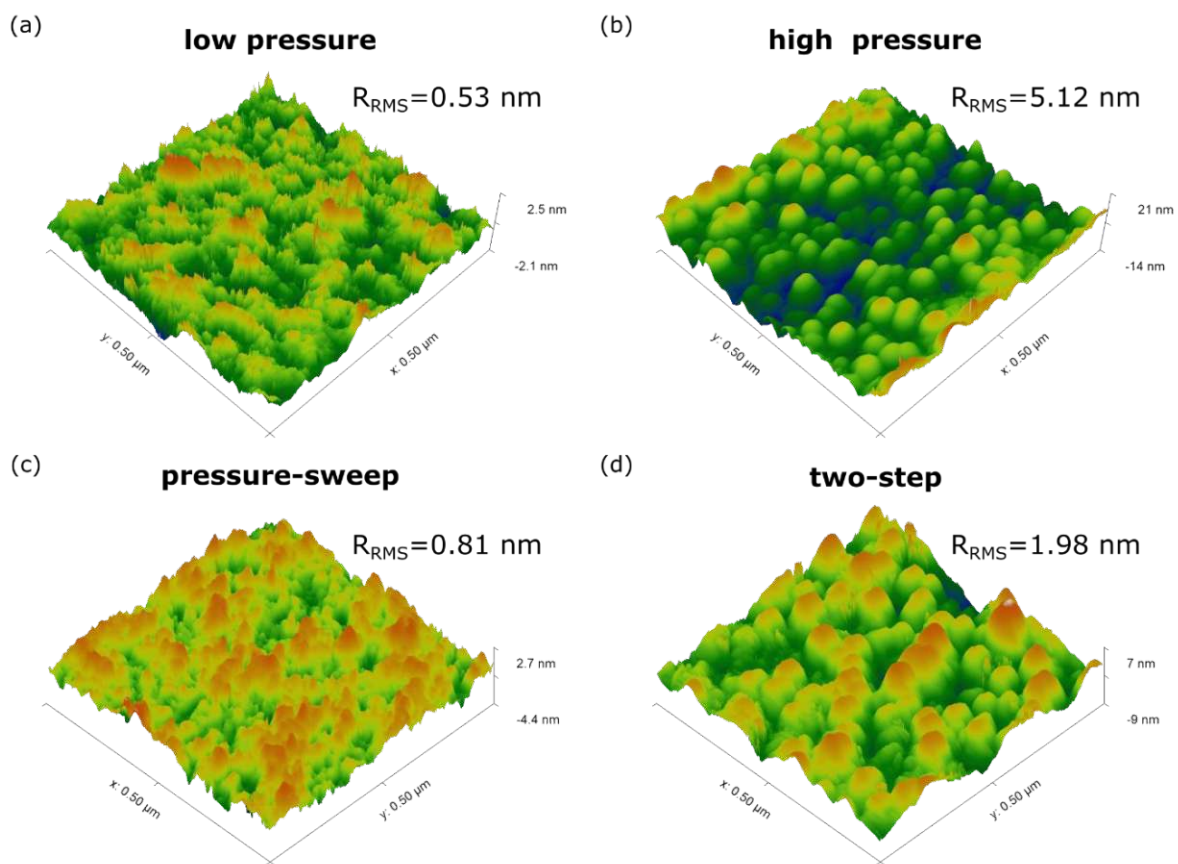


Figure 45: AFM images of thin films deposited with all four different parameter sets.

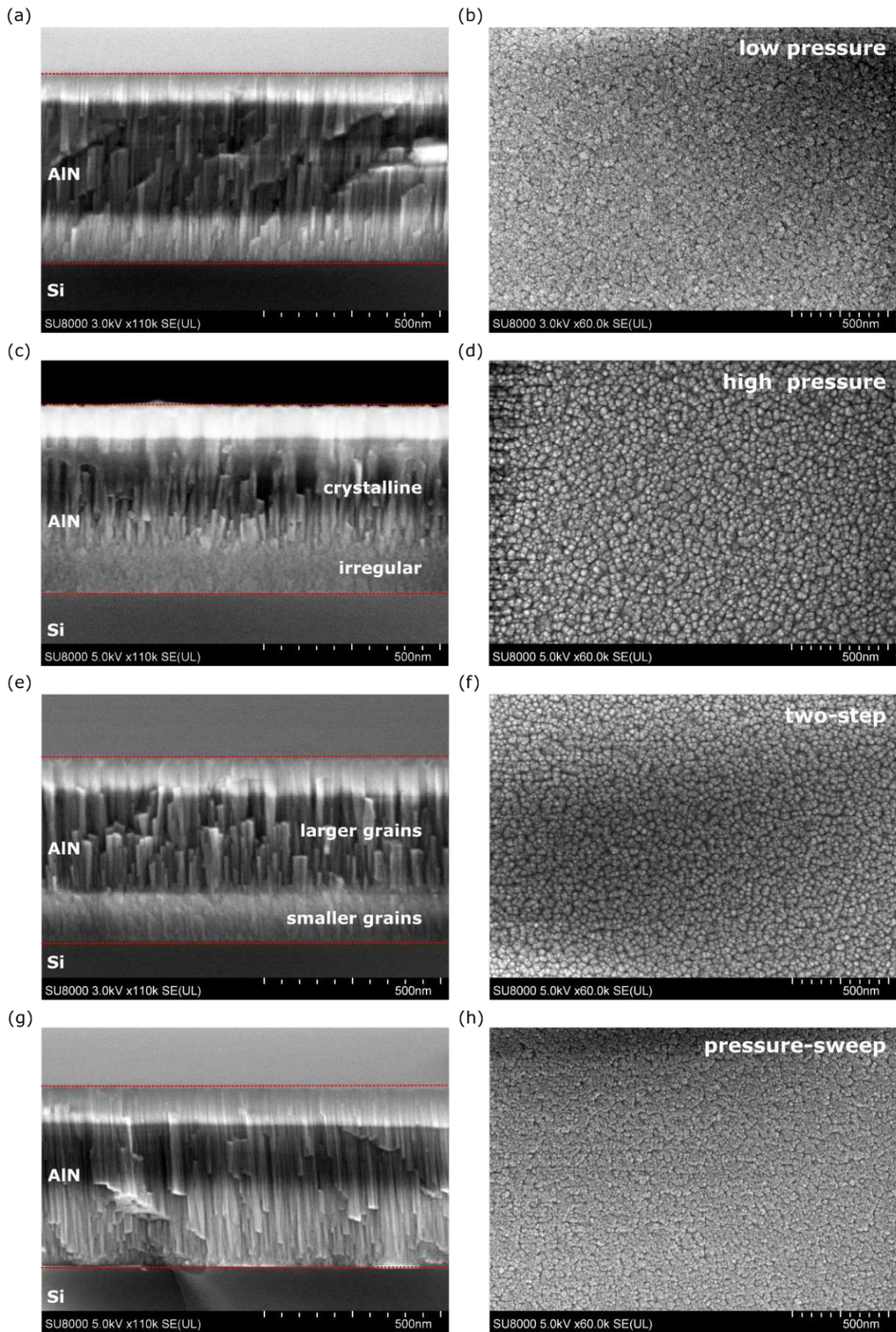


Figure 46: SEM images of the cross section and the surface in top view for all four samples, sputtered with different parameter sets.

4.4.3. Stress Tailored Scandium Aluminum Nitride

The method developed in the previous chapter was also used to synthesize stress-reduced $Al_{71}Sc_{29}N$ thin films and it was compared to a second thin film sputtered under standard conditions. Table 11 gives an overview of parameters and results of both thin films.

Sample Nr	σ MPa	d_{33} $pC N^{-1}$	$p_{Sputter}$ Pa	$t_{Sputter}$ s	d_{ScAlN} nm
S_1	-1030	8.38	2	1820	1050
S_2	-516	9.20	2 + (2 - 14)	455 + 1830	948

Table 11: Various parameters of samples sputtered with constant and swept sputter pressure.

Again, Bragg-Brentano scans and rocking curves around the (002) peak are performed to study the structural composition. The sample S_2 sputtered with a pressure sweep shows a double peak at 36° , similar to the thin films sputtered with varying pressure in section 4.2.2. In contrast to the previous samples the microstructural quality, the intrinsic stress and the piezoelectric coefficient are improved compared to the sample S_1 . Therefore, the additional peak at 36.5° is not an indication for a deteriorated thin film quality. The SEM images in Figure 15 (a-b) again show a similar surface structure as observed for low- and pressure swept samples. While the sample sputtered with a constant pressure of $0.2 Pa$ shows the presence of grains grown in a non-(002) direction, the swept sample shows a finer surface structure with slightly bigger grains than the high-pressure sample in section 4.2.2. This could be led back to the thin film thickness which is twice the value of S_{15} .

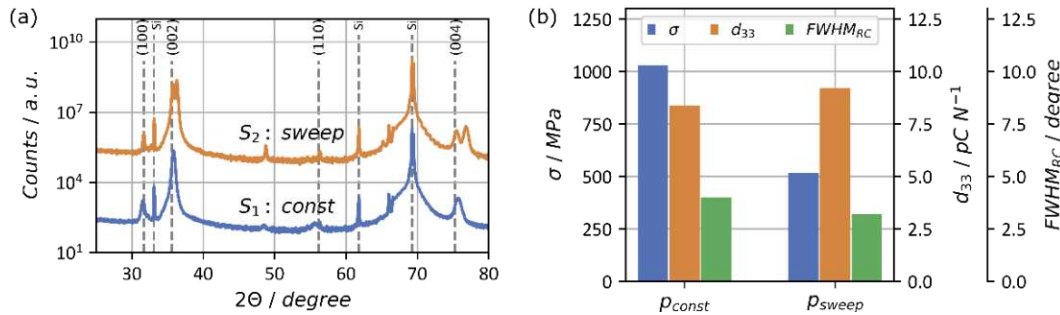


Figure 47: Comparison of thin film stress σ and piezoelectric longitudinal coefficient d_{33} of the samples S_1 and S_2 sputter under constant and swept pressure conditions, respectively.

The piezoelectric coefficient increased slightly, compared to the samples sputtered with standard conditions and the intrinsic stress increased by $500 MPa$ which is approximately the same value as for the stress tailored pure AlN thin film in the previous section.

These results indicate that the stress-tailoring method from the previous section not only works on pure AlN thin films but could be a versatile sputter procedure used for varying dopants of AlN, including scandium and even yttrium.

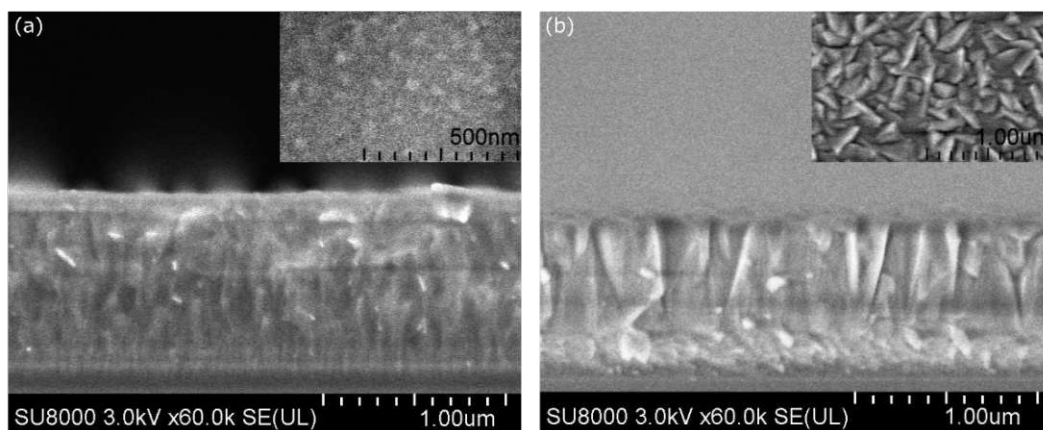


Figure 48: SEM micrographs of the cross-section and the surface (inset) of an AlScN thin film with (a) the standard sputter process and (b) with the modified sputter process.

4.5 Conclusions

This chapter started with a general overview about AlN followed by the characterization of scandium doped AlN thin films with a composition of 33% of scandium and 67% of aluminum in the sputter target. The AlScN thin films were sputter deposited with varying parameters such as plasma power, gas composition and chamber pressure to obtain the optimized sputter conditions. It was shown that the piezoelectric coefficient d_{33} was increased by 143% to 12.22 pC N^{-1} . Simultaneously, the intrinsic compressive stress increases by 142% to -1.75 GPa , making the use of AlScN in MEMS sensor elements almost impossible. While increasing the sputter pressure to 1.4 Pa led to a nearly unstressed thin film. But this measure also decreased the piezoelectric coefficient down to 1.1 pC N^{-1} .

After scandium as a dopant, the possibility of using yttrium was explored by using a target with 15% yttrium and 85% aluminum. By applying a similar approach, AlYN thin films were deposited under various sputter conditions by varying again plasma power, pressure and gas composition. Although the thin films showed a high contamination of oxygen – which can influence the growth conditions of aluminum nitride crystals – the piezoelectric coefficient d_{33} could be increased by 55% to 7.79 pC N^{-1} , thus reaching the value, predicted by DFT calculations. Stress measurements of the samples showed even higher compressive stresses than for scandium as alloying element with values reaching up to -2.15 GPa .

The end of this chapter shows a newly designed stress tailoring sputter process for AlN thin films by continuously changing the sputter pressure value during deposition from lower to higher values. This combines the advantages of good piezoelectric coefficients and low compressive thin film stress. The conventionally sputtered thin films with low sputter pressure have a good d_{33} of 4.14 pC N^{-1} but suffer from high compressive thin film stress of -722 MPa . In contrast thin films sputter with high pressure show low thin film stress of -102 MPa but have a poor d_{33} of 0.61 pC N^{-1} . The thin films sputter with the modified process showed a reduced stress value of -170 MPa and a d_{33} of 5.76 pC N^{-1} , proofing that this modified process is a promising approach to avoid high film stress values.

5. Energy Harvester

Parts of this chapter are published in [260]

In this chapter the design, fabrication and characterization of an energy harvester is presented. As already mentioned in chapter 2 the aim was to provide enough power to operate a sensor node, comprising one or more sensors, a readout circuit and a wireless transmission unit to send the collected data to a base station located in the nacelle. As the design of such an energy harvesting device greatly depends on its targeted output power, a conventional battery powered sensor node *G-Link 200* from *LORD*, comprising an acceleration sensor was used to estimate the power consumption of such a system. Depending on the sampling frequency, the power consumption of the sensor node ranges up to about 50 mW at 4 kHz for a transmission gain of 0 dbm , which is shown in Figure 49 (a). Additionally, the power consumption also depends on the necessary transmission gain which depends on the distance between the sensor node and its base station providing a maximum distance with clear sight of 1 km at 20 dbm , as illustrated in Figure 49 (b) for a sampling frequency of 64 Hz . As a result of these measurements, a targeted power generation of the energy harvester of $5 - 10\text{ mW}$ was specified covering a sampling rate of 64 Hz and a minimum sensor to nacelle distance of 10 m .

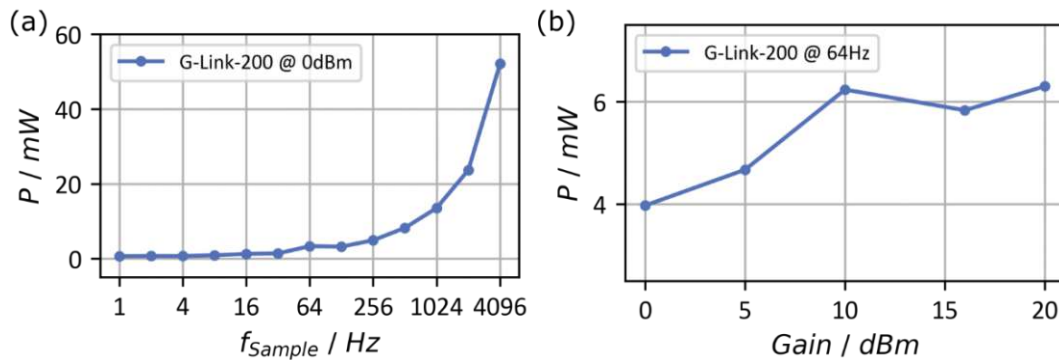


Figure 49: (a) Power consumption of a LORD G-Link 200 sensor node as a function of its sampling frequency. (b) Power consumption of the same sensor node as a function of its transmission gain. The inserted straight lines serve as guide to the eyes.

5.1 Basic Considerations

In a first step the possibility to directly harvest energy from the vibrational frequency spectrum occurring at a wind turbine rotor blade is evaluated. A wireless sensor node of the type *LORD G-Link 200* including an acceleration sensor was installed and operated for a two-week period in a test wind turbine of the type *Vestas V90*, shown in Figure 50 (a). This wind turbine has a fixed nominal frequency of 0.3 Hz or 20 rpm under normal operating conditions. A sample plot of an acceleration spectrum is given in Figure 50 (b) and a spectrogram from a timeframe of 5 minutes in Figure 50 (c). As can be seen, the most dominant resonance frequency is at 0.3 Hz with an acceleration of 1 g_0 , which represents the fundamental rotational frequency of the wind turbine. The next resonance is at 26.4 Hz and has an acceleration value of about $2 \cdot 10^{-2}\text{ g}_0$.

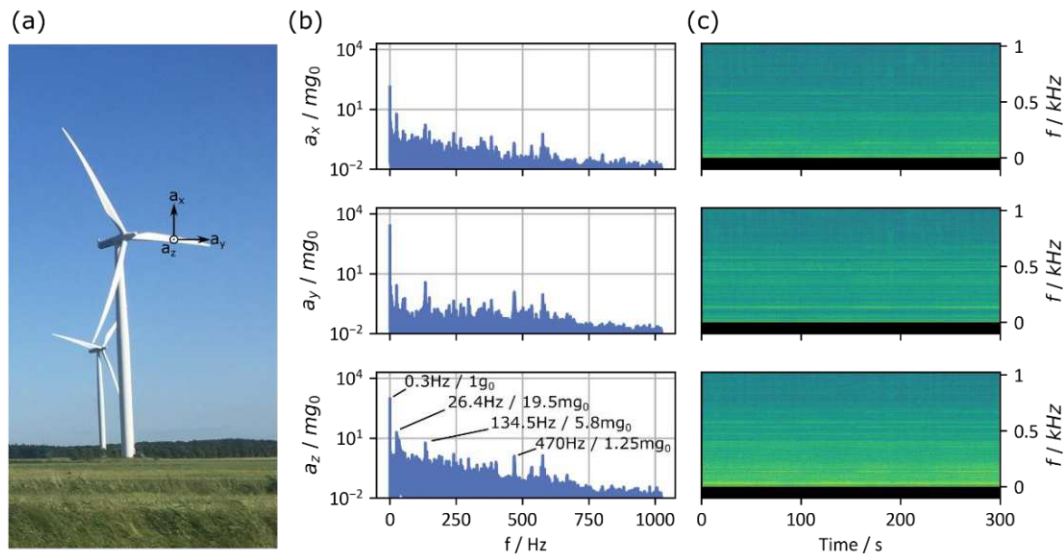


Figure 50: (a) Picture of a Vestas V90 where the sample frequency spectrum was taken. (b) Frequency spectra of a rotor blade for all three directions of the blade in a cartesian coordination system. (c) Spectrograms of a rotor blade for a time duration of 300 s.

Three technical limitations occur when considering designing a vibrational energy harvester tailored to the characteristics of this frequency spectrum:

- The **resonance frequencies** are very low. Considering a MEMS cantilever type vibrational energy harvester, manufactured with CMOS technology, it is very difficult to reach resonance frequencies below a few Hertz.
- The **accelerations** are very low, which inherently leads to very poor energy generation.
- If the energy harvester is tuned to a certain resonance frequency, it will only perform well in a very narrow **bandwidth** around this center frequency. Considering that every rotor blade has a unique frequency spectrum, it is obvious that one would have to adapt the EH design for each rotor blade. Additionally, both aging and wear effects might change the characteristic frequencies of the rotor blade, making the EH less effective over time.

These limitations led to the conclusion that a vibrational energy harvester is not an adequate solution.

Due to the above-mentioned challenges, a more versatile design of an energy harvester is needed. It should be tailored to the requirements present in all wind turbines, no matter of its type, manufacturer, or place of operation. In the following sections, the design and implementation of a hybrid energy harvesting system which is independent of those limitations are presented and evaluated with a prototype operated under real world conditions in a wind turbine.

5.2 Design Aspects

One commonality inside a rotor blade of all wind turbines is, that the gravitational force acting on an object changes its direction periodically, depicted in Figure 51 (a-c). This boundary condition was taken as basis for the design and the development of an energy harvester. Furthermore, two different transduction mechanisms – piezoelectric and electromagnetic – were used to transform mechanical energy into electric energy, hence this sub-system was labeled as hybrid energy harvester (HEH).

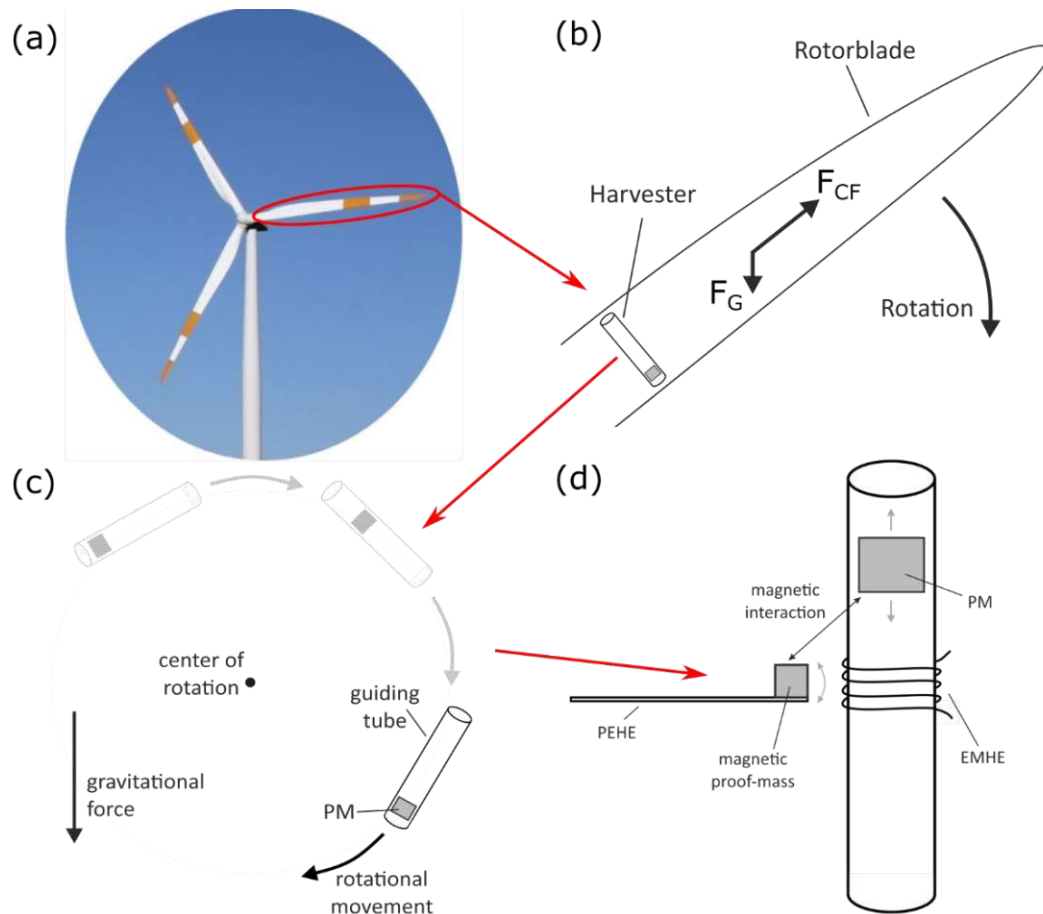


Figure 51: (a) Picture of a wind turbine and its rotor blades. (b) Location and direction of the HEH inside the rotor blade including the force vectors of gravitation and centrifugal force. (c) Movement of the HEH from an outside perspective. (d) Detailed schematic of the HEH.

The hybrid energy harvesting device consists of two key components - an electromagnetic energy harvesting element (EMHE) and a piezoelectric energy harvesting element (PEHE), as schematically displayed in Figure 51 (d). The core element of the EMHE is a permanent magnet (PM) which is accelerated by a slowly rotating force vector, whereas the trajectory of the PM is restricted to a linear movement by a guiding tube which is placed within close proximity to the PEHE. This guiding tube is located tangential to the rotation circumference (see Figure 51 (c)). One or several coils are wound around the guiding tube, which convert the changing magnetic field caused by the moving PM into electric energy via Faradays law of induction. The PEHE are cantilever like vibrational energy harvesters, as shown in Figure 51 (d). They are fabricated by standard silicon micromachining and based on an electrode – piezo – electrode stack for energy conversion. A magnetic proof mass is mounted at the tip of the cantilever, also called tip magnet (TM) which is needed for the magnetic plugging mechanism. When the PM moves through the tube and passes a PEHE, it interacts with

the proof mass of the PEHE and pulls it down until the PM gets too far away, where it releases the PEHE and the cantilever starts vibrating with its intrinsic fundamental resonance frequency.

Both parts can be scaled up to increase the generated energy by placing several EMHEs along the guiding tube and by placing several PEHEs along the tube's length or around its circumference.

FEM Simulation for the EMHE and the PEHE

As an initial step and to estimate the output power of the hybrid energy harvester, time dependent FEM simulations with COMSOL were performed. To keep the necessary computation time of such FEM simulations on an acceptable level, both parts of the energy harvester were simulated separately. First the electromagnetic part with a PM (I) accelerated by $1 g_0$ inside a guiding tube (III), surrounded by one electromagnetic coil (II) was simulated by an axial symmetric analysis, shown in Figure 52 (a). The dimensions and specifications of the individual parts are given in Table 12. The mesh is shown in Figure 52 (b) and consist of two parts, a quadratic mesh with a maximum element size of 2 mm for the tube and a automatically generated triangular mesh with the setting *finer* for the outer part, including the permanent magnet, the coil and surrounding empty space. To simulate the falling PM a moving mesh component has been added, with a prescribed z-displacement given in equation (5.1) for the PM.

$$d_z = \frac{1}{2} \sqrt{g_0 \cdot t^2} \quad (5.1)$$

The surrounding components were automatically adjusted by the software to fit the moving PM.

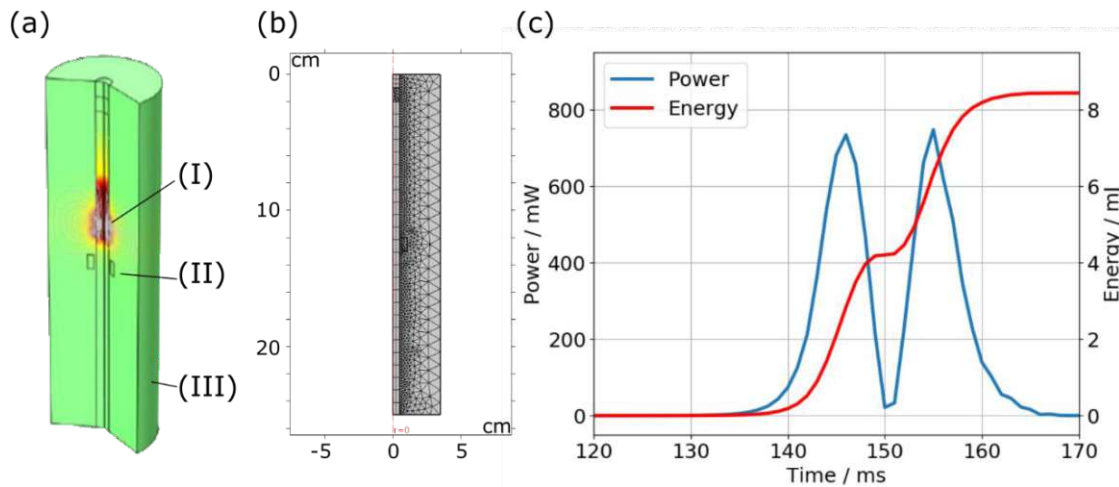


Figure 52: (a) FEM model and (b) mesh for the EMHE with a guiding tube, a permanent magnet and a single coil. (c) Generated output power and energy after a fall from the permanent magnet.

The excitation of the PEHE was realized by applying a force profile of the vertical force F_y onto the tip of the cantilever. This force profile has been generated by a separate 2D-simulation, shown in Figure 53 (a) with one magnet (I), representing the permanent magnet in the tube passing by another magnet (II), representing the tip-magnet of the cantilever. The mesh of this simulation consisted of an automatically generated triangular mesh in the settings *finer* and a moving mesh component applied to the PM. The prescribed mesh displacement in z-direction for the PM is the same as for the previous simulation (compare equation (5.1)) To simplify the simulations for the PEHE only the vertical force component acting on the second magnet was taken as input excitation for the PEHE model, shown in Figure 53 (b).

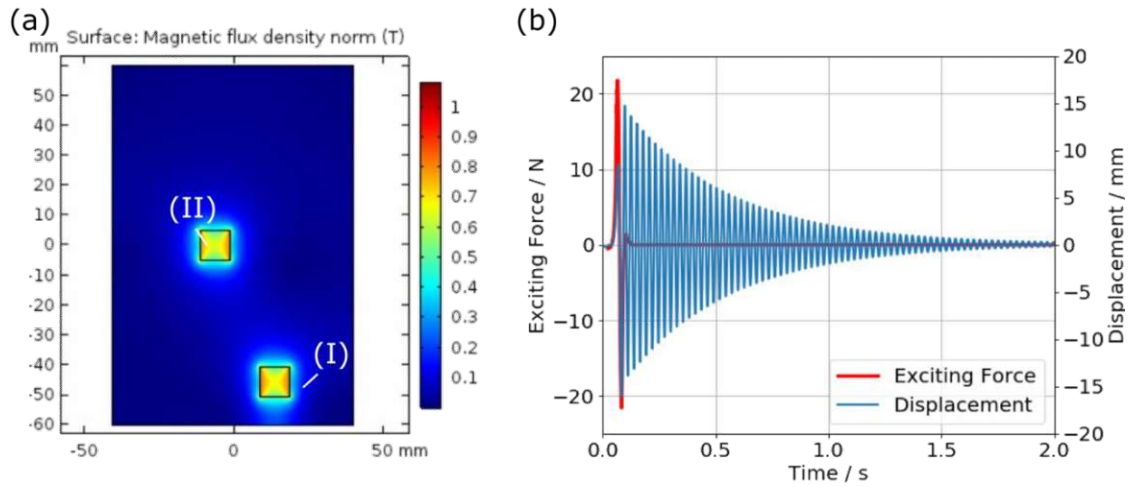


Figure 53: (a) Model of the COMSOL simulation used for simulating the vertical force component F_y on the tip magnet of the cantilever. (b) Vertical force component used to excite the cantilever (red) and cantilever tip displacement as a function of time (blue).

Figure 54 (a) shows the FEM model of the cantilever (I) with its fixed base (II) and its proof mass (III). The used mesh was automatically generated by COMSOL with the settings “finer” Figure 54 (b) shows the simulated generated power and the accumulated energy as a function of time. Exact dimensions and used materials can again be found in Table 12.

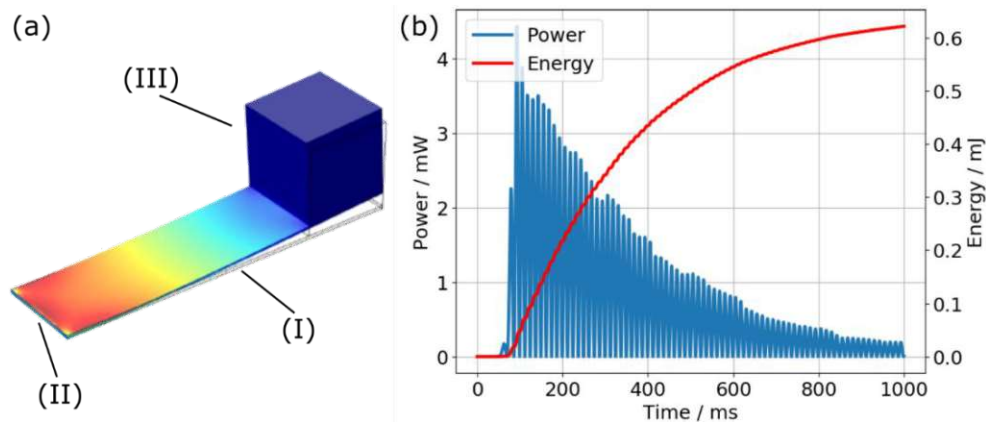


Figure 54: (a) FEM model of a cantilever (I) with a fixed base (II) and a proof mass (III) on the tip of the cantilever. (b) Generated power and energy over time after an initial excitation through magnetic plucking.

In both cases, the ideal load resistor has been determined with parametric simulations, in which the resistor values are changed from $1 \cdot 10^{-3}$ to $1 \cdot 10^2 \Omega$ for the EMHE and from $1 \cdot 10^2$ to $1 \cdot 10^6 \Omega$ for the PEHE. The ideal load resistor values for each EH were used to simulate the curves above. The reduced speed of the falling PM due to the slowly turning guiding tube as well as any friction losses have been neglected.

EMHE			PEHE		
PM (L x W x H)	1x1x1 cm ³	NdFeB	Substrate (L x W x H)	40x10x0.35 mm ³	Silicon
PM magnetization	1.3 T	-	Piezo layer thickness	2 μm	AlN
Guiding tube length	25 cm	-	Proof mass L x W x H)	0.5x1x0.5 cm ³	NdFeB
Coil windings	100	Copper	Resonance frequency	32 Hz	-
Load resistance (for max. power output)	100 mΩ	-	Load resistance (for max. power output)	90 kΩ	-

Table 12: Key parameters of the EMHE and the PEHE used in FEM simulations.

Based on these FEM simulations representing a best case scenario the EMHE generates 8,44 mJ (see Figure 52 (c)) and the PEHE (see Figure 54 (b)) 0,62 mJ per fall of the magnet and twice this value per full rotation. When assuming a rotational frequency of 0.3 Hz of the wind turbine which corresponds to 20 rpm, it leads to an output power of 5,63 mW and 0,41 mW for the EMHE and the PEHE, respectively. These results indicate that the requested specifications for the power generation made at the beginning of this section can be reached and were used as a rough guideline in the fabrication of the prototype discussed in the next sections.

5.3 Piezoelectric Harvester

While the FEM simulations show that the PEHEs do not produce more energy than the EMHE it still is an interesting approach as the low-power strain sensor is fabricated with the same technology. Even more, it opens opportunities to further improve the PEHEs by advanced designs or by the integration of piezoelectric materials with enhanced piezoelectric constants. First, a model is presented which helps to analyze the cantilevered PEHEs with respect to their fundamental resonance frequency used for energy harvesting. Next, device fabrication is discussed, followed by the characterization of the PEHEs by harmonic excitation and by magnetic plugging.

5.3.1. Cantilever Model

A central property of a resonator is its resonance spectrum. When it is excited at its resonances the resonators displacement is significantly increased compared to off resonance operation. The frequencies and the corresponding mode shapes at which those resonances occur can be described by the Euler-Bernoulli beam theory for one dimensional mode shapes and by Kirchhoff-Love plate theory for two dimensional modes. A detailed derivation for various kinds of resonators (i.e., double clamped beam, cantilever, plate, etc.) can be found in [261]. However, as this section is about the special case of a cantilever including a tip-mass operated at its first flexural mode, a short summary of the results taken from [262] is given in the following.

An overview of the used model is shown in Figure 55 (a) and consists of a cantilever with the length L , mass m and a moment of inertia I fixed to a base.

$$I = \frac{Ah^2}{12} \quad (5.2)$$

On the tip of the cantilever, a tip-mass is mounted with the mass M_t and its rotary moment of inertia I_t , which can be set to 0 for certain simplifications as explained in the latter. The r^{th} mode shape can then be expressed by the following equation:

$$\phi_r(x) = C_r \left[\cos \frac{\lambda_r}{L} x - \cosh \frac{\lambda_r}{L} x + \zeta_r \left(\sin \frac{\lambda_r}{L} x - \sinh \frac{\lambda_r}{L} x \right) \right] \quad (5.3)$$

With C_r being the modal amplitude and ζ_r being defined as:

$$\zeta_r = \frac{\sin \lambda_r - \sinh \lambda_r + \lambda_r \frac{M_t}{mL} (\cos \lambda_r - \cosh \lambda_r)}{\cos \lambda_r - \cosh \lambda_r + \lambda_r \frac{M_t}{mL} (\sin \lambda_r - \sinh \lambda_r)} \quad (5.4)$$

The eigenvalues λ_r can be obtained by solving the following equation for λ_r :

$$1 + \cos \lambda_r \cosh \lambda_r + \frac{M_t}{mL} (\cos \lambda_r \sinh \lambda_r - \sin \lambda_r \cosh \lambda_r) - \frac{\lambda_r^3 I_t}{mL^3} (\cos \lambda_r \sin \lambda_r + \sinh \lambda_r \cos \lambda_r) + \frac{\lambda_r^4 M_t I_t}{m^2 L^3} (1 - \cos \lambda_r \cosh \lambda_r) = 0 \quad (5.5)$$

Depending on the structure of the cantilever, certain simplifications can be made e.g., in the case of a cantilever without tip-mass ($M_t = 0$ and $I_t = 0$) equation (5.5) simplifies to:

$$1 + \cos \lambda \cosh \lambda = 0 \quad (5.6)$$

Or in presence of a tip mass, but excluding two dimensional flexural modes ($I_t = 0$) we get:

$$1 + \cos \lambda_r \cosh \lambda_r + \frac{M_t}{mL} (\cos \lambda_r \sinh \lambda_r - \sin \lambda_r \cosh \lambda_r) = 0 \quad (5.7)$$

In both cases the eigenvalues λ_r can be obtained by numerical approximation applying e.g. Newton's method. For a cantilever made from silicon (100) with a length of 30 mm, a thickness of 0.25 mm and a tip mass of 0.446 g, the first three eigenvalues λ_r are: 1.0991, 3.9877 and 7.1059. The resulting mode shape functions are shown in Figure 55 (b).

The frequencies at which these eigenfunctions occur are called resonance frequencies and can be calculated with:

$$\omega_r = \lambda_r^2 \sqrt{\frac{YI}{mL^4}} \quad (5.8)$$

With Y being the Young's modulus and I the moment of inertia. All used parameters are listed with their respective units in Table 13.

Term	Unit	Description
C_r	1	Modal Amplitude
I_t	m^4	Rotary moment of inertia
M_T	kg	Tip-mass
λ_r	1	Eigenvalue
ω_r	Hz	Eigenfrequency
A	m^2	Area of cross section of cantilever
h	m	Height of cantilever
Y	Pa	Young's modulus
I	m^4	Moment of inertia
L	m	Length of cantilever
m	kg	Mass
r	-	Mode number

Table 13: Cantilever model parameters

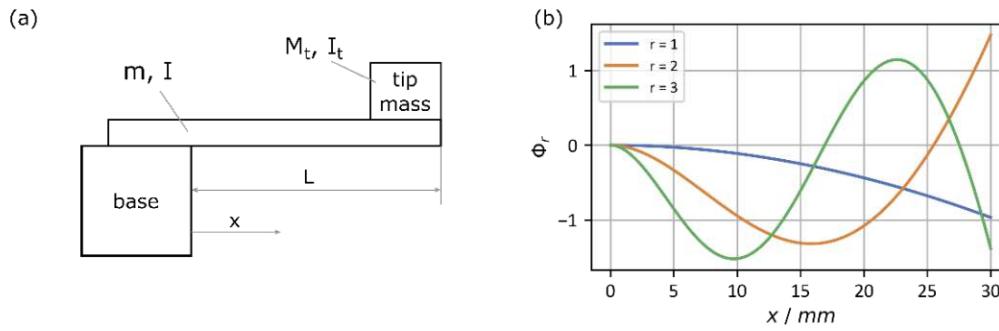


Figure 55: (a) Schematic of a cantilever with tip mass used in the model. (b) Mode shapes as a function of x for the first three fundamental bending modes.

5.3.2. Fabrication

The PEHEs are based on a micromachined single sided clamped beam structure, as illustrated in Figure 56 (a-j). A standard phosphorus doped, (100) silicon wafer is used as substrate. The bottom electrode consists of 200 nm gold and two 50 nm chromium layers on top and bottom to increase adhesion. The gold is thermally evaporated, whereas the Cr is deposited via e-beam evaporation and all three materials were patterned by the same lift-off process, shown in Figure 56 (a-c). The piezoelectric active material consists of AlN and is reactively sputter deposited under pure nitrogen atmosphere. All sputter parameters for the AlN deposition are presented in Table 14. The top electrode is similarly deposited as the bottom electrode with a 50 nm chromium layer and a 200 nm gold layer and is patterned together with the AlN in one single lift-off process depicted in Figure 56 (d-f). After all layers are deposited, the wafer is DRIE etched from the backside to reduce locally the thickness for cantilever realization. The final release was done again by DRIE etching from the frontside through the whole wafer. To protect the other side during both DRIE etching steps a positive photo resist was used to cover the whole wafer shown in Figure 56 (g-j).

Parameter	Value
Power	800 W
Pressure	0.2 Pa
N ₂ flow rate	50 sccm
Ar flow rate	0 sccm
Target/Substrate Distance	65 cm

Table 14: Sputter parameters for the piezoelectric AlN thin film of the PEHEs.

After fabrication, the single cantilever devices were cleaned with acetone and isopropyl alcohol. As the topside of the bottom electrode was fully covered with Cr and the connecting wires were soldered onto the electrodes, an additional chromium etch step with *CR etch 200* from *MicroChemicals* was performed to open the pads of the bottom electrode. Connecting wires were soldered onto the pads and the whole cantilever was glued onto a 3D-printed PLA holder, which could then be fixed onto the shaker for the harmonic excitation or into the hybrid energy harvester setup, as illustrated in Figure 57 (a) to (c). At the end, a magnetic proof mass was glued onto the cantilevers' tip.

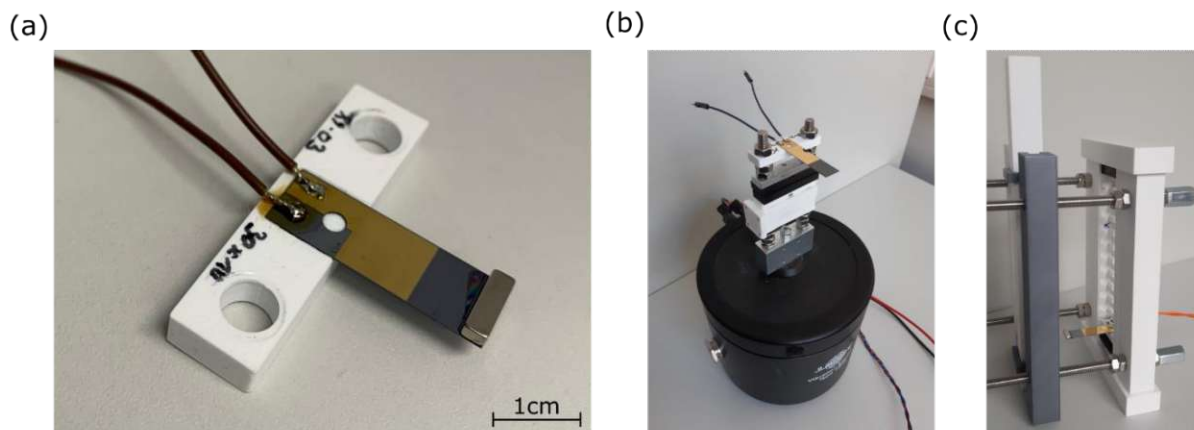
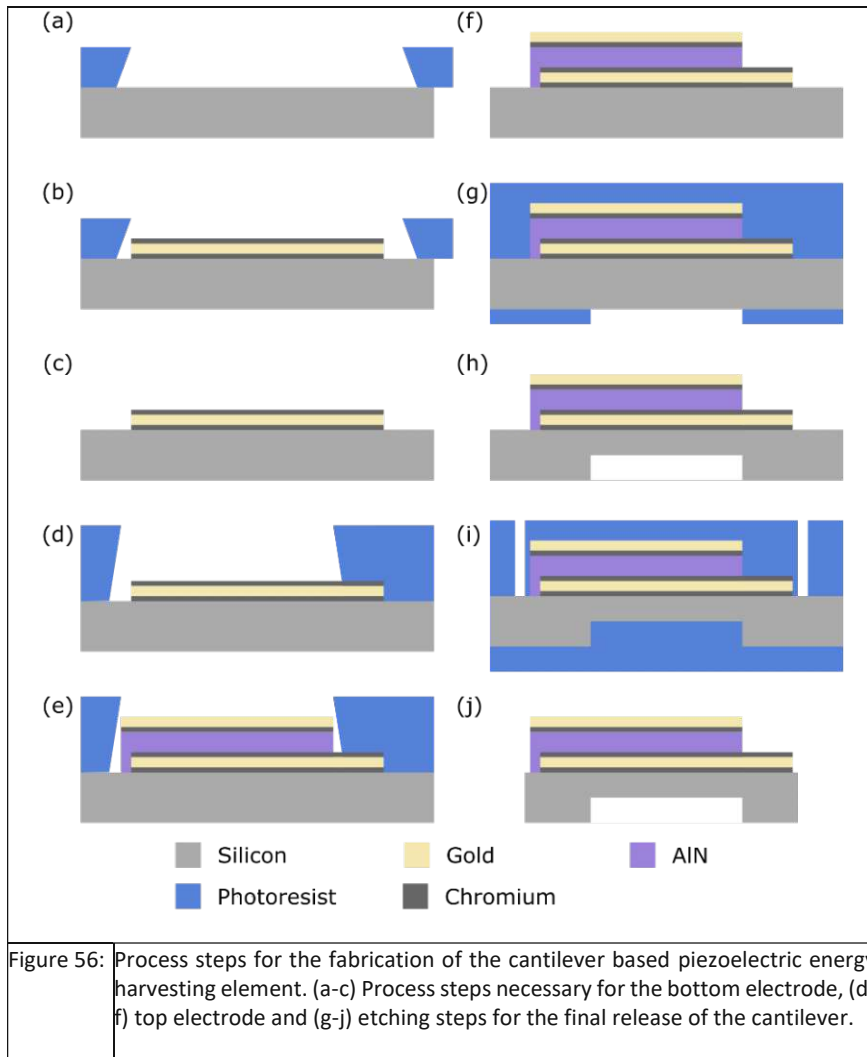


Figure 57: (a) Optical micrographs of a micromachined cantilever with 3D-printed fixation, mounted on the shaker (b) and in the hybrid energy harvester setup (c).

5.3.3. Harmonic Excitation

Harmonic Excitation refers to the continuous excitation of the cantilever with a periodic acceleration at one of the cantilever's resonance frequencies, whereas the amplitude is constant. Typically, the

amplitude is small in comparison to the cantilevers thickness to avoid non-linear effects and to limit the maximum bending moment of the cantilever. These dynamic investigations were performed on the shaker setup described in chapter 3. They were done to initially evaluate the performance and to study various characteristics like spectrum of resonance frequencies, optimal load resistance or generated output power (in this work the term output power refers to the maximal value in the frequency spectrum, which equals the amplitude), of the PEHEs compared to the less well defined boundary conditions during magnetic plugging, thus making the interpretation of the results more challenging. Several different sizes of cantilevers were fabricated with two different widths of 5 mm and 10 mm and six different lengths from 20 mm to 45 mm in steps of 5 mm.

The resonance frequency, the generated power output and the Q-factor of several cantilevers varying in length with a varying tip-mass, but with a constant width of 5 mm and 10 mm and a thickness of 250 μm were measured at an acceleration amplitude of 1 g_0 . Figure 58 (a) and (b) show the generated power as a function of frequency for both cantilever widths, respectively. To determine the resonance frequency f_R , the power at f_R and the corresponding Q-factor, a Lorentzian was fitted to the frequency spectra to determine the first and the latter device parameter. The resonance frequencies, shown in Figure 58 (c) decrease with increasing cantilever lengths which is in very good agreement with the model from section 5.3.1. Furthermore, f_R is independent from the cantilever's width, which is not surprising as the model for Euler-Bernoulli beams does not show any dependence on the width. The Q-factors for the resonator lie within a range of 100 – 600 with decreasing values for increasing lengths, due to the increased mass and reduced spring constant which longer cantilevers typically exhibit [261]. These results are also in agreement with earlier publications like [263]. Figure 58 (d) represents the power generated at the cantilever's resonance frequency. While it was expected to generate twice as much power for the broader cantilever, this could not be confirmed by the measurements. There could be various reasons for this finding. One maybe attributed to the load resistor which should be half the value for the broader cantilever when compared to the narrower device. According to the measurement R_L is in all cases higher than the calculated values (black and grey lines). Another reason could be the properties of the piezoelectric AlN layer. Although all cantilevers in these measurements were fabricated on one wafer, important thin film properties like thickness and crystal quality may vary across the wafer surface, resulting in lower values towards the edge region.

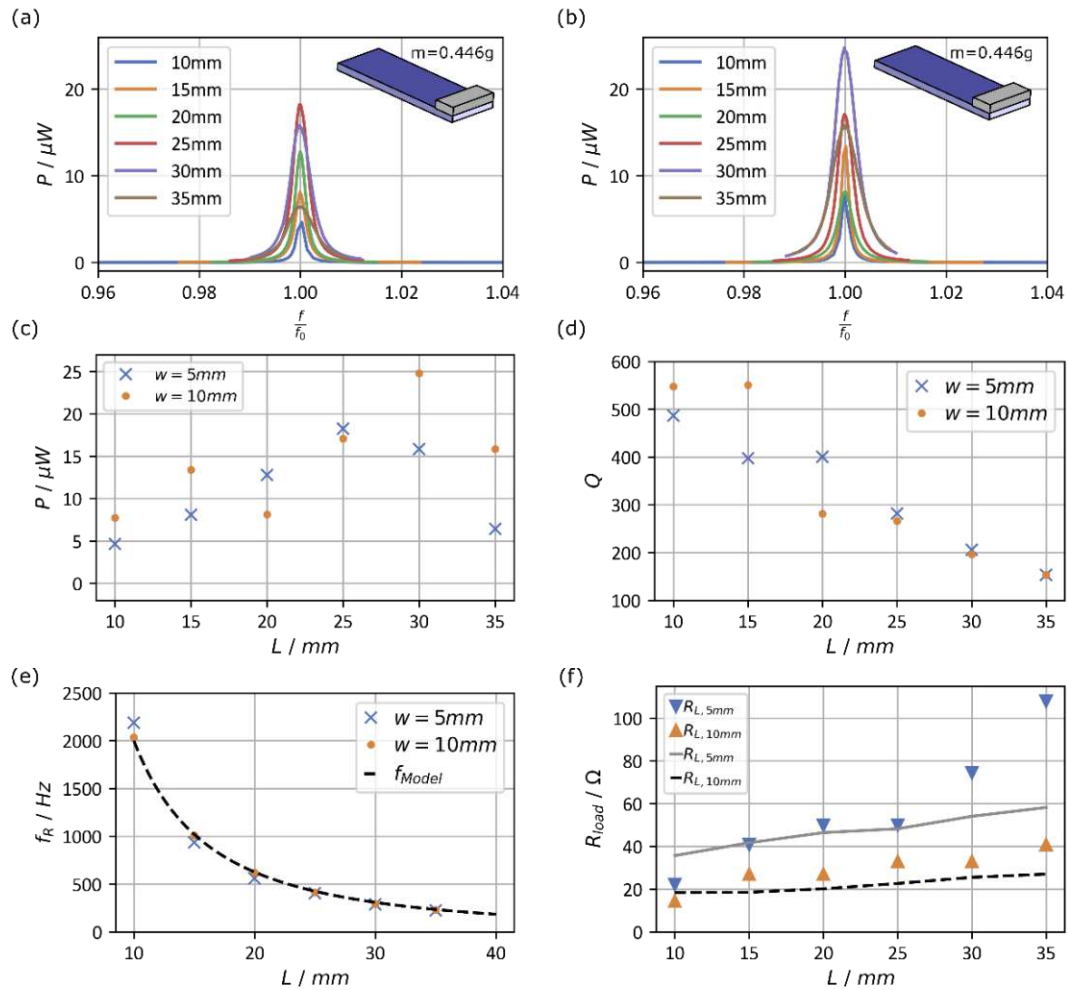


Figure 58: Generated power output as a function of frequency at an acceleration amplitude of $1 g_0$ of different cantilevers varying in length with a width of (a) 5 mm and (b) 10 mm . (c) Generated power, (d) Q-factor, (e) resonance frequency and (f) load resistor as a function of cantilever length including theoretical values of the load resistor.

Influence of Acceleration and Tip-Mass

Two other parameters which highly influence the power output are the acceleration with which the cantilever tip and the proof- or tip-mass of the cantilever is moved. Figure 59 (a) shows the generated power as a function of frequency for a cantilever which parameters can be found in Table 15. It shows that the resonance frequency is independent of the acceleration, but the output power increases with increasing acceleration amplitude. The Q-factor is also independent from the acceleration amplitude, shown in Figure 59 (g) for different lengths. Similar to Figure 58 (a) the Q-factor decrease for higher lengths but only ranging from 140 – 280, due to the increased mass.

Cantilever Properties	Value
Length	20 mm
Width	10 mm
Thickness	350 μm
Proof-Mass Dim.	3x10x2 mm ³
Proof-Mass Weight	0.446 g, 0.892 g, 1.338 g

Table 15: Cantilever properties

Figure 59 (b-d) show the power output for the same cantilever as before, but with different proof-masses of 0.446 g, 0.892 g and 1.338 g for accelerations ranging from 0.25 g_0 – 1.5 g_0 . In general, higher proof masses reduce the resonance frequency and at the same time increase the generated output power. But Figure 59 (e) also shows that for a given proof mass the increase in output power levels off at a certain acceleration amplitude. This can be explained by the increasing non-Lorentzian shape of the power spectra for higher accelerations, as illustrated in Figure 59 (b-d). While the curves for low acceleration amplitudes are still of Lorentzian shapes, the curves associated with higher accelerations have relatively lower maxima and broader peak shapes. This behavior can also be interpreted in another way, shown in Figure 59 (f) – at a fixed acceleration the output power can be increased by applying higher proof masses up to a certain threshold.

Figure 59 (g) shows resonance frequency and Q-factor as a function of proof-mass. Similar to the cantilever's length, an increased proof mass leads to a reduction in its resonance frequency which again is not surprising as this is predicted by the Euler-Bernoulli beam equations. On the contrary, the Q-factor initially increases with heavier proof masses before it decreases again. The reason for the decrease lies in the peak shape of the output power. As heavier proof-masses lead to a non-Lorentzian peak shape with broader and relatively lower peaks, the Q-Factor has to decrease as well. Depending on the applied acceleration amplitude the peak of $Q(m)$ lies closer to $m = 0$ the higher the acceleration amplitude is.

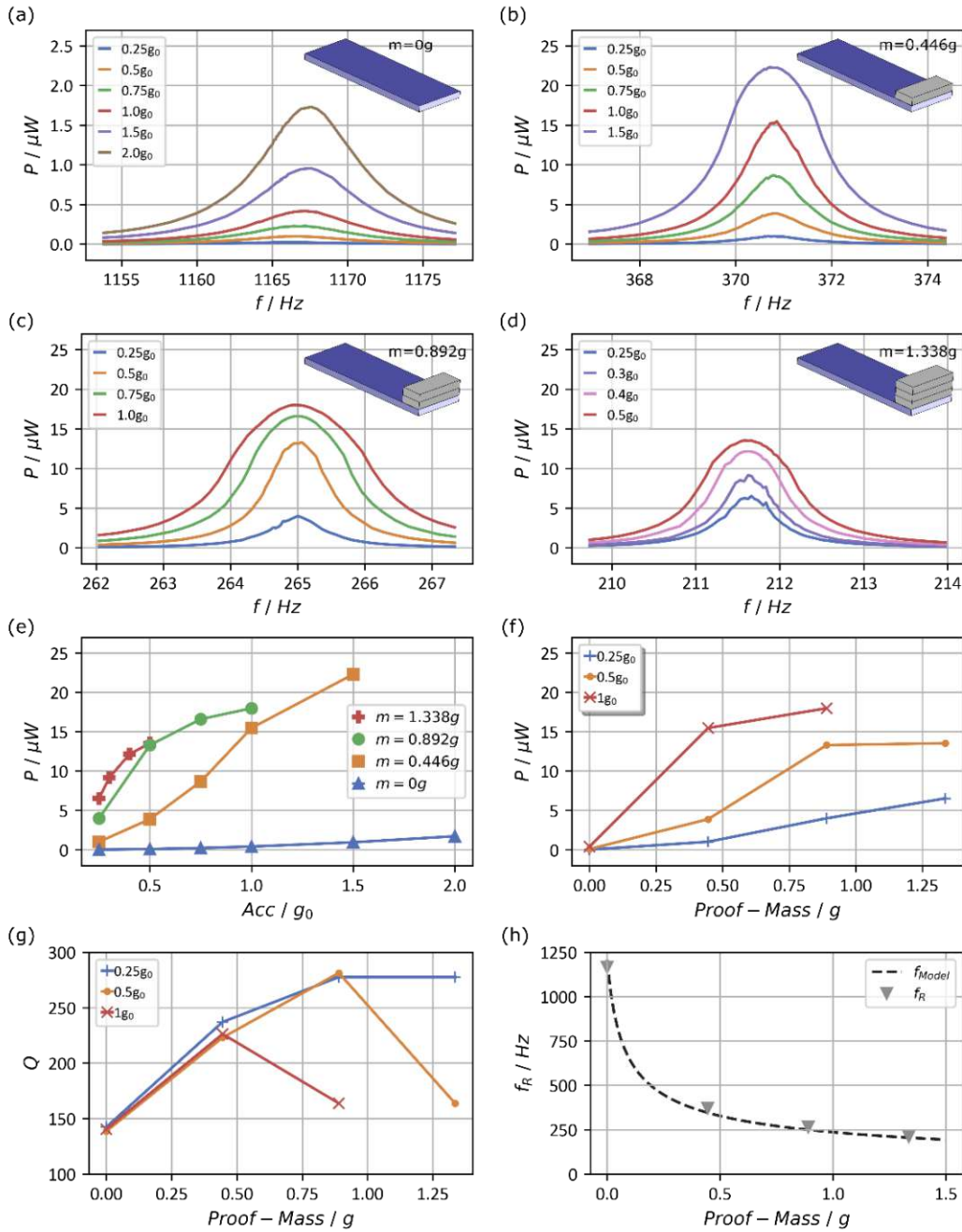


Figure 59: Generated output power as a function of frequency for a cantilever with a proof-mass of (a) 0 g, (b) 0.446 g, (c) 0.892 g and (d) 1.336 g for acceleration ranging from 0.25 g_0 to 2 g_0 . (e) Generated power as a function of acceleration amplitude and (f) as a function of proof-mass. (g) Resonance frequency and Q-factor as a function of the cantilevers proof-mass. Inserted lines in (e-g) serve as guide to the eye.

Normalized Power Density

As the generated power strongly depends on parameters like cantilever dimensions, weight of proof mass or acceleration amplitude it lacks comparison when evaluating the pure power output directly. Therefore, the normalized power density p_{NPD} is used, which relates the output power to the overall volume of the harvester (cantilever + proof-mass) and the acceleration amplitude [264], described in equation (5.9).

$$p_{NPD} = \frac{p}{(V_C + V_{PM}) \cdot g_0^2} \quad (5.9)$$

While a lot of published studies only use the volume of the cantilever (sometimes also only the volume of the piezoelectrically active material) to estimate the power density, in this work a rectangular volume enveloping all moving parts including the cantilever and the proof mass is used as representative volume, shown in Figure 60 (a) and (b) for top and side view, respectively. However, this approach does still not account for the additional space required for the movement of the individual parts, but it gives a more realistic comparison.

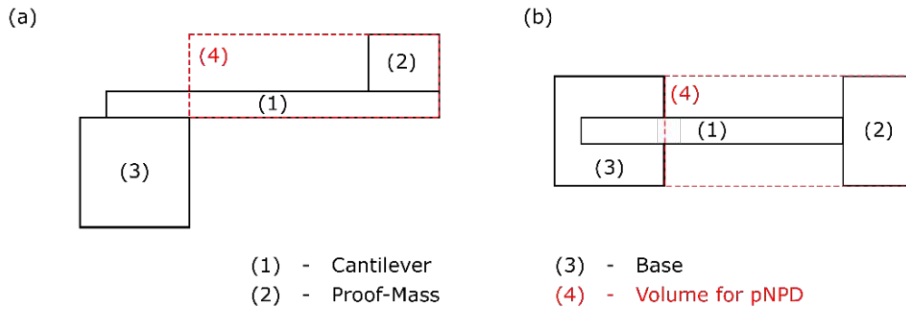


Figure 60: Schematic side (a) and top view (b) for the defined volume of a cantilever with proof-mass to calculate the normalized power density.

Figure 61 (a) shows the power densities of previously presented harvesters as a function of acceleration. The cantilevers with masses of 0 g and 0.446 g clearly indicate that P is proportional to the squared acceleration as these devices show nearly constant values in p_{NPD} . When attaching larger masses, however, p_{NPD} decreases for higher accelerations which is due to operation closer to the cantilever's yield strength as also described before.

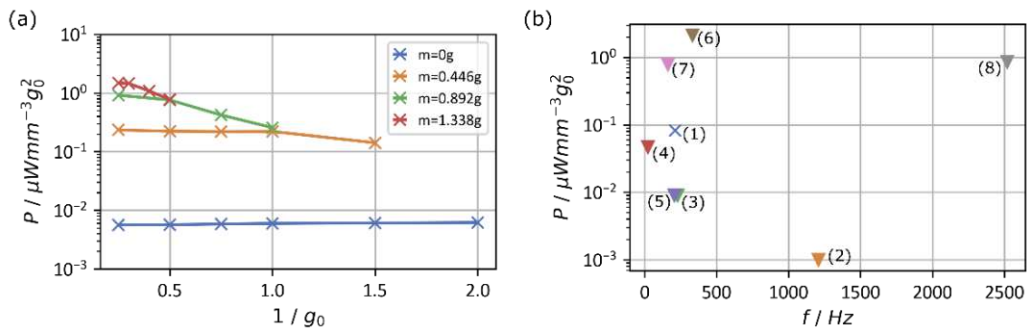


Figure 61: (a) Normalized power density as a function of acceleration amplitude and (b) as a function of the cantilevers' resonance frequencies in comparison with state-of-the-art energy harvesters. Numbers correspond to the table in section 2.2). Inserted lines serve as guide to the eye.

Figure 61 (b) shows p_{NPD} as a function of frequency for all presented cantilevers and comparable state-of-the-art energy harvesters (compare chapter 2). Although the energy harvesters fabricated underperform with respect to those reported in literature, the results provide important information about the expected performance for the next part, where the cantilevers were used under a magnetic plugging excitation scheme which in the following leads to the final section, discussing the complete design and characterization of a hybrid energy harvester.

5.3.4. Magnetic Plugging

Magnetic plugging is the selected approach for energy harvesting with the piezoelectric devices presented in this work. While the general mechanism was explained in section 5.2 this section explains in detail how the cantilevered PEHs are excited through magnetic plugging. The prototype

setup is shown in Figure 62 and consists of the PEHE (I) with its connectors (II), the guiding tube for the PM (III) and 4 threaded rods (IV) which were used to precisely alter the distance d_0 between the PEHE and the guiding tube.

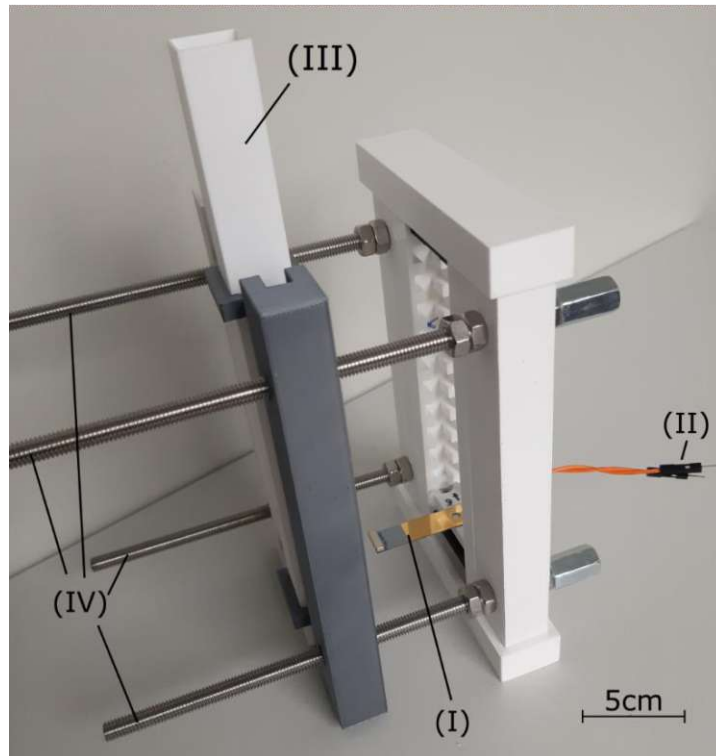


Figure 62: Hybrid harvester prototype setup, consisting of the PEHE (1), its electrical connectors (2), the guiding tube for the PM (3) and 4 threaded rods (4) which are used to alter the distance between the PEHE and the guiding tube.

The cantilever is excited through the magnetic forces acting on the tip-magnet when the permanent magnet falling through the tube is passing by. Figure 63 shows the displacement characteristics and six key states of the cantilever giving insight into the detailed interaction between the two magnets. The cantilever starts at zero displacement $y = 0$ (I) without any external forces. When the PM is approaching the cantilever, it gets bent towards the PM due to the attractive forces resulting in a positive displacement (II) restricted by the elastic spring constant of the cantilever. When the PM is just above the tip magnet it starts to drag the cantilever with it, passing by at $y = 0$ (III) and pushing it to a maximum negative displacement $y = y_{min}$ (IV). At this point the spring force exceeds the magnetic force and the cantilever snaps through (V), which excites the cantilever in its own resonance (VI), where it continues resonating until it stops due to damping or the next plugging event occurs.

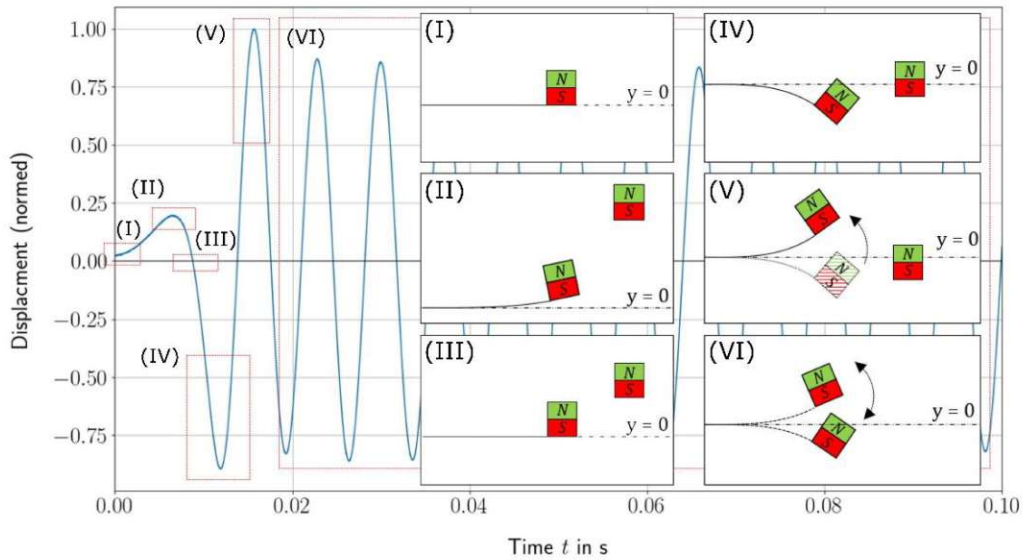


Figure 63: Normalized displacement characteristics of the cantilever during magnetic plugging and detailed view of key states (I)-(VI) of the cantilever and the moving magnet.

Several parameters must be considered to optimize the excitation of the cantilever and the generated energy, which will be discussed in the following.

Magnet distance

The distance d_0 between the TM and the PM is a crucial parameter which has to be optimized, while taking the magnetic force and the maximum fracture strength of the cantilever into account. The magnetic force is reduced by the reciprocal of d_0^3 [265], so that smaller values of d_0 are favorable. The maximum fracture strength of the cantilever is influenced by the used material (silicon) and its shape – mainly length and thickness, whereas longer and thinner cantilevers break more easily. Figure 64 (a) (blue curve) shows the produced energy of a cantilever with varying distance from 4 mm to 9 mm.

Magnet alignment

The magnets can be aligned either in an attracting or a repelling configuration. Figure 64 (a) shows a comparison of an attracting and a repelling setup for various distances d_0 . It shows that attractive forces produce approximately 10 times more energy than repelling ones. This can be explained by the influence of the TM onto the PM. In the repelling alignment the accelerating movement of the PM is reduced by the repelling forces of the two magnets, which then leads to a reduced excitation intensity of the cantilever and *vice versa*.

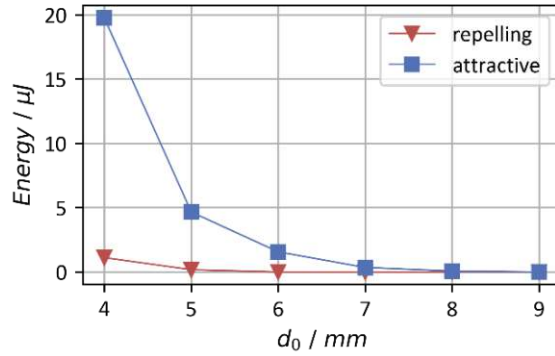


Figure 64. Generated output energy as a function of cantilever to guiding tube distance for attractive (blue) and repelling (red) configuration of PM and TM. The used cantilever had geometrical dimensions of $25 \times 5 \times 0.25 \text{ mm}^3$. Inserted lines serve as guide to the eye.

Weight Ratio

As explained before the magnetic forces act not only on the TM, but also on the PM. If the magnetic force on the PM exceeds the external forces (gravitation) the PM is caught by the TM and stops moving. Depending on the distance (contact, near field, far field) these forces can only be calculated numerically. To realize a reliable plugging mechanism, the weight of the PM has been increased by using multiple magnets stacked on each other.

Magnet Velocity

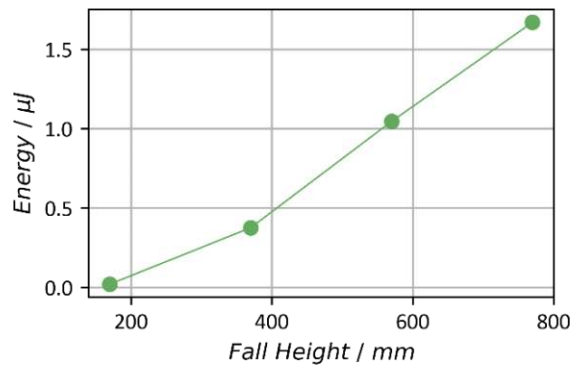


Figure 65: Generated output energy as a function of fall height of the PM, with $d_0 = 7 \text{ mm}$. The used cantilever had dimensions of $25 \times 5 \times 0.25 \text{ mm}^3$. Inserted lines serve as guide to the eye.

The velocity of the permanent magnet defines how fast the magnetic field direction is changing and with it the pulling force on the TM of the cantilever. In the HEH design, the velocity can mainly be influenced by the length of the guiding tube. A longer tube results in a longer acceleration time and, hence in higher velocities of the magnet. Figure 65 shows experimentally generated output energies for four different tube lengths. In general, after the cantilever snapped through and starts resonating, it is additionally damped by the attracting (or repelling) forces of the PM. The amount of damping depends on the distance d_0 between the PM and the TM and decreases while the PM

is moving away. Therefore, a higher velocity of the PM results in a faster decreasing damping coefficient and additionally increases the vibrational amplitude of the cantilever.

Magnetic Field Strength

The harvested energy directly correlates with the cantilever excitation amplitude and therefore, increasing the magnetic field strength of the PM seems to be a straightforward improvement. To confirm this, two cuboidal PMs with different lengths L_{PM} , widths W_{PM} , thicknesses H_{PM} , volumes V_{PM} and their masses m_{PM} were used on two cantilevers with different dimensions L_C , W_C , H_C , their volumes V_C and masses m_{PM} . Exact values of the mentioned parameters and the horizontal distance d_0 between the cantilever and the PM for all four combinations can be taken from Table 16. While the longer cantilever showed - as expected - an increased energy output when it is excited with the bigger and stronger magnet, the shorter cantilever showed the opposite behavior, shown in Figure 66 (a) and (b). One explanation is the duration of the change in magnetic field strength, which is far longer for the bigger than for the smaller magnet, especially after the PM has passed by the cantilever, where the magnetic field of the PM acts restraining on the cantilever oscillation. This can be seen in the inset of Figure 66 (a) where the static deflection of the cantilever takes two full periods of the cantilever's vibration to revert (*). This does not happen for the smaller magnet. While in this presented case the longer cantilever C2 produces more energy for both PMs, these results also show that the length of the cantilever and the magnetic field strength of the PM have to be balanced.

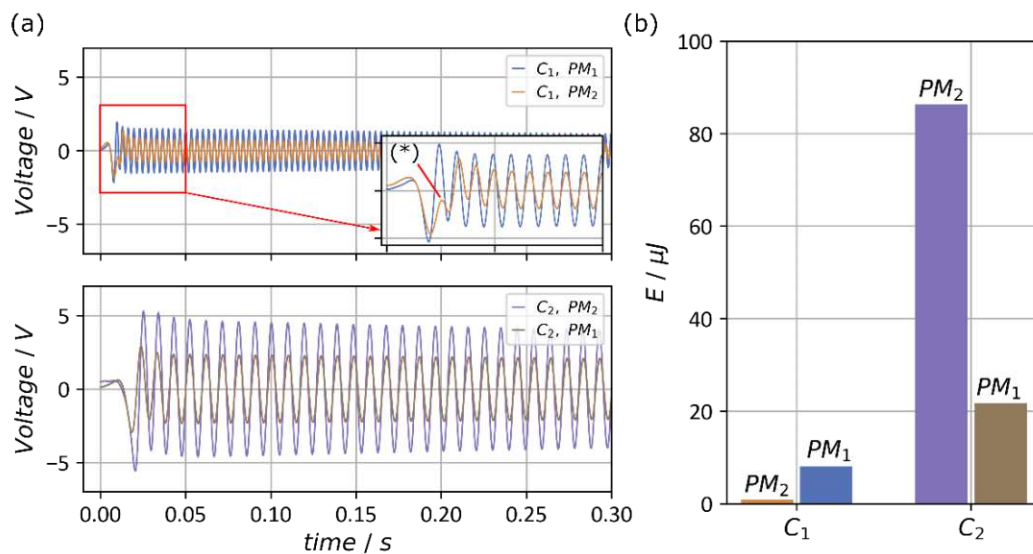


Figure 66: (a) Generated output voltage as a function of time for cantilevers C_1 and C_2 excited with two different permanent magnets PM_1 and PM_2 . (b) Generated energy outputs after a time of three seconds for all combinations of cantilevers and magnets.

	C_1	C_2		PM_1	PM_2
L_C / mm	15	25	L_{PM} / mm	15	40
W_C / mm	5	10	W_{PM} / mm	15	40
H_C / mm	0.25	0.25	H_{PM} / mm	8	20
V_{TM} / mm^3	10x3x2	10x3x2	V_{PM} / cm^3	1.8	32
m_{TM} / g	0.445	0.445	m_{PM} / g	13.5	240
d_0 / mm	4 / 5	8 / 12			

Table 16: Dimensions of the cantilever, its proof mass and the distance between the guiding tube and the cantilever used in Figure 66.

PEHE quality factor

As explained in chapter 3 the quality factor can be defined by several methods, whereas the ring down method is regarded as most suitable when considering the excitation by magnetic plugging. Figure 67 (a) shows quality factors of several different cantilevers obtained during harmonic excitation with a fitting function according to section 3.6 and during magnetic plugging measured by the ring down method according to section 3.9. The Q-factors obtained with both methods diverge by up to 50%. This seems quite a lot considering that the Q-factors are sufficiently high to neglect divergences due to the deviations of the chosen method. When examining the ring down of the cantilever during magnetic plucking more closely, one can see that the fitting function does not match with the measured curve equally well at all times. By fitting the ring down characteristics at three different time intervals with a duration of 0.04 s (~ 10 periods) each, it becomes apparent that the damping within the system changes during the ring down procedure. This can be caused by three reasons:

- At the beginning of the ringdown the cantilevers displacement is $> 10 mm$ which compared to the used lengths of 15 – 35 mm is rather large. As the Q-factors are typically defined for displacements being small to the cantilever's dimensions, other damping mechanisms must be considered. This additional damping source decreases as the displacement gets smaller, leading to an increase in the Q-factor during ring down.
- The falling permanent magnet additionally adds damping to the vibration of the cantilever. As it falls further down the damping reduces, leading to a decaying damping coefficient over time and hence, increased Q-factors when fitting later intervals of the ring down curve.
- Another effect coming into play is the frame of the prototype guiding the permanent magnet and holding the cantilevers in place. As it is 3D-printed with PLA filament, which is a rather soft material, it additionally adds damping as it bends and moves, while the cantilever is vibrating, especially for larger cantilever displacements.

As all three mechanisms are dependent on the displacement, it can be expected that the Q-factor calculated from the ring down approaches the same value received during harmonic perturbation, while the ring-down progresses with time. This is confirmed by the inset in Figure 67 (b) which shows a Q-factor of 760 for the harmonic perturbation compared to 755 for the ring down.

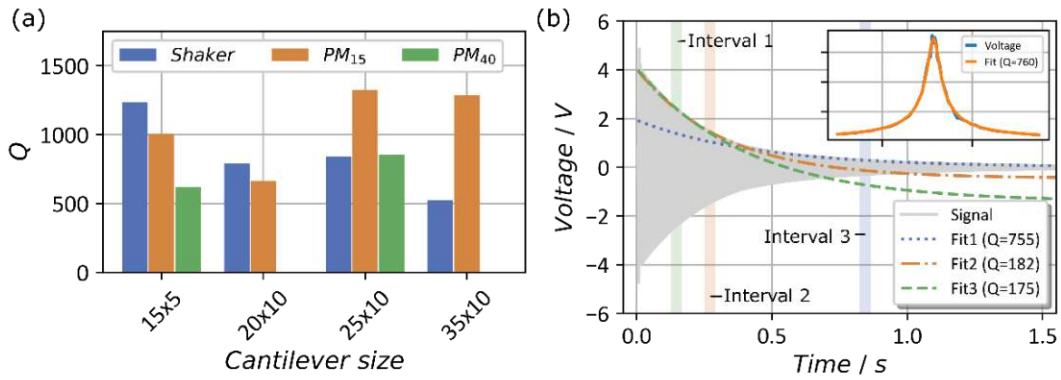


Figure 67: (a) Q-factors of 4 different sized cantilevers for 3 excitation methods (harmonic perturbation, magnetic plucking with small and large PM). (b) Exemplary voltage output of a magnetic plucking event with fitted amplitude envelope to estimate the Q-factor for three different fitting intervals. The inset shows the output voltage as a function of frequency of the same cantilever with a fitted voltage curve and the corresponding Q-factors.

The Q-factor together with the time interval between two plucking events also determines how much energy can be harvested. For low Q-factors the cantilever rings down to low displacements until the next plucking occurs, while for high Q-factors the displacement stays at high values in between different plucking events. Therefore, high Q-factors are desired. Figure 68 (a) shows the ring down of generated voltage for four different PEHEs. The curve *C1* represents measured data of a cantilever with $Q \approx 1000$, whereas *C2* and *C3* are simulated PEHEs with $Q = 3000$ and $Q = 9000$, respectively to show the influence of the Q-factor onto the generated voltage. The curve *C4* is an ideal PEHE with $Q \approx \infty$ representing the theoretical maximum of harvestable energy for the given cantilever dimensions and the given electromechanical coupling of the piezoelectric transducer. Figure 68 (b) shows the generated energy for four different time durations. It shows that not only the amount of harvested energy differs depending on the Q-factor, but depending on the time the differences in harvested energy vary. For very short durations below 1 s the Q-factor does not play a decisive role. However, the longer the harvesting time period the more important a high Q-factor is. This means that for the previously mentioned testing wind turbine with a nominal rotational frequency of 20 rpm, converting into a plucking event every 1.5 s a Q-factor of approximately 1000 is sufficiently high.

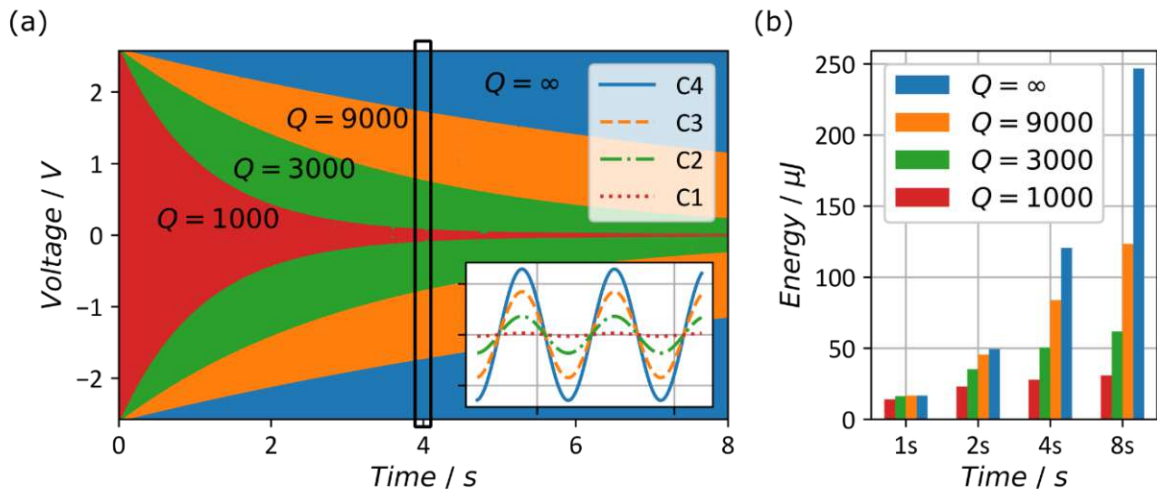


Figure 68: (a) Generated voltages as a function of time for one measured cantilever with the dimensions $25 \times 5 \times 0.25 \text{ mm}^2$ and three simulated cantilevers (same dimensions) with adapted Q-factors. (b) Harvested energies for different time durations for all four cantilevers.

All those parameters are not independent from each other. If the distance d_0 between the magnets is increased, the excitation strength of the PEHE would get reduced and if the magnetic field strength and velocity of the falling PM is increased, the PEHE would be excited stronger. Therefore, by carefully adjusting these parameters the generated energy could be optimized with respect to external parameters such as overall size or weight of the harvester.

5.4 Electromagnetic Harvester

In this chapter the electromagnetic part of the HEH is studied. First the fabrication is explained followed by theoretical considerations about the dimensions, alignment and interconnections of the coils and the used magnet. At the end a detailed characterization of an optimized prototype is presented, which was also used in field measurements in a wind turbine.

5.4.1. Design and Fabrication

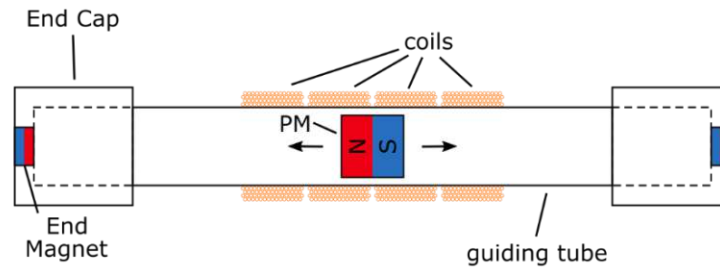


Figure 69: Schematic drawing of the electromagnetic harvester comprising the guiding tube, end caps including end magnets, the PM and several coils

The design of the electromagnetic harvesters (EMH) is shown in Figure 69 and consists of the guiding tube, the PM, several coils surrounding the tube and two endcaps with embedded end-magnets. The end-magnets are aligned so that they repel the PM, which softens the stopping of the PM and reduces wear and shock loads. The guiding tubes and the endcaps are made from polylactic acid (PLA) fabricated in a 3D-printer.

The generated energy of the harvester mainly depends on the tube length (which was fixed to 200 mm due to the limitations of the used 3D-printer), the PM and the circuitry of the coils, which will be discussed in the following.

Coil Dimensions and Permanent Magnet Size

In the ideal case a bigger magnet with the same magnetization (same field line density) has a higher magnetic flux related to its perimeter. Therefore, a coil surrounding the magnet with the same diameter as the magnet will carry a higher induced voltage. Considering an ideal wire with zero resistance, an increased number of windings automatically leads to a higher generated energy if the magnet passes through the coil center. In a more realistic case, the magnetic field is not ideal due to the field lines not encircling the whole coil, reducing the induced voltage in windings which are further away from the coil center. Additionally, the resistance of the coil wire increases with its length and decreases with its diameter, which means that windings further away from the center add a higher resistance to the overall coil resistance, compared to windings closer to the center.

To estimate the optimal number of windings for the two permanent magnets used before (Table 16), FEM simulations have been performed with COMSOL. The model consists of one coil and a PM moving through this coil, accelerated by $1 g_0$. Frictional losses are neglected as well as the reverse magnetic field generated from the coils, decelerating the PM. The load resistor was set equal to the resistance of the coil to achieve impedance matching for maximum power transfer.

With the resistance of a coil with $n = 1$ and $m = 1,2 \dots 4$ windings, according to Figure 70 (a)

$$R_{n=1,m=1} = \rho \left(\frac{16d_T}{d_W^2\pi} \right) = 16\rho N \left(\frac{1d_T}{d_W^2\pi} + \frac{0}{d_w\pi} \right) \quad (5.10)$$

$$R_{n=1,m=2} = R_{n=1,m=1} + \rho \left(\frac{16(d_T + 2d_W)}{d_W^2\pi} \right) = 16\rho N \left(\frac{2d_T}{d_W^2\pi} + \frac{2}{d_w\pi} \right) \quad (5.11)$$

$$R_{n=1,m=3} = R_{n=1,m=2} + \rho \left(\frac{16d_T + 4d_W}{d_W^2\pi} \right) = 16\rho N \left(\frac{3d_T}{d_W^2\pi} + \frac{6}{d_w\pi} \right) \quad (5.12)$$

the overall coil resistance was finally calculated by the expression:

$$R_{n=N,m=M} = 16\rho N \left(\frac{Md_T}{d_W^2\pi} + \frac{M(M-1)}{d_w\pi} \right) \quad (5.13)$$

With N being the number of windings in x -direction and M being the number of windings in y -direction, ρ is the specific resistance of copper, d_w is the wire diameter and d_t is the tube diameter, all shown in Figure 70 (a). This estimation presents a conservative way to calculate the coil's resistance. More sophisticated methods, including random or helical winding can be found in [266].

The tubes diameter was taken from the diameter of the two magnet sizes plus an additionally few millimeters of material strength. With these parameters, a parametric sweep over the wire diameter can be performed, resulting in resistance values of the coils of

$$\begin{aligned} R_{15 \times 15} &= 189 \, \Omega \\ R_{40 \times 40} &= 678 \, \Omega \end{aligned} \quad (5.14)$$

The resulting number of windings are:

$$\begin{aligned} N_{15 \times 15, total} &= 2600 \\ N_{40 \times 40, total} &= 1800 \end{aligned} \quad (5.15)$$

The necessary lengths of the coil wire can also be calculated with:

$$L_w = 4N (Nd_T + d_w M(M-1)) \quad (5.16)$$

Which calculates to:

$$\begin{aligned} L_{w,15 \times 15} &= 196 \, m \\ L_{w,40 \times 40} &= 313 \, m \end{aligned} \quad (5.17)$$

Figure 70 (b) shows the measured open circuit voltage of two manufactured coils after the permanent magnet has passed by and the inset is the corresponding generated energy from this time frame. The voltage output is about 10 times larger for the bigger magnet, whereas the energy is 20 times higher, confirming the assumption stated at the beginning.

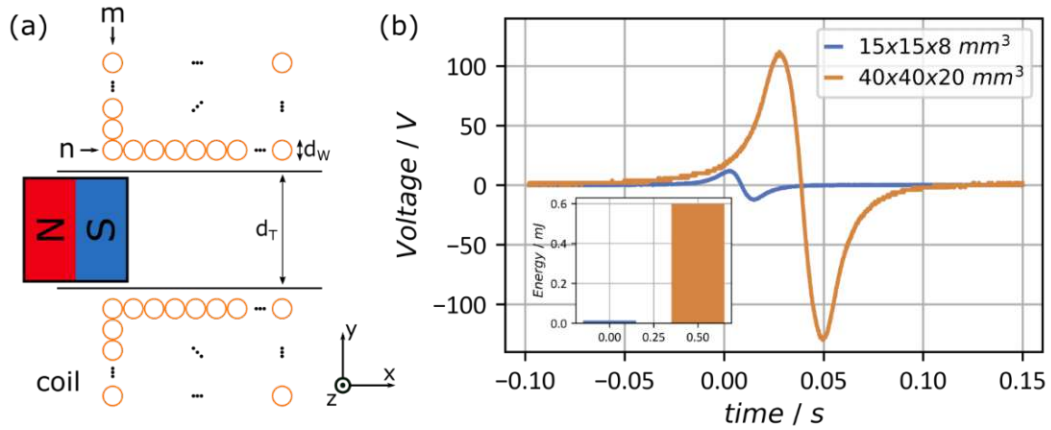


Figure 70: (a) Detailed schematic of one coil and the parameters to calculate the optimal wire/length ratios. (b) Generated voltage of two optimized coils for two different sized PMs.

Coil Circuitry

To increase the harvested energy per fall of the PM, a combination of multiple coils can be used. Figure 47 (a-g) show several multi-coil setups with four coils each. To analyze the resulting voltage curves only two of those four coils are wired to the output. In total, there are 6 possibilities to wire two coils together. Three configurations are in series, the other three are in anti-series. Figure 73 (a-d) shows the produced ac-voltages and Figure 73 (e) the corresponding energy outputs. We can see that the total output voltage is a superposition of the single coil voltages. As the induced voltages depend on the timely derivative of the magnetic flux, the sign of the voltage depends on the movement of the PM and on the poling of the coil. Therefore, if the coils are wired in a clever way, the energy output can be increased. In the displayed case, the most harvested energy can be generated by a combination of coils one and four in an anti-series circuit. This can be explained by the opposite sign of the voltages for *e.g.*, coil one and two, when the magnet moves through those coils. When the PM exits coil one, the sign of the harvested voltage gets negative. At the same time the PM enters the next coil, resulting in a positive sign for the voltage. Depending on the distance of the coils, the generated voltages add up or cancel each other out.

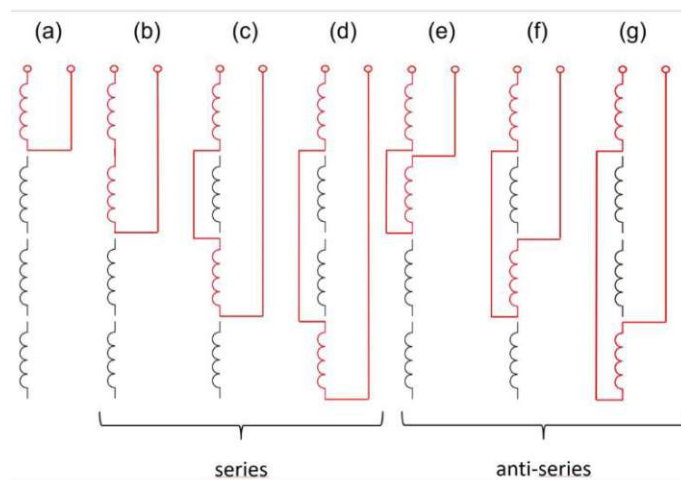


Figure 71: Possible configurations for different multi coil setups for single coil (a), in series (b-d) and in anti-series (e-g).

Details about the dimensions and characteristics of the used parts can be found in Table 17.

Furthermore, the usage of multiple PMs and their configuration and a fitting coil circuitry can also increase the generated voltages, which will be explained in the next section discussing the configurations of a multi-magnet setup in combination with the multi-coil circuitry.

Object	Value
Single magnet	15x15x8 mm ³
Dual anti-series magnet	40x15x8 mm ³
Magnetization	1.3 T
Coil length	8 mm
Coil resistance	189 Ω
Coil windings	2600
Wire cross section	0.15 mm ²
Load resistance	189 Ω, 287 Ω

Table 17: Magnet and coil dimensions used for estimating the output voltages and generated energy.

Permanent Magnet Configuration

As already mentioned before, the PM can be modified, meaning two or more magnets are stacked onto each other. For simplicity, a single magnet (Figure 72 (a)) is compared with a two magnets arrangement aligned in series (Figure 72 (b)) and an anti-series configuration (Figure 72 (c)). In contrast to the series configuration, where the magnetic field is stronger with essentially the same shape, in the anti-series configuration the magnetic field is distorted and the direction of the field lines changes along the magnet configuration.

Ideally, the magnets would be stacked without a gap between them, but the repelling forces are too strong for the used adhesive. Therefore, a 3d-printed spacer has been glued in between with twice the length as one magnet. This spacer considers the size of the coils, meaning that when one magnet is exactly in coil one, the other magnet is in coil four (compare Figure 47)

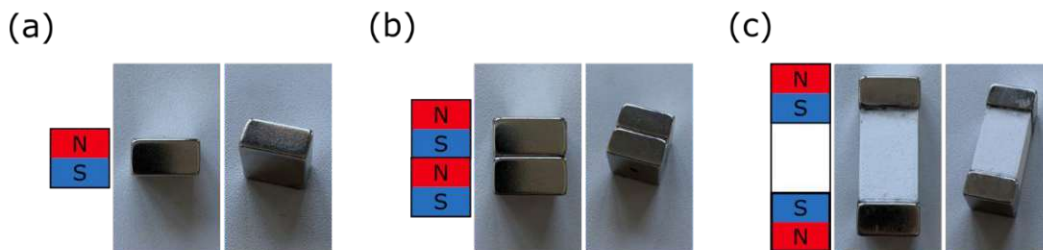


Figure 72: Various configurations for the PM. (a) Single magnet, (b) two magnets in series and (c) two magnets in anti-series configuration with spacer.

In general, it would be possible to stack more than two magnets in anti-series configuration, which would further increase the generated energy per fall. Due to the limitations of the tube length of around 200 mm, the length of the stacked magnet was set to 40 mm, which provides enough room that the PM can enter and exit the coils completely and gives additional space for acceleration.

The generated output voltages and corresponding energies are given in Figure 73 (a-d) for a single magnet, in Figure 73 (f-j) for a combination of two stacked magnets in series configuration and in Figure 73 (k-o) for two stacked magnets in anti-series configuration. Figure 73 (e, j, o) shows the generated energies for one fall of the magnet. The in series stacking arrangement increases the generated energy by a factor of approximately five. The enhanced anti-series stacking can further optimize the generated energy to a maximum of $\sim 10 \text{ mJ}$ per fall of the PM, corresponding to a seven-fold increase compared to a single coil setup.

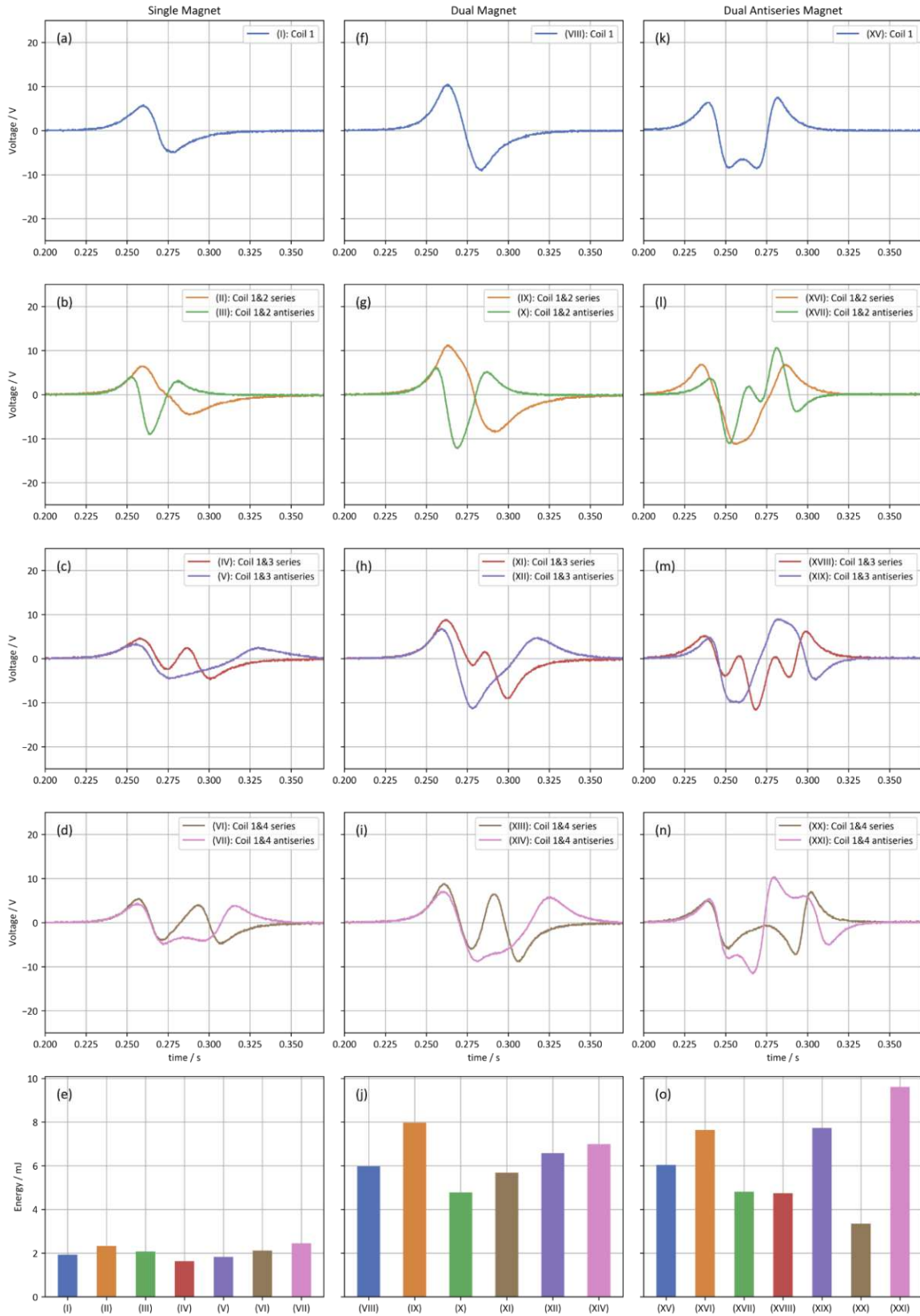


Figure 73: Generated output voltages for different multi-coil configurations and all three magnet configurations described before (columns). (e), (j) and (o) display the generated energy, whereas curves and columns of the same colour are related to each other.

5.4.2. Characterization

With the knowledge about magnet configuration and the influence of the coil circuitry from the previous sections a prototype was fabricated, as shown in Figure 74 (a). It was later also tested under real-world conditions in a wind turbine, see section 5.5.2. It has a dual guiding tube setup with a modified PM consisting of two magnets in anti-series configuration, as illustrated in Figure 72 (c) before. Exact dimensions of the parts can be taken from Table 18 at the end of the chapter.

In total, there were 12 + 18 coils whereas every third coil is connected in anti-series to the previous one and subsequently to a bridge rectifier, according to the best performing coil circuitry from Figure 73 (o). The outputs of the rectifiers are connected in series to increase the output voltage level, which facilitates subsequent voltage conversion compared to a parallel circuit which increases the output current with lower output voltage. Figure 74 (b) gives an overview of the schematics including the rectifier circuit.

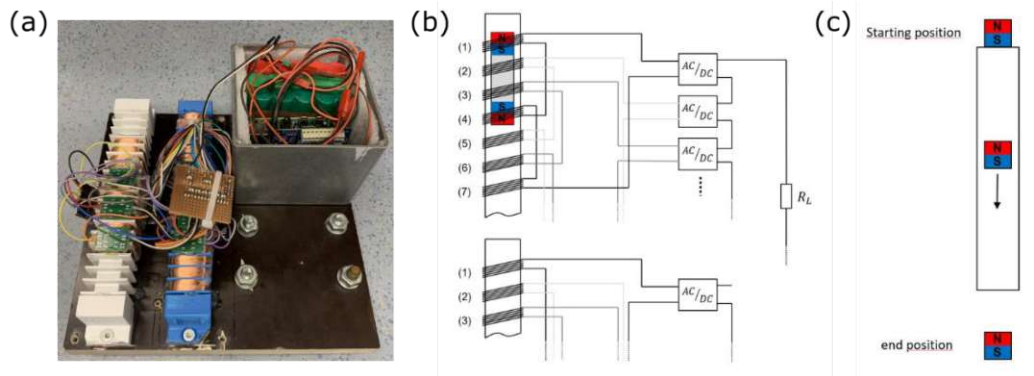


Figure 74: (a) Photograph of the optimized electro-magnetic energy harvester comprising of two guiding tubes, 12 + 18 coils and a read-out circuit. (b) Circuit schematic of the coils. (c) Testing procedure of the magnet when moved through the guiding tube.

Figure 75 (a) shows the output voltage as a function of time for various load resistors starting from 1 k Ω to 8.2 k Ω . The curve with the highest load resistor is also the one producing the highest output voltage, but it is not the one generating the most energy. Figure 75 (b) depicts the generated energy as a function of the applied load resistor and confirms that the optimal load resistor is around 5.6 k Ω . In the optimal case 22 mJ of energy could be generated for one fall of the magnet, which can be used to estimate the output power in a wind turbine with 20 rpm to 15 mW.

Comparing the 22 mJ of generated energy to the 9.5 mJ of energy generated with the two-coil setup in Figure 73 (o) the increase seems moderate given the number of additional coils. This is a result of the increased load resistor when several coils are connected. Even if the PM is passing through only one coil, the current is flowing through the whole circuit including all inner resistances of the other coils. Considering the approximately fourfold increase of output voltage (10 mJ \Rightarrow 40 mJ) which has to be squared for the energy, the fourteenfold increase in the load resistor (390 mJ \Rightarrow 5600 mJ) and the doubling of the duration of output signal, a doubling of the output energy seems very reasonable.

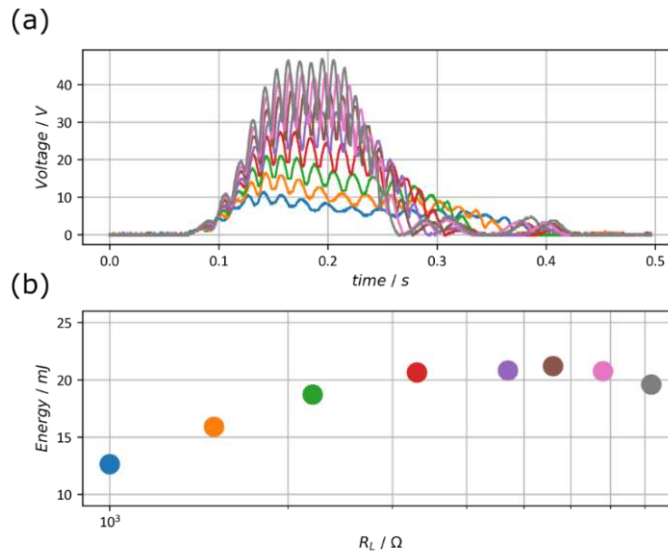


Figure 75: (a) Generated voltage of the optimized electro-magnetic energy harvester for one fall of the PM for different load resistors. (b) Accumulated energy for different load resistors. Colors of both plots correspond to each other.

It is worth mentioning, as referred to in a later section, that Figure 74 (c) shows data where due to measurements in the lab, the endcaps were removed, and the starting point of the PM was just above the guiding tube. After the fall of the PM, it had enough space to exit the tube without being decelerated which would not be the case if endcaps were present. The reason for this lies in the higher reproducibility of the measurements in the lab.

Property	Value
PM size	15x15x8 mm ³
PM magnetization	1.3 T
Tube size	2x 15x15x200 mm ³
No. of coils	12 + 18
Coil windings	200
Coil diameter	27 mm
Wire cross section	0.15 mm ²
Total outer dimensions including endcaps	320 cm ³
Load resistance	5600 Ω

Table 18: Magnet and coil dimensions used for estimating the output voltages and generated energy.

Normalized Power Density

Similar as in section 5.3.3 for the PEHE in harmonic perturbation mode a normalized power density for impact-based energy harvesters $p_{NPD,IP}$ can be defined as:

$$p_{NPD,IP} = \frac{p}{V_{tot}} \quad (5.18)$$

whereas V_{tot} is the total volume of a rectangular box enveloping all parts of the EH. In this case $p_{NPD,IP}$ is not related to the acceleration. However, the generated power depends on the frequency of the falls. Considering that the peak is approximately 0.2 s long the peaks can occur with a frequency of 5 Hz at which the generated power calculates to 110 mW and $p_{NPD,IP} = 373.75$. Figure 76 shows $p_{NPD,IP}$ as a function of frequency for comparable impact-based energy harvesters from chapter 2.

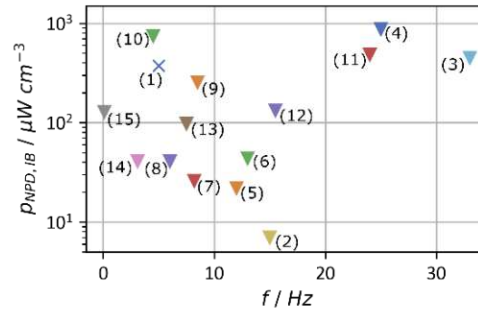


Figure 76: Normalized power density as a function of impact frequency in comparison with state-of-the-art energy harvesters. Numbers correspond to the table in section 2.2.

5.5 Measurements in a Wind Turbine

To demonstrate that the previously presented design of a hybrid energy harvester not only works in the lab, but also in a real-world scenario, two prototypes were installed in a wind turbine and the results are presented in this chapter. In section 5.5.1 the results of a HEH prototype with one PEHE and one EMHE are shown, serving as a proof of concept. Next, in section 5.5.2 the field measurements of an electromagnetic-only harvester, optimized for enhanced power generation and consisting of several EMEHs are shown.

5.5.1. Hybrid Energy Harvester

The HEH installed in the wind turbine consisted of three elements, a tube with the PM inside, one PEHE and one EMHE, shown in Figure 77 (a). The system installed in the wind turbine is shown in Figure 77 (b). The exact dimensions of the elements and their load resistors can be taken from Table 19.

EMHE			PEHE		
PM	1x1x1 cm ³	NdFeB	Substrate	30x10x0.25 mm ³	Si
B_{PM}	1.3 T	-	h_{piezo}	2 μm	AlN
l_{tube}	20 cm	-	m_{TM}	0.5x1x0.5 cm ³	NdFeB
N_{EMHE}	1000	Cu	f_{Res}	32 Hz	-
R_{load}	42 Ω	-	R_{load}	330 kΩ	-

Table 19: Dimensions plus additional parameter associated with the EMHE and the PEHE.

To measure the output voltages and the amount of generated energy in the wind turbine, a custom-built measurement setup was designed consisting of a *Raspberry Pi*, a data acquisition board (DAQ) *MCC118 DAQ* from MC Computing and individual load resistors for the PEHE and the EMHE, shown in Figure 77. It operates on three packs of five *18650* lithium-ion batteries each, providing a total of *16 Ah* at *3.6 V* which roughly lasts for two days. The *Raspberry Pi* runs a python script controlling the DAQ board and stores all the measurement data with an SQLite database on a USB flash drive. The setup can be controlled via WIFI to facilitate the access in the wind turbine.

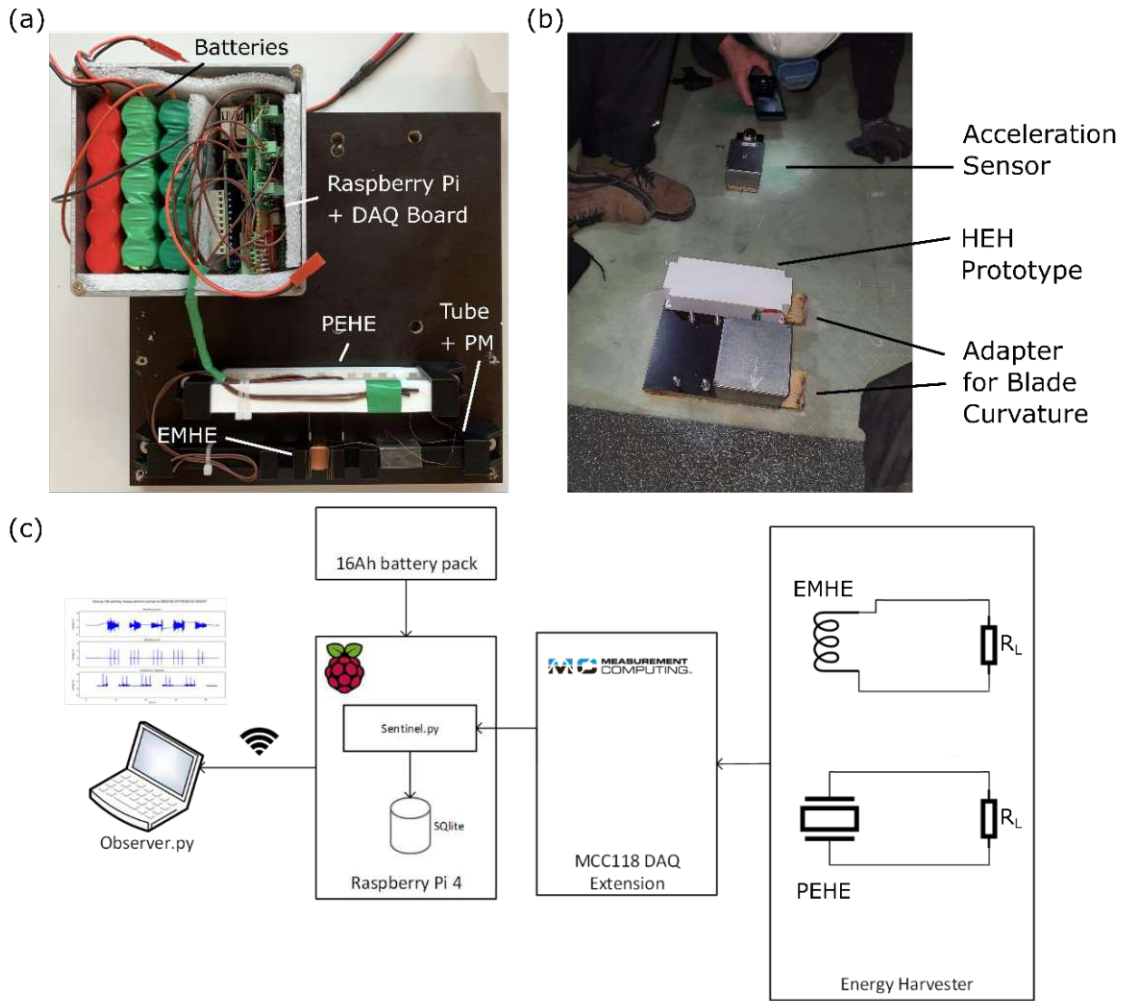


Figure 77: (a) Prototype HEH for a real-world proof of concept including the wireless measurement setup, a guiding tube with the PM inside, a PEHE and an EMEHE. (b) Final prototype including the covers as it was installed in the wind turbine.

Results

The measurement data from the wind turbine was analyzed and a representative sample of about 4000 s is shown in Figure 78 (a). It starts with the wind turbine being in full operation for about 700 s, then the wind turbine decreases its rotational speed for about 3000 s, until it finally stops after 3900 s. Red curves correspond to the output voltage of the EMHE and blue curves correspond to the PEHE. Figure 78 (b) shows a time frame of 70 s while the turbine was in full operation. The EMHE produces continuous double peaks whenever the PM falls through the guiding tube for the whole duration. The PEHE gets excited whenever a double peak occurs, which is also shown in more detail in Figure 78 (c) for a single fall of the PM. In Figure 78 (d) the rotational speed of the wind turbine decreased so much, that the PM does not fall through the whole tube but gets caught due to the increased frictional forces between the PM and the side wall of the guiding tube and the attracting forces of the TM. This results in a single negative peak in the EMHE and a very low excitation amplitude for the PEHE. However, in the second half of the rotation the PM falls back into one end of the tube resulting in the small ripples in the output voltage of the EMHE.

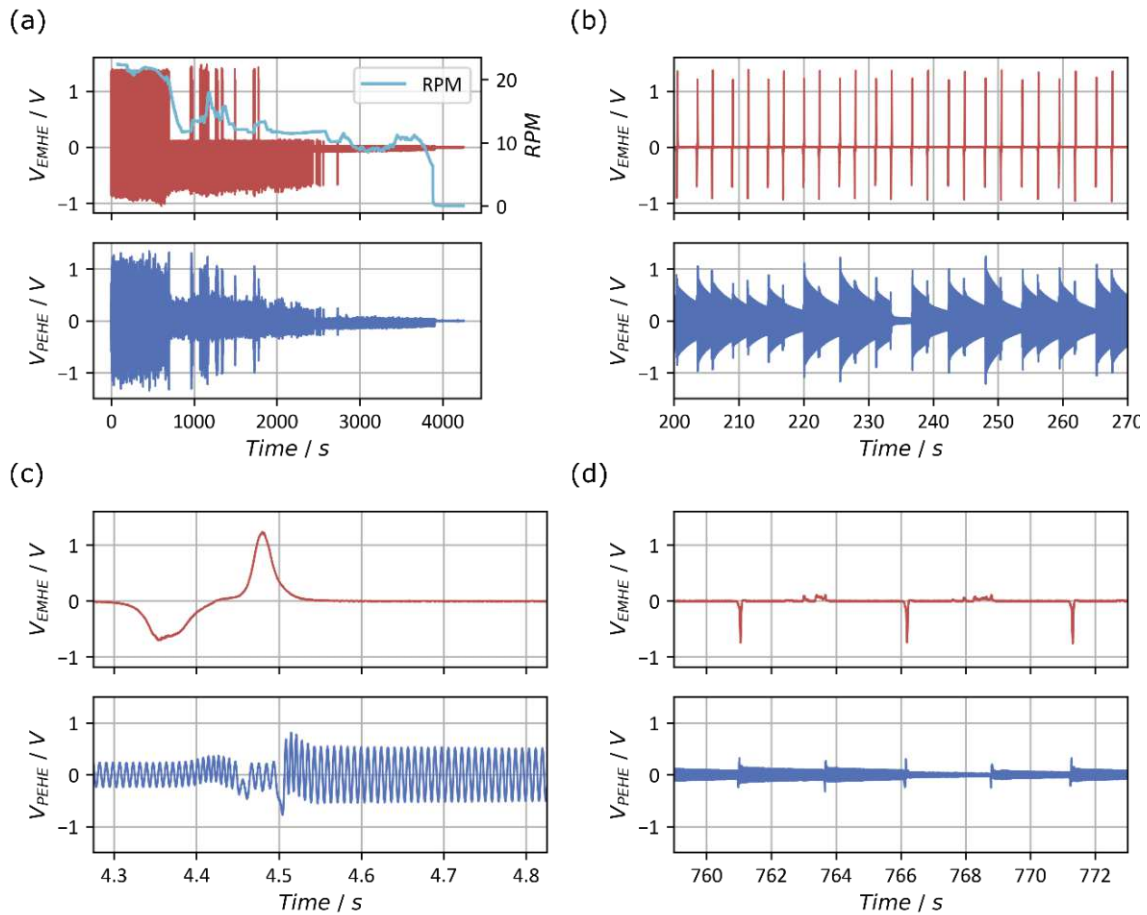


Figure 78: Measurement data of the EMHE and the PEHE from the HEH prototype for various time durations. (a) Wind turbine going from full operation into stop, (b) a zoomed time duration during full operation, (c) a single double peak (0.5 rounds) and (d) three consecutive double peaks (1.5 rounds).

In Figure 78 (b) it is already visible that the excitation of the PEHE is not always equally strong and three different cases can be identified.

Full excitation

Figure 79 (a) shows two excitation events under optimal conditions, the PEHE always gets excited to approximately 1 V, after which the output voltage is exponentially decaying until the next fall of the PM occurs.

Continuous decay

Figure 79 (b) the first excitation is equally strong as in the previous case, but during the second excitation the cantilever does not change its amplitude, except a short but small peak and it decays with the same amplitude as before. The corresponding double peak from the EMHE shows an irregular pattern at zero crossing. This indicates that the attractive force of the TM catches the PM for a moment and pulls it back, just to release it shortly after.

De-excitation

Similar to the previous case in Figure 79 (c) the first excitation starts with a full amplitude but when the second plucking event happens, the cantilever's excitation is nearly stopped. Again, the double peak of the EMHE shows an irregularity at the zero crossing.

The reasons for the latter two cases are a combination of several factors like position of the cantilever as well as the speed and magnetic field strength of the PM and TM, respectively. The exact reasons resulting in the behavior are not fully understood and need more investigations in the future. However, the case of de-excitation only happened in 9% and the case of continuous decay in 21% of excitation events. Furthermore, by optimizing the weight and speed of the PM it most probably will be possible to prevent both cases.

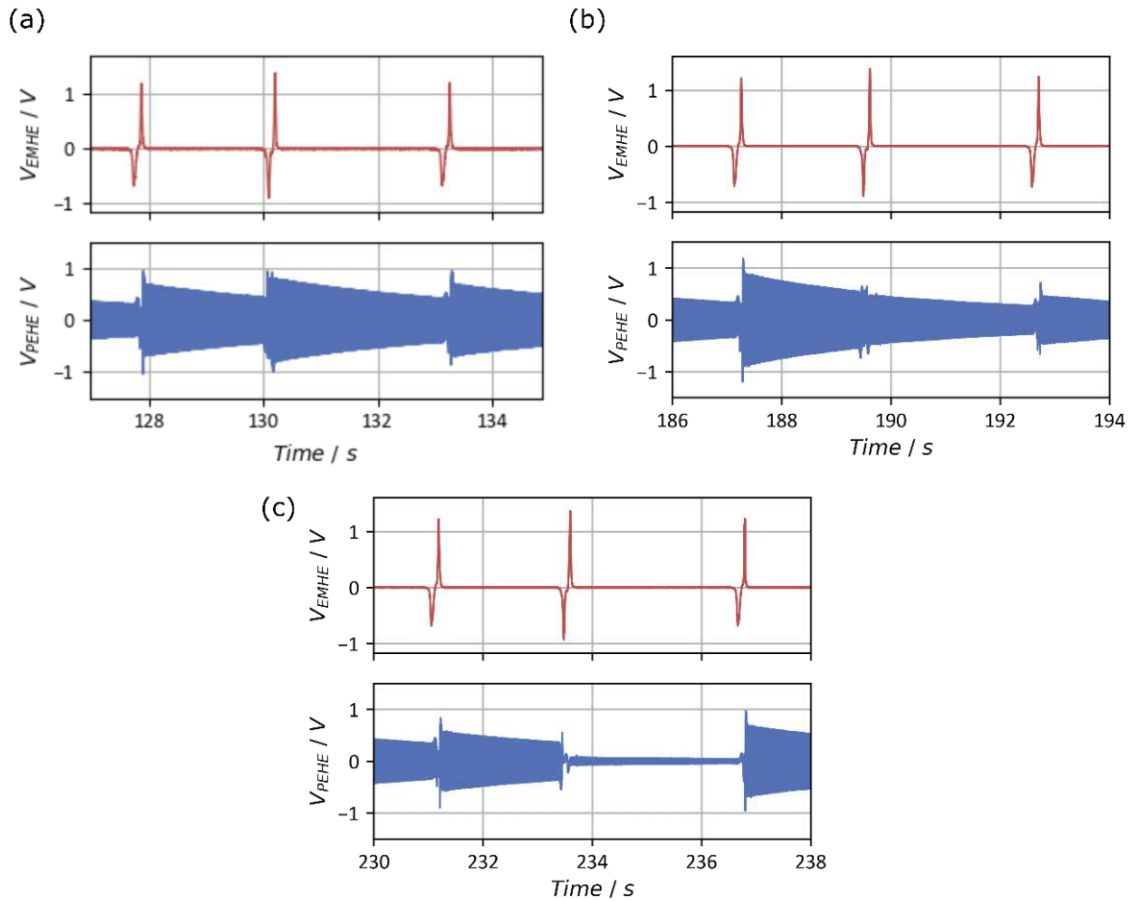


Figure 79: Output voltages of the EMHE and the PEHE from the HEH prototype for three different cases. (a) Normal conditions, where the PEHE gets completely excited at each fall of the PM. (b) The PEHE does not get excited at the second fall of the PM. (c) The PEHE gets de-excited and comes nearly to still stand at the second fall of the PM.

Under full operation it was possible to harvest $200 - 600 \mu W$ with the EMHE and $1.2 - 1.5 \mu W$ with the PEHE. Those numbers do not seem very high. However, the proof of principle was successfully accomplished. As the possibilities to increase the power output of the PEHE were limited, an electromagnetic-only energy harvester was scaled up to increase the amount of generated energy and tested again in the same wind turbine, which is discussed in the next section.

5.5.2. Optimized Electromagnetic Harvester

The optimized electromagnetic energy harvester presented in section 5.4.2 was installed in a wind turbine to test this design under real world conditions, as illustrated in Figure 80 (a) and (b). Together with this energy harvesting module another prototype was installed including a bigger PM of $40 \times 40 \times 20 \text{ mm}^3$. Unfortunately, this version failed and no proper measurements could be taken, as is visible in Figure 81 (a) and (b). The prototype was operated for two days and an exemplary

duration of one hour of data is presented in the following including a start-up and an emergency stop.

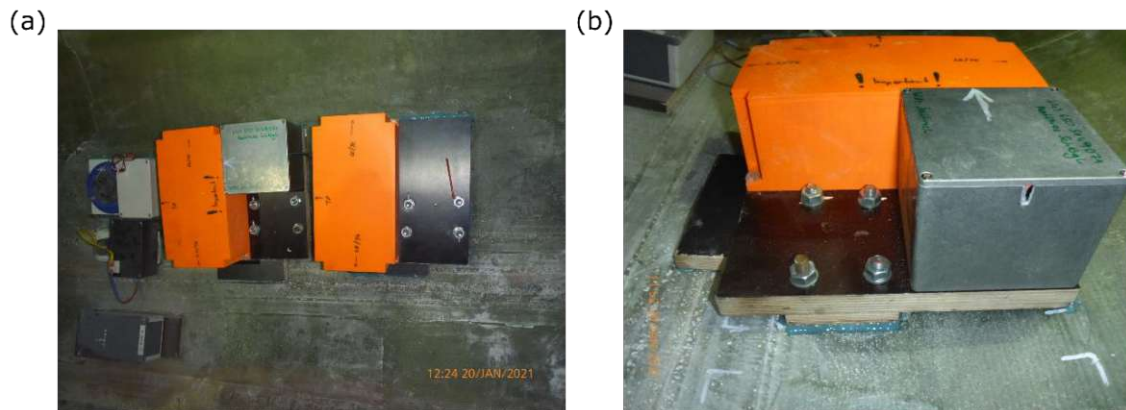


Figure 80: Prototype of the optimized electromagnetic harvester installed in the wind turbine.

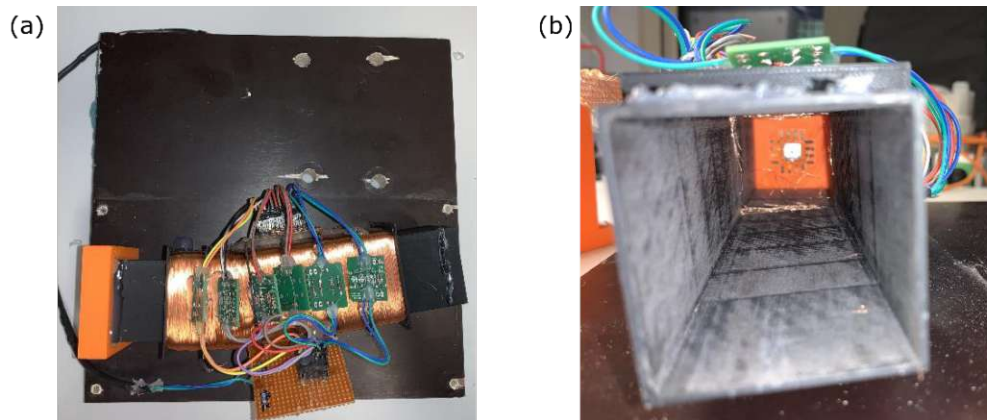


Figure 81: Photographs of another prototype with a bigger permanent magnet with a dimension of $40 \times 40 \times 20 \text{ mm}^3$, which unfortunately failed during transportation or installation.

Results

Figure 82 (a-d) show the output voltage of the EH in red and the acceleration along the blade length measured by an accelerometer installed next to the EH in green. Figure 82 (a) shows a representative time frame of one hour, where a startup followed by an emergency stop (for testing purposes) and another startup occurred. Figure 82 (b) shows the start-up of the wind turbine. The acceleration shows that the turbine rotations increase over a time period of three minutes. In this time the EH responds with increasing amplitude peaks until it reaches full operation with a peak height of 15 V . The reduced peak heights during the start-up phase result from reduced speed of the PM while falling through the guiding tube. The reason for this lies in the increased time, which the guiding tube needs to turn from horizontal to vertical.

The emergency stop shown in Figure 82 (c) shows a very fast stopping of the turbine within 1.5 rotations with an increased acceleration amplitude peak and the EH behaves accordingly, proving that even during those non-standard conditions the EH works as expected. Figure 82 (d) shows one rotation of the rotor blade with two double peaks. While the peak shape is similar to the one measured in the lab, the peak duration 2.5 times as long and the peak voltage is a little bit less than

half of the measurements performed in the lab. The reason for this will be discussed in the next section.

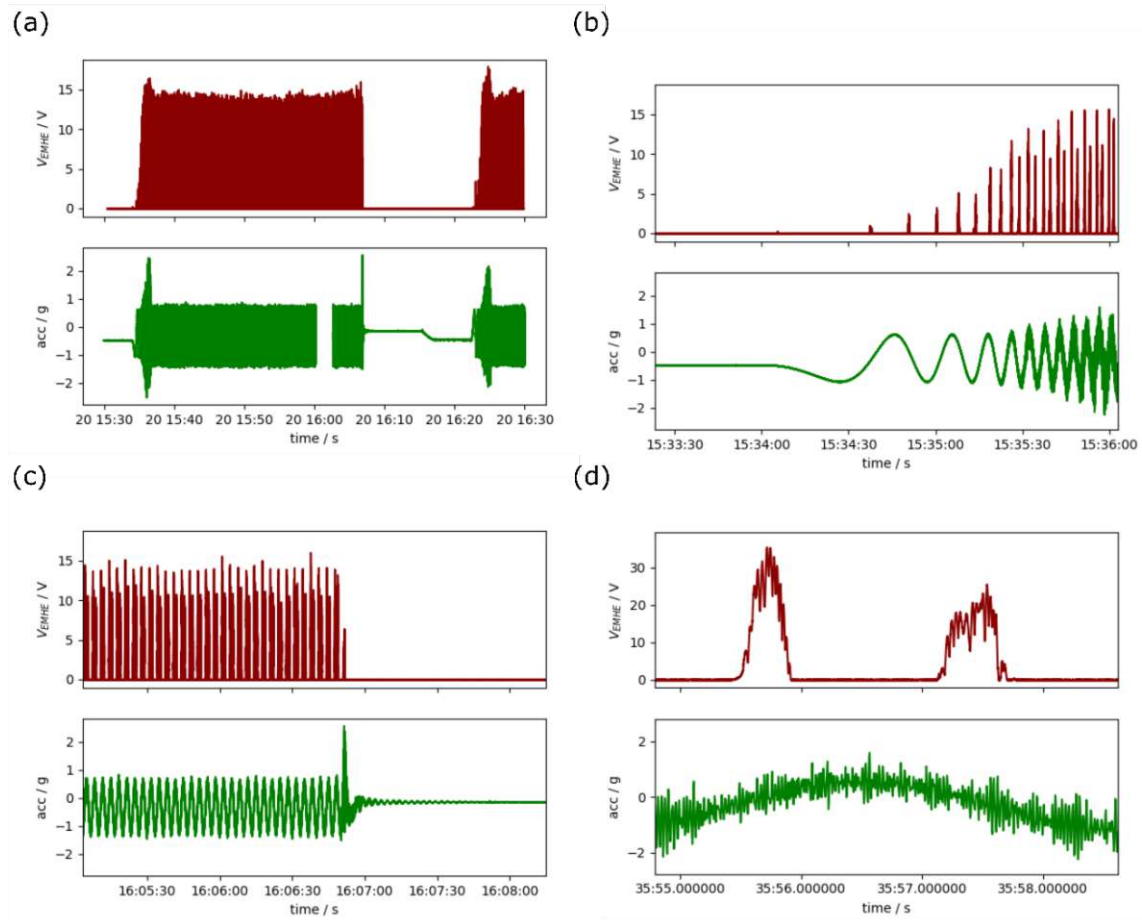


Figure 82: (a) Exemplary measurement data from the prototype of the optimized electromagnetic harvester for a time duration of one hour, including a start-up and an emergency stop. (b) and (c) shorter time frames of the start-up and the emergency stop. (d) detailed view of two generated voltage peaks, corresponding with one rotation of the rotor blade.

Comparison lab versus field-measurements

The electromagnetic energy harvester could generate on average 6 mW at a peak voltage of 15 V during operation in the wind turbine, whereas in the lab 25 mW were generated with a peak voltage of about 40 V for a rotational frequency of 20 rpm . The reason for this difference is twofold. First the rotational frequency of the test turbine was 16 rpm – a bit lower than the assumed 20 rpm . Second, the speed of the PM is reduced, due to frictional forces, generated by centrifugal forces in the rotor blade, and a straight down movement of the PM through the tube under lab conditions. Figure 83 shows the movement of the PM and the tube in the lab compared to the movement in the rotor blade. While in the lab the PM falls in a direct line from top to bottom, accelerated constantly with 1 g without friction, in the rotor blade the tube gets slowly turned from a horizontal into a vertical position. This creates additional friction for the PM while sliding, resulting in a reduced speed and hence, a reduced induced voltage. The generated energy goes with the square of the induced voltage, which explains the large difference in both values.

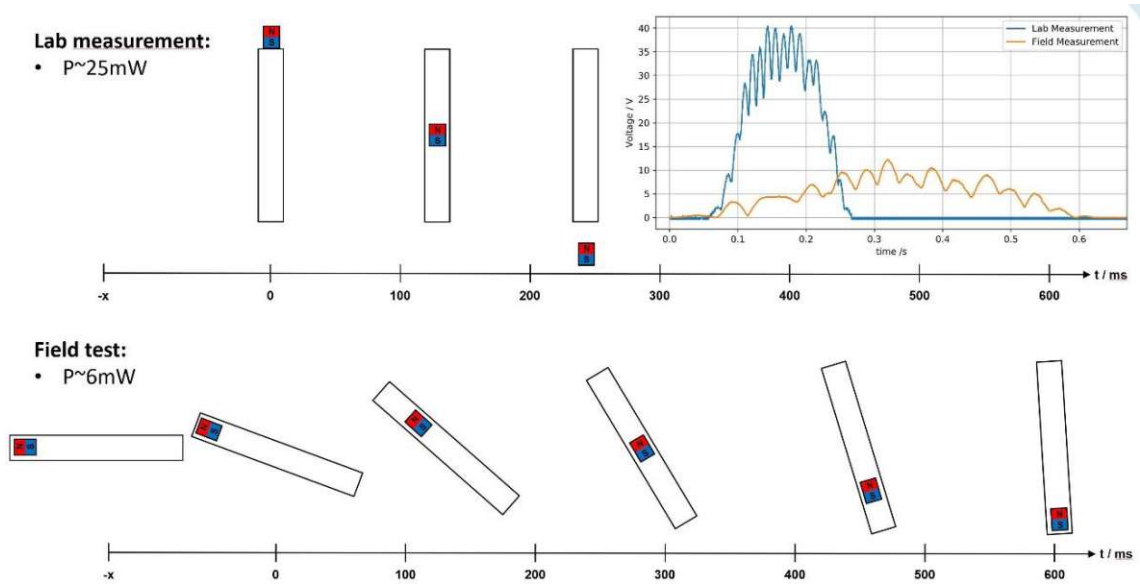


Figure 83: Comparison of the movement of the guiding tube and the PM between lab- and field-measurements.

5.6 Conclusions

Although the design of the presented hybrid energy harvester was successfully realized and tested in a real-world turbine, the energy output of the piezoelectric device was three orders of magnitude lower than its electromagnetic counterpart. Even if several PEHEs are combined or with other current state-of-the-art piezoelectric materials like AlScN, PZT or KNN providing 10-50 times increase in the FOM for energy harvesting, it cannot compete with the electromagnetic device. However, piezoelectric materials are an intensively researched field and new material combinations with increased piezoelectric coefficients are reported every few years. Therefore, it is possible that those materials could make a similar quantum leap providing another 10-to-100-fold increase. This would make the PEHE as good or even better than the EMHE for this design.

The second optimized prototype of an electromagnetic-only energy harvester was successfully tested in a wind turbine and provided 6 mW of continuous output power which is enough to power a wireless sensor node. The possibilities of optimizing and scaling up the design even further allows a versatile energy harvesting device for use in wind turbine rotor blades even for higher power demands.

6. Resonant MEMS Strain Sensors

Parts of this chapter are published in [154], [267].

This chapter presents a newly developed resonant MEMS strain sensor based on a double clamped beam structure, also called microbridge. First, some theoretical considerations will be presented on the operation principle and an analytical model taken from [268], which makes it possible to partially predict the behavior of the sensor. Next, a detailed description of the design and fabrication process is given, followed by the characterization of several sensor devices with varying properties. In detail, the responsivity or gauge factor – one of the main properties of a strain sensor – is analyzed. At the end of the chapter, a stress-tailoring process is introduced and the influence on the MEMS sensor performance and output characteristics is studied.

6.1 Basic Sensor Design Considerations

The MEMS sensor device in this work is based on a micromachined beam structure clamped on both ends, also called microbridge. It is operated as a resonator and is electrically excited with an integrated piezoelectric aluminum nitride thin film, shown in Figure 15 (a-b). Besides device- and ambient-related parameters, the resonance frequency spectrum of microbridge resonators depends on the intrinsic stress σ of the thin films and on the externally applied strain ε . Positive values of ε are associated with a longitudinal expansion and an increased tensile stress of the structure which results in an increase in resonance frequencies for all specific modes. In contrast, negative values of ε lead to compression of the microbridge which results in a decrease in resonance frequencies. The latter statement only holds true, as long as the microbridge remains in a flat state. If the compressive stress exceeds a critical value, the microbridge starts to buckle. In this state, the resonance behavior is different resulting in a distortion of the mode shapes, which will be discussed in the “Experimental Details” section.

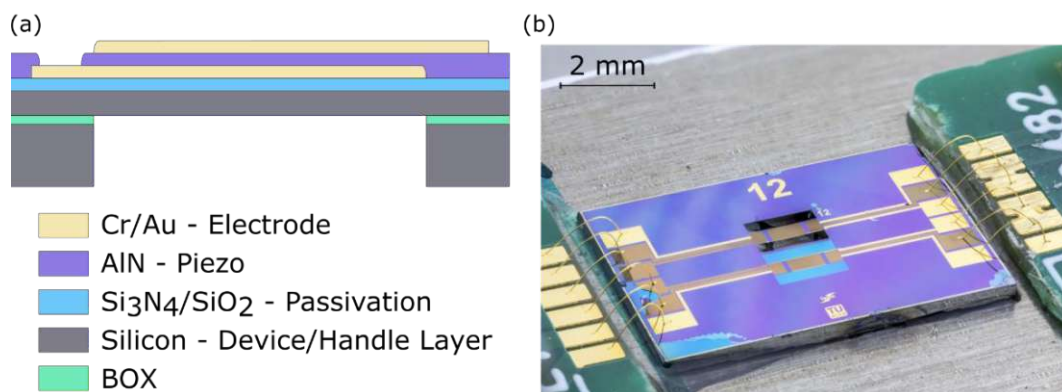


Figure 84: (a) Schematic cross-section of a microbridge-type resonant strain gauge sensor. (b) Optical micrograph of a glued and wire-bonded MEMS strain gauge sensor.

6.2 Analytical Model

Bouwstra *et al.* analyzed the frequency behavior of strained microbridges and developed an analytic expression to predict the frequency changes [268]. In the study, the authors started from the Euler-Bernoulli beam equations and the standard equations for unstrained flexural modes (5.13). Next, they incorporated the dependence on an externally applied force F and hence, the strain ε to cover buckled and non-buckled states of the microbridge. The strain value which separates those two states is called buckling point at the strain value ε_C and will be discussed in detail in the Results section.

As we are interested in the frequency as a function of strain $f_n(\varepsilon)$ for our devices, we start directly with this dependency and omit the force dependency.

$$f_n(0) = \frac{k_n^2}{2\pi} \sqrt{\frac{\hat{E}I}{\rho A l^4}} \quad \forall \varepsilon \geq \varepsilon_C \quad (6.1)$$

$$f_n(\varepsilon) = f_n(0) \sqrt{1 + \gamma_n \frac{\varepsilon E A l^2}{12 \hat{E} I}} \quad \forall \varepsilon \geq \varepsilon_C \quad (6.2)$$

$$\hat{E} = \frac{E}{1 - \nu^2} \quad (6.3)$$

with the moment of inertia for a beam with a rectangular cross section $I = A \cdot h^2 \cdot 12^{-1}$, E being the Young's modulus, ν being the Poisson ratio and \hat{E} being the modified Young's modulus to account for the suppression of the in-plane dilation accompanying axial strain. $f_n(0)$ is the resonance frequency of mode n at zero strain. The coefficient γ_n accounts for the contribution of the applied axial force to the modal stiffness, relative to the contribution of the flexural rigidity and k_n represents the eigenvalues of the frequency equation for a double clamped Euler-Bernoulli beam [268]. This equation is only valid for values of ε , where the expression below the square root is ≥ 0 . The value of ε where the square root is exactly 0 is also called buckling point or critical strain value. At this point the microbridge changes its state from being buckled to being flat or *vice versa*, which will be discussed in more detail below when characterizing the fabricated microbridges. For $\varepsilon < \varepsilon_C$, Bouwstra *et al.* found that the frequency of the first and second flexural mode behave according to equations (6.4) and (6.5), respectively.

$$f_n(\varepsilon) = f_n(0) \sqrt{-\varepsilon/\varepsilon_C - 1} \quad \forall \varepsilon < \varepsilon_C \quad (6.4)$$

$$f_n(\varepsilon) = 1.98 \cdot f_n(0) \quad \forall \varepsilon < \varepsilon_C \quad (6.5)$$

$$\text{with } \varepsilon_C = \frac{4\pi^2 \hat{E} I}{E A l^2}. \quad (6.6)$$

Furthermore, center deflections of the unloaded beam z and the loaded beam y are introduced in [268] which have an influence on the frequency in the range of $-1.3 < \varepsilon/\varepsilon_C < 1$ as follows:

$$f_n(\varepsilon) = f_n(0) \sqrt{1 + \gamma_n \frac{\varepsilon E A l^2}{12 \hat{E} I} + 0.12 \frac{E A y^2}{\hat{E} I}} \quad (6.7)$$

$$\text{with } y = \frac{z}{1 + \varepsilon/\varepsilon_C}. \quad (6.8)$$

The values for the material properties used in the model were taken from literature and the geometric dimensions have been determined with scanning electron microscopy for the samples under test. Important parameters can be found in Table 20 and Table 21. The averaged values for the Youngs modulus E , the Poisson ratio ν and the density ρ have been weighted by their thickness according to:

$$X = \frac{h_{Si}}{h} X_{Si} + \frac{h_{AlN}}{h} X_{AlN} + \frac{h_{Au}}{h} X_{Au} + \frac{h_{Cr}}{h} X_{Cr} \quad (6.9)$$

With X being a placeholder for E , ν or ρ , subscripts indicate the material, $h_{material}$ is the thickness of the according material and h is the total thickness of the microbridge.

When combining equations (6.7), (6.8) and (6.9), the shift in resonance frequency at a given mode is plotted as a function of applied strain and discussed in Figure 88 together with measurement data of the fabricated devices.

Parameter	Description	Value	Ref.
E	Youngs modulus (YM)	182 GPa	-
E_{Si}	YM of silicon	169 GPa	[269]
E_{AlN}	YM of AlN	252 GPa	[192]
E_{Au}	YM of gold	69 GPa	[270]
E_{Cr}	YM of chromium	210 GPa	[271]
ν	Poisson ratio (PR)	0.28	-
ν_{Si}	PR of silicon	0.27	[272]
ν_{AlN}	PR of AlN	0.24	[192]
ν_{Au}	PR of gold	0.42	[273]
ν_{Cr}	PR of chromium	0.21	[274]
\hat{E}	Modified YM to account for the suppression of the in-plane dilation accompanying axial strain.	197 GPa	[268]
ρ	Overall density	5993 kg m ⁻³	-
ρ_{Si}	Density of silicon	2300 kg m ⁻³	[275]
ρ_{AlN}	Density of AlN	3100 kg m ⁻³	[276]
ρ_{Au}	Density of gold	19000 kg m ⁻³	[275]
ρ_{Cr}	Density of chromium	7190 kg m ⁻³	-
h	Microbridge thickness	1.57 μ m	-
l	Microbridge length	1500 μ m	-
w	Microbridge width	100 μ m	-
z	Center deflection of the unloaded beam	1.68/21.83 μ m	-

Table 20: List of all parameters used in the model including description, units and values with references when taken from literature.

n	k_n	γ_n	f_n/f_0
1	4.730	1.000	0.295
2	7.853	2.757	0.145
>3	$(n + \frac{1}{2})\pi$	$(\frac{k_n}{4.73})^2$	$12(\frac{k_n - 2}{k_n^3})$

Table 21: Eigenvalues of the frequency equations k_n , the coefficients γ_n and the frequency ratios of higher flexural modes related to the first flexural mode at zero strain condition according to [268].

6.3 Design and Fabrication Aspects

The fabrication process is based on an SOI (silicon-on-insulator) wafer with either 680 nm or 2 μm device layer and a 400 μm handle layer, separated by a 0.5 μm thin buried oxide (BOX). The top surface of the wafer is passivated by a stress-compensated combination of 0.25 μm thermally oxidized SiO₂ followed by 0.08 μm of stoichiometric Si₃N₄ synthesized by low-pressure chemical vapor deposition. The bottom electrode consists of a 0.18 μm thick gold electrode layer in combination with a 0.02 μm thick chromium thin film as adhesion promoter underneath, deposited by e-beam evaporation. The piezoelectrically active material is made of 0.7 μm aluminum nitride sputter deposited by a “Von Ardenne” LS 730S at 800 W of plasma power and 0.2 Pa chamber pressure under pure nitrogen atmosphere. The sputter target was a 6” pure aluminum target and the substrate-target distance was 65 mm. Top and bottom electrodes are designed such that they cover the same AlN related area on the microbridge, thus forming a typical capacitive structure. Both electrodes were patterned with a standard lift-off process. The piezoelectric aluminum nitride layer was also patterned by a photoresist-based lift-off process. Deep reactive ion etching was applied to pattern both the device and handle layer followed by a hydrofluoric acid dip to remove the BOX. The wafer was diced with a wafer saw and finally cleaned in acetone and isopropanol baths. To investigate the influence of the geometrical dimensions the length, width and thickness of the microbridges was varied. A schematic of the cross-section of the microbridge can be seen in Figure 15 (a). Exact dimensions can be taken from Table 22.

Nr	Microbridge Dimensions	Process
S1	1000 x 100 x 3 μm ³	Std.
S2	1000 x 200 x 3 μm ³	Std.
S3	1000 x 400 x 3 μm ³	Std.
S4	1500 x 100 x 3 μm ³	Std.
S5	1500 x 100 x 1.5 μm ³	Std.
S6	1500 x 100 x 1.5 μm ³	Modified

Table 22: Microbridge dimension.

6.3.1. Buckling

Due to the intrinsic compressive stress which sputtered aluminum nitride thin films at a thickness of 700 nm exhibit when deposited under the mentioned conditions with the available sputter equipment, the microbridges are buckled after the manufacturing process. The deflection shape

due to buckling has been studied with a Fries Research Technology MicroProf MPR 1261 white light interferometer and is shown in Figure 85 (a).

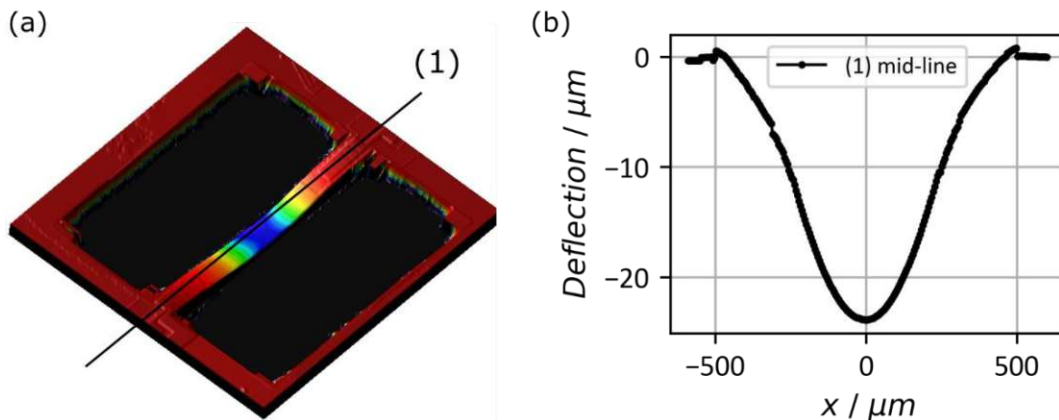


Figure 85: 3-dimensional measurement with a white light interferometer of a buckled microbridge after fabrication in (a) and a deflection profile along the beam length in (b).

Figure 85 (b) shows a deflection profile along the microbridges length and the maximum deflection can be measured to $D = 23.8 \mu\text{m}$. The buckling could also be visualized with a Hitachi SU8030 scanning electron microscope (SEM) with an acceleration voltage of 5 kV and an emission current of 20 mA. Figure 86 (a) shows the microbridge after the manufacturing process in the buckled state, whereas in Figure 86 (b) the microbridge has been stretched to reach the non-buckled state, by pre-straining it when the sensor is glued onto the measurement setup, which is explained in more detail in section 3.7.

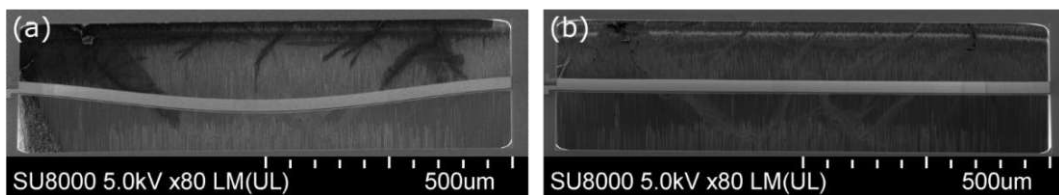


Figure 86: SEM images of the microbridge in a buckled state in (a) and in a non-buckled state in (b) when fixing the device with tensile pre-loading.

6.3.2. Electrode Design

When exciting the microbridge in a specific mode shape, positive and negative charges are generated at different locations along the microbridge, depending on the corresponding sign of the emerging strain field. If those generated charges are collected by a full area electrode on top and bottom of the piezo-active material, the positive and negative charges cancel each other out and only the net charge difference can be measured. Therefore, designing an electrode configuration which matches the occurring distribution of charges, can increase the measurement signal significantly.

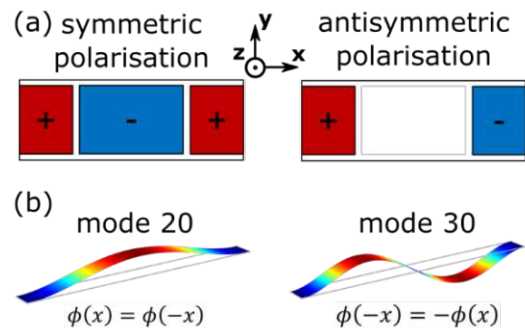


Figure 87: (a) Electrode configurations for a symmetric and antisymmetric polarization of the applied electrical field and (b) their corresponding mode shapes.

The same holds true when the microbridge is excited via an electric field applied at the electrodes. An easy and intuitive way to name modes follows the convention of Leissa's nomenclature [277]. The vibrational modes are called XY-modes whereas X equals the number of nodal-lines parallel to the fixed anchor and Y equals the number of nodal-lines perpendicular to the anchor. Depending on the electrode design, depicted in Figure 9 (a-b) certain mode shapes $\phi(x)$ are excited more efficiently than others. For symmetrically polarized electrodes, the excitation of even modes such as 20 and 40 is preferred, for which $\phi(x) = \phi(-x)$. They feature an even number of nodal lines along the length of the microbridge. For antisymmetrically polarized electrodes, the odd modes like 30 and 50 with $\phi(-x) = -\phi(x)$ are excited more efficiently. Those modes feature an odd number of nodal lines along the length.

6.4 LDV Measurements for MEMS Sensor Evaluation

In this chapter the characteristic behavior of MEMS microbridges is analyzed by performing optical measurements with an LDV. Starting from a simple frequency response of the displacement and its resonances, followed by a simultaneous variation of the externally applied strain, the frequency behavior as a function of strain is studied. Afterwards various effects like non-linearities, which arise when the microbridge is excited too strong, or the influence of the adhesive on the resonance spectrum are analyzed.

6.4.1. Resonance Spectrum

The strain sensors are characterized by attaining the frequency responses of the displacement and the according mode shapes for a broad range of applied strain values with the LDV and the strain measurement setup, introduced in sections 3.6 and 3.7, respectively. An exemplary frequency response and the according mode shapes are shown in Figure 88 (a). Figure 88 (b) shows the mechanical displacements d_a averaged over the resonator surface for the resonance peak of the 20-mode. As expected, not only the resonance frequency depends on the applied strain, but also the peak height. Next, the resonance frequency values are plotted as a function of the applied strain ε , as yielded in Figure 88 (c) which also includes illustrations of selected mode shapes.

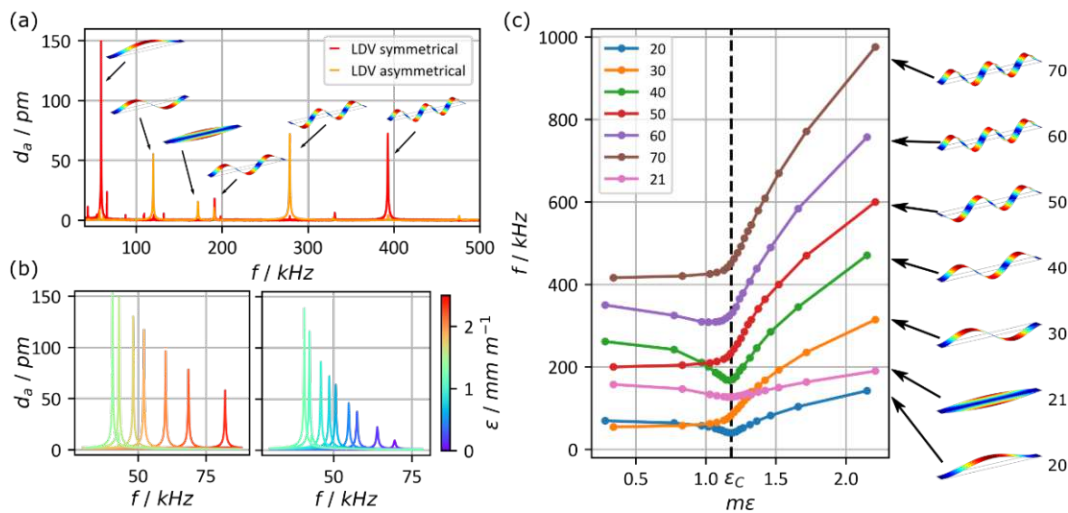


Figure 88: (a) Resonance response spectra of a resonantly operated microbridge-type strain sensor excited in two different electrode configurations and measured optically with the LDV. (b) The vibrational displacement around the resonance frequency for the 20-mode for different strain values both in the buckling and the non-buckling regime. (c) Selected resonance frequencies measured with the LDV as a function of the applied strain and corresponding mode shapes.

Bouwstra *et al.* [268] studied the resonance frequency spectra of strained micromachined clamped-clamped beam structures. They started with both flat and initially buckled microbridges and investigated the behavior of the first and second flexural as well as of the first torsional mode, respectively. Starting from the general Euler-Bernoulli beam theory they developed an expression to estimate the resonance frequencies in the buckling and the non-buckling regime. They found out, that while the even 20-modes resonance frequency changes in the buckling regime, the odd 30-mode is not affected by the buckling induced strain. They explained this with the orthogonality between the symmetric deflection shape of the buckling and the anti-symmetric vibration shape.

Another type of modes are torsional modes which contain one or more nodal lines along the length of the microbridge. Torsional modes can also be classified into even and uneven modes, with the

same behavior as their non-torsional counterpart. They are less suitable for strain sensing as shown below but are discussed for the sake of completeness.

6.4.2. Displacement

As already noticeable in Figure 88 (b) the height of the resonance peaks changes depending on the applied strain. Figure 89 (a) shows the peak maxima $d_{a,max}$ of the frequency spectra averaged over the surface for the modes 20 and 30. The x-axes in the following plots have been shifted such that the critical strain ε_c is at $\varepsilon = 0$. Two different regimes were defined, depending on whether the microbridge is buckled or not. In the latter regime both modes show a similar decaying amplitude with increased strain for both modes, with the usual expected mode shapes, compare Figure 89 (b) and (e). In the buckled regime, however, the mode shapes measured by the LDV are distorted (Figure 89 (c)) and can only be interpreted when the static displacement due to buckling is superposed onto the measurement, shown in Figure 89 (d) and (g). This distorted mode shape also makes it obvious why the averaged amplitude over the whole measured surface gives a better understanding of the general behavior of the displacement compared to a single point measurement. While the amplitude of the resonance peak for the 20-mode decreases rapidly with increasing compressive strain, the 30-mode is less affected, compare Figure 89 (f).

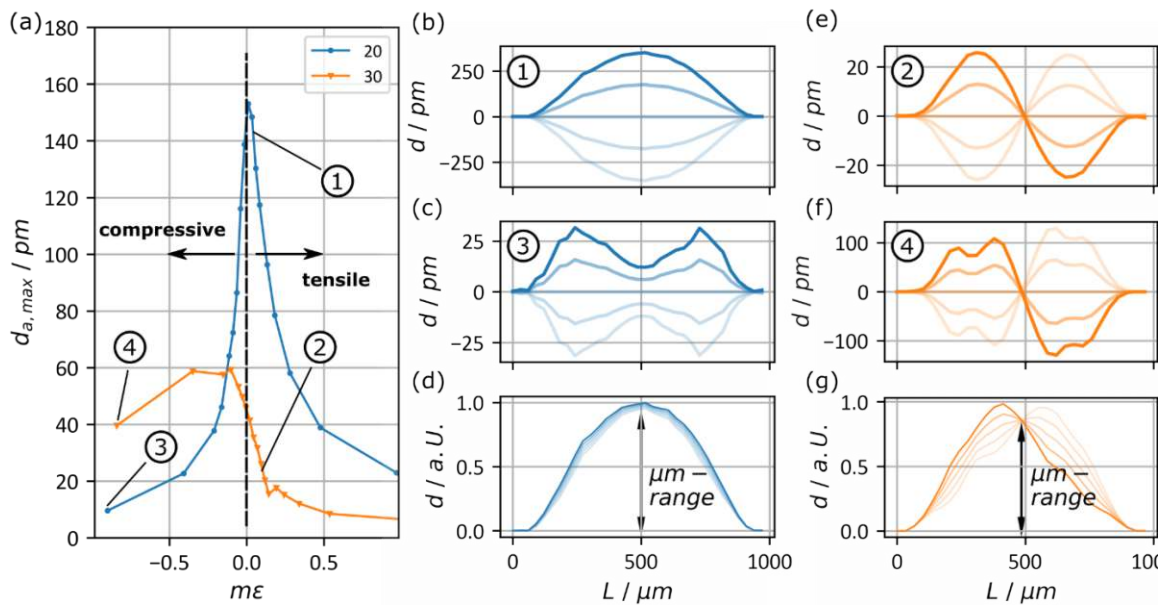


Figure 89: (a) Averaged mechanical displacement d_a over applied strain for the 20 and 30-mode, (b) mode shape of the 20-mode at the buckling point, (c) in the compressively stressed regime at $\varepsilon = -0.9 \text{ mm m}^{-1}$ but below the critical stress value causing buckling and (d) in the buckled regime, meaning above the critical stress value causing buckling of the microbridge. (e-g) Mode shapes of the 30-mode under the same circumstances as in (b-d).

This behavior has already been observed in experimental studies in several publications [278]–[280]. Nayfeh *et al.* [281] developed an analytical expression to estimate the form of the mode shapes depending on the buckled deflection. They showed that even mode shapes are distorted, while odd mode shapes are not affected by the buckling. However, our measurements show that if the strain exceeds a certain value – in this case $-0.5 \text{ m}\varepsilon$ – then the odd mode shapes also get distorted which explains the decrease in the amplitude for very high negative strain values (see point 4 in Figure 89).

Important to note is that the initial deflection due to buckling reaches several micrometers, while vibrational displacements are in the pico-meter range. Therefore, in Figure 89 (d) the buckling deflection has been scaled down to give a qualitative view on the vibrational behavior in the buckling regime.

6.4.3. Non-Linear Effects

The displacement in general is dependent on the amplitude of the excitation voltage [282]. Higher amplitudes lead to higher displacement until a certain value, where the normal linear resonance behavior is changed into a non-linear behavior [283], which can be described by a Duffing resonator [284]–[286]. This can be seen in Figure 90 (a-b), showing frequency responses of the modes 30 and 31 of a sensor device with dimensions of $1000 \times 100 \times 3 \mu\text{m}^3$. For this measurement a frequency up-sweep immediately followed by a down-sweep was performed on the LDV, for four different excitation voltages between 0.01 V to 1.0 V. The resonance measured with an excitation voltage of 0.1 V showed the highest displacement, while showing no non-linear distortions. As the focus in this work lies in the frequency behavior of the sensor device as a function of strain, a linear resonance behavior was preferred. Therefore, an excitation voltage amplitude of 0.1 V was applied in all measurements with either optical or electrical readout, thus avoiding non-linear effects.

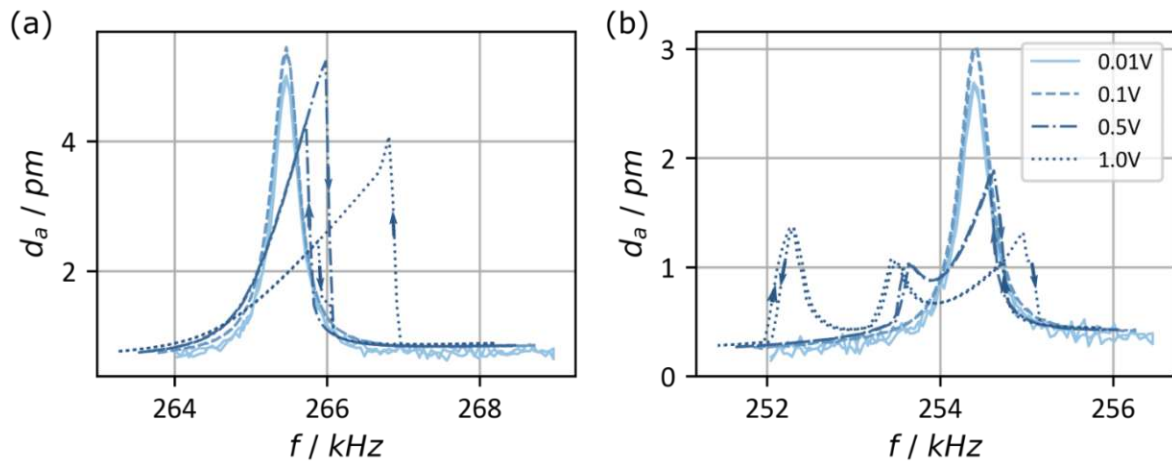


Figure 90: Exemplary frequency spectra of the modes 30 in (a) and 31 in (b) of a device with dimensions of $1000 \times 100 \times 3 \mu\text{m}^3$ during a frequency up-sweep, immediately followed by a down-sweep for four different excitation voltages, showing non-linear effects.

6.4.4. Influence of the Adhesive

A common method to mount metallic foil-type strain gauges to the device under test is by inserting an adhesive between the sensor and the underlying surface, respectively. Because of the strong difference in elasticity of the adhesive in comparison to the sensor device materials as well as the specimen a creeping effect can occur which changes the transferred strain characteristics over time. Figure 91 (a) shows the resonance frequency of sensor device S1 for five different applied external strain values. The given strain value is then kept constant for 15 min and afterwards the strain is reverted back to the initial value and again kept constant for 15 min. After an initial frequency jump of Δf_ε the resonance frequency drifts slowly back by Δf_c due to creeping resulting from the viscoelastic nature of the polymer-based adhesive. This behavior can be described by Burger’s mechanical model, which usually describes the time dependent strain behavior of a material under

stress [287], [288]. It consists of a static component ε_s , a time dependent linear component $\varepsilon_l(t)$ and a time dependent, exponentially decaying component $\varepsilon_e(t)$ shown in equation (6.10).

$$\varepsilon = \varepsilon_s + \varepsilon_l(t) + \varepsilon_e(t) \quad (6.10)$$

Figure 91 (b) shows the frequency shift Δf_C due to creeping without the frequency shift Δf_ε originating from the externally applied strain. If we compare the graph to the model in equation (4) we have to consider that creeping of the adhesive is relaxing the strain transferred to the specimen, thus reducing the nominal mechanical load. Comparable to the adhesive the measured frequency shift can be described by three components: a static, a time dependent linear and a time dependent exponential component, as given in equation (6.11).

$$\Delta f_C = \Delta f_{C,s} + \Delta f_{C,l}(t) + \Delta f_{C,e}(t) = \Delta f_{C,s} + lt + d + e_1 \cdot \exp(e_2 t) \quad (6.11)$$

The value of $\Delta f_{C,s}$ cannot be evaluated as it is not possible to distinguish this latter quantity from Δf_ε generated by the externally applied strain. The inset in Figure 91 (b) shows a representation of the time dependent components for one curve and the model with fitted parameters l, d, e_1, e_2 , indicating that our adhesive is well represented by Burger's Model. This creeping behavior influences the frequency measurements and cannot be easily compensated as the strain and creep history of a polymer-based adhesive is included in its actual behavior. Nevertheless, if we compare Δf_C to Δf_ε and estimate the reduction in responsivity for the sensor device we obtain a value of 1 – 2% plus the reduction due to the static component of the creep $\Delta f_{C,s}$.

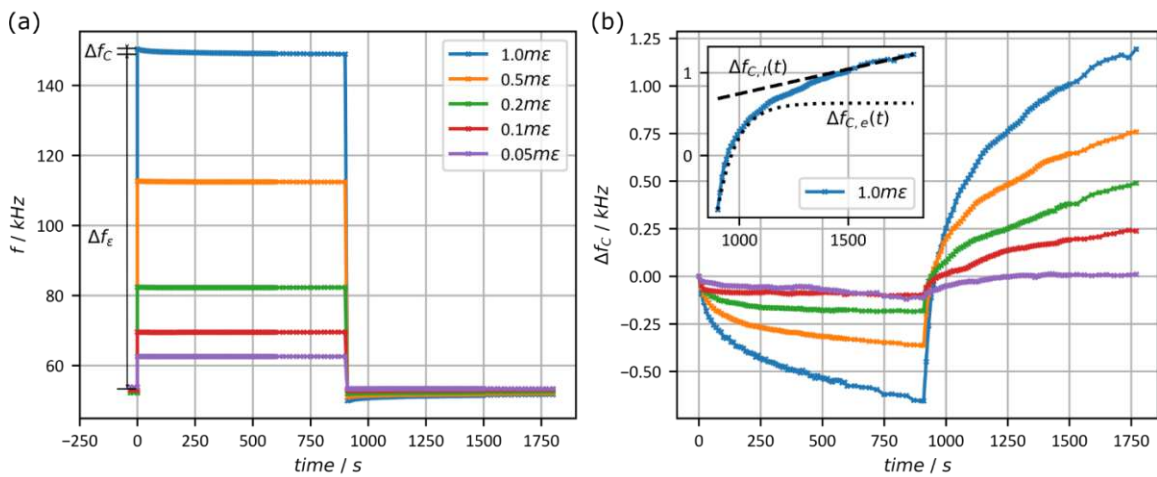


Figure 91: Resonance frequency of the first flexural mode over time for five different applied strain values. (b) Frequency shift of sensor device S1 over time at room temperature due to creeping arising from the high elasticity of the adhesive for five different applied strain values.

In order to achieve a better reproducibility in the frequency domain, we estimated the dwell time to stabilize $\Delta f_{C,e}(t)$ to about 600 s per 1 mε of applied strain before starting a mechanical load measurement.

Methods to reduce the influence of creeping range from decreasing the overall thickness of the sensor device by polishing the handle layer of the SOI wafer [289] to the substitution of the polymer based adhesive by an eutectic bonding process [290]. Both methods do not only reduce creeping, but also showed increased reliability due to a better match between the stiffness of the sensor material, the specimen and the adhesion layer, respectively.

6.5 Electrical Characterization

Besides the optical readout via an LDV, the piezoelectric sensor devices can also be read out electrically via a self-actuating and self-sensing approach. This is realized by an impedance analyzer, whereas the built-in function generator provides the excitation voltages with varying frequencies, through which strain is created in the piezoelectric layer and the resonator starts to oscillate. At the same time charges are generated in the piezo-active material, which are used together with the excitation voltage to calculate a conductance spectrum. This approach has the advantage that only a single piezoelectric layer can be used for both – actuation and sensing – and no other additional measurement instrumentation *e.g.*, LDV is necessary. A more detailed explanation about the self-actuating/self-sensing approach can be found in [291], [292].

Figure 92 (a) shows frequency responses of the displacement measured with the LDV and in comparison, the conductance spectra of the same device, with symmetrical and asymmetrical electrode configurations. Figure 92 (b) shows the resonance frequencies for the 20- and 30-mode as a function of strain. As expected, the resonance frequencies obtained by both measurement approaches fit very well together.

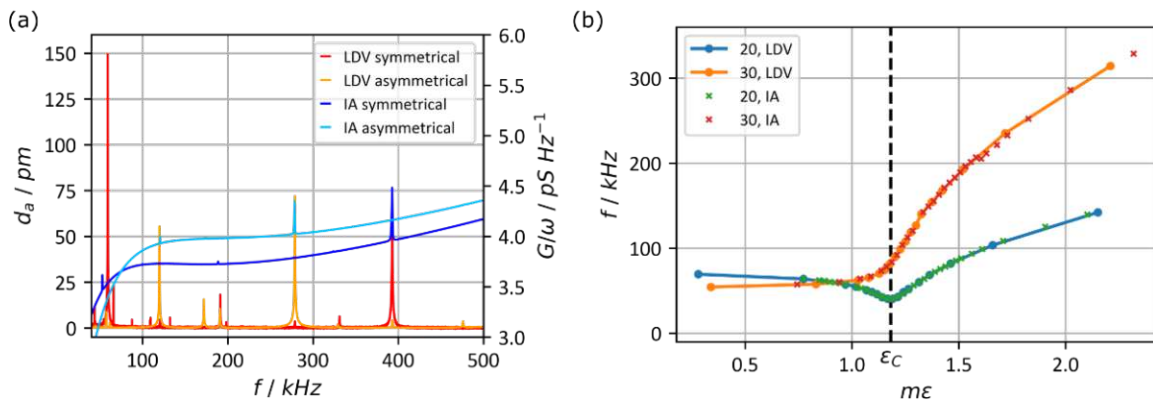


Figure 92: (a) Frequency response of a device with symmetrical and asymmetrical electrode configuration measured with the LDV (red and orange curves) and with the IA (dark blue and light blue). (b) Frequency of the resonance peaks as a function of strain for the modes 20 and 30 measured with both methods.

A more detailed comparison of those two measurement approaches is given in section 6.6.3, when discussing the influence of the width of the microbridge on the output signal height.

6.6 Design-dependent MEMS Sensor Performance

In this chapter the influence of the geometrical dimensions of the microbridge on the frequency behavior and the averaged displacement of the 20-mode is analyzed. The parameters length, thickness and width are varied and the frequency as a function of strain is measured for several exemplary sensor devices. When varying the device width, the modes 30, 21 and 31 are also studied to evaluate the influence on optical and electrical readout. Additionally, the model presented in section 6.2 is fitted to the data and deviations to the data are discussed.

6.6.1. Length

The frequency response of the 20-mode for the two devices S_1 and S_4 , with a length of $1000 \mu m$ (blue) and $1500 \mu m$ (ocher) are plotted in Figure 93 (a). The other geometrical parameters of the devices can be taken from Table 22. The fitted models $S_{1,Model}$ and $S_{4,Model}$ were also plotted in black and grey, respectively. In the non-buckling regime, the longer device shows lower frequency values in general, the slope of the frequency as a function of strain is lower than for the shorter device and the model fits the data very well. These results are in line with the general expectation of longer beams having lower resonance frequencies than those being shorter. Figure 93 (b) shows that the averaged displacement d_a for the longer beam is approximately 60% higher, which is a result of the longer microbridge, fitting well to the general expectation.

In the buckling regime the data shows the same tendencies with the shorter microbridge having higher resonance frequencies compared to the longer microbridge, which is in contrast to the results predicted by the model. The data also diverges quite strongly from the predicted model. While S_1 seemingly approaches the model for very low strain values, the divergence gets stronger for S_4 . Those differences will be discussed in more detail in section 6.8 with regards to the thin film stress.

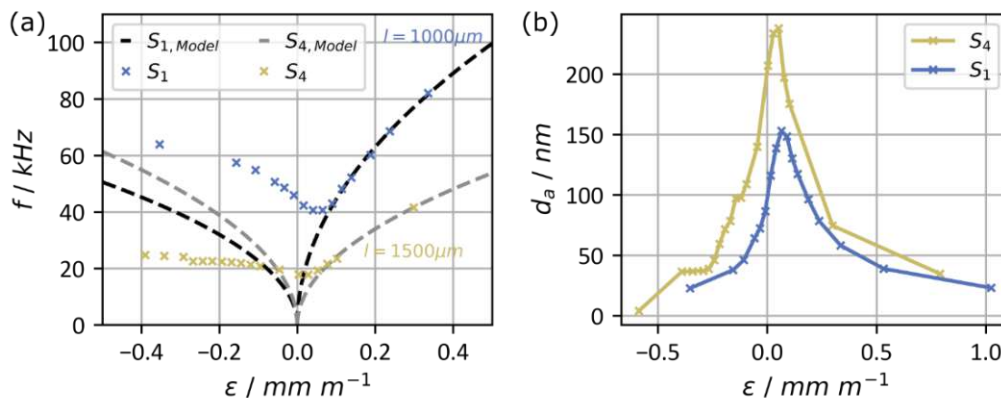


Figure 93: (a) Resonance frequency of the first flexural mode as a function of strain for the two devices S_1 and S_4 plus the theoretical predictions $S_{1,Model}$ and $S_{4,Model}$. (b) Displacement averaged over all scan points as a function of strain for the same samples as in (a). Lines in (b) serve as guide to the eye.

6.6.2. Thickness

The influence of the thickness on the resonance frequency as a function of strain is shown in Figure 94 (a) for the devices S_4 and S_5 with silicon thicknesses of $2000\ nm$ and $680\ nm$, respectively. The

other dimensional parameters can again be found in Table 22. Similar as in the previous section, the model is fitted to the data and plotted in black for S_4 and in grey for S_5 .

The model matches the measured data again very well in the non-buckling regime, with the thinner microbridge having slightly lower frequency values and a lower slope than the thicker device.

In the buckling regime the measured values of device S_5 fit better to the model than in the previous case, but the model again overestimates the measured frequencies. One of the reasons for this could be curve veering, which is not incorporated in the analytical model and is analyzed in more detail in section 6.7.

The averaged displacement, shown in Figure 94 (b), shows higher values for the thinner beam. This can be explained by the fact that the forces produced by the piezoelectric layer are equal for both devices as the piezo-active material is deposited under the same conditions and the excitation voltage is the same in both cases. At the same time the thinner device can be strained more easily due to its lower stiffness in axial direction, thus being displaced stronger when applying the same force.

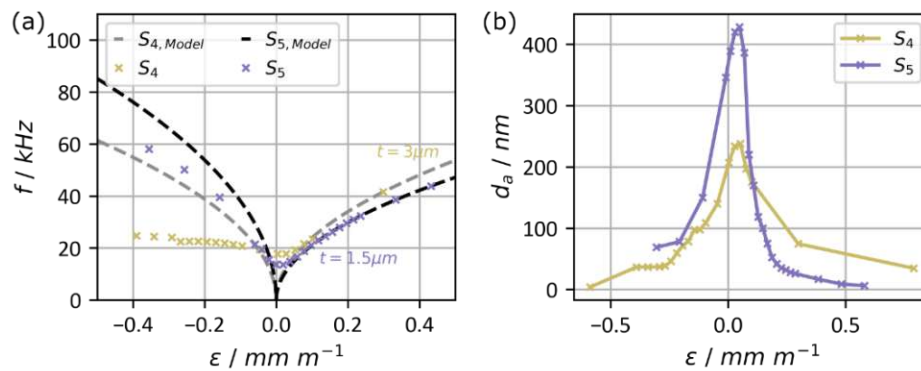


Figure 94: Resonance frequency of the first flexural mode as a function of strain for the two devices S_4 and S_5 plus the theoretical predictions $S_{4,Model}$ and $S_{5,Model}$. (b) Displacement averaged over all scan points as a function of strain for the same samples as in (a). Lines in (b) serve as guide to the eye.

6.6.3. Width

Next the influence of the microbridge's width on the frequency and the averaged displacement is studied as a function of strain for the modes 20 and 30. Therefore, three microbridges S_1 , S_2 and S_3 having widths of $100\mu\text{m}$, $200\mu\text{m}$ and $400\mu\text{m}$, are analyzed. Additional to the optical measurements, electrical measurements of the conductance spectra as a function of strain were performed and compared to their optical counterpart at the end of this subsection.

Figure 95 (a) shows that the frequency of the 20-mode in the non-buckling regime does not change substantially with width, which is in good agreement with the analytical model. However, in the buckling regime the three microbridges diverge from each other and from the model. On the other hand, Figure 95 (b) shows that the width does not have a substantial influence on the averaged displacement. Any deviations are most likely resulting from manufacturing uncertainties.

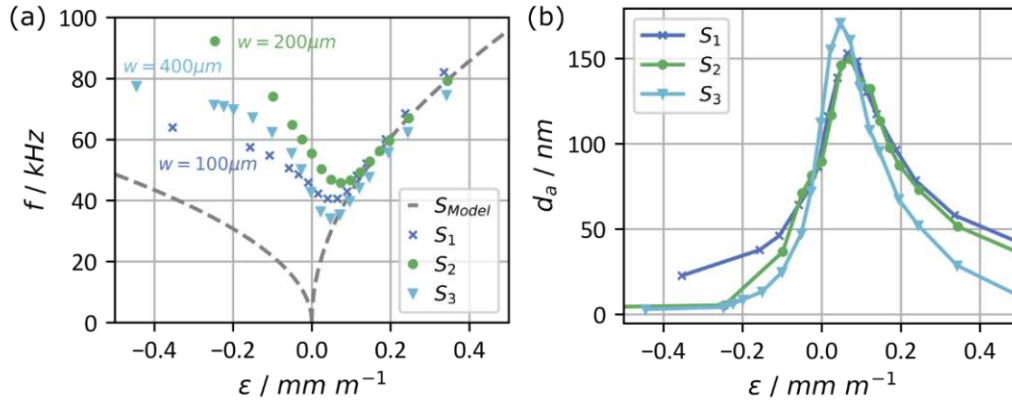


Figure 95: (a) Resonance frequency of the first flexural mode as a function of strain for the three devices S_1 , S_2 and S_3 plus the theoretical predictions S_{Model} . (b) Displacement averaged over all scan points as a function of strain for the same devices as in (a). Lines in (b) serve as guide to the eye.

The measurements of the 30-mode show similar results with the resonance frequency in Figure 96 (a) being in good agreement in the non-buckling regime and diverging slightly in the buckling regime. The averaged displacement in Figure 96 (b) shows more variation of the displacement, especially in the buckling regime. It is reasonable to assume that inaccuracies in the manufacturing process and the differences in intrinsic stress of the different layers are responsible for this behaviour.

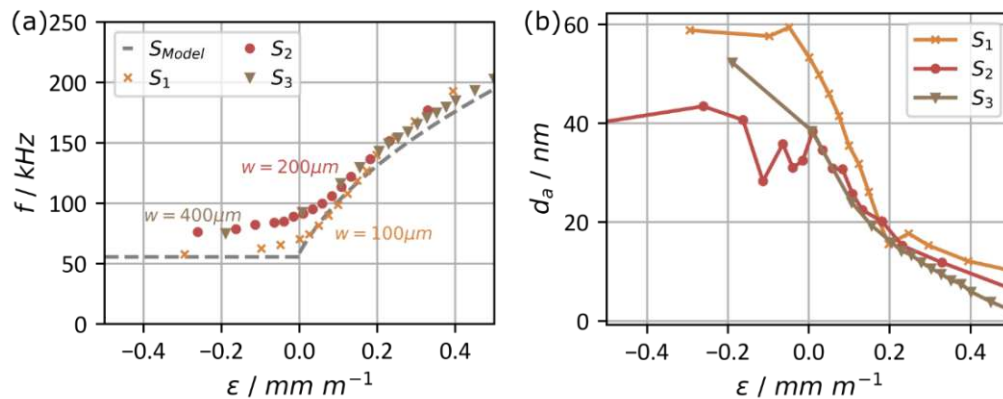


Figure 96: Resonance frequency of the second flexural mode as a function of strain for the three devices S_1 , S_2 and S_3 plus the theoretical predictions S_{Model} . (b) Displacement averaged over all scan points as a function of strain for the same devices as in (a). Lines in (b) serve as guide to the eye.

Figure 97 (a-b) and Figure 98 (a-b) show the frequency and the conductance of the same modes for all three microbridges measured with the impedance analyzer. The frequency as a function of strain shows very much the same values and behavior as from the optical measurements, again confirming the equivalence of both measurement techniques. The conductance shows higher peaks for devices with higher widths, due to the larger area which in turn leads to a higher amount of generated polarization charges, when the microbridge is vibrating. This leads to the conclusion that wider microbridges are preferable when measured electrically, due to the increase signal strength.

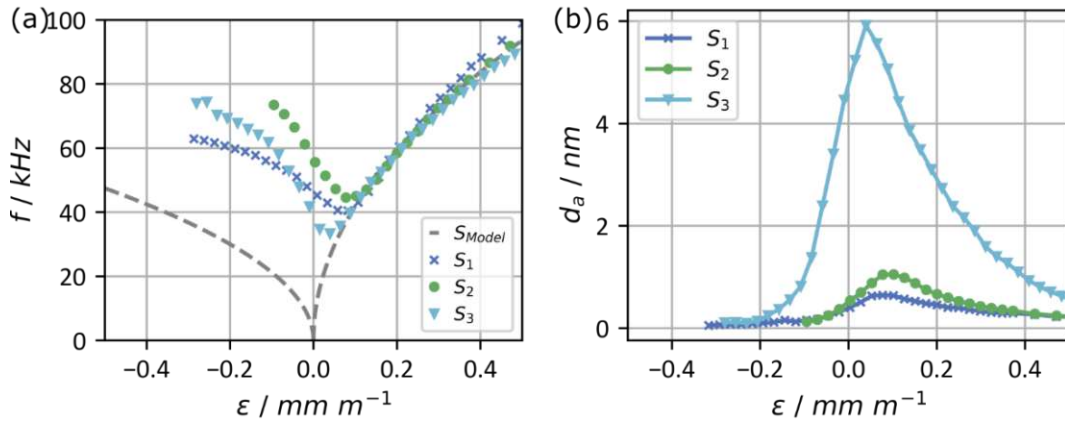


Figure 97: (a) Resonance frequency of the first flexural mode as a function of strain measured with the impedance analyzer, for the three devices S_1 , S_2 and S_3 plus the theoretical predictions S_{Model} . (b) Conductance peaks as a function of strain for the same devices as in (a). Lines in (b) serve as guide to the eye.

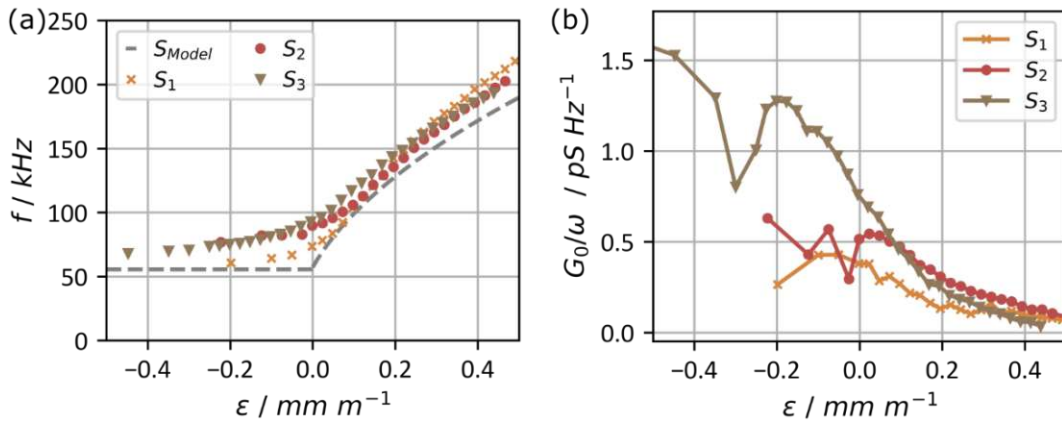


Figure 98: (a) Resonance frequency of the second flexural mode as a function of strain measured with the impedance analyzer, for the three devices S_1 , S_2 and S_3 plus the theoretical predictions models S_{Model} . (b) Conductance peaks as a function of strain for the same devices as in (a). Lines in (b) serve as guide to the eye.

However, the increased microbridge width also results in a drawback. Figure 99 (a) shows the frequency as a function of strain for the torsional modes 21 (colored curves) and the model of the 20-mode for all three microbridge widths, measured with the LDV. In general, the torsional modes have higher frequency values, but by increasing the microbridge width the frequency of those modes drops down to the point, where they come very close to their corresponding non-torsional counterpart. This has also been observed for cantilever type resonators [124] and has some consequences. One of them is the so-called curve veering effect, where modes seemingly cross over, but instead of crossing they veer away. In this veering zone, the displacement, the resonance frequency and the Q-factor of both modes are affected, making it more difficult to provide correct readouts when used as a sensor device. This will be discussed in more detail in sections 6.7 and 6.8.

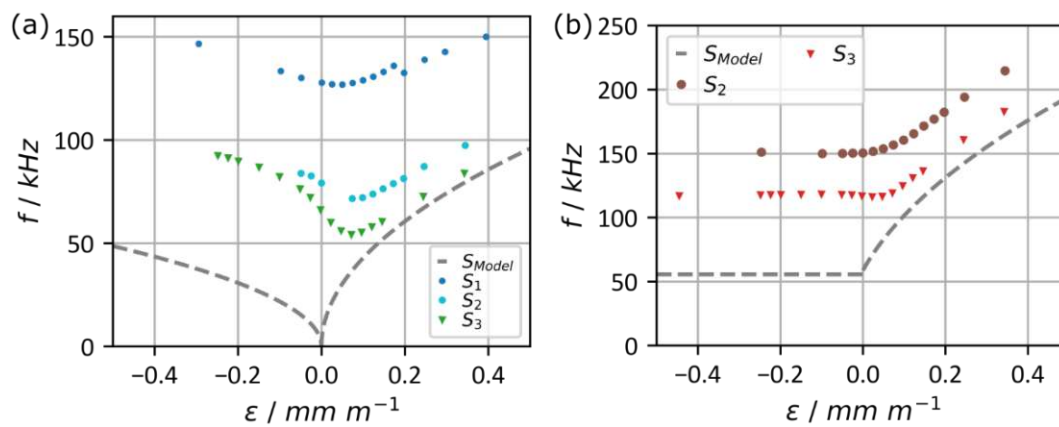


Figure 99: (a) Resonance frequency of the first torsional mode (21) as a function of strain measured with the LDV, for the three devices S_1 , S_2 and S_3 plus the theoretical predictions S_{Model} . (b) Resonance frequency of the second torsional mode (31) as a function of strain for the same devices and under the same conditions as in (a).

6.7 Curve Veering

Another effect coming into play occurs when the resonance frequencies of different modes get shifted in a way that they seemingly cross-over. But instead of crossing they veer away, so that this phenomenon is called curve veering or avoided crossing [293]. The region where those modes veer is typically referred to as “transition zone” [294]. Several publications have experimentally validated the curve veering effect for microbridge-type resonators [295]–[298], but it also has been shown for other resonator designs [299], [300].

Figure 100 (a) shows the frequency response for 5 different strain values, covering the modes 20 and 30 of a device with dimensions of $1000 \times 400 \times 3 \mu\text{m}$, using an antisymmetric electrode configuration. The modes 20 and 30 are highlighted in blue and orange, respectively. Figure 100 (b) shows the measured mode shape of the resonance at lower frequencies and Figure 100 (c) the mode shape at higher frequencies. The mode shapes change depending on the strain and on the distance in frequency between the two resonance peaks. In the transition zone the mode shapes are distorted and cannot be clearly identified, indicated with grey highlighting.

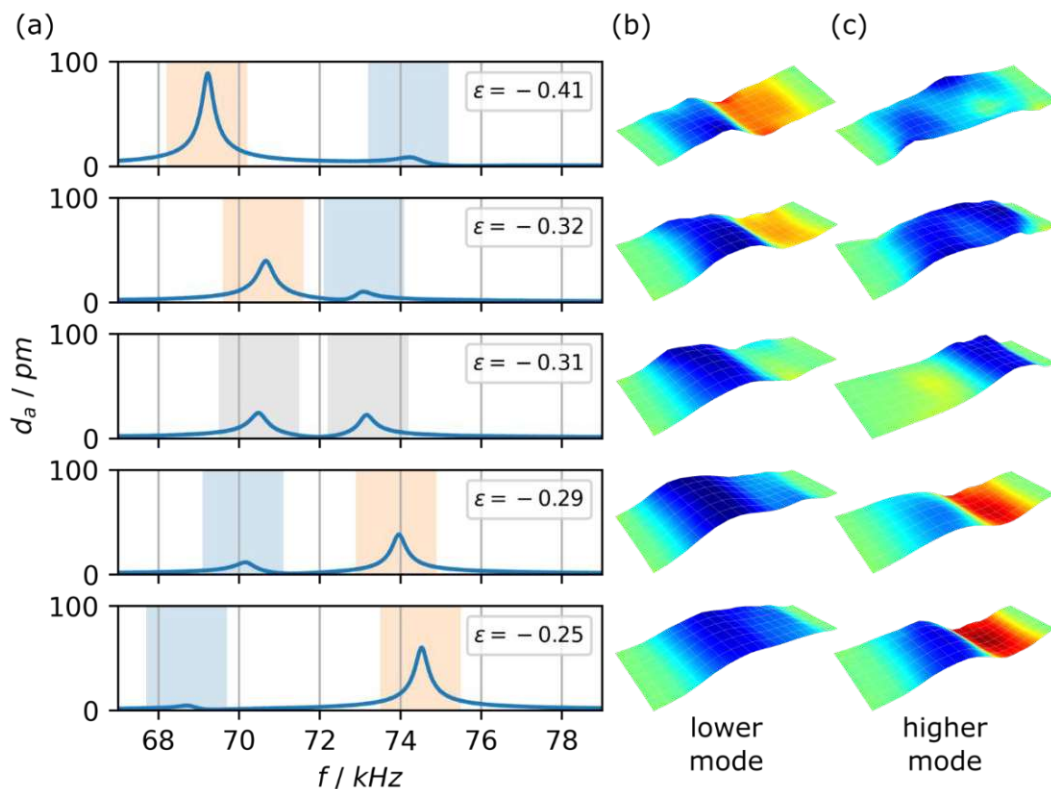


Figure 100: (a) Frequency spectra of a microbridge for five different strain values showing the resonances of the 20-mode (marked in blue) and 30-mode (marked in orange) close to their veering point. The areas marked in gray show mode shapes where a clear assignment to a certain mode is not possible, due to the mixing of the two mode shapes. (b) Mode shapes measured with the LDV of the lower resonance and (c) of the higher resonance.

Figure 101 (a) shows the resonance frequency as a function of the applied strain for both modes. The mode shapes are indicated by the blue and orange areas for the modes 20 and 30. The grey and black curves are the actual measured resonance peaks. As explained before, they approach each other, but instead of crossing they veer away and exchange their mode shape. Figure 101 (b) shows the maximum values for the displacement of the two modes and it is obvious that the modes not only exchange their shape, but also their amplitudes.

When this device concept is exploited as strain sensor, curve veering might affect the accuracy of the measurement results in these transition zones in two ways. First, the wrong mode can be followed when crossing the transition zone, which would lead to false result interpretations *e.g.*, decreasing instead of increasing frequency with increasing strain, as shown in Figure 101 (a) for mode 30 (orange area). Second, when following the correct mode, an abrupt change occurs from one to the other mode, leading to higher and difficult to predict values of the responsivity. A simple possibility to avoid both cases is to define a working point in the frequency spectrum which avoids any transition zones. Another approach is to simultaneously measure the resonance frequency and its amplitude, as this changes together with the mode shape. In this case, the mode with the higher amplitude (i.e. mode 30) would be the mode of choice, as depicted in Figure 101 (b).

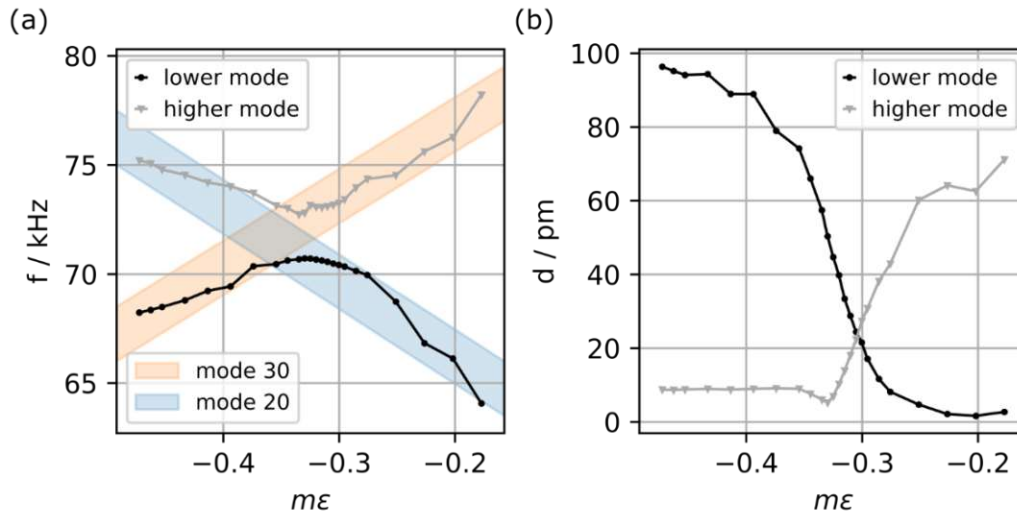


Figure 101: (a) Shift of resonance frequency as a function of strain for the 20- and the 30-mode of a microbridge around the buckling point, clearly showing the avoided crossing phenomenon. The blue and orange marks indicate how the modes would behave without the veering effect. (b) The corresponding displacements of the 20- and the 30-mode. Inserted lines serve as guide to the eye.

6.8 Q-Factor

The quality factors of all modes were determined by using equations discussed in chapter 3.6 and 3.8, for the displacement measured with the LDV and the conductance measured with the impedance analyzer. In general, the Q-factors of all modes exhibit reasonable values between 200 to 400 being in excellent agreement with those reported in literature [103], [301] for microbridge type resonators at room temperature in air. However, the change in Q-factor when the external applied strain is varied shows interesting behavior and is analyzed in the following.

Figure 102 (a-c) show the Q-factor for the 20-mode for both measurement methods. The higher data scatter of the Q-factor determined by the impedance analyzer for the sample $S_{1,IA}$ most probably is caused by the very low signal of this resonance and hence, the low signal to noise ratio making the fit very difficult. However, the fitted results from the impedance analyzer match on average well to the results from the LDV. For microbridges with widths of $200\ \mu\text{m}$ and $400\ \mu\text{m}$ the results fit exactly in a range of $-0.25 \dots 0.25\ \text{mm}\ \text{m}^{-1}$ and diverge only slightly for higher strain values, which again is caused by the lower output signal strength for higher strain values, compare Figure 95 (b) and Figure 96 (b).

The comparison of the LDV measurements of the three devices in Figure 102 (d) shows that the Q-factor of microbridges with different width behaves differently when strain varies. For the 20-modes the Q-factor of the thinnest microbridge shows rising values with increasing strain values, which is expected and agrees to results already reported in literature. The wider microbridges also show rising Q-factor values up to a strain value of approximately $0.2\ \text{mm}\ \text{m}^{-1}$. Above, the values start to decline, whereas the widest microbridge shows typically lower values than the thinner one. Schmid *et al.* showed that one of the reasons for reduced Q-factors of wider microbridges stems from the increased drag-force and squeeze-film air damping due to the increased width [302]. However, this does not explain the differences when the microbridges experience higher strain values. One reason for this might be an effect called dissipation dilution where the mechanism which normally dissipates energy due to the intrinsic loss mechanisms is “diluted” and therefore higher Q-factors can be achieved [303], [304]. This has been experimentally validated with highly strained Si_3N_4 nanosized mechanical resonators [305]–[307].

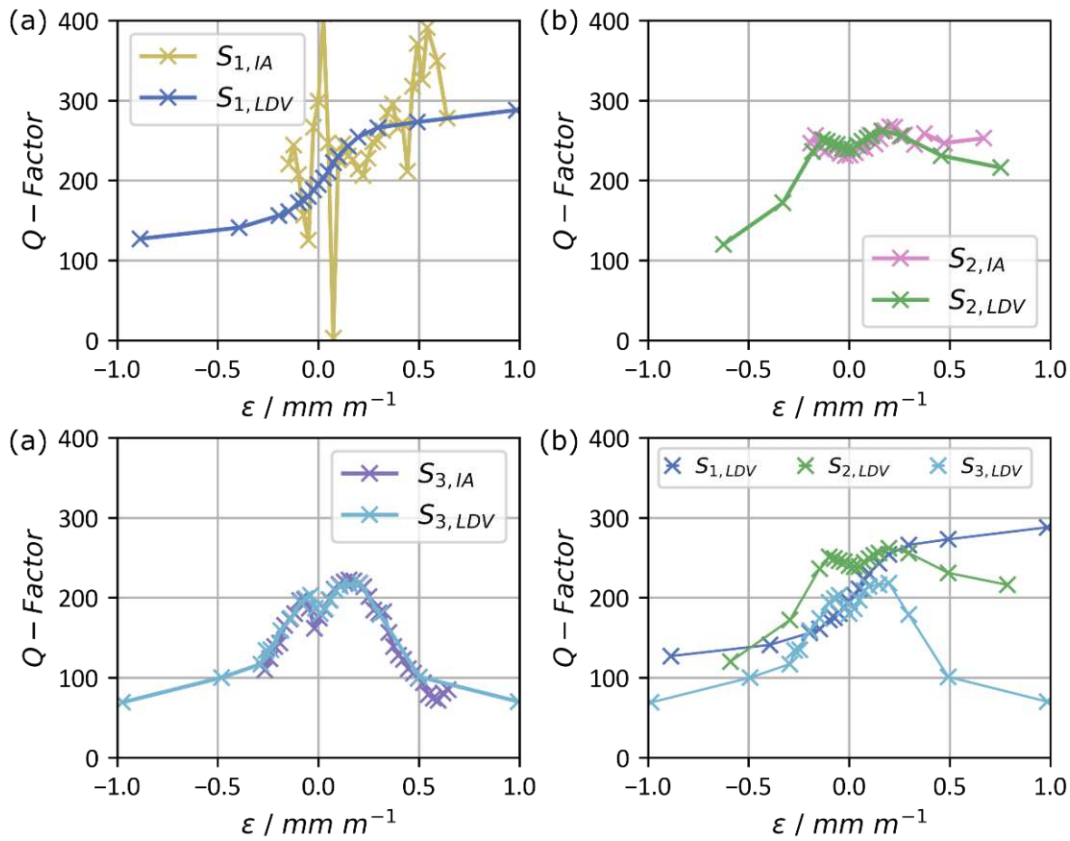


Figure 102: Q-factor as a function of strain of the 20-mode for microbridge-widths of (a) $100 \mu\text{m}$, (b) $200 \mu\text{m}$ and (c) $400 \mu\text{m}$ for LDV and IA measurements. (d) Comparison of the Q-factors measured with the LDV for all three microbridge widths. Inserted lines serve as guide to the eye.

Another explanation is that for larger width microbridges, the higher order torsional modes are shifted towards lower frequencies. Comparing Figure 102 (d) with Figure 99 (a) shows, that approximately at the same strain value at which the Q-factors begin to decline, the torsional modes get very close in frequency to their non-torsional counterparts. As stated in the previous section, these modes might veer with each other and partially exchange their energy and hence, the Q-factor declines. However, to prove this hypothesis further experiments are necessary.

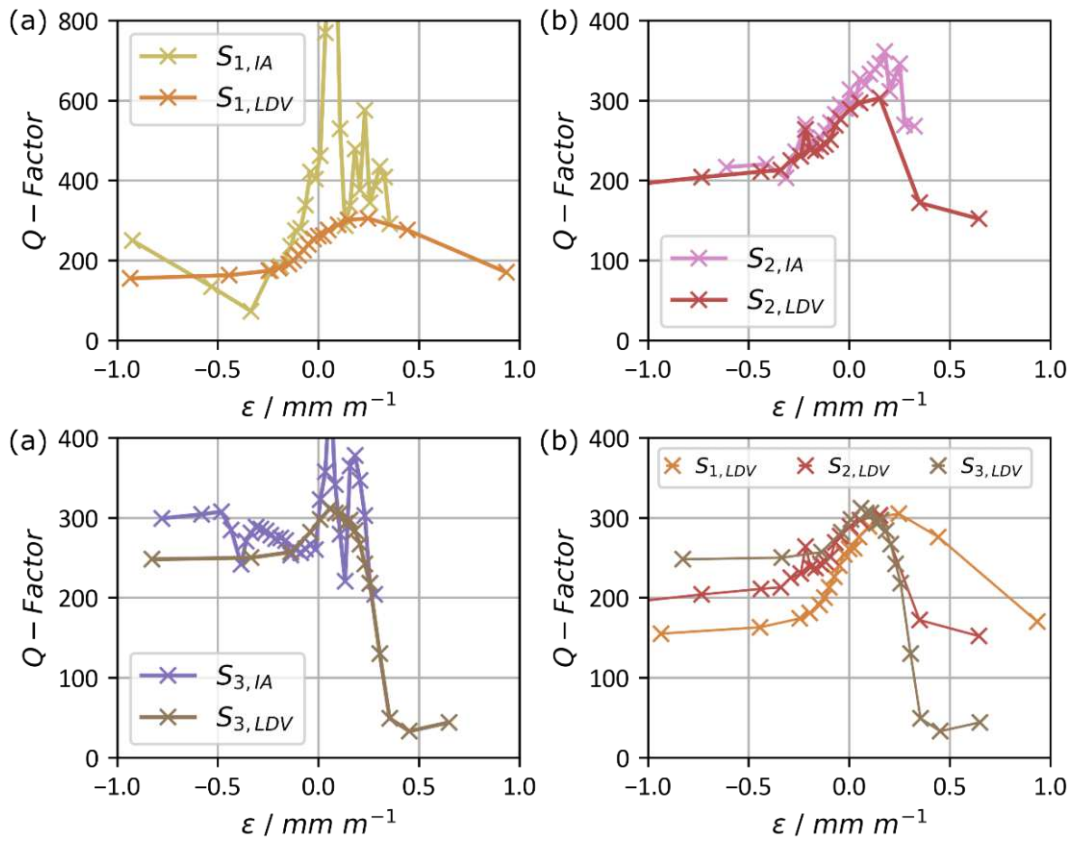


Figure 103: Q-factor as a function of strain of the 30-mode for microbridge-widths of (a) $100 \mu\text{m}$, (b) $200 \mu\text{m}$ and (c) $400 \mu\text{m}$ for LDV and IA measurements. (d) Comparison of the Q-factors measured with the LDV for all three microbridge widths. Inserted lines serve as guide to the eyes.

Figure 1 (a-c) show the 30-mode of the same devices as before, again measured with both techniques and Figure 1 (d) depicts the comparison of the LDV measurement. Similar to the measurements of the 20-mode, the IA measurements show a high data scatter compared to the LDV measurements. The Q-factors increase up to a strain value of approximately 0.2 mm m^{-1} , and decrease afterwards. In contrast to the 20-mode, Q-factors of the narrowest microbridge also decline for very high strain values. Another interesting observation is that in the buckling regime narrower microbridges show lower Q-factors for the 30-mode, while for the 20-mode the ordering is reversed. The reason for this could be different intrinsic stress levels in the microbridges.

6.9 Responsivity and Sensitivity

A central key figure when analyzing the performance of sensors in general is their responsivity or in the special case of a strain sensor their gauge factor k . For resistive strain gauges the dimensionless gauge factor $k_{resistive}$ is defined as the slope of the relative resistance change depending on ε and is calculated according to

$$k_{resistive} = \frac{\partial \Delta R(\varepsilon)}{\partial \varepsilon} / R_0 \quad (6.12)$$

where ΔR is the change in resistance for a given strain ε and R_0 is the resistance at $\varepsilon = 0$. Similar, a dimensionless gauge factor for resonant strain sensors $k_{resonant}$ can be defined with

$$k_{resonant} = \frac{\partial \Delta f(\varepsilon)}{\partial \varepsilon} / f_0 \quad (6.13)$$

where Δf is the change in resonance frequency for a given strain ε and $f_0 = f(\varepsilon)$ is the resonance frequency in the defined reference point. Due to the non-linear behavior of $f(\varepsilon)$ and reasons given in previous sections like curve veering or buckling, the definition of a working point is important. Figure 104 (a) shows the gauge factors of a representative sample S_1 for the even modes 20, 40 and 60 and in Figure 104 (b) for the odd modes 30, 50 and 70. In the non-buckling regime all modes show positive values for the gauge factor, with very high values of up to 5000 for the 20-mode and up to 4000 for the 30-mode. In the buckling regime, even modes show negative gauge factors with slightly reduced values compared to the non-buckling regime, whereas the gauge factors for odd modes almost vanish. Lower order modes have a higher gauge factor than higher order modes making them the better choice for an application as strain sensor.

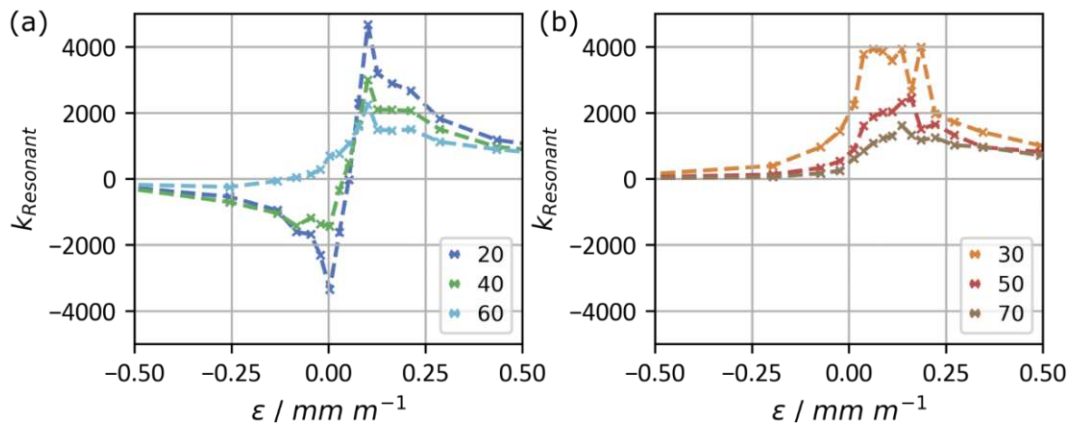


Figure 104: Gauge factor as a function of strain for (a) the even modes 20, 40 and 60 and (b) the uneven modes 30, 50 and 70.

When comparing samples S_1 and S_4 which have different lengths of $1000 \mu\text{m}$ and $1500 \mu\text{m}$, the 20-mode shows equal gauge factors but slightly shifted curves. One of the reasons might be inaccuracies coming from the fit. The 30-modes show higher values for the gauge factor, close to the buckling point, which could be a measurement error as the curve from S_1 looks slightly disformed with a flat top in the non-buckling regime.

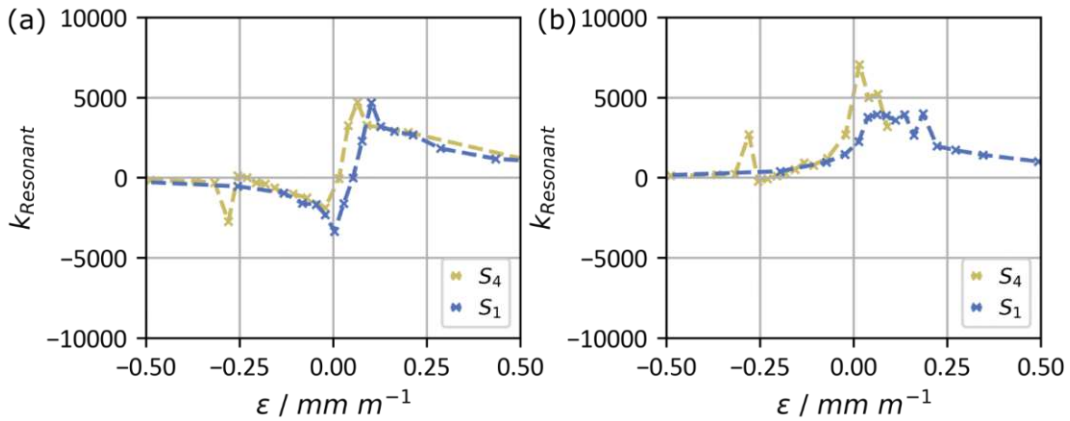


Figure 105: Gauge factor as a function of strain for two different microbridges differing in length for the (a) 20-mode and (b) the 30-mode.

Samples S_4 and S_5 which have different thicknesses of 3000 nm and 1500 nm show that thinner microbridges have higher gauge factors. In this case the gauge factor is 39% higher with ~ 6500 for the 20-mode and 17% higher with ~ 8300 for the 30-mode.

Obviously, the highest gauge factors can be achieved close to the buckling point, which is also the area where the data diverges from the model the most. One of the root causes for this divergence is intrinsic stress in the deposited thin films and will be analyzed in the next section, where a modified stress tailoring deposition technique is used to lower intrinsic stress and improve the gauge factor in the vicinity of the buckling point.

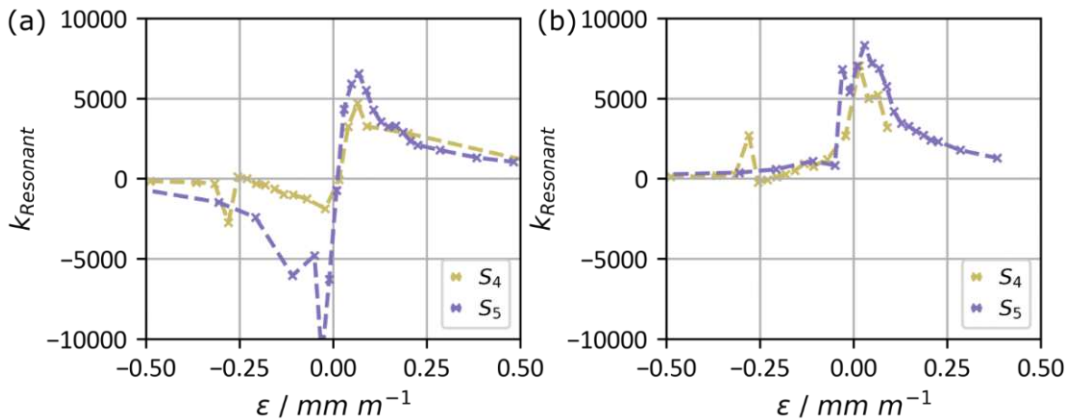


Figure 106: Gauge factor as a function of strain for two different microbridges differing in thickness for the (a) 20-mode and (b) the 30-mode.

Although such high gauge factors were predicted for resonant strain sensors with finite element simulations [308], most previous experimental work only reached gauge factors of up to 500 (see Table 4 in section 2.3), making our device approximately one order of magnitude more responsive than most of the current state-of-the-art. Even compared to other types of strain sensors (see Table 4 in section 2.3) e.g., piezoresistive materials like carbon nanotubes or strain sensors based on spintronic technology, our MEMS sensor shows a competitive gauge factor.

Obviously, if operated as a strain sensor the device has to be operated at a working point, so that if negative strain is applied the sensor does not change its buckling regime, as in that case, the gauge factor changes its sign and it would not be possible to distinguish positive from negative strain values. The smaller the range of possible applied strain, the closer the working point can be set to the buckling point, which results in higher gauge factors.

This working point can be set by pre-straining the MEMS sensor before or during the mounting process. In the featured measurement-setup the macroscopic Al cantilever beam was bent upwards before the sensor was glued onto its surface. The subsequent release into the Al cantilevers zero position acts as a pre-straining moving its buckling point to the left in (compare section 3.7). In a real-world application this pre-straining process is difficult to achieve as it is not often possible to pre-bend the surface of the test object. In this case, the pre-straining can be done during the packaging process, which must be done anyway to protect the sensor from damage.

6.10 Influence of Intrinsic Thin Film Stress

The previous sections have shown that the microbridges show various effects *e.g.*, shift of the buckling point or a reduced responsivity for low strain values which cannot be predicted properly by the analytical model introduced in section 6.2. One reason is the residual intrinsic stress of the deposited thin films which is analyzed in the following sections. Therefore, two sensor devices of equal dimensions but with different residual stress levels of their piezoelectric layers are compared, regarding their buckling, resonance frequencies and responsivity as a function of strain.

6.10.1. Buckling

To determine the impact of the developed stress-reduced AlN thin film from section 4.4 on device level, two sensor devices – S_5 and S_6 from Table 22 – based on SOI wafers were fabricated with two different sputter conditions, whereas one comprises the standard constant low pressure and the second the adapted pressure sweep process steps.

After fabrication, the devices sputtered with low pressure AlN show buckling with a deflection of the bridge center in the range of $10 - 15 \mu m$, as demonstrated by the white light interferometric measurements in Figure 107 (a). In contrast, microbridges where the functional AlN layer is sputtered with the adapted pressure sweep show no buckling and remain flat, as depicted in Figure 107 (b). The insets show a 2D scan over the whole surface of the microbridge, while the plotted data represent the line scan along the axis of the microbridge. The irregularities along the line scan marked with a (*) most likely result from phase modifications of the reflected white light due to the presence of transitions between materials with different optical properties on the surface (*i.e.*, from AlN to Au) [309].

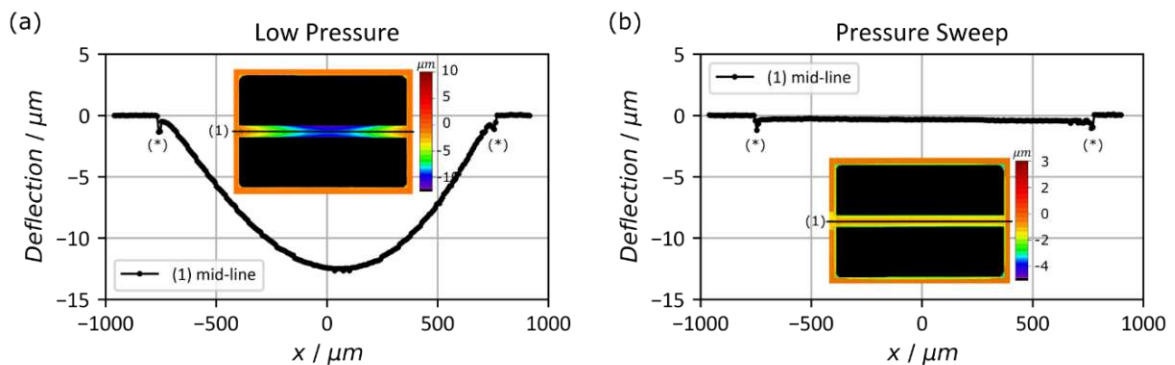


Figure 107: White light interferometer images and line scans along the microbridge axis for the low-pressure sample (a) and the pressure sweep sample (b).

The bottom and top electrodes show a tensile stress of $177 MPa$ and $164 MPa$, respectively. The residual stress of the full stack can be calculated by the sum of the individual stress values of each layer multiplied by its relative thickness in %. This results in a compressive stress for the low-pressure sample with a value of $-293 MPa$ and for the pressure-sweep sample the stress changes to a tensile value of $6.6 MPa$, explaining the white-light interferometric measurements with one microbridge being buckled, while the other is not, although both piezoelectric layers are compressively stressed.

The mechanical stress state of the microbridge represented either by a buckled or flat topography has a huge influence on the frequency behavior of the resonator, which will be discussed in the following.

6.10.2. Frequency Response

Figure 108 shows the resonance frequencies as a function of strain of both devices for modes up to the 6th order, whereas the 50-mode could not be measured, due to the low output signal height. The curves have been shifted so that $\varepsilon_{C,ps} = \varepsilon_{C,lp} = 0$ for reasons of comparison. Additionally, the predictions of the analytical model given by equations (5.13) and (6.2) are inserted. The resonance frequencies of the modes 20 and 30 for both devices overlap for $\varepsilon > 0.05$. For higher order modes the device with higher intrinsic stress shows higher resonance frequencies in comparison to the stress-reduced device. Additionally, the deviation of the 60 modes is higher than for the 40 modes, which leads to the assumption that stress has a larger impact on higher compared to lower order modes. Comparing the model to the measured data we can see that while the model fits nearly perfectly to the data of the 20 modes, the agreement gets worse for higher order modes. A possible explanation for this difference is the error made with the introduction of γ_n which is a coefficient for the contribution of the applied axial force to the modal stiffness, relative to the contribution of the flexural rigidity and k_n which represents the eigenvalue when solving the frequency equation of an Euler-Bernoulli beam [268]. These values are estimated at zero axial force and neglect effects like shear deformation, dynamic elongation of the beam due to the vibration and different forms of damping, therefore represent an additional error source for higher order modes and higher values of strain.

For $\varepsilon < -0.05$ the mode shapes are difficult to identify for two reasons: mode veering (compare section 6.7) and the influence of the static buckling deflection (compare section 6.4.2) onto the dynamic vibrational displacement.

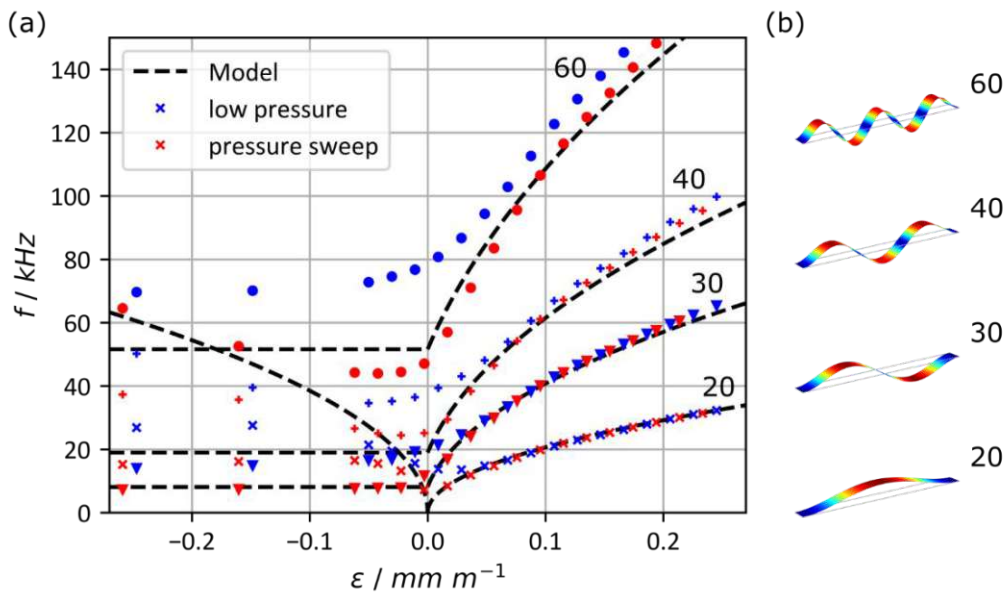


Figure 108: (a) Comparison of the resonance frequencies as a function of strain for the low pressure and the pressure sweep device, including the predicted resonance frequencies of the model.

For the strain range $-0.05 < \varepsilon < 0.05$ the first and second flexural mode are investigated separately, as depicted in Figure 109 (a-b). The 20-mode of the pressure sweep sample has lower frequency values around and at ε_C compared to the low-pressure sample. This has been explained in the model of Bouwstra *et al.* by an initial deflection z , which shifts the value of the frequencies around ε_C to higher values (compare equation (6.7)) [268]. Although their extended model, which includes the initial deflection, shows qualitatively the same behavior as our microbridges, the model is only valid in a very narrow range around ε :

$$-1.3 < \frac{\varepsilon}{\varepsilon_c} < 1. \quad (6.14)$$

Our data suggests that the influence of the initial buckling is much stronger than predicted by the model and as a result we could not fit the data to the extended model.

For $\varepsilon < -0.05$, both curves seem to approach the model as far as this can be evaluated due to the difficulties of identifying the modes as described before. The pressure-sweep sample approaches $\sim 8 \text{ kHz}$ which is in good agreement with the model, whereas the low-pressure sample approaches $\sim 18 \text{ kHz}$. This deviation indicates that the modelled initial deflection is not sufficient to explain all effects of thin film stress, especially in the buckling regime.

For higher modes we can see that in the non-buckling regime the data for the two different devices increasingly diverges from the model with increasing mode order. In the buckling regime we see a similar behavior, but due to mode veering it is even more difficult to estimate the correct frequency behavior and to give proper explanations.

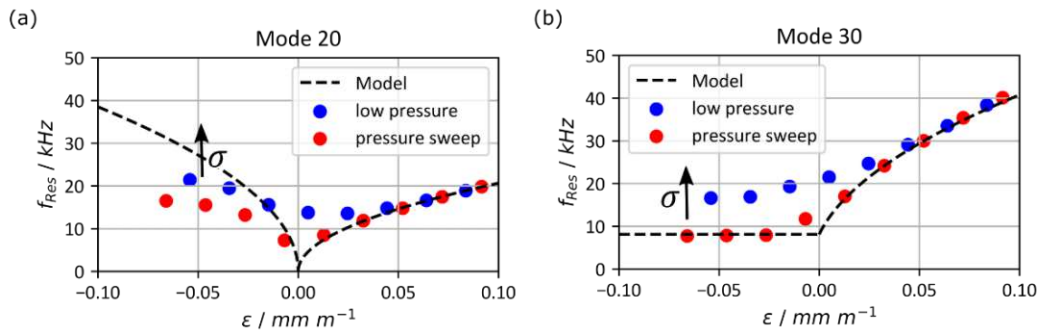


Figure 109: Frequency of the resonance peaks for the 20-mode (a) and the 30-mode (b) for low-pressure and the pressure sweep sensor devices.

6.10.3. Responsivity

As the microbridge is initially buckled after fabrication, which shifts ε_c towards higher values of ε compared to unbuckled microbridges, the initial working point ε_{WP} is in the buckled regime of the sensor device which is not suitable for strain sensing as the frequency is ambiguous when crossing ε_c and gauge factors in the buckling-regime are lower. One way to circumvent this as described before, is by pre-straining the device when mounting it to the structure under test or during packaging, both of which are challenging tasks. Obviously, another way is to adapt the thin film stress in a way that ε_c is modified such that its working point is set to a desirable value.

Figure 110 (a) shows the responsivity $R(\varepsilon)$ for the modes 20, 30, 40 and 60 for the pressure sweep device and for the model. Although higher modes have a higher slope, lower mode numbers show higher relative responsivities due to their lower frequencies. For $\varepsilon > 0.1$, the data is in good agreement with the model, but for values $\varepsilon < 0.1$ the model diverges from the calculated data as the initial deflection is not incorporated in the model.

Figure 110 (b) shows the comparison of the mode 20 of the pressure sweep device (orange), the low-pressure device (blue) and the model (black). Similar to $f(\varepsilon)$ (compare Figure 108) where the frequency at the critical strain value reached a lower minimum for devices with lower initial buckling or stress, the responsivity reaches a higher maximum. For the 20-mode this makes the pressure-

sweep device more than twice as responsive as the low-pressure sample with $R_{pressure-sweep} \approx 17000$ compared to $R_{low-pressure} \approx 6500$.

Comparing the results with the ones from section 6.9, where all devices were fabricated using the same standard low-pressure sputter process, the responsivity could be increased by a factor ~ 4 . This shows that the device performance in case of a MEMS resonant strain sensor strongly depends on the residual stress.

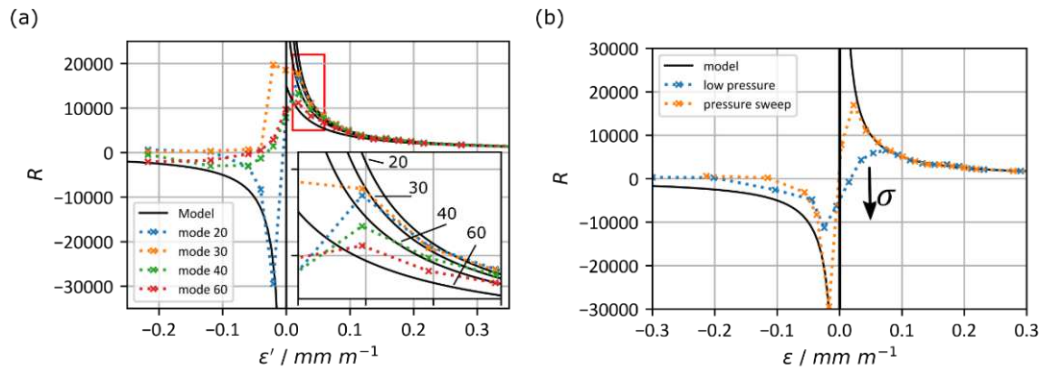


Figure 110: (a) Responsivity of various modes for the pressure sweep device. (b) Comparison of the responsivity of the 20-modes for the low pressure and the pressure sweep device.

6.11 Conclusions

The resonant MEMS strain sensor presented in this chapter can be measured optically and electrically and has shown to be a versatile tool in the area of strain sensors showing highly promising results.

The resonance frequency, displacement and the Q-factor of multiple modes of several microbridges, differing in their geometrical dimensions are analyzed and show a characteristic dependence on the applied external strain. While the change in length and thickness directly have an effect on all three measurement parameters, the width only influences the Q-factor. However, wider devices produce a higher electrical signal due to their bigger surface area, which in turn generates a higher number of electrical charges, making them favorable when an electrical readout is necessary.

Additionally, the measurements have been compared to an analytical model from [268]. In the non-buckling regime, the model predicts the behavior very good, whereas in the buckling regime the measurements deviate strongly from the predicted values.

The Q-factor shows a unique behavior, when microbridges with different widths are compared. Hypothesis of the cause are developed and compared with state-of-the-art literature, but a final model including all effects is still missing, showing future potential research opportunities.

Various other effects like buckling, non-linearity, creeping and curve veering on the shift of resonance frequencies are also studied and show the restrictions of the microbridges when used as a strain sensor. However, the responsivity shows very high values, three orders of magnitude higher than conventional resistive strain gauge sensors with values up to 6500.

By introducing sensor devices manufactured with the stress tailoring sputter process introduced in chapter 4, the amount of residual intrinsic stress in the device is decreased and the frequency behavior of the microbridges significantly improved. As a result, the responsivity can be increased by a factor of 2.6 from already very high values of 6500 to 17000.

7. Conclusions and Outlook

In this work a piezoelectric resonant MEMS strain sensor and a piezoelectric/electromagnetic hybrid energy harvesting device for the use in a sensor node mounted in wind turbine rotor blades was studied. Additionally, detailed investigations of sputter deposited piezoelectric aluminum nitride alloyed with scandium and yttrium were performed for the use in the hybrid energy harvester and the MEMS strain sensor.

Optimal deposition conditions of alloyed AlN were attained by varying the parameters power, gas composition and pressure. The results from XRD, SEM, TEM and EDX measurements showed that under optimal deposition conditions, the thin films exhibit highly c-axis oriented crystal grains, which is a necessity for good piezoelectric coefficients. The piezometer measurements of the longitudinal piezoelectric coefficient d_{33} of $Al_{0.71}Sc_{0.29}N$ showed comparable values to those attained from literature. The $Al_{0.91}Y_{0.09}N$ alloy resulted in a d_{33} increased by 55% compared to pure AlN, which is in very good agreement with previously performed DFT simulations done by Mayrhofer *et al* and Žukauskaitė *et al*. Furthermore, thin film stress of – an important parameter when it comes to MEMS beam resonators in single or double clamped form – of both, AlScN and AlYN was analyzed and showed rather high compressively stressed values up into the *GPa* range. To control the thin film stress and at the same time maintain the high piezoelectric values, a modified sputter process was developed where the sputter pressure is gradually increased during deposition. With this procedure, thin films with compressive intrinsic stress in the low MPa range without any reduction in the piezoelectric coefficient d_{33} were synthesized, which later on were used to fabricate microbridges used as resonant MEMS strain sensors.

With the knowledge of the optimal fabrication conditions of piezoelectric AlN and its alloys, a design of a hybrid energy harvesting device was developed for the special conditions in a rotor blade of a wind turbine. It consists of an electromagnetic and a piezoelectric harvester and uses the rotating gravitational force vector inside the rotor blade to transform the kinetic energy of a moving permanent magnet into electric energy. First, a prototype as a proof-of-concept was built and characterized in the lab. While the piezoelectric harvester showed comparable values to similar designs in research, the electromagnetic harvester generated three orders of magnitude more power, which was the reason to focus more on the latter one for the continued work. Based on the first prototype, an improved second version of the electromagnetic energy harvester was fabricated and tested in a real-world wind turbine, where it generated 6 *mW* in comparison to 25 *mW* in the lab under optimal conditions. The amount of generated power proved similar to other energy harvesters in literature when relating to the harvester size, represented by the power density. The advantage of the electromagnetic energy harvester is that it can be further scaled up for larger power output, which in case of a rotor blade is also feasible as space is not an issue in this special case. While the piezoelectric harvester was too weak in terms of energy generation with the used materials, the studies in this work could become interesting if piezoelectric materials and their piezoelectric coefficients in combination with their dielectric permittivity are further developed.

Future research should target the improvement of the piezoelectric harvester either by e.g., implementing the piezoelectric materials with higher d_{31} or by stacking several piezoelectric thin films on top of each other [310], [311]. This could make both harvesting approaches equally potent in terms of energy generation. Furthermore, a power management circuit including an energy buffer (e.g., battery or super capacitor), which collects power from both harvesters and provides a steady voltage level to continuously power a sensor node is an important addition for a real-world application.

The piezoelectric MEMS resonant strain sensor is based on a microbridge structure, excited by a piezoelectric aluminum nitride thin film. After fabrication the sensor devices were characterized by attaining their mode shapes and frequency responses as a function of strain optically via laser Doppler vibrometer measurements. An electric read out was also provided by electrical impedance analyzer measurements. The externally applied strain was varied over a broad range of $\pm 1 \mu\epsilon$ around the buckling point, which presents the strain value where the microbridge changes from the non-buckling regime or flat state to the buckling regime or buckled state. The covered frequency bandwidth was 1 MHz which was enough to cover modes up to the 7th order, depending on the geometrical dimensions of the microbridge. The frequency responses were compared to an analytical model developed by Bouwstra *et al.* and were in very good agreement in the non-buckling regime but in poor agreement when the microbridges were buckled, showing that the model still has to be refined in this regime. Beside buckling, various other effects like creeping due to the adhesive, mode veering non-linearities or the influence of thin film stress were observed and studied in detail. To see the influence of the microbridge geometry on the frequency responses, the length, width and thickness were varied. While the increased length and reduced thickness leads to a higher slope of frequency as a function of strain, the width has no influence. However, the conductance spectra of the electrical read out showed a significant increase in the measurement signal for wider microbridges, explainable with the larger amount of generated charges due to the increased area of wider microbridges. The changing width also influences the amount of higher order two dimensional modes. When these two-dimensional modes cross the standard Euler-Bernoulli modes, it results in additional curve veering effects, restricting the use of the strain sensor in the according strain ranges. The Q-factor – an important parameter for resonators showed comparable values to other state-of-the-art resonators of similar size. However, when measuring the Q-factor as a function of strain, it shows an unexpected behavior with increasing strain. Close to the buckling point, the Q-factor increases with increasing strain, but after a strain value of approximately $0.25 \mu\epsilon$, the Q-factor decreases again. For increased widths of the microbridge the Q-factor decrease also increases. This behavior could not be explained and should be investigated in the future. The relative responsivity, also called gauge factor for strain sensors, showed very high values up to 6 500 for a microbridge geometry of $1500 \times 100 \times 1.5 \mu\text{m}^3$, which is a comparable value compared with state-of-the-art research (compare Table 4). In the end, the modified sputter process introduced in the materials chapter was used to fabricate sensor devices with a stress reduced piezo active thin film, further increasing the responsivity by a factor of 2.6 to 17 000.

The strain sensors already showed very promising results, but several open questions remain for future research. As already mentioned, the behavior of the Q-factor as a function of strain is still not fully understood. Another topic is the analytical description of the frequency response in the buckling regime, which showed large divergences compared to the measurements. While for the application as strain sensor the buckling regime was avoided, a more thorough understanding could make the use in other applications possible, not only as strain sensor but also in fields like acoustic applications [312], switching devices [313], [314] or energy harvesters [315], [316]. Further work could also comprise a more sophisticated read out through electric oscillator circuits [317] or a phase-locked-loop [318], making fast dynamic changes of the strain state measurable more easily. Another important, more application focused improvement could be an improved adhesion between the sensor and the DUT/package by e.g. bonding [290] reducing the creeping effect.

It can be concluded that both devices, the hybrid energy harvester and the MEMS resonant strain sensor show promising results and could be developed further for the implementation in a wireless sensor node.

Bibliography

- [1] IPCC, 1992, *Climate change 1990 and 1992: IPCC first assessment report overview and policymaker summaries and 1992 IPCC supplement*. Geneva, Switzerland: IPCC, 1992.
- [2] IPCC, 1995, *Climate Change 1995: Synthesis Report. IPCC Second Assessment Report*. 1995.
- [3] IPCC, 2001, Ed., *Climate Change 2001: Synthesis Report. A Contribution of Working Groups I, II, and III to the Third Assessment Report of the Intergovernmental Panel on Climate Change*. Cambridge, United Kingdom and New York, NY, USA: Cambridge University Press, 2001.
- [4] IPCC, 2007, *Climate Change 2007: Synthesis Report. Contribution of Working Groups I, II and III to the Fourth Assessment Report of the Intergovernmental Panel on Climate Change*. Geneva, Switzerland: Cambridge University Press, 2008.
- [5] IPCC, 2014, *Climate Change 2014: Synthesis Report. Contribution of Working Groups I, II and III to the Fifth Assessment Report of the Intergovernmental Panel on Climate Change*. Geneva, Switzerland.
- [6] P. A. Arias *et al.*, “Climate Change 2022: Technical Summary,” p. 112.
- [7] H. Ritchie, M. Roser, and P. Rosado, “CO2 and Greenhouse Gas Emissions,” *Our World Data*, 2020.
- [8] A. Sikora, “European Green Deal – legal and financial challenges of the climate change,” *ERA Forum*, vol. 21, no. 4, pp. 681–697, Jan. 2021, doi: 10.1007/s12027-020-00637-3.
- [9] H. Ritchie, M. Roser, and P. Rosado, “Energy,” *Our World Data*, 2022.
- [10] “Revision of the Renewable Energy Directive: Fit for 55 package | Think Tank | European Parliament.”
[https://www.europarl.europa.eu/thinktank/en/document/EPRS_BRI\(2021\)698781](https://www.europarl.europa.eu/thinktank/en/document/EPRS_BRI(2021)698781)
(accessed Dec. 10, 2022).
- [11] “It’s official: The EU Commission wants 30 GW a year of new wind up to 2030,” *WindEurope*, Jul. 14, 2021. <https://windeurope.org/newsroom/press-releases/its-official-the-eu-commission-wants-30-gw-of-new-wind-a-year-up-to-2030/> (accessed Dec. 10, 2022).
- [12] L. Ziegler, E. Gonzalez, T. Rubert, U. Smolka, and J. J. Melero, “Lifetime extension of onshore wind turbines: A review covering Germany, Spain, Denmark, and the UK,” *Renew. Sustain. Energy Rev.*, vol. 82, pp. 1261–1271, Feb. 2018, doi: 10.1016/j.rser.2017.09.100.
- [13] A. Ndiaye, A. Charki, A. Kobi, C. M. F. Kébé, P. A. Ndiaye, and V. Sambou, “Degradations of silicon photovoltaic modules: A literature review,” *Sol. Energy*, vol. 96, pp. 140–151, Oct. 2013, doi: 10.1016/j.solener.2013.07.005.
- [14] A. B. Wilson and L. Killmayr, “Offshore wind energy in Europe,” *PE 659313*, p. 12, Nov. 2020.
- [15] P. Gipe and E. Möllerström, “An overview of the history of wind turbine development: Part II—The 1970s onward,” *Wind Eng.*, p. 0309524X221122594, Sep. 2022, doi: 10.1177/0309524X221122594.
- [16] P. Gipe and E. Möllerström, “An overview of the history of wind turbine development: Part I—The early wind turbines until the 1960s,” *Wind Eng.*, vol. 46, no. 6, pp. 1973–2004, Dec. 2022, doi: 10.1177/0309524X221117825.
- [17] J. F. Mandell, D. S. Cairns, D. D. Samborsky, R. B. Morehead, and D. J. Haugen, “Prediction of Delamination in Wind Turbine Blade Structural Details,” *J. Sol. Energy Eng.*, vol. 125, no. 4, pp. 522–530, Nov. 2003, doi: 10.1115/1.1624613.
- [18] C. Q. Gómez Muñoz, F. P. García Marquez, B. Hernandez Crespo, and K. Makaya, “Structural health monitoring for delamination detection and location in wind turbine blades employing guided waves,” *Wind Energy*, vol. 22, no. 5, pp. 698–711, 2019, doi: 10.1002/we.2316.
- [19] I. Amenabar, A. Mendikute, A. López-Arraiza, M. Lizaranzu, and J. Aurrekoetxea, “Comparison and analysis of non-destructive testing techniques suitable for delamination inspection in wind turbine blades,” *Compos. Part B Eng.*, vol. 42, no. 5, pp. 1298–1305, Jul. 2011, doi: 10.1016/j.compositesb.2011.01.025.

- [20] M. A. S. Shohag, E. C. Hammel, D. O. Olawale, and O. I. Okoli, "Damage mitigation techniques in wind turbine blades: A review," *Wind Eng.*, vol. 41, no. 3, pp. 185–210, Jun. 2017, doi: 10.1177/0309524X17706862.
- [21] E. A. Mayda and C. P. van Dam, "Bubble-Induced Unsteadiness on A Wind Turbine Airfoil," *J. Sol. Energy Eng.*, vol. 124, no. 4, pp. 335–344, Nov. 2002, doi: 10.1115/1.1510525.
- [22] B. Zhou, X. Zhang, and H. Li, "Study on Air Bubble Defect Evolution in Wind Turbine Blade by Infrared Imaging with Rheological Theory," *Appl. Sci.*, vol. 9, no. 22, Art. no. 22, Jan. 2019, doi: 10.3390/app9224742.
- [23] T.-C. Le, T.-H.-T. Luu, H.-P. Nguyen, T.-H. Nguyen, D.-D. Ho, and T.-C. Huynh, "Piezoelectric Impedance-Based Structural Health Monitoring of Wind Turbine Structures: Current Status and Future Perspectives," *Energies*, vol. 15, no. 15, Art. no. 15, Jan. 2022, doi: 10.3390/en15155459.
- [24] S. Fæster, N. F.-J. Johansen, L. Mishnaevsky Jr, Y. Kusano, J. I. Bech, and M. B. Madsen, "Rain erosion of wind turbine blades and the effect of air bubbles in the coatings," *Wind Energy*, vol. 24, no. 10, pp. 1071–1082, 2021, doi: 10.1002/we.2617.
- [25] M. B. Lachowicz and M. M. Lachowicz, "Influence of Corrosion on Fatigue of the Fastening Bolts," *Materials*, vol. 14, no. 6, Art. no. 6, Jan. 2021, doi: 10.3390/ma14061485.
- [26] H. D. M. de Azevedo, A. M. Araújo, and N. Bouchonneau, "A review of wind turbine bearing condition monitoring: State of the art and challenges," *Renew. Sustain. Energy Rev.*, vol. 56, pp. 368–379, Apr. 2016, doi: 10.1016/j.rser.2015.11.032.
- [27] D. Coronado and J. Wenske, "Monitoring the Oil of Wind-Turbine Gearboxes: Main Degradation Indicators and Detection Methods," *Machines*, vol. 6, no. 2, Art. no. 2, Jun. 2018, doi: 10.3390/machines6020025.
- [28] J.-Y. Hsu, Y.-F. Wang, K.-C. Lin, M.-Y. Chen, and J. H.-Y. Hsu, "Wind Turbine Fault Diagnosis and Predictive Maintenance Through Statistical Process Control and Machine Learning," *IEEE Access*, vol. 8, pp. 23427–23439, 2020, doi: 10.1109/ACCESS.2020.2968615.
- [29] D. Astolfi, "A Study of the Impact of Pitch Misalignment on Wind Turbine Performance," *Machines*, vol. 7, no. 1, Art. no. 1, Mar. 2019, doi: 10.3390/machines7010008.
- [30] M. Bertelè, C. L. Bottasso, and S. Cacciola, "Automatic detection and correction of pitch misalignment in wind turbine rotors," *Wind Energy Sci.*, vol. 3, no. 2, pp. 791–803, Oct. 2018, doi: 10.5194/wes-3-791-2018.
- [31] U. Elosegui, I. Egana, A. Ulazia, and G. Ibarra-Berastegi, "Pitch Angle Misalignment Correction Based on Benchmarking and Laser Scanner Measurement in Wind Farms," *Energies*, vol. 11, no. 12, Art. no. 12, Dec. 2018, doi: 10.3390/en1123357.
- [32] R. Wagner, T. f. Pedersen, M. Courtney, I. Antoniou, S. Davoust, and R. I. Rivera, "Power curve measurement with a nacelle mounted lidar," *Wind Energy*, vol. 17, no. 9, pp. 1441–1453, 2014, doi: 10.1002/we.1643.
- [33] O. M. Bouzid, G. Y. Tian, K. Cumanan, and D. Moore, "Structural Health Monitoring of Wind Turbine Blades: Acoustic Source Localization Using Wireless Sensor Networks," *J. Sens.*, vol. 2015, p. e139695, Jul. 2015, doi: 10.1155/2015/139695.
- [34] Z. Herrasti, I. Val, I. Gabilondo, J. Berganzo, A. Arriola, and F. Martínez, "Wireless sensor nodes for generic signal conditioning: Application to Structural Health Monitoring of wind turbines," *Sens. Actuators Phys.*, vol. 247, pp. 604–613, Aug. 2016, doi: 10.1016/j.sna.2016.06.027.
- [35] B. Wondra, S. Malek, M. Botz, S. D. Glaser, and C. U. Grosse, "Wireless High-Resolution Acceleration Measurements for Structural Health Monitoring of Wind Turbine Towers," *Data-Enabled Discov. Appl.*, vol. 3, no. 1, p. 4, Jan. 2019, doi: 10.1007/s41688-018-0029-y.
- [36] K. Lee, A. Aihara, G. Puntsagdash, T. Kawaguchi, H. Sakamoto, and M. Okuma, "Feasibility study on a strain based deflection monitoring system for wind turbine blades," *Mech. Syst. Signal Process.*, vol. 82, pp. 117–129, Jan. 2017, doi: 10.1016/j.ymsp.2016.05.011.
- [37] P. Wang, Y. Yan, G. Y. Tian, O. Bouzid, and Z. Ding, "Investigation of Wireless Sensor Networks for Structural Health Monitoring," *J. Sens.*, vol. 2012, p. e156329, May 2012, doi: 10.1155/2012/156329.

- [38] L. Lu, Y. He, Y. Ruan, and W. Yuan, "Wind Turbine Planetary Gearbox Condition Monitoring Method Based on Wireless Sensor and Deep Learning Approach," *IEEE Trans. Instrum. Meas.*, vol. 70, pp. 1–16, 2021, doi: 10.1109/TIM.2020.3028402.
- [39] G. Kilic and M. S. Unluturk, "Testing of wind turbine towers using wireless sensor network and accelerometer," *Renew. Energy*, vol. 75, pp. 318–325, Mar. 2015, doi: 10.1016/j.renene.2014.10.010.
- [40] A. S. Zalhaf, M. Abdel-Salam, D.-E. A. Mansour, S. Ookawara, and M. Ahmed, "Assessment of wind turbine transient overvoltages when struck by lightning: experimental and analytical study," *IET Renew. Power Gener.*, vol. 13, no. 8, pp. 1360–1368, 2019, doi: 10.1049/iet-rpg.2018.5442.
- [41] V. V. Kochervinskii, "Piezoelectricity in crystallizing ferroelectric polymers: Poly(vinylidene fluoride) and its copolymers (A review)," *Crystallogr. Rep.*, vol. 48, no. 4, pp. 649–675, Jul. 2003, doi: 10.1134/1.1595194.
- [42] J. G. Smits and A. Ballato, "Dynamic admittance matrix of piezoelectric cantilever bimorphs," *J. Microelectromechanical Syst.*, vol. 3, no. 3, pp. 105–112, Sep. 1994, doi: 10.1109/84.311560.
- [43] D. Damjanovic, "Ferroelectric, dielectric and piezoelectric properties of ferroelectric thin films and ceramics," *Rep. Prog. Phys.*, vol. 61, no. 9, p. 1267, Sep. 1998, doi: 10.1088/0034-4885/61/9/002.
- [44] S. Trolrier-McKinstry and P. Muralt, "Thin Film Piezoelectrics for MEMS," *J. Electroceramics*, vol. 12, no. 1, pp. 7–17, Jan. 2004, doi: 10.1023/B:JECR.0000033998.72845.51.
- [45] H. S. Kim, J.-H. Kim, and J. Kim, "A review of piezoelectric energy harvesting based on vibration," *Int. J. Precis. Eng. Manuf.*, vol. 12, no. 6, pp. 1129–1141, Dec. 2011, doi: 10.1007/s12541-011-0151-3.
- [46] T. Zhang *et al.*, "High piezoelectricity of Pb(Zr,Ti)O₃-based ternary compound thin films on silicon substrates," *Appl. Phys. Lett.*, vol. 94, no. 12, p. 122909, Mar. 2009, doi: 10.1063/1.3103553.
- [47] P. Muralt, J. Antifakos, M. Cantoni, R. Lanz, and F. Martin, "Is there a better material for thin film BAW applications than AlN?," in *IEEE Ultrasonics Symposium, 2005.*, Sep. 2005, vol. 1, pp. 315–320. doi: 10.1109/ULTSYM.2005.1602858.
- [48] S. Roundy, "On the Effectiveness of Vibration-based Energy Harvesting," *J. Intell. Mater. Syst. Struct.*, vol. 16, no. 10, pp. 809–823, Oct. 2005, doi: 10.1177/1045389X05054042.
- [49] L. Qiao, G. Li, H. Tao, J. Wu, Z. Xu, and F. Li, "Full characterization for material constants of a promising KNN-based lead-free piezoelectric ceramic," *Ceram. Int.*, vol. 46, no. 5, pp. 5641–5644, Apr. 2020, doi: 10.1016/j.ceramint.2019.11.009.
- [50] S. Fichtner, T. Reimer, S. Chemnitz, F. Lofink, and B. Wagner, "Stress controlled pulsed direct current co-sputtered Al_{1-x}Sc_xN as piezoelectric phase for micromechanical sensor applications," *APL Mater.*, vol. 3, no. 11, p. 116102, Nov. 2015, doi: 10.1063/1.4934756.
- [51] M. Akiyama, T. Tabaru, K. Nishikubo, A. Teshigahara, and K. Kano, "Preparation of scandium aluminum nitride thin films by using scandium aluminum alloy sputtering target and design of experiments," *J. Ceram. Soc. Jpn.*, vol. 118, no. 1384, pp. 1166–1169, 2010, doi: 10.2109/jcersj2.118.1166.
- [52] K. Umeda, H. Kawai, A. Honda, M. Akiyama, T. Kato, and T. Fukura, "Piezoelectric properties of ScAlN thin films for piezo-MEMS devices," in *2013 IEEE 26th International Conference on Micro Electro Mechanical Systems (MEMS)*, Jan. 2013, pp. 733–736. doi: 10.1109/MEMSYS.2013.6474347.
- [53] F. K. Shaikh and S. Zeadally, "Energy harvesting in wireless sensor networks: A comprehensive review," *Renew. Sustain. Energy Rev.*, vol. 55, pp. 1041–1054, Mar. 2016, doi: 10.1016/j.rser.2015.11.010.
- [54] A. Cadei, A. Dionisi, E. Sardini, and M. Serpelloni, "Kinetic and thermal energy harvesters for implantable medical devices and biomedical autonomous sensors," *Meas. Sci. Technol.*, vol. 25, no. 1, p. 012003, Nov. 2013, doi: 10.1088/0957-0233/25/1/012003.

- [55] M. Q. Le *et al.*, “Review on energy harvesting for structural health monitoring in aeronautical applications,” *Prog. Aerosp. Sci.*, vol. 79, pp. 147–157, Nov. 2015, doi: 10.1016/j.paerosci.2015.10.001.
- [56] J. Davidson and C. Mo, “Recent Advances in Energy Harvesting Technologies for Structural Health Monitoring Applications,” *Smart Mater. Res.*, vol. 2014, p. e410316, Apr. 2014, doi: 10.1155/2014/410316.
- [57] B. Wang, Z. Long, Y. Hong, Q. Pan, W. Lin, and Z. Yang, “Woodpecker-mimic two-layer band energy harvester with a piezoelectric array for powering wrist-worn wearables,” *Nano Energy*, vol. 89, p. 106385, Nov. 2021, doi: 10.1016/j.nanoen.2021.106385.
- [58] S. Bai *et al.*, “Electromagnetic-triboelectric energy harvester based on vibration-to-rotation conversion for human motion energy exploitation,” *Appl. Energy*, vol. 329, p. 120292, Jan. 2023, doi: 10.1016/j.apenergy.2022.120292.
- [59] X. Le, Q. Shi, P. Vachon, E. J. Ng, and C. Lee, “Piezoelectric MEMS—evolution from sensing technology to diversified applications in the 5G/Internet of Things (IoT) era,” *J. Micromechanics Microengineering*, vol. 32, no. 1, p. 014005, Dec. 2021, doi: 10.1088/1361-6439/ac3ab9.
- [60] A. Harb, “Energy harvesting: State-of-the-art,” *Renew. Energy*, vol. 36, no. 10, pp. 2641–2654, Oct. 2011, doi: 10.1016/j.renene.2010.06.014.
- [61] O. Rubes, J. Chalupa, F. Ksica, and Z. Hadas, “Development and experimental validation of self-powered wireless vibration sensor node using vibration energy harvester,” *Mech. Syst. Signal Process.*, vol. 160, p. 107890, Nov. 2021, doi: 10.1016/j.ymsp.2021.107890.
- [62] J. Jang, David F. Berdy, J. Lee, D. Peroulis, and B. Jung, “A Wireless Condition Monitoring System Powered by a Sub-100 μW Vibration Energy Harvester,” *IEEE Trans. Circuits Syst. Regul. Pap.*, vol. 60, no. 4, pp. 1082–1093, Apr. 2013, doi: 10.1109/TCSI.2012.2215395.
- [63] G. J. Snyder, “Thermoelectric Energy Harvesting,” in *Energy Harvesting Technologies*, S. Priya and D. J. Inman, Eds. Boston, MA: Springer US, 2009, pp. 325–336. doi: 10.1007/978-0-387-76464-1_11.
- [64] A. Nozariasbmarz *et al.*, “Review of wearable thermoelectric energy harvesting: From body temperature to electronic systems,” *Appl. Energy*, vol. 258, p. 114069, Jan. 2020, doi: 10.1016/j.apenergy.2019.114069.
- [65] P. Teimourzadeh Baboli, D. Babazadeh, A. Raeiszadeh, S. Horodyvskyy, and I. Koprek, “Optimal Temperature-Based Condition Monitoring System for Wind Turbines,” *Infrastructures*, vol. 6, no. 4, Art. no. 4, Apr. 2021, doi: 10.3390/infrastructures6040050.
- [66] K. Fischer, M. Steffes, K. Pelka, B. Tegtmeier, and M. Dörenkämper, “Humidity in Power Converters of Wind Turbines—Field Conditions and Their Relation with Failures,” *Energies*, vol. 14, no. 7, Art. no. 7, Jan. 2021, doi: 10.3390/en14071919.
- [67] K. Worms *et al.*, “Lightning-safe Monitoring of Wind Turbine Rotor Blades Using Optically Powered Sensors,” in *Sensors and Measuring Systems 2014; 17. ITG/GMA Symposium*, Jun. 2014, pp. 1–4.
- [68] S. Selvan, M. Zaman, R. Gobbi, and H. Y. Wong, “Recent advances in the design and development of radio frequency-based energy harvester for powering wireless sensors: a review,” *J. Electromagn. Waves Appl.*, vol. 32, no. 16, pp. 2110–2134, Nov. 2018, doi: 10.1080/09205071.2018.1497548.
- [69] S. A. Bhalerao, A. V. Chaudhary, R. B. Deshmukh, and R. M. Patrikar, “Powering Wireless Sensor Nodes using Ambient RF Energy,” in *2006 IEEE International Conference on Systems, Man and Cybernetics*, Oct. 2006, vol. 4, pp. 2695–2700. doi: 10.1109/ICSMC.2006.385281.
- [70] E. Grundkötter and J. Melbert, “Adaptive power management of energy autonomous structural health monitoring systems for wind turbines,” in *2021 IEEE International Instrumentation and Measurement Technology Conference (I2MTC)*, May 2021, pp. 1–6. doi: 10.1109/I2MTC50364.2021.9459989.
- [71] H. J. Visser and R. J. M. Vullers, “RF Energy Harvesting and Transport for Wireless Sensor Network Applications: Principles and Requirements,” *Proc. IEEE*, vol. 101, no. 6, pp. 1410–1423, Jun. 2013, doi: 10.1109/JPROC.2013.2250891.

- [72] I. Gablech *et al.*, "Simple and Efficient AlN-Based Piezoelectric Energy Harvesters," *Micromachines*, vol. 11, no. 2, Art. no. 2, Feb. 2020, doi: 10.3390/mi11020143.
- [73] S. W. Ibrahim and W. G. Ali, "A review on frequency tuning methods for piezoelectric energy harvesting systems," *J. Renew. Sustain. Energy*, vol. 4, no. 6, p. 062703, Nov. 2012, doi: 10.1063/1.4766892.
- [74] X. He, D. Li, H. Zhou, X. Hui, and X. Mu, "Theoretical and Experimental Studies on MEMS Variable Cross-Section Cantilever Beam Based Piezoelectric Vibration Energy Harvester," *Micromachines*, vol. 12, no. 7, Art. no. 7, Jul. 2021, doi: 10.3390/mi12070772.
- [75] Y. Liu *et al.*, "Design and Performance of ScAlN/AlN Trapezoidal Cantilever-Based MEMS Piezoelectric Energy Harvesters," *IEEE Trans. Electron Devices*, vol. 68, no. 6, pp. 2971–2976, Jun. 2021, doi: 10.1109/TED.2021.3072612.
- [76] S. Du *et al.*, "A new electrode design method in piezoelectric vibration energy harvesters to maximize output power," *Sens. Actuators Phys.*, vol. 263, pp. 693–701, Aug. 2017, doi: 10.1016/j.sna.2017.06.026.
- [77] L. Deng, Z. Wen, X. Zhao, C. Yuan, G. Luo, and J. Mo, "High Voltage Output MEMS Vibration Energy Harvester in ₃₁ Mode With PZT Thin Film," *J. Microelectromechanical Syst.*, vol. 23, no. 4, pp. 855–861, Aug. 2014, doi: 10.1109/JMEMS.2013.2296034.
- [78] D. Pan and F. Dai, "Design and analysis of a broadband vibratory energy harvester using bi-stable piezoelectric composite laminate," *Energy Convers. Manag.*, vol. 169, pp. 149–160, Aug. 2018, doi: 10.1016/j.enconman.2018.05.032.
- [79] S. S. Chauhan, M. M. Joglekar, and S. K. Manhas, "High Power Density CMOS Compatible Micro-Machined MEMs Energy Harvester," *IEEE Sens. J.*, vol. 19, no. 20, pp. 9122–9130, Oct. 2019, doi: 10.1109/JSEN.2019.2923972.
- [80] H. Liu, H. Fu, L. Sun, C. Lee, and E. M. Yeatman, "Hybrid energy harvesting technology: From materials, structural design, system integration to applications," *Renew. Sustain. Energy Rev.*, vol. 137, p. 110473, Mar. 2021, doi: 10.1016/j.rser.2020.110473.
- [81] Q. C. Tang, Y. L. Yang, and X. Li, "Bi-stable frequency up-conversion piezoelectric energy harvester driven by non-contact magnetic repulsion," *Smart Mater. Struct.*, vol. 20, no. 12, p. 125011, Nov. 2011, doi: 10.1088/0964-1726/20/12/125011.
- [82] N. Chen, T. Wei, H. J. Jung, and S. Lee, "Quick self-start and minimum power-loss management circuit for impact-type micro wind piezoelectric energy harvesters," *Sens. Actuators Phys.*, vol. 263, pp. 23–29, Aug. 2017, doi: 10.1016/j.sna.2017.05.042.
- [83] H. J. Jung, D. Song, S. K. Hong, Y. Song, and T. H. Sung, "Effective Piezoelectric Area for Hitting-Type Piezoelectric Energy Harvesting System," *Jpn. J. Appl. Phys.*, vol. 52, no. 10S, p. 10MB03, Oct. 2013, doi: 10.7567/JJAP.52.10MB03.
- [84] W.-H. Wu, K.-C. Kuo, Y.-H. Lin, and Y.-C. Tsai, "Non-contact magnetic cantilever-type piezoelectric energy harvester for rotational mechanism," *Microelectron. Eng.*, vol. 191, pp. 16–19, May 2018, doi: 10.1016/j.mee.2018.01.026.
- [85] E. Fakeih, A. S. Almansouri, J. Kosel, M. I. Younis, and K. N. Salama, "A Wideband Magnetic Frequency Up-Converter Energy Harvester," *Adv. Eng. Mater.*, vol. 23, no. 6, p. 2001364, 2021, doi: 10.1002/adem.202001364.
- [86] Z. Xu, W. Wang, J. Xie, Z. Xu, M. Zhou, and H. Yang, "An Impact-Based Frequency Up-Converting Hybrid Vibration Energy Harvester for Low Frequency Application," *Energies*, vol. 10, no. 11, Art. no. 11, Nov. 2017, doi: 10.3390/en10111761.
- [87] L. Gu and C. Livermore, "Impact-driven, frequency up-converting coupled vibration energy harvesting device for low frequency operation," *Smart Mater. Struct.*, vol. 20, no. 4, p. 045004, Mar. 2011, doi: 10.1088/0964-1726/20/4/045004.
- [88] Z. Li, Z. Yan, J. Luo, and Z. Yang, "Performance comparison of electromagnetic energy harvesters based on magnet arrays of alternating polarity and configuration," *Energy Convers. Manag.*, vol. 179, pp. 132–140, Jan. 2019, doi: 10.1016/j.enconman.2018.10.060.
- [89] A. Luo *et al.*, "An inertial rotary energy harvester for vibrations at ultra-low frequency with high energy conversion efficiency," *Appl. Energy*, vol. 279, p. 115762, Dec. 2020, doi: 10.1016/j.apenergy.2020.115762.

- [90] A. Nammari, L. Caskey, J. Negrete, and H. Bardaweel, "Fabrication and characterization of non-resonant magneto-mechanical low-frequency vibration energy harvester," *Mech. Syst. Signal Process.*, vol. 102, pp. 298–311, Mar. 2018, doi: 10.1016/j.ymssp.2017.09.036.
- [91] L. B. Zhang, H. L. Dai, Y. W. Yang, and L. Wang, "Design of high-efficiency electromagnetic energy harvester based on a rolling magnet," *Energy Convers. Manag.*, vol. 185, pp. 202–210, Apr. 2019, doi: 10.1016/j.enconman.2019.01.089.
- [92] K. Fan, S. Liu, H. Liu, Y. Zhu, W. Wang, and D. Zhang, "Scavenging energy from ultra-low frequency mechanical excitations through a bi-directional hybrid energy harvester," *Appl. Energy*, vol. 216, pp. 8–20, Apr. 2018, doi: 10.1016/j.apenergy.2018.02.086.
- [93] Q. Luo, X. He, S. Jiang, and X. Wang, "Impact-Based Electromagnetic Energy Harvester with High Output Voltage under Low-Level Excitations," *Energies*, vol. 10, no. 11, Art. no. 11, Nov. 2017, doi: 10.3390/en10111848.
- [94] Y. Shen and K. Lu, "Scavenging power from ultra-low frequency and large amplitude vibration source through a new non-resonant electromagnetic energy harvester," *Energy Convers. Manag.*, vol. 222, p. 113233, Oct. 2020, doi: 10.1016/j.enconman.2020.113233.
- [95] K. Fan, Y. Zhang, H. Liu, M. Cai, and Q. Tan, "A nonlinear two-degree-of-freedom electromagnetic energy harvester for ultra-low frequency vibrations and human body motions," *Renew. Energy*, vol. 138, pp. 292–302, Aug. 2019, doi: 10.1016/j.renene.2019.01.105.
- [96] M. Martinez-Luengo, A. Kolios, and L. Wang, "Structural health monitoring of offshore wind turbines: A review through the Statistical Pattern Recognition Paradigm," *Renew. Sustain. Energy Rev.*, vol. 64, pp. 91–105, Oct. 2016, doi: 10.1016/j.rser.2016.05.085.
- [97] K. Schroeder, W. Ecke, J. Aplitz, E. Lembke, and G. Lenschow, "A fibre Bragg grating sensor system monitors operational load in a wind turbine rotor blade," *Meas. Sci. Technol.*, vol. 17, no. 5, p. 1167, Apr. 2006, doi: 10.1088/0957-0233/17/5/S39.
- [98] M. Benedetti, V. Fontanari, and D. Zonta, "Structural health monitoring of wind towers: remote damage detection using strain sensors," *Smart Mater. Struct.*, vol. 20, no. 5, p. 055009, Apr. 2011, doi: 10.1088/0964-1726/20/5/055009.
- [99] T. Rubert *et al.*, "Field Demonstration of Real-Time Wind Turbine Foundation Strain Monitoring," *Sensors*, vol. 18, no. 1, Art. no. 1, Jan. 2018, doi: 10.3390/s18010097.
- [100] P. K. Stein, "A Brief History of Bonded Resistance Strain Gages from Conception to Commercialization," *Exp. Tech.*, vol. 14, no. 5, pp. 13–19, 1990, doi: 10.1111/j.1747-1567.1990.tb01474.x.
- [101] A. C. Ruge, "Strain gauge," US2350972A, Jun. 06, 1944 Accessed: Nov. 28, 2021. [Online]. Available: <https://patents.google.com/patent/US2350972A/en>
- [102] A. Maskay and M. Pereira da Cunha, "High-temperature static strain langasite SAWR sensor: Temperature compensation and numerical calibration for direct strain reading," *Sens. Actuators Phys.*, vol. 259, pp. 34–43, Jun. 2017, doi: 10.1016/j.sna.2017.03.023.
- [103] K. E. Wojciechowski, B. E. Boser, and A. P. Pisano, "A MEMS resonant strain sensor operated in air," in *17th IEEE International Conference on Micro Electro Mechanical Systems. Maastricht MEMS 2004 Technical Digest*, Jan. 2004, pp. 841–845. doi: 10.1109/MEMS.2004.1290718.
- [104] D. J. Lichtenwalner, A. E. Hydrick, and A. I. Kingon, "Flexible thin film temperature and strain sensor array utilizing a novel sensing concept," *Sens. Actuators Phys.*, vol. 135, no. 2, pp. 593–597, Apr. 2007, doi: 10.1016/j.sna.2006.07.019.
- [105] V. Yokaribas, P. Kraemer, A. B. Mende, J. Ruhkopf, M. C. Lemme, and C.-P. Fritzen, "Novel Methodologies for Multiaxial Strain Measurements with Piezoresistive Films based on Graphene Nanoplatelets," *Small Sci.*, vol. n/a, no. n/a, p. 2100088, doi: 10.1002/smssc.202100088.
- [106] J. Shen, T. Wang, Y. Luo, X. Zeng, and C. Cao, "Study on the influence of transverse effect on strain monitoring of space station," *Optik*, vol. 178, pp. 794–801, Feb. 2019, doi: 10.1016/j.ijleo.2018.09.087.

- [107] B. Maundy and S. J. G. Gift, "Strain Gauge Amplifier Circuits," *IEEE Trans. Instrum. Meas.*, vol. 62, no. 4, pp. 693–700, Apr. 2013, doi: 10.1109/TIM.2013.2246904.
- [108] A. S. Fiorillo, C. D. Critello, and S. A. Pullano, "Theory, technology and applications of piezoresistive sensors: A review," *Sens. Actuators Phys.*, vol. 281, pp. 156–175, Oct. 2018, doi: 10.1016/j.sna.2018.07.006.
- [109] P. Schmid *et al.*, "Influence of the AlN/Pt-ratio on the electro-mechanical properties of multilayered AlN/Pt thin film strain gauges at high temperatures," *Sens. Actuators Phys.*, vol. 302, p. 111805, Feb. 2020, doi: 10.1016/j.sna.2019.111805.
- [110] Y.-C. Lu, C.-Y. Chiang, Y.-C. Chen, Y.-C. Lin, T. Ono, and Y.-C. Tsai, "Study and fabrication of a flexible Zr-based metallic glass thin film strain gauge," *Jpn. J. Appl. Phys.*, vol. 59, no. SI, p. SIIG10, Apr. 2020, doi: 10.35848/1347-4065/ab7f1b.
- [111] M. L. Meyer, "A unified rational analysis for gauge factor and cross-sensitivity of electric-resistance strain gauges," *J. Strain Anal.*, vol. 2, no. 4, pp. 324–331, Oct. 1967, doi: 10.1243/03093247V024324.
- [112] C. S. Smith, "Piezoresistance Effect in Germanium and Silicon," *Phys. Rev.*, vol. 94, no. 1, pp. 42–49, Apr. 1954, doi: 10.1103/PhysRev.94.42.
- [113] W. D. Edwards and R. P. Beaulieu, "Germanium piezoresistive element on a flexible substrate," *J. Phys. [E]*, vol. 2, no. 7, pp. 613–615, Jul. 1969, doi: 10.1088/0022-3735/2/7/314.
- [114] X. Li *et al.*, "Giant Piezoresistance in B-Doped SiC Nanobelts with a Gauge Factor of –1800," *ACS Appl. Mater. Interfaces*, vol. 12, no. 42, pp. 47848–47853, Oct. 2020, doi: 10.1021/acami.0c13800.
- [115] C. Stampfer, A. Jungen, R. Linderman, D. Obergfell, S. Roth, and C. Hierold, "Nano-Electromechanical Displacement Sensing Based on Single-Walled Carbon Nanotubes," *Nano Lett.*, vol. 6, no. 7, pp. 1449–1453, Jul. 2006, doi: 10.1021/nl0606527.
- [116] P. Moyo, J. M. W. Brownjohn, R. Suresh, and S. C. Tjin, "Development of fiber Bragg grating sensors for monitoring civil infrastructure," *Eng. Struct.*, vol. 27, no. 12, pp. 1828–1834, Oct. 2005, doi: 10.1016/j.engstruct.2005.04.023.
- [117] H.-E. Joe, H. Yun, S.-H. Jo, M. B. G. Jun, and B.-K. Min, "A review on optical fiber sensors for environmental monitoring," *Int. J. Precis. Eng. Manuf.-Green Technol.*, vol. 5, no. 1, pp. 173–191, Jan. 2018, doi: 10.1007/s40684-018-0017-6.
- [118] F. M. Sánchez-Arévalo and G. Pulos, "Use of digital image correlation to determine the mechanical behavior of materials," *Mater. Charact.*, vol. 59, no. 11, pp. 1572–1579, Nov. 2008, doi: 10.1016/j.matchar.2008.02.002.
- [119] J. Sirohi and M. S. Lawson, "Measurement of helicopter rotor blade deformation using digital image correlation," *Opt. Eng.*, vol. 51, no. 4, p. 043603, Apr. 2012, doi: 10.1117/1.OE.51.4.043603.
- [120] S. Li, X. Li, Y. Qin, and Y. Zhao, "Local strain gauge based on the nanowires ring resonator embedded in a flexible substrate," *Micro Nano Lett.*, vol. 15, no. 14, pp. 1028–1032, 2020, doi: 10.1049/mnl.2020.0313.
- [121] Y. Fuji *et al.*, "An ultra-sensitive spintronic strain-gauge sensor with gauge factor of 5000 and demonstration of a Spin-MEMS Microphone," in *2017 19th International Conference on Solid-State Sensors, Actuators and Microsystems (TRANSDUCERS)*, Jun. 2017, pp. 63–66. doi: 10.1109/TRANSDUCERS.2017.7993988.
- [122] J. G. Njiri, N. Beganovic, M. H. Do, and D. Söffker, "Consideration of lifetime and fatigue load in wind turbine control," *Renew. Energy*, vol. 131, pp. 818–828, Feb. 2019, doi: 10.1016/j.renene.2018.07.109.
- [123] E. Weymar and M. Finkbeiner, "Statistical analysis of empirical lifetime mileage data for automotive LCA," *Int. J. Life Cycle Assess.*, vol. 21, no. 2, pp. 215–223, Feb. 2016, doi: 10.1007/s11367-015-1020-6.
- [124] D. Platz and U. Schmid, "Vibrational modes in MEMS resonators," *J. Micromechanics Microengineering*, vol. 29, no. 12, p. 123001, Oct. 2019, doi: 10.1088/1361-6439/ab4bad.

- [125] G. Pfusterschmied *et al.*, “Roof tile-shaped modes in quasi free–free supported piezoelectric microplate resonators in high viscous fluids,” *Sens. Actuators B Chem.*, vol. 237, pp. 999–1006, Dec. 2016, doi: 10.1016/j.snb.2016.02.029.
- [126] M. Schneider, G. Pfusterschmied, F. Patocka, and U. Schmid, “High performance piezoelectric AlN MEMS resonators for precise sensing in liquids,” *E Elektrotechnik Informationstechnik*, vol. 137, no. 3, pp. 121–127, Jun. 2020, doi: 10.1007/s00502-020-00794-w.
- [127] F. Patocka, M. Schneider, N. Dörr, C. Schneidhofer, and U. Schmid, “Position-dependent mass responsivity of silicon MEMS cantilevers excited in the fundamental, two-dimensional roof tile-shaped mode,” *J. Micromechanics Microengineering*, vol. 29, no. 4, p. 045009, Feb. 2019, doi: 10.1088/1361-6439/ab062a.
- [128] S. Ghosh and J. E.-Y. Lee, “Resonant tuning fork strain gauge operating in air with decoupled piezoelectric transducers,” in *2017 IEEE SENSORS*, Oct. 2017, pp. 1–3. doi: 10.1109/ICSENS.2017.8234100.
- [129] C. D. Do, A. Erbes, J. Yan, K. Soga, and A. A. Seshia, “Vacuum Packaged Low-Power Resonant MEMS Strain Sensor,” *J. Microelectromechanical Syst.*, vol. 25, no. 5, pp. 851–858, Oct. 2016, doi: 10.1109/JMEMS.2016.2587867.
- [130] F. T. Goericke, M. W. Chan, G. Vigevani, I. Izyumin, B. E. Boser, and A. P. Pisano, “High temperature compatible aluminum nitride resonating strain sensor,” in *2011 16th International Solid-State Sensors, Actuators and Microsystems Conference*, Jun. 2011, pp. 1994–1997. doi: 10.1109/TRANSDUCERS.2011.5969198.
- [131] R. G. Azevedo *et al.*, “A SiC MEMS Resonant Strain Sensor for Harsh Environment Applications,” *IEEE Sens. J.*, vol. 7, no. 4, pp. 568–576, Apr. 2007, doi: 10.1109/JSEN.2007.891997.
- [132] L. Belsito, M. Bosi, F. Mancarella, M. Ferri, and A. Roncaglia, “Nanostrain Resolution Strain Sensing by Monocrystalline 3C-SiC on SOI Electrostatic MEMS Resonators,” *J. Microelectromechanical Syst.*, vol. 29, no. 1, pp. 117–128, Feb. 2020, doi: 10.1109/JMEMS.2019.2949656.
- [133] M. W. Chan, D. R. Myers, B. D. Sosnowchik, L. Lin, and A. P. Pisano, “Localized strain sensing using high spatial resolution, highly-sensitive MEMS resonant strain gauges for failure prevention,” in *2011 16th International Solid-State Sensors, Actuators and Microsystems Conference*, Jun. 2011, pp. 2859–2862. doi: 10.1109/TRANSDUCERS.2011.5969185.
- [134] L. Belsito *et al.*, “Fabrication of high-resolution strain sensors based on wafer-level vacuum packaged MEMS resonators,” *Sens. Actuators Phys.*, vol. 239, pp. 90–101, Mar. 2016, doi: 10.1016/j.sna.2016.01.006.
- [135] M. Suster, J. Guo, N. Chaimanonart, W. H. Ko, and D. J. Young, “A High-Performance MEMS Capacitive Strain Sensing System,” *J. Microelectromechanical Syst.*, vol. 15, no. 5, pp. 1069–1077, Oct. 2006, doi: 10.1109/JMEMS.2006.881489.
- [136] C. Zhang, S.-Y. Zhang, and L.-F. Wang, “A Sawtooth MEMS Capacitive Strain Sensor for Passive Telemetry in Bearings,” *IEEE Sens. J.*, vol. 21, no. 20, pp. 22527–22535, Oct. 2021, doi: 10.1109/JSEN.2021.3107441.
- [137] P. Song, G. Wang, and Y. Zhang, “Preparation and performance of graphene/carbon black silicone rubber composites used for highly sensitive and flexible strain sensors,” *Sens. Actuators Phys.*, vol. 323, p. 112659, Jun. 2021, doi: 10.1016/j.sna.2021.112659.
- [138] D. Depla, S. Mahieu, and J. E. Greene, “Chapter 5 - Sputter Deposition Processes,” in *Handbook of Deposition Technologies for Films and Coatings (Third Edition)*, P. M. Martin, Ed. Boston: William Andrew Publishing, 2010, pp. 253–296. doi: 10.1016/B978-0-8155-2031-3.00005-3.
- [139] M. Steward and M. G. Cain, “Direct Piezoelectric Measurement: The Berlincourt Method,” *springerprofessional.de*. <https://www.springerprofessional.de/en/direct-piezoelectric-measurement-the-berlincourt-method/1643972> (accessed Mar. 24, 2022).
- [140] C. G. Pope, “X-Ray Diffraction and the Bragg Equation,” *J. Chem. Educ.*, vol. 74, no. 1, p. 129, Jan. 1997, doi: 10.1021/ed074p129.

- [141] M. Miyanaga, N. Mizuhara, S. Fujiwara, M. Shimazu, H. Nakahata, and T. Kawase, "Evaluation of AlN single-crystal grown by sublimation method," *J. Cryst. Growth*, vol. 300, no. 1, pp. 45–49, Mar. 2007, doi: 10.1016/j.jcrysgro.2006.10.233.
- [142] D. Mani, A. Kupsch, B. R. Müller, and G. Bruno, "Diffraction Enhanced Imaging Analysis with Pseudo-Voigt Fit Function," *J. Imaging*, vol. 8, no. 8, Art. no. 8, Aug. 2022, doi: 10.3390/jimaging8080206.
- [143] A. Sanz-Hervás, M. Clement, E. Iborra, L. Vergara, J. Olivares, and J. Sangrador, "Degradation of the piezoelectric response of sputtered c-axis AlN thin films with traces of non-(0002) x-ray diffraction peaks," *Appl. Phys. Lett.*, vol. 88, no. 16, p. 161915, Apr. 2006, doi: 10.1063/1.2191425.
- [144] B. J. Inkson, "2 - Scanning electron microscopy (SEM) and transmission electron microscopy (TEM) for materials characterization," in *Materials Characterization Using Nondestructive Evaluation (NDE) Methods*, G. Hübschen, I. Altpeter, R. Tschuncky, and H.-G. Herrmann, Eds. Woodhead Publishing, 2016, pp. 17–43. doi: 10.1016/B978-0-08-100040-3.00002-X.
- [145] S. J. Rothberg *et al.*, "An international review of laser Doppler vibrometry: Making light work of vibration measurement," *Opt. Lasers Eng.*, vol. 99, pp. 11–22, Dec. 2017, doi: 10.1016/j.optlaseng.2016.10.023.
- [146] Y. Fujino, K. Kaito, and M. Abe, "Detection of structural damage by ambient vibration measurement using laser Doppler vibrometer," in *Health Monitoring and Management of Civil Infrastructure Systems*, Aug. 2001, vol. 4337, pp. 167–178. doi: 10.1117/12.435589.
- [147] L. Scislo, "Quality Assurance and Control of Steel Blade Production Using Full Non-Contact Frequency Response Analysis and 3D Laser Doppler Scanning Vibrometry System," in *2021 11th IEEE International Conference on Intelligent Data Acquisition and Advanced Computing Systems: Technology and Applications (IDAACS)*, Sep. 2021, vol. 1, pp. 419–423. doi: 10.1109/IDAACS53288.2021.9661060.
- [148] A. Ratner *et al.*, "Laser Doppler Vibrometry for Evaluating the Quality of Welds in Lithium-Ion Supercells," *Energies*, vol. 15, no. 12, Art. no. 12, Jan. 2022, doi: 10.3390/en15124379.
- [149] L. Antognoli, S. Moccia, L. Migliorelli, S. Casaccia, L. Scalise, and E. Frontoni, "Heartbeat Detection by Laser Doppler Vibrometry and Machine Learning," *Sensors*, vol. 20, no. 18, Art. no. 18, Jan. 2020, doi: 10.3390/s20185362.
- [150] D. M. Siringoringo and Y. Fujino, "Noncontact Operational Modal Analysis of Structural Members by Laser Doppler Vibrometer," *Comput.-Aided Civ. Infrastruct. Eng.*, vol. 24, no. 4, pp. 249–265, 2009, doi: 10.1111/j.1467-8667.2008.00585.x.
- [151] P. Castellini, M. Martarelli, and E. P. Tomasini, "Laser Doppler Vibrometry: Development of advanced solutions answering to technology's needs," *Mech. Syst. Signal Process.*, vol. 20, no. 6, pp. 1265–1285, Aug. 2006, doi: 10.1016/j.ymsp.2005.11.015.
- [152] O. A. Bauchau and J. I. Craig, "Euler-Bernoulli beam theory," in *Structural Analysis*, O. A. Bauchau and J. I. Craig, Eds. Dordrecht: Springer Netherlands, 2009, pp. 173–221. doi: 10.1007/978-90-481-2516-6_5.
- [153] M. Schlögl, M. Schneider, and U. Schmid, "Piezoelectricity in Y0.09Al0.91N thin films," *Mater. Sci. Eng. B*, vol. 276, p. 115543, Feb. 2022, doi: 10.1016/j.mseb.2021.115543.
- [154] M. Schlögl, J. Weißenbach, M. Schneider, and U. Schmid, "Stress engineering of polycrystalline aluminum nitride thin films for strain sensing with resonant piezoelectric microbridges," *Sens. Actuators Phys.*, vol. 349, p. 114067, Jan. 2023, doi: 10.1016/j.sna.2022.114067.
- [155] N. D. Patel and P. S. Nicholson, "High frequency, high temperature ultrasonic transducers," *NDT Int.*, vol. 23, no. 5, pp. 262–266, Oct. 1990, doi: 10.1016/0308-9126(90)92152-Q.
- [156] Z. Cheng *et al.*, "Experimental observation of high intrinsic thermal conductivity of AlN," *Phys. Rev. Mater.*, vol. 4, no. 4, p. 044602, Apr. 2020, doi: 10.1103/PhysRevMaterials.4.044602.
- [157] M. Schneider, A. Bittner, A. Klein, and U. Schmid, "Impact of film thickness and temperature on the dielectric breakdown behavior of sputtered aluminum nitride thin films," *Microelectron. Eng.*, vol. 140, pp. 47–51, Jun. 2015, doi: 10.1016/j.mee.2015.06.001.

- [158] A. Severino and F. Iucolano, "Impact of growth conditions on stress and quality of aluminum nitride (AlN) thin buffer layers," *Phys. Status Solidi B*, vol. 253, no. 5, pp. 801–808, 2016, doi: 10.1002/pssb.201552638.
- [159] S. Dai *et al.*, "Study on Preparation, Thermal Conductivity, and Electrical Insulation Properties of Epoxy/AlN," *IEEE Trans. Appl. Supercond.*, vol. 29, no. 2, pp. 1–6, Mar. 2019, doi: 10.1109/TASC.2018.2890752.
- [160] M. Haruguchi, M. Hayashi, K. Irikura, H. Habuka, and Y. Takahashi, "Anticorrosive Behavior of Aluminum Nitride Surface Exposed to Chlorine Trifluoride Gas at High Temperatures," *ECS J. Solid State Sci. Technol.*, vol. 10, no. 3, p. 034006, Mar. 2021, doi: 10.1149/2162-8777/abea5d.
- [161] H. Hoche, S. Groß, T. Troßmann, J. Schmidt, and M. Oechsner, "PVD coating and substrate pretreatment concepts for magnesium alloys by multinary coatings based on Ti(X)N," *Surf. Coat. Technol.*, vol. 228, pp. S336–S341, Aug. 2013, doi: 10.1016/j.surfcoat.2012.05.106.
- [162] G. Krugel, A. Sharma, W. Wolke, J. Rentsch, and R. Preu, "Study of hydrogenated AlN as an anti-reflective coating and for the effective surface passivation of silicon," *Phys. Status Solidi RRL – Rapid Res. Lett.*, vol. 7, no. 7, pp. 457–460, 2013, doi: 10.1002/pssr.201307153.
- [163] H. Kim, Y. Kwon, and B. J. Choi, "AlN passivation effect on Au/GaN Schottky contacts," *Thin Solid Films*, vol. 670, pp. 41–45, Jan. 2019, doi: 10.1016/j.tsf.2018.12.008.
- [164] J. R. Grandusky, S. R. Gibb, M. C. Mendrick, and L. J. Schowalter, "Properties of Mid-Ultraviolet Light Emitting Diodes Fabricated from Pseudomorphic Layers on Bulk Aluminum Nitride Substrates," *Appl. Phys. Express*, vol. 3, no. 7, p. 072103, Jul. 2010, doi: 10.1143/APEX.3.072103.
- [165] M. W. Jeong, S. W. Jeon, S. H. Lee, and Y. Kim, "Effective heat dissipation and geometric optimization in an LED module with aluminum nitride (AlN) insulation plate," *Appl. Therm. Eng.*, vol. 76, pp. 212–219, Feb. 2015, doi: 10.1016/j.applthermaleng.2014.11.027.
- [166] C.-P. Wang, Y.-C. Huang, and H.-Q. Liu, "Efficiency improvement of power LED modules using a hybrid aluminum nitride substrate," *Microelectron. Eng.*, vol. 223, p. 111227, Feb. 2020, doi: 10.1016/j.mee.2020.111227.
- [167] F. Patocka, C. Schneidhofer, N. Dörr, M. Schneider, and U. Schmid, "Novel resonant MEMS sensor for the detection of particles with dielectric properties in aged lubricating oils," *Sens. Actuators Phys.*, vol. 315, p. 112290, Nov. 2020, doi: 10.1016/j.sna.2020.112290.
- [168] R. M. R. Pinto, V. Gund, R. A. Dias, K. K. Nagaraja, and K. B. Vinayakumar, "CMOS-Integrated Aluminum Nitride MEMS: A Review," *J. Microelectromechanical Syst.*, vol. 31, no. 4, pp. 500–523, Aug. 2022, doi: 10.1109/JMEMS.2022.3172766.
- [169] P. Li, Y. Luo, L. Guo, and Y. Zhang, "Design and simulation of an aluminum nitride piezoelectric resonant pressure sensor," *AIP Adv.*, vol. 12, no. 6, p. 065320, Jun. 2022, doi: 10.1063/5.0088626.
- [170] F. Patocka, M. Schlögl, C. Schneidhofer, N. Dörr, M. Schneider, and U. Schmid, "Piezoelectrically excited MEMS sensor with integrated planar coil for the detection of ferrous particles in liquids," *Sens. Actuators B Chem.*, vol. 299, p. 126957, Nov. 2019, doi: 10.1016/j.snb.2019.126957.
- [171] M. Nemoz, R. Dagher, S. Matta, A. Michon, P. Vennéguès, and J. Brault, "Dislocation densities reduction in MBE-grown AlN thin films by high-temperature annealing," *J. Cryst. Growth*, vol. 461, pp. 10–15, Mar. 2017, doi: 10.1016/j.jcrysgr.2016.12.089.
- [172] C.-P. Huang, K. Gupta, C.-H. Wang, C.-P. Liu, and K.-Y. Lai, "High-quality AlN grown with a single substrate temperature below 1200 °C," *Sci. Rep.*, vol. 7, no. 1, Art. no. 1, Aug. 2017, doi: 10.1038/s41598-017-07616-8.
- [173] W. Wang, W. Yang, Z. Liu, H. Wang, L. Wen, and G. Li, "Interfacial reaction control and its mechanism of AlN epitaxial films grown on Si(111) substrates by pulsed laser deposition," *Sci. Rep.*, vol. 5, no. 1, Art. no. 1, Jun. 2015, doi: 10.1038/srep11480.
- [174] A. Sanz-Hervás *et al.*, "Comparative study of c-axis AlN films sputtered on metallic surfaces," *Diam. Relat. Mater.*, vol. 14, no. 3, pp. 1198–1202, Mar. 2005, doi: 10.1016/j.diamond.2004.11.010.

- [175] M.-A. Dubois and P. Muralt, "Stress and piezoelectric properties of aluminum nitride thin films deposited onto metal electrodes by pulsed direct current reactive sputtering," *J. Appl. Phys.*, vol. 89, no. 11, pp. 6389–6395, Jun. 2001, doi: 10.1063/1.1359162.
- [176] A. Ababneh, U. Schmid, J. Hernando, J. L. Sánchez-Rojas, and H. Seidel, "The influence of sputter deposition parameters on piezoelectric and mechanical properties of AlN thin films," *Mater. Sci. Eng. B*, vol. 172, no. 3, pp. 253–258, Sep. 2010, doi: 10.1016/j.mseb.2010.05.026.
- [177] C. Fei *et al.*, "AlN piezoelectric thin films for energy harvesting and acoustic devices," *Nano Energy*, vol. 51, pp. 146–161, Sep. 2018, doi: 10.1016/j.nanoen.2018.06.062.
- [178] N. S. VanDamme, S. M. Richard, and S. R. Winzer, "Liquid-Phase Sintering of Aluminum Nitride by Europium Oxide Additives," *J. Am. Ceram. Soc.*, vol. 72, no. 8, pp. 1409–1414, 1989, doi: 10.1111/j.1151-2916.1989.tb07662.x.
- [179] Q. X. Guo, K. Yahata, T. Tanaka, M. Nishio, and H. Ogawa, "Low-temperature growth of aluminum nitride on sapphire substrates," *J. Cryst. Growth*, vol. 257, no. 1, pp. 123–128, Sep. 2003, doi: 10.1016/S0022-0248(03)01565-3.
- [180] Y. Huttel, H. Gomez, A. Cebollada, G. Armelles, and M. I. Alonso, "Epitaxial growth of AlN on sapphire (0001) by sputtering: a structural, morphological and optical study," *J. Cryst. Growth*, vol. 242, no. 1, pp. 116–123, Jul. 2002, doi: 10.1016/S0022-0248(02)01375-1.
- [181] H. Okano, Y. Takahashi, T. Tanaka, K. S. K. Shibata, and S. N. S. Nakano, "Preparation of c-Axis Oriented AlN Thin Films by Low-Temperature Reactive Sputtering," *Jpn. J. Appl. Phys.*, vol. 31, no. 10R, p. 3446, Oct. 1992, doi: 10.1143/JJAP.31.3446.
- [182] Z.-H. Chen, C. Li, Y.-H. Chen, S. Chu, C.-C. Tsai, and C.-S. Hong, "Enhancement of c-Axis Oriented Aluminum Nitride Films via Low Temperature DC Sputtering," *IEEE Sens. J.*, vol. 21, no. 16, pp. 17673–17677, Aug. 2021, doi: 10.1109/JSEN.2021.3077274.
- [183] F. Martin, P. Muralt, M.-A. Dubois, and A. Pezous, "Thickness dependence of the properties of highly c-axis textured AlN thin films," *J. Vac. Sci. Technol. A*, vol. 22, no. 2, pp. 361–365, Mar. 2004, doi: 10.1116/1.1649343.
- [184] S. Pawar, K. Singh, S. Sharma, A. Pandey, S. Dutta, and D. Kaur, "Growth assessment and scrutinize dielectric reliability of c-axis oriented insulating AlN thin films in MIM structures for microelectronics applications," *Mater. Chem. Phys.*, vol. 219, pp. 74–81, Nov. 2018, doi: 10.1016/j.matchemphys.2018.08.013.
- [185] R. B. Karabalin *et al.*, "Piezoelectric nanoelectromechanical resonators based on aluminum nitride thin films," *Appl. Phys. Lett.*, vol. 95, no. 10, p. 103111, Sep. 2009, doi: 10.1063/1.3216586.
- [186] N. Sinha *et al.*, "Piezoelectric aluminum nitride nanoelectromechanical actuators," *Appl. Phys. Lett.*, vol. 95, no. 5, p. 053106, Aug. 2009, doi: 10.1063/1.3194148.
- [187] B. Narayanan KN, D. R. Nair, and A. DasGupta, "Extraction of D31 Piezoelectric Coefficient of AlN Thin Film," in *2021 IEEE 34th International Conference on Micro Electro Mechanical Systems (MEMS)*, Jan. 2021, pp. 623–625. doi: 10.1109/MEMS51782.2021.9375172.
- [188] S. Muensit, E. M. Goldys, and I. L. Guy, "Shear piezoelectric coefficients of gallium nitride and aluminum nitride," *Appl. Phys. Lett.*, vol. 75, no. 25, pp. 3965–3967, Dec. 1999, doi: 10.1063/1.125508.
- [189] H. Kim, S. Kerrigan, M. Bourham, and X. Jiang, "AlN Single Crystal Accelerometer for Nuclear Power Plants," *IEEE Trans. Ind. Electron.*, vol. 68, no. 6, pp. 5346–5354, Jun. 2021, doi: 10.1109/TIE.2020.2992002.
- [190] S. Marauska *et al.*, "Sputtered thin film piezoelectric aluminum nitride as a functional MEMS material," *Microsyst. Technol.*, vol. 18, no. 6, pp. 787–795, Jun. 2012, doi: 10.1007/s00542-012-1493-1.
- [191] V. V. Felmetzger, P. N. Laptev, and S. M. Tanner, "Innovative technique for tailoring intrinsic stress in reactively sputtered piezoelectric aluminum nitride films," *J. Vac. Sci. Technol. A*, vol. 27, no. 3, pp. 417–422, May 2009, doi: 10.1116/1.3089242.
- [192] M. Schneider, A. Bittner, and U. Schmid, "Thickness dependence of Young's modulus and residual stress of sputtered aluminum nitride thin films," *Appl. Phys. Lett.*, vol. 105, no. 20, p. 201912, Nov. 2014, doi: 10.1063/1.4902448.

- [193] M. Gillinger, M. Schneider, A. Bittner, P. Nicolay, and U. Schmid, "Impact of annealing temperature on the mechanical and electrical properties of sputtered aluminum nitride thin films," *J. Appl. Phys.*, vol. 117, no. 6, p. 065303, Feb. 2015, doi: 10.1063/1.4907208.
- [194] N. R. Moody, D. Medlin, D. Boehme, and D. P. Norwood, "Film thickness effects on the fracture of tantalum nitride on aluminum nitride thin film systems," *Eng. Fract. Mech.*, vol. 61, no. 1, pp. 107–118, Aug. 1998, doi: 10.1016/S0013-7944(98)00055-1.
- [195] J. Olivares, E. Iborra, M. Clement, L. Vergara, J. Sangrador, and A. Sanz-Hervás, "Piezoelectric actuation of microbridges using AlN," *Sens. Actuators Phys.*, vol. 123–124, pp. 590–595, Sep. 2005, doi: 10.1016/j.sna.2005.03.066.
- [196] K. E. Knisely, B. Hunt, B. Troelsen, E. Douglas, B. A. Griffin, and J. E. Stevens, "Method for controlling stress gradients in PVD aluminum nitride," *J. Micromechanics Microengineering*, vol. 28, no. 11, p. 115009, Sep. 2018, doi: 10.1088/1361-6439/aad91a.
- [197] H. Mehner, S. Leopold, and M. Hoffmann, "Variation of the intrinsic stress gradient in thin aluminum nitride films," *J. Micromechanics Microengineering*, vol. 23, no. 9, p. 095030, Aug. 2013, doi: 10.1088/0960-1317/23/9/095030.
- [198] R. Ali, M. Renzelli, M. I. Khan, M. Sebastiani, and E. Bemporad, "Effects of Residual Stress Distribution on Interfacial Adhesion of Magnetron Sputtered AlN and AlN/Al Nanostructured Coatings on a (100) Silicon Substrate," *Nanomaterials*, vol. 8, no. 11, Art. no. 11, Nov. 2018, doi: 10.3390/nano8110896.
- [199] B. Ivira *et al.*, "Solidly mounted resonators aging under harsh environmental conditions," *J. Phys. Conf. Ser.*, vol. 34, pp. 668–673, Apr. 2006, doi: 10.1088/1742-6596/34/1/110.
- [200] B. Ivira, R. Y. Fillit, Ph. Benech, F. Ndagijimana, G. Parat, and P. Ancey, "BAW resonators reliability in the GHz range," in *IECON 2006 - 32nd Annual Conference on IEEE Industrial Electronics*, Nov. 2006, pp. 3133–3138. doi: 10.1109/IECON.2006.347778.
- [201] B. W. Sheldon, A. Rajamani, A. Bhandari, E. Chason, S. K. Hong, and R. Beresford, "Competition between tensile and compressive stress mechanisms during Volmer-Weber growth of aluminum nitride films," *J. Appl. Phys.*, vol. 98, no. 4, p. 043509, Aug. 2005, doi: 10.1063/1.1994944.
- [202] A. Pandey *et al.*, "Growth and evolution of residual stress of AlN films on silicon (100) wafer," *Mater. Sci. Semicond. Process.*, vol. 52, pp. 16–23, Sep. 2016, doi: 10.1016/j.mssp.2016.05.004.
- [203] "Stress control in reactively sputtered AlN and TiN films: Journal of Vacuum Science & Technology A: Vol 5, No 4." <https://avs.scitation.org/doi/abs/10.1116/1.574480> (accessed Jun. 25, 2022).
- [204] L. Zhang, X. Zhang, J. Song, and H. Zheng, "Thermo-induced curvature and interlayer shear stress analysis of MEMS double-layer structure," *Contin. Mech. Thermodyn.*, vol. 32, no. 4, pp. 1127–1139, Jul. 2020, doi: 10.1007/s00161-019-00816-9.
- [205] H.-H. Lo, W.-L. Chen, P. J. Wang, W. Lai, Y.-K. Fuh, and T. T. Li, "Residual stress classification of pulsed DC reactive sputtered aluminum nitride film via large-scale data analysis of optical emission spectroscopy," *Int. J. Adv. Manuf. Technol.*, Jan. 2022, doi: 10.1007/s00170-022-08714-2.
- [206] E. Iborra, J. Olivares, M. Clement, L. Vergara, A. Sanz-Hervás, and J. Sangrador, "Piezoelectric properties and residual stress of sputtered AlN thin films for MEMS applications," *Sens. Actuators Phys.*, vol. 115, no. 2, pp. 501–507, Sep. 2004, doi: 10.1016/j.sna.2004.03.053.
- [207] H. Y. Liu, G. S. Tang, F. Zeng, and F. Pan, "Influence of sputtering parameters on structures and residual stress of AlN films deposited by DC reactive magnetron sputtering at room temperature," *J. Cryst. Growth*, vol. 363, pp. 80–85, Jan. 2013, doi: 10.1016/j.jcrysgro.2012.10.008.
- [208] A. Assali, F. Laidoudi, R. Serhane, F. Kanouni, and O. Mezilet, "Highly Enhanced Electroacoustic Properties of YAlN/Sapphire Based Surface Acoustic Wave Devices for Next Generation of Microelectromechanical Systems," *Mater. Today Commun.*, vol. 26, p. 102067, Mar. 2021, doi: 10.1016/j.mtcomm.2021.102067.

- [209] P. Daoust, M. Côté, P. Desjardins, and R. A. Masut, "Impact of applied biaxial stress on the piezoelectric, elastic, and dielectric properties of scandium aluminum nitride alloys determined by density functional perturbation theory," *AIP Adv.*, vol. 11, no. 9, p. 095017, Sep. 2021, doi: 10.1063/5.0065744.
- [210] M. A. Caro *et al.*, "Piezoelectric coefficients and spontaneous polarization of ScAlN," *J. Phys. Condens. Matter*, vol. 27, no. 24, p. 245901, May 2015, doi: 10.1088/0953-8984/27/24/245901.
- [211] M. Akiyama, K. Kano, and A. Teshigahara, "Influence of growth temperature and scandium concentration on piezoelectric response of scandium aluminum nitride alloy thin films," *Appl. Phys. Lett.*, vol. 95, no. 16, p. 162107, Oct. 2009, doi: 10.1063/1.3251072.
- [212] Z. Gu, J. H. Edgar, J. Pomeroy, M. Kuball, and D. W. Coffey, "Crystal growth and properties of scandium nitride," *J. Mater. Sci. Mater. Electron.*, vol. 15, no. 8, pp. 555–559, Aug. 2004, doi: 10.1023/B:JMSE.0000032591.54107.2c.
- [213] R. Niewa, D. A. Zherebtsov, M. Kirchner, M. Schmidt, and W. Schnelle, "New Ways to High-Quality Bulk Scandium Nitride," *Chem. Mater.*, vol. 16, no. 25, pp. 5445–5451, Dec. 2004, doi: 10.1021/cm048667y.
- [214] S. Satoh, K. Ohtaka, T. Shimatsu, and S. Tanaka, "Crystal structure deformation and phase transition of AlScN thin films in whole Sc concentration range," *J. Appl. Phys.*, vol. 132, no. 2, p. 025103, Jul. 2022, doi: 10.1063/5.0087505.
- [215] S. Mertin *et al.*, "Enhanced piezoelectric properties of c-axis textured aluminium scandium nitride thin films with high scandium content: Influence of intrinsic stress and sputtering parameters," in *2017 IEEE International Ultrasonics Symposium (IUS)*, Sep. 2017, pp. 1–4. doi: 10.1109/ULTSYM.2017.8092187.
- [216] J. Tang, D. Niu, Z. Tai, and X. Hu, "Deposition of highly c-axis-oriented ScAlN thin films at different sputtering power," *J. Mater. Sci. Mater. Electron.*, vol. 28, no. 7, pp. 5512–5517, Apr. 2017, doi: 10.1007/s10854-016-6213-7.
- [217] R. Petrich *et al.*, "Investigation of ScAlN for piezoelectric and ferroelectric applications," in *2019 22nd European Microelectronics and Packaging Conference & Exhibition (EMPC)*, Sep. 2019, pp. 1–5. doi: 10.23919/EMPC44848.2019.8951824.
- [218] A. Pérez-Campos, M. Sinusía Lozano, F. J. Garcia-Garcia, Z. Chen, and G. F. Iriarte, "Synthesis of ScAlN thin films on Si (100) substrates at room temperature," *Microsyst. Technol.*, vol. 24, no. 6, pp. 2711–2718, Jun. 2018, doi: 10.1007/s00542-017-3660-x.
- [219] C. S. Sandu *et al.*, "Impact of negative bias on the piezoelectric properties through the incidence of abnormal oriented grains in Al_{0.62}Sc_{0.38}N thin films," *Thin Solid Films*, vol. 697, p. 137819, Mar. 2020, doi: 10.1016/j.tsf.2020.137819.
- [220] K. Knisely, E. Douglas, J. Mudrick, M. Rodriguez, and P. Kotula, "Thickness dependence of Al_{0.88}Sc_{0.12}N thin films grown on silicon," *Thin Solid Films*, vol. 675, pp. 66–72, Apr. 2019, doi: 10.1016/j.tsf.2019.02.023.
- [221] M. S. Lozano *et al.*, "Piezoelectric characterization of Sc_{0.26}Al_{0.74}N layers on Si (001) substrates," *Mater. Res. Express*, vol. 5, no. 3, p. 036407, Mar. 2018, doi: 10.1088/2053-1591/aab232.
- [222] J. Yang, X. Meng, C. Yang, and Y. Zhang, "Influence of sputtering power on crystal quality and electrical properties of Sc-doped AlN film prepared by DC magnetron sputtering," *Appl. Surf. Sci.*, vol. 287, pp. 355–358, Dec. 2013, doi: 10.1016/j.apsusc.2013.09.155.
- [223] J. Tang, D. Niu, Y. Yang, D. Zhou, and C. Yang, "Preparation of ScAlN films as a function of sputtering atmosphere," *J. Mater. Sci. Mater. Electron.*, vol. 27, no. 5, pp. 4788–4793, May 2016, doi: 10.1007/s10854-016-4359-y.
- [224] R.-D. Cong, H. Cui, J. Zhang, and Q.-L. Cui, "Synthesis and Characterization of Rare Earth Nitride ScN and YN Microcrystalline," *Journal of Inorganic Materials*, pp. 1171–1176, 2016.
- [225] A. le Febvrier, N. Tureson, N. Stalkerich, G. Greczynski, and P. Eklund, "Effect of impurities on morphology, growth mode, and thermoelectric properties of (111) and (001) epitaxial-like ScN films," *J. Phys. Appl. Phys.*, vol. 52, no. 3, p. 035302, Nov. 2018, doi: 10.1088/1361-6463/aaeb1b.

- [226] S. Barth *et al.*, “Sputter deposition of stress-controlled piezoelectric AlN and AlScN films for ultrasonic and energy harvesting applications,” *IEEE Trans. Ultrason. Ferroelectr. Freq. Control*, vol. 61, no. 8, pp. 1329–1334, Aug. 2014, doi: 10.1109/TUFFC.2014.3040.
- [227] P. Pobedinskas *et al.*, “Thickness dependent residual stress in sputtered AlN thin films,” *Thin Solid Films*, vol. 522, pp. 180–185, Nov. 2012, doi: 10.1016/j.tsf.2012.08.015.
- [228] M. Reusch *et al.*, “Microstructure and mechanical properties of stress-tailored piezoelectric AlN thin films for electro-acoustic devices,” *Appl. Surf. Sci.*, vol. 407, pp. 307–314, Jun. 2017, doi: 10.1016/j.apsusc.2017.02.147.
- [229] J. Olivares *et al.*, “Combined assessment of piezoelectric AlN films using X-ray diffraction, infrared absorption and atomic force microscopy,” *Diam. Relat. Mater.*, vol. 16, no. 4, pp. 1421–1424, Apr. 2007, doi: 10.1016/j.diamond.2006.11.065.
- [230] P. M. Mayrhofer *et al.*, “Microstructure and piezoelectric response of YxAl1-xN thin films,” *Acta Mater.*, vol. 100, pp. 81–89, Nov. 2015, doi: 10.1016/j.actamat.2015.08.019.
- [231] A. e Žukauskaite *et al.*, “YxAl1-xN thin films,” *J. Phys. Appl. Phys.*, vol. 45, no. 42, p. 422001, Oct. 2012, doi: 10.1088/0022-3727/45/42/422001.
- [232] C. Tholander, I. A. Abrikosov, L. Hultman, and F. Tasnádi, “Volume matching condition to establish the enhanced piezoelectricity in ternary (Sc,Y)0.5(Al,Ga,In)0.5N alloys,” *Phys. Rev. B*, vol. 87, no. 9, p. 094107, Mar. 2013, doi: 10.1103/PhysRevB.87.094107.
- [233] T. H. Okabe, T. N. Deura, T. Oishi, K. Ono, and D. R. Sadoway, “Electrochemical deoxidation of yttrium-oxygen solid solutions,” *J. Alloys Compd.*, vol. 237, no. 1, pp. 150–154, Apr. 1996, doi: 10.1016/0925-8388(95)02129-9.
- [234] S. Mertin *et al.*, “Piezoelectric and structural properties of c-axis textured aluminium scandium nitride thin films up to high scandium content,” *Surf. Coat. Technol.*, vol. 343, pp. 2–6, Jun. 2018, doi: 10.1016/j.surfcoat.2018.01.046.
- [235] S. Khan *et al.*, “Texture of the nano-crystalline AlN thin films and the growth conditions in DC magnetron sputtering,” *Prog. Nat. Sci. Mater. Int.*, vol. 25, no. 4, pp. 282–290, Aug. 2015, doi: 10.1016/j.pnsc.2015.08.006.
- [236] S. Manna, G. L. Brennecka, V. Stevanović, and C. V. Ciobanu, “Tuning the piezoelectric and mechanical properties of the AlN system via alloying with YN and BN,” *J. Appl. Phys.*, vol. 122, no. 10, p. 105101, Sep. 2017, doi: 10.1063/1.4993254.
- [237] E. Smecca *et al.*, “AlN texturing and piezoelectricity on flexible substrates for sensor applications,” *Appl. Phys. Lett.*, vol. 106, no. 23, p. 232903, Jun. 2015, doi: 10.1063/1.4922229.
- [238] M. Akiyama, C.-N. Xu, K. Nonaka, K. Shobu, and T. Watanabe, “Statistical approach for optimizing sputtering conditions of highly oriented aluminum nitride thin films,” *Thin Solid Films*, vol. 315, no. 1, pp. 62–65, Mar. 1998, doi: 10.1016/S0040-6090(97)00697-4.
- [239] Y. Bian *et al.*, “Aluminum nitride thin film growth and applications for heat dissipation,” *Surf. Coat. Technol.*, vol. 267, pp. 65–69, Apr. 2015, doi: 10.1016/j.surfcoat.2014.11.060.
- [240] H. Jin *et al.*, “Deposition of c-axis orientation aluminum nitride films on flexible polymer substrates by reactive direct-current magnetron sputtering,” *Thin Solid Films*, vol. 520, no. 15, pp. 4863–4870, May 2012, doi: 10.1016/j.tsf.2012.03.015.
- [241] M. Clement, E. Iborra, J. Sangrador, A. Sanz-Hervás, L. Vergara, and M. Aguilar, “Influence of sputtering mechanisms on the preferred orientation of aluminum nitride thin films,” *J. Appl. Phys.*, vol. 94, no. 3, pp. 1495–1500, Aug. 2003, doi: 10.1063/1.1587267.
- [242] S. S. Chauhan, M. M. Joglekar, and S. K. Manhas, “Influence of Process Parameters and Formation of Highly c-Axis Oriented AlN Thin Films on Mo by Reactive Sputtering,” *J. Electron. Mater.*, vol. 47, no. 12, pp. 7520–7530, Dec. 2018, doi: 10.1007/s11664-018-6695-6.
- [243] P. M. Mayrhofer, C. Eisenmenger-Sittner, M. Stöger-Pollach, H. Euchner, A. Bittner, and U. Schmid, “The impact of argon admixture on the c-axis oriented growth of direct current magnetron sputtered ScxAl1-xN thin films,” *J. Appl. Phys.*, vol. 115, no. 19, p. 193505, May 2014, doi: 10.1063/1.4876260.

- [244] J. Schulte and G. Sobe, "Magnetron sputtering of aluminium using oxygen or nitrogen as reactive gas," *Thin Solid Films*, vol. 324, no. 1, pp. 19–24, Jul. 1998, doi: 10.1016/S0040-6090(97)01197-8.
- [245] E. Särhammar, E. Strandberg, N. Martin, and T. Nyberg, "Sputter Rate Distribution and Compositional Variations in Films Sputtered from Elemental and Multi-Element Targets at Different Pressures," *Int. J. Mater. Sci. Appl.*, vol. 3, no. 2, Art. no. 2, Jan. 2014, doi: 10.11648/j.ijmsa.20140302.14.
- [246] M. Akiyama, T. Kamohara, K. Kano, A. Teshigahara, and N. Kawahara, "Influence of oxygen concentration in sputtering gas on piezoelectric response of aluminum nitride thin films," *Appl. Phys. Lett.*, vol. 93, no. 2, p. 021903, Jul. 2008, doi: 10.1063/1.2957654.
- [247] M. A. Signore *et al.*, "Role of oxygen contaminant on the physical properties of sputtered AlN thin films," *J. Alloys Compd.*, vol. 649, pp. 1267–1272, Nov. 2015, doi: 10.1016/j.jallcom.2015.05.289.
- [248] L. Vergara *et al.*, "Influence of oxygen and argon on the crystal quality and piezoelectric response of AlN sputtered thin films," *Diam. Relat. Mater.*, vol. 13, no. 4, pp. 839–842, Apr. 2004, doi: 10.1016/j.diamond.2003.10.063.
- [249] A. Mahmood *et al.*, "Optical and surface analysis of DC-reactive sputtered AlN films," *Diam. Relat. Mater.*, vol. 12, no. 8, pp. 1315–1321, Aug. 2003, doi: 10.1016/S0925-9635(03)00076-1.
- [250] M. Schneider, "Einfluss der Schichtdicke und der Substratvorbehandlung auf die elektromechanischen Eigenschaften von gesputterten Aluminiumnitriddünnfilmen," Thesis, TU Wien, 2014.
- [251] T. Tabaru and M. Akiyama, "Residual stress reduction in piezoelectric Sc_{0.4}Al_{0.6}N films by variable-pressure sputtering from 0.4 to 1.0 Pa," *Thin Solid Films*, vol. 692, p. 137625, Dec. 2019, doi: 10.1016/j.tsf.2019.137625.
- [252] M. Fischeneder, E. Wistrela, A. Bittner, M. Schneider, and U. Schmid, "Tailored wafer holder for a reliable deposition of sputtered aluminium nitride thin films at low temperatures," *Mater. Sci. Semicond. Process.*, vol. 71, pp. 283–289, Nov. 2017, doi: 10.1016/j.mssp.2017.08.010.
- [253] M. Fischeneder, A. Bittner, M. Schneider, and U. Schmid, "Enhanced process stability for the low temperature sputter deposition of aluminium nitride thin films," *Mater. Res. Express*, vol. 5, no. 6, p. 066412, Jun. 2018, doi: 10.1088/2053-1591/aac9db.
- [254] M. B. Assouar, O. Elmazria, L. Le Brizoual, M. Belmahi, and P. Alnot, "Growth of piezoelectric aluminium nitride for layered SAW devices," in *Proceedings of the 2002 IEEE International Frequency Control Symposium and PDA Exhibition (Cat. No.02CH37234)*, May 2002, pp. 333–336. doi: 10.1109/FREQ.2002.1075903.
- [255] H. Cheng, Y. Sun, and P. Hing, "The influence of deposition conditions on structure and morphology of aluminum nitride films deposited by radio frequency reactive sputtering," *Thin Solid Films*, vol. 434, no. 1, pp. 112–120, Jun. 2003, doi: 10.1016/S0040-6090(03)00428-0.
- [256] T. P. Drüsedau and J. Bläsing, "Optical and structural properties of highly c-axis oriented aluminum nitride prepared by sputter-deposition in pure nitrogen," *Thin Solid Films*, vol. 377–378, pp. 27–31, Dec. 2000, doi: 10.1016/S0040-6090(00)01380-8.
- [257] F. Hörich *et al.*, "Demonstration of lateral epitaxial growth of AlN on Si (111) at low temperatures by pulsed reactive sputter epitaxy," *J. Cryst. Growth*, vol. 571, p. 126250, Oct. 2021, doi: 10.1016/j.jcrysgro.2021.126250.
- [258] J. P. Kar, G. Bose, and S. Tuli, "A study on the interface and bulk charge density of AlN films with sputtering pressure," *Vacuum*, vol. 81, no. 4, pp. 494–498, Nov. 2006, doi: 10.1016/j.vacuum.2006.07.006.
- [259] J. A. Pérez Taborda, J. C. Caicedo, M. Grisales, W. Saldarriaga, and H. Riascos, "Deposition pressure effect on chemical, morphological and optical properties of binary Al-nitrides," *Opt. Laser Technol.*, vol. 69, pp. 92–103, Jun. 2015, doi: 10.1016/j.optlastec.2014.12.009.

- [260] M. Schlögl, M. Schneider, and U. Schmid, "Design and Simulation of a Scalable Hybrid Energy Harvesting Device for Low Frequency Rotations," *J. Phys. Conf. Ser.*, vol. 1837, no. 1, p. 012007, Mar. 2021, doi: 10.1088/1742-6596/1837/1/012007.
- [261] S. Schmid, L. G. Villanueva, and M. L. Roukes, *Fundamentals of Nanomechanical Resonators*. Cham: Springer International Publishing, 2016. doi: 10.1007/978-3-319-28691-4.
- [262] A. Erturk and D. J. Inman, "An experimentally validated bimorph cantilever model for piezoelectric energy harvesting from base excitations," *Smart Mater. Struct.*, vol. 18, no. 2, p. 025009, Jan. 2009, doi: 10.1088/0964-1726/18/2/025009.
- [263] K. Naeli and O. Brand, "Dimensional considerations in achieving large quality factors for resonant silicon cantilevers in air," *J. Appl. Phys.*, vol. 105, no. 1, p. 014908, Jan. 2009, doi: 10.1063/1.3062204.
- [264] L. V. Minh, M. Hara, T. Yokoyama, T. Nishihara, M. Ueda, and H. Kuwano, "Highly piezoelectric MgZr co-doped aluminum nitride-based vibrational energy harvesters [Correspondence]," *IEEE Trans. Ultrason. Ferroelectr. Freq. Control*, vol. 62, no. 11, pp. 2005–2008, Nov. 2015, doi: 10.1109/TUFFC.2014.006750.
- [265] Y. Zhang *et al.*, "Comparative study on equivalent models calculating magnetic force between permanent magnets," *J. Intell. Manuf. Spec. Equip.*, vol. 1, no. 1, pp. 43–65, Jan. 2020, doi: 10.1108/JIMSE-09-2020-0009.
- [266] J. Hagedorn, F. S.-L. Blanc, and J. Fleischer, Eds., *Handbook of Coil Winding*. Berlin, Heidelberg: Springer, 2018. doi: 10.1007/978-3-662-54402-0.
- [267] M. Schlögl, S. Köpl, J. Hiesberger, M. Schneider, and U. Schmid, "Mechanical and electrical characterization of resonant piezoelectric microbridges for strain sensing," *Sens. Actuators Phys.*, vol. 346, p. 113829, Oct. 2022, doi: 10.1016/j.sna.2022.113829.
- [268] S. Bouwstra and B. Geijselaers, "On the resonance frequencies of microbridges," in *TRANSDUCERS '91: 1991 International Conference on Solid-State Sensors and Actuators. Digest of Technical Papers*, Jun. 1991, pp. 538–542. doi: 10.1109/SENSOR.1991.148932.
- [269] M. A. Hopcroft, W. D. Nix, and T. W. Kenny, "What is the Young's Modulus of Silicon?," *J. Microelectromechanical Syst.*, vol. 19, no. 2, pp. 229–238, Apr. 2010, doi: 10.1109/JMEMS.2009.2039697.
- [270] M. C. Salvadori, I. G. Brown, A. R. Vaz, L. L. Melo, and M. Cattani, "Measurement of the elastic modulus of nanostructured gold and platinum thin films," *Phys. Rev. B*, vol. 67, no. 15, p. 153404, Apr. 2003, doi: 10.1103/PhysRevB.67.153404.
- [271] J. Lintymer, N. Martin, J.-M. Chappé, P. Delobelle, and J. Takadoum, "Nanoindentation of chromium zigzag thin films sputter deposited," *Surf. Coat. Technol.*, vol. 200, no. 1, pp. 269–272, Oct. 2005, doi: 10.1016/j.surfcoat.2005.02.066.
- [272] J. J. Wortman and R. A. Evans, "Young's Modulus, Shear Modulus, and Poisson's Ratio in Silicon and Germanium," *J. Appl. Phys.*, vol. 36, no. 1, pp. 153–156, Jan. 1965, doi: 10.1063/1.1713863.
- [273] J. G. Noel, "Review of the properties of gold material for MEMS membrane applications," *IET Circuits Devices Syst.*, vol. 10, no. 2, pp. 156–161, 2016, doi: 10.1049/iet-cds.2015.0094.
- [274] "Material Property Database: PVD Chromium," *Material Property Database*, May 06, 2022. <http://www.mit.edu/~6.777/matprops/chromium.htm> (accessed May 06, 2022).
- [275] Markku Tilli *et al.*, *Handbook of Silicon Based MEMS Materials and Technologies - 1st Edition*. Elsevier, 2009.
- [276] S. Venkataraj, D. Severin, R. Drese, F. Koerfer, and M. Wuttig, "Structural, optical and mechanical properties of aluminium nitride films prepared by reactive DC magnetron sputtering," *Thin Solid Films*, vol. 502, no. 1, pp. 235–239, Apr. 2006, doi: 10.1016/j.tsf.2005.07.281.
- [277] A. W. Leissa, "Vibration of Plates," *ZAMM - J. Appl. Math. Mech.*, vol. 51, no. 3, pp. 243–243, 1969, doi: 10.1002/zamm.19710510331.
- [278] A. R. Behera, H. Shaik, G. M. Rao, and R. Pratap, "A Technique for Estimation of Residual Stress and Young's Modulus of Compressively Stressed Thin Films Using Microfabricated

- Beams," *J. Microelectromechanical Syst.*, vol. 28, no. 6, pp. 1039–1054, Dec. 2019, doi: 10.1109/JMEMS.2019.2948016.
- [279] X. Song and H. Liu, "Free Vibration of Bistable Clamped-Clamped Beams: A Preliminary Study," presented at the ASME 2020 International Design Engineering Technical Conferences and Computers and Information in Engineering Conference, Nov. 2020. doi: 10.1115/DETC2020-22560.
- [280] H. Wang *et al.*, "Vibration of mechanically-assembled 3D microstructures formed by compressive buckling," *J. Mech. Phys. Solids*, vol. 112, pp. 187–208, Mar. 2018, doi: 10.1016/j.jmps.2017.12.002.
- [281] A. H. Nayfeh, W. Kreider, and T. J. Anderson, "Investigation of natural frequencies and mode shapes of buckled beams," *AIAA J.*, May 2012, doi: 10.2514/3.12669.
- [282] Y. Yang *et al.*, "Nonlinearity of Degenerately Doped Bulk-Mode Silicon MEMS Resonators," *J. Microelectromechanical Syst.*, vol. 25, no. 5, pp. 859–869, Oct. 2016, doi: 10.1109/JMEMS.2016.2586099.
- [283] H. M. Ouakad and M. I. Younis, "The dynamic behavior of MEMS arch resonators actuated electrically," *Int. J. Non-Linear Mech.*, vol. 45, no. 7, pp. 704–713, Sep. 2010, doi: 10.1016/j.ijnonlinmec.2010.04.005.
- [284] F. Tajaddodianfar, M. R. H. Yazdi, and H. N. Pishkenari, "Nonlinear dynamics of MEMS/NEMS resonators: analytical solution by the homotopy analysis method," *Microsyst. Technol.*, vol. 23, no. 6, pp. 1913–1926, Jun. 2017, doi: 10.1007/s00542-016-2947-7.
- [285] D. Younesian, M. Sadri, and E. Esmailzadeh, "Primary and secondary resonance analyses of clamped–clamped micro-beams," *Nonlinear Dyn.*, vol. 76, no. 4, pp. 1867–1884, Jun. 2014, doi: 10.1007/s11071-014-1254-z.
- [286] N. Kacem, S. Hentz, D. Pinto, B. Reig, and V. Nguyen, "Nonlinear dynamics of nanomechanical beam resonators: improving the performance of NEMS-based sensors," *Nanotechnology*, vol. 20, no. 27, p. 275501, Jun. 2009, doi: 10.1088/0957-4484/20/27/275501.
- [287] P. Majda and J. Skrodzewicz, "A modified creep model of epoxy adhesive at ambient temperature," *Int. J. Adhes. Adhes.*, vol. 29, no. 4, pp. 396–404, Jun. 2009, doi: 10.1016/j.ijadhadh.2008.07.010.
- [288] M. Dolz, M. J. Hernández, and J. Delegido, "Creep and recovery experimental investigation of low oil content food emulsions," *Food Hydrocoll.*, vol. 22, no. 3, pp. 421–427, May 2008, doi: 10.1016/j.foodhyd.2006.12.011.
- [289] L. Belsito, M. Ferri, and A. Roncaglia, "Large Strain Measurements by Vacuum-Packaged MemS Resonators Manufactured on Ultrathin Silicon Chips," in *2019 20th International Conference on Solid-State Sensors, Actuators and Microsystems Eurosensors XXXIII (TRANSDUCERS EUROSENSORS XXXIII)*, Jun. 2019, pp. 2009–2012. doi: 10.1109/TRANSDUCERS.2019.8808240.
- [290] B. D. Sosnowchik, R. G. Azevedo, D. R. Myers, M. W. Chan, A. P. Pisano, and L. Lin, "Rapid Silicon-to-Steel Bonding by Induction Heating for MEMS Strain Sensors," *J. Microelectromechanical Syst.*, vol. 21, no. 2, pp. 497–506, Apr. 2012, doi: 10.1109/JMEMS.2011.2179013.
- [291] M. Kucera *et al.*, "Design-dependent performance of self-actuated and self-sensing piezoelectric-AlN cantilevers in liquid media oscillating in the fundamental in-plane bending mode," *Sens. Actuators B Chem.*, vol. 200, pp. 235–244, Sep. 2014, doi: 10.1016/j.snb.2014.04.048.
- [292] S. Tiwari, R. Kumar, S. A. Chandorkar, and R. Pratap, "Fully Differential Actuation and Sensing in Piezoelectric Diaphragm Resonators for High Signal to Background Resonant Sensing," *J. Microelectromechanical Syst.*, vol. 29, no. 5, pp. 888–893, Oct. 2020, doi: 10.1109/JMEMS.2020.3001246.
- [293] A. W. Leissa, "On a curve veering aberration," *Z. Für Angew. Math. Phys. ZAMP*, vol. 25, no. 1, pp. 99–111, Jan. 1974, doi: 10.1007/BF01602113.
- [294] R. W. Claassen and C. J. Thorne, "Vibrations of a Rectangular Cantilever Plate," *J. Aerosp. Sci.*, vol. 29, no. 11, pp. 1300–1305, Nov. 1962, doi: 10.2514/8.9800.

- [295] A. Z. Hajjaj, N. Alcheikh, and M. I. Younis, "The static and dynamic behavior of MEMS arch resonators near veering and the impact of initial shapes," *Int. J. Non-Linear Mech.*, vol. 95, pp. 277–286, Oct. 2017, doi: 10.1016/j.ijnonlinmec.2017.07.002.
- [296] N. Alcheikh, A. Z. Hajjaj, and M. I. Younis, "Highly sensitive and wide-range resonant pressure sensor based on the veering phenomenon," *Sens. Actuators Phys.*, vol. 300, p. 111652, Dec. 2019, doi: 10.1016/j.sna.2019.111652.
- [297] N. Alcheikh, H. M. Ouakad, S. B. Mbarek, and M. I. Younis, "Crossover/Veering in V-Shaped MEMS Resonators," *J. Microelectromechanical Syst.*, pp. 1–13, 2021, doi: 10.1109/JMEMS.2021.3126551.
- [298] N. Alcheikh, S. B. Mbarek, S. Amara, and M. I. Younis, "Highly Sensitive Resonant Magnetic Sensor Based on the Veering Phenomenon," *IEEE Sens. J.*, vol. 21, no. 12, pp. 13165–13175, Jun. 2021, doi: 10.1109/JSEN.2021.3065733.
- [299] T. Rabenimanana, V. Walter, N. Kacem, P. Le Moal, G. Bourbon, and J. Lardiès, "Mass sensor using mode localization in two weakly coupled MEMS cantilevers with different lengths: Design and experimental model validation," *Sens. Actuators Phys.*, vol. 295, pp. 643–652, Aug. 2019, doi: 10.1016/j.sna.2019.06.004.
- [300] V. Pachkawade, "State-of-the-Art in Mode-Localized MEMS Coupled Resonant Sensors: A Comprehensive Review," *IEEE Sens. J.*, vol. 21, no. 7, pp. 8751–8779, Apr. 2021, doi: 10.1109/JSEN.2021.3051240.
- [301] C. Gui, R. Legtenberg, H. A. C. Tilmans, J. H. J. Fluitman, and M. Elwenspoek, "Nonlinearity and hysteresis of resonant strain gauges," *J. Microelectromechanical Syst.*, vol. 7, no. 1, pp. 122–127, Mar. 1998, doi: 10.1109/84.661394.
- [302] S. Schmid, B. Malm, and A. Boisen, "Quality factor improvement of silicon nitride micro string resonators," in *2011 IEEE 24th International Conference on Micro Electro Mechanical Systems*, Jan. 2011, pp. 481–484. doi: 10.1109/MEMSYS.2011.5734466.
- [303] S. A. Fedorov *et al.*, "Generalized dissipation dilution in strained mechanical resonators," *Phys. Rev. B*, vol. 99, no. 5, p. 054107, Feb. 2019, doi: 10.1103/PhysRevB.99.054107.
- [304] S. Schmid, L. G. Villanueva, and M. L. Roukes, "Quality Factor," in *Fundamentals of Nanomechanical Resonators*, S. Schmid, L. G. Villanueva, and M. L. Roukes, Eds. Cham: Springer International Publishing, 2016, pp. 57–90. doi: 10.1007/978-3-319-28691-4_2.
- [305] Q. P. Unterreithmeier, E. M. Weig, and J. P. Kotthaus, "Universal transduction scheme for nanomechanical systems based on dielectric forces," *Nature*, vol. 458, no. 7241, Art. no. 7241, Apr. 2009, doi: 10.1038/nature07932.
- [306] S. S. Verbridge, J. M. Parpia, R. B. Reichenbach, L. M. Bellan, and H. G. Craighead, "High quality factor resonance at room temperature with nanostrings under high tensile stress," *J. Appl. Phys.*, vol. 99, no. 12, p. 124304, Jun. 2006, doi: 10.1063/1.2204829.
- [307] B. M. Zwickl *et al.*, "High quality mechanical and optical properties of commercial silicon nitride membranes," *Appl. Phys. Lett.*, vol. 92, no. 10, p. 103125, Mar. 2008, doi: 10.1063/1.2884191.
- [308] S. P. Beeby, G. Ensell, B. R. Baker, M. J. Tudor, and N. M. White, "Micromachined silicon resonant strain gauges fabricated using SOI wafer technology," *J. Microelectromechanical Syst.*, vol. 9, no. 1, pp. 104–111, Mar. 2000, doi: 10.1109/84.825784.
- [309] M.-C. Park and S.-W. Kim, "Compensation of phase change on reflection in white-light interferometry for step height measurement," *Opt. Lett.*, vol. 26, no. 7, pp. 420–422, Apr. 2001, doi: 10.1364/OL.26.000420.
- [310] A. Keshmiri, X. Deng, and N. Wu, "New energy harvester with embedded piezoelectric stacks," *Compos. Part B Eng.*, vol. 163, pp. 303–313, Apr. 2019, doi: 10.1016/j.compositesb.2018.11.028.
- [311] C. Wang, Z. Song, Z. Gao, G. Yu, and S. Wang, "Preparation and performance research of stacked piezoelectric energy-harvesting units for pavements," *Energy Build.*, vol. 183, pp. 581–591, Jan. 2019, doi: 10.1016/j.enbuild.2018.11.042.
- [312] M. Dorfmeister, "Piezoelectrically actuated bistable MEMS membranes for acoustic applications," Thesis, Wien, 2020.

- [313] J. Qiu, J. H. Lang, and A. H. Slocum, "A curved-beam bistable mechanism," *J. Microelectromechanical Syst.*, vol. 13, no. 2, pp. 137–146, Apr. 2004, doi: 10.1109/JMEMS.2004.825308.
- [314] C. Goll, W. Bacher, B. Büstgens, D. Maas, W. Menz, and W. K. Schomburg, "Microvalves with bistable buckled polymer diaphragms," *J. Micromechanics Microengineering*, vol. 6, no. 1, p. 77, Mar. 1996, doi: 10.1088/0960-1317/6/1/017.
- [315] R. Xu, H. Akay, and S.-G. Kim, "Buckled MEMS Beams for Energy Harvesting from Low Frequency Vibrations," *Research*, vol. 2019, Aug. 2019, doi: 10.34133/2019/1087946.
- [316] B. Andò, S. Baglio, A. R. Bulsara, V. Marletta, I. Medico, and S. Medico, "A double piezo — Snap through buckling device for energy harvesting," in *2013 Transducers & Eurosensors XXVII: The 17th International Conference on Solid-State Sensors, Actuators and Microsystems (TRANSDUCERS & EUROSENSORS XXVII)*, Jun. 2013, pp. 43–45. doi: 10.1109/Transducers.2013.6626696.
- [317] S. D. Caliskan, S. Kang, V. Rajaram, Z. Qian, and M. Rinaldi, "Threshold-Triggered Mems-Cmos Infrared Resonant Detector with Near-Zero Standby Power Consumption," in *2019 20th International Conference on Solid-State Sensors, Actuators and Microsystems & Eurosensors XXXIII (TRANSDUCERS & EUROSENSORS XXXIII)*, Jun. 2019, pp. 637–640. doi: 10.1109/TRANSDUCERS.2019.8808404.
- [318] K. Allidina, M. A. Taghvaei, F. Nabki, P.-V. Cicek, and M. N. El-Gamal, "A MEMS-based vacuum sensor with a PLL frequency-to-voltage converter," in *2009 16th IEEE International Conference on Electronics, Circuits and Systems - (ICECS 2009)*, Dec. 2009, pp. 583–586. doi: 10.1109/ICECS.2009.5410846.

Abbreviations

AlN	aluminum nitride
AlScN	aluminum scandium nitride
AlYN	aluminum yttrium nitride
BOX	burried oxide
DAQ	data acquisition board
DFT	density functional theory
EDX	energy dispersive X-ray spectroscopy
EGD	European Green Deal
EH	energy harvester
EMH	electromagnetic harvester
EMHE	electromagnetic harvesting element
FOM	figure of merit
FWHM	full width at half maximum
GMST	global mean surface temperature
HEH	hybrid energy harvester
HRTEM	high resolution transmission electron microscopy
IA	impedance analyzer
IoT	internet of things
IPCC	international panel on climate change
KNN	potassium sodium niobate
LDV	laser Doppler vibrometer
MEMS	micro electromechanical system
MSA	micro system analyzer
PEHE	piezoelectric harvesting element
PLA	polylactic acid
PM	permanent magnet
PR	Poisson ratio
PVD	physical vapor deposition
PZT	lead zirconate titanate
RF	radio frequency
SAED	selected area electron diffraction
Sc	scandium
SEM	scanning electron microscopy
Si	silicon
SOI	silicon on insulator
TEM	transmission electron microscopy
TM	tip magnet
VE	vibrational exciter
WSN	wireless sensor network
XRD	X-ray diffractometry
Y	yttrium
YM	Youngs modulus

Publications

Journal papers as first author:

- **M. Schlögl**, M. Schneider, und U. Schmid, „Piezoelectricity in Y0.09Al0.91N thin films“, Mater. Sci. Eng. B, vol. 276, p. 115543, 2022, doi: 10.1016/j.mseb.2021.115543.
- **M. Schlögl**, S. Köpl, J. Hiesberger, M. Schneider, und U. Schmid, „Mechanical and electrical characterization of resonant piezoelectric microbridges for strain sensing“, Sens. Actuators Phys., vol. 346, p. 113829, 2022, doi: 10.1016/j.sna.2022.113829.
- **M. Schlögl**, J. Weißenbach, M. Schneider, und U. Schmid, „Stress engineering of polycrystalline aluminum nitride thin films for strain sensing with resonant piezoelectric microbridges“, Sens. Actuators Phys., vol. 349, p. 114067, 2023, doi: 10.1016/j.sna.2022.114067.

Journal papers as co-author:

- F. Patocka, **M. Schlögl**, M. Schneider, und U. Schmid, „Novel MEMS Sensor for Detecting Magnetic Particles in Liquids“, Proceedings, vol. 2, no. 13, 2018, doi: 10.3390/proceedings2130868.
- F. Patocka, **M. Schlögl**, C. Schneidhofer, N. Dörr, M. Schneider, und U. Schmid, „Piezoelectrically excited MEMS sensor with integrated planar coil for the detection of ferrous particles in liquids“, Sens. Actuators B Chem., vol. 299, p. 126957, 2019, doi: 10.1016/j.snb.2019.126957.

Conference Talks:

- **M. Schlögl**, M. Schneider, und U. Schmid, „Design and Simulation of a Scalable Hybrid Energy Harvesting Device for Low Frequency Rotations“, J. Phys. Conf. Ser., vol. 1837, no. 1, p. 012007, 2021, doi: 10.1088/1742-6596/1837/1/012007.

